Investigation of materials for alkali-ion and zinc-gas batteries

A Thesis Submitted for the Degree of

Doctor of Philosophy

By

Surishi Vashishth

JNCASR

Chemistry and Physics of Materials Unit
Jawaharlal Nehru Centre for Advanced Scientific Research
(A Deemed University)
Bangalore - 560064 (INDIA)

January 2024

Dedicated to my admirable parents

&

brother

DECLARATION

I hereby declare that the thesis entitled "***Investigation of materials for alkali-ion and zinc-gas batteries.***" is an authentic record of research work carried out by me at the Chemistry and Physics of Materials Unit, Jawaharlal Nehru Centre for Advanced Scientific Research, Bangalore, India under the supervision of **Prof. M. Eswaramoorthy** and that it has not been submitted elsewhere for the award of any degree or diploma.

In keeping with the general practice in reporting scientific observations, due acknowledgment has been made whenever the work described is based on the findings of other investigators. Any omission that might have occurred due to oversight or error in judgment is regretted.

Surishi

Surishi Vashishth

Jawaharlal Nehru
Centre for Advanced
Scientific Research

JNCASR

Prof. M. Eswaramoorthy
Chemistry and Physics of Materials Unit
Jawaharlal Nehru Centre for Advanced
Scientific Research (JNCASR)
Bangalore-560064, India
Phone : +91 80 2208 2870

E-mail: eswar@jncasr.ac.in

Date
January 12, 2024

CERTIFICATE

I hereby certify that the work described in this thesis titled “***Investigation of materials for alkali-ion and zinc-gas batteries***” has been carried out by **Surishi Vashishth** at the Chemistry and Physics of Materials Unit, Jawaharlal Nehru Centre for Advanced Scientific Research, Bangalore, India under my supervision and it has not been submitted elsewhere for the award of any degree or diploma.

M. Eswaramoorthy
(Research Supervisor)

ACKNOWLEDGEMENTS

I extend my profound gratitude to those who provided invaluable assistance throughout my Ph.D. journey. At the forefront is my research supervisor, **Prof. M. Eswaramoorthy***, whose consistent support was a cornerstone of my academic endeavor. Engaging in research under his esteemed guidance was not only professionally enriching but also personally rewarding. His introduction to the realms of materials science and batteries has been instrumental in my academic development. I am particularly grateful for the autonomy he afforded me in selecting research topics, which has been pivotal in my scholarly growth. His vibrant enthusiasm, continuous encouragement, and steadfast support played a significant role in the realization of my research. Prof. Eswaramoorthy's incisive and thought-provoking inquiries consistently inspired deeper exploration and comprehension of complex subjects. His stature as an individual is marked by exemplary ethics and principles, making him a paragon in both the professional and personal spheres. The entirety of my doctoral studies was a journey marked by incessant learning, not only in scientific domains but also in life lessons, a fact continuously emphasized by my mentor. The experience with Prof. Eswaramoorthy was exceptionally enlightening and gratifying.*

I wish to convey my deepest appreciation to **Prof. C. N. R. Rao, FRS***, for being an unwavering source of inspiration throughout my research journey. Additionally, I am sincerely thankful to him for cultivating a dynamic and stimulating research environment, which has been instrumental in facilitating the progress of my work.*

I would like to thank Prof. Sridhar Rajaram for introducing me to research in my initial 6 months of Ph.D. His teachings on the importance of punctuality, discipline and perfectionism helped me to get back on track during the long journey of Ph.D.

I thank the past and present chairpersons of CPMU for allowing me to use the various facilities of the centre.

I am thankful to Prof. Hemalatha Balaram from JNCASR, Prof. Siddharth P. Sarma, Prof. N. Ravishankar and Prof. S. Sampath from IISc for their informative courseworks.

My special thanks to my labmates, the "Nanocat" group members. I would like to segregate this into two groups: the senior group and the present group. I would like to thank the senior group members Dr. Amritroop Achari, Dr. Dheeraj Kumar Singh, Dr. Sisir Maity, Dr. Sonu K.P., Dr. Soumita Chakraborty and Dr. Suchismita Biswas for creating a wonderful learning atmosphere throughout my Ph.D. I thoroughly enjoyed the intellectually rich environment created by them. I would also like to thank them for being very supportive and affectionate. I *would like to especially thank Dr. Dheeraj for introducing me to the field of batteries. My heart holds immense gratitude for my current lab members, Soumita, Suchi di , Momin, Divya, Nijita, Abhishek, Swaraj, Daizy, Ujjwal, Elizabeth and Avinash. I would also like to thank some of the visiting researchers Subbu, Dr. Mehraj, Dr. Shivanna M., Dr. Sushumna, Dr. Monoj Kumar and Dr. Sudhakar for their cooperation and useful discussions. I will be eternally grateful to the "Nanocat" family for creating such a vibrant work atmosphere.*

I would like to specially thank who will always be alive in the memories. Your presence is greatly missed.

It is a great pleasure to thank Prof. Premkumar Senguttuvan, Prof. Kanishka Biswas and Prof. Peter Sebastian.

I am thankful to DESY-India for providing me with an opportunity to perform EXAFS measurements.

I would like to thank a special bunch of people for chilling moments and parties: Rohit, Vinita, Nijita, Soumita, Suchi, Swaraj, Abhishek, Ankit, Daizy, Bhupesh, Divya, Akshay, Shashank, Reetendra, Nikita di, Meenakshi di (Pahwa and Tayade), Devesh and Aditi.

I am thankful to the following people for various technical assistance: Mrs. Usha (TEM); Mr. Kanan, Ms. Meenkashi and Mrs. Selvi (FESEM); Mr. Vasu (IR, TGA); Mr. Sachin (XPS); Mr. Kanan, Mr. Arun and Mr. Rahul (TEM), Mr. Anil (XRD), Mrs. Durgasri (NMR), Mr. Nandkishore, Mrs. Remya (XPS) and Mr. Rajkumar. I would like to especially thank Mr. Raja Subramaniam for providing excellent research assistance. I am grateful to Ujjwal (Ph.D.), Raghavendra, Vijay, Shalini and Roshiny for working with me on various projects.

I am thankful to the academic and administrative staff of JNCASR for their assistance.

Besides the research life, I am thankful to Prof. M. Eswaramoorthy and his family members for their hospitality and affection.

Financial assistance from JNCASR is gratefully acknowledged.

A deep sense of gratitude to my parents, for their constant support to me in every aspect.

Surishi

PREFACE

This thesis is divided into two parts. **Part 1** deals with using a boron-doped graphene anode for alkali-ion batteries and also the influence of SEI formation followed by tin/carbon composite as anode for Li-ion batteries. **Part 2** covers the synthesis and application of Pd-based electrocatalysts for Zn-air and Zn-CO_2 batteries.

Part 1:

Chapter 1.1 offers an in-depth analysis of anode materials for alkali-ion batteries, i.e., lithium, sodium, and potassium ions. It delves into the fundamental properties required of anode materials, such as capacity, stability, rate capability, and safety. Various anode materials, including graphite, silicon/tin, and phosphides/sulfides, are discussed, focusing on their ion-hosting abilities and associated challenges. Strategies like nanostructuring to enhance performance are examined. Additionally, the chapter addresses the significant influence of electrolytes and the solid electrolyte interphase on battery efficiency and the preparation methods of electrodes and electrolytes. Furthermore, the necessary measurements for evaluating anode and electrolyte performance are reviewed. This chapter is an essential guide for comprehending the progress and obstacles in the anode/ electrolyte technology field specific to alkali-ion batteries.

Chapter 1.2a focuses on boron-doped thermally exfoliated graphene (BTEG) as a universal anode material for alkali-ion batteries. BTEG demonstrates promising capacity values of 1014 mAh g^{-1}, 315 mAh g^{-1}, and 369 mAh g^{-1} at 25 mA g^{-1} for Li, Na, and K ion batteries respectively. Long-term cycling stability at a high current density of 1 A g^{-1} shows capacity retention of 75%, 100%, and 87% for Li, Na, and K ion batteries, respectively. Mechanistic studies are carried out to understand the type of active sites for alkali ion charge storage, which are responsible for their universal performance as an anode. Operando Raman measurement helps track microstructural changes on cycling with Li/ Na/ K. Diffusion and reaction kinetics are monitored for BTEG with Li, Na, K on charge/discharge by galvanostatic intermittent titration technique and in-situ electrochemical impedance spectroscopy.

Chapter 1.2b discusses the understanding of solid electrolyte interphase (SEI) that forms on BTEG and Li/ Na/ K metal surfaces. Symmetric cell studies of alkali metals show higher polarization losses associated with potassium-based electrolytes, i.e., KPF_6, than $LiPF_6$ and $NaPF_6$. The optimization from 0.8M KPF_6 to 5M KFSI reduces polarization losses and, therefore, increases the reversibility of BTEG for K ion batteries. X-ray photoelectron spectroscopy (XPS) technique was used to analyze SEI on BTEG for all electrolytes. It shows higher inorganic content for 5M KFSI than 0.8M KPF_6, which helps attain high-capacity retention values, as shown in Chapter 2a. This comprehensive study underscores the importance of electrolyte composition in the performance and durability of alkali ion batteries (half-cell configuration).

Chapter 1.3 presents an industrially viable synthesis strategy of soot-derived tin-carbon with core shell morphology, followed by argon/ hydrogen annealing for Li-ion batteries. The composite is engineered to withstand the extensive volumetric fluctuations inherent in battery anodes' alloying and de-alloying processes. A graphitic carbon matrix ensures a stable electrical conduit to the tin nanoparticles, a critical factor in preserving the anode's structural integrity. Sn/C after H_2 treatment demonstrates remarkable cycle stability, retaining 94.6% after 700 cycles at a high current density of 500 mA g^{-1}.

Part 2:

Chapter 2.1 underscores the development of zinc-gas batteries, particularly Zn-air and Zn-CO_2 batteries, which blend innovation with environmental sustainability. It delves into the electrochemical processes, material science challenges, and the technical aspects of these systems. While Zn-air batteries have evolved from primary to rechargeable forms, furthering Zn-CO_2 batteries' potential in sustainable energy, key challenges remain. These include electrode stability and the reaction kinetics of electrocatalysts for oxygen and CO_2 reduction/evolution reactions. Overcoming these barriers requires a multidisciplinary approach focused on material science and electrochemistry, with ongoing efforts to optimize efficiency by designing various electrocatalysts guided by evaluation and scalability considerations.

Chapter 2.2 discusses an innovatively employed bifunctional boron-carbon-nitrogen (BCN) matrix to anchor palladium nanoparticles and cobalt oxide (Co_3O_4) nanosheets (BCN@CoPd) for oxygen reduction/evolution reaction (ORR/ OER) and zinc-air

battery. Notably, the synergistic interaction of Pd with Co_3O_4 on BCN leads to substantially lower overpotentials, achieving an impressive ultra-low voltage gap (OER and ORR) of just 0.58 V with a low mass loading of 2 $\mu g\ cm^{-2}$. For ORR, BCN@CoPd reached a half-wave potential ($E_{1/2}$) of 0.87V (730 $A\ g^{-1}{}_{Pd}$) with mass activity surpassing platinum/carbon (Pt/C) by 20 times at 0.9V. In OER performance, BCN@CoPd exhibited an overpotential (η_{10}) of 220 mV, better than RuO_2 (300 mV), and showed mass activity which is 317 times higher than RuO_2 at 1.45V (η_{10}). Operando Fourier transform infrared, and Raman spectroscopy revealed O-O stretching and the structural evolution of Pd and Co_3O_4. Leveraging this bifunctional electrocatalytic performance, we achieved a high-capacity, long-lasting rechargeable zinc-air battery with 904 $mAh\ g^{-1}{}_{Zn}$ at 50 $mA\ cm^{-2}$ and stable operation for 330 hours.

Chapter 2.3 presents a detailed analysis of Zn-CO_2 batteries using a nickel-palladium (NiPd) catalyst, which exhibits enhanced Faradaic efficiency and stability compared to pure palladium (Pd). The NiPd catalyst achieved a Faradaic efficiency of 83% for formate production over 1.5 hours of discharge as compared to pure Pd's 45% efficiency over 1 hour at 0.5 $mA\ cm^{-2}$. Notably, the NiPd catalyst maintained its Faradaic efficiency even at increased current densities, showcasing its robustness. In contrast, pure Pd exhibited reduced stability under similar conditions. Furthermore, the NiPd catalyst demonstrated a peak power density of 5 $mW\ cm^{-2}$, markedly higher than the 0.7 $mW\ cm^{-2}$ achieved by pure Pd.

TABLE OF CONTENTS

PART-1

Chapter 1.1: Introduction of anodes for alkali-ion batteries

Chapter-1.2a: Boron doped thermally exfoliated graphene as universal anode for alkali-ion batteries

Chapter-1.2b: Understanding of SEI formation on performance of alkali-ion batteries.

Chapter 1.3: Sn@C composite as an anode for Li-ion battery

PART-2

Chapter 2.1: Introduction to zinc-gas batteries

Chapter 2.2: Pd/Co_3O_4 incorporated BCN composite for Zn-air battery

Chapter 2.3: NiPd as an efficient electrocatalyst for Zinc-CO_2 batteries

Chapter 3: Conclusion

Chapter 4: Perspective

PART 1

Chapter – 1.1

Introduction on anodes for alkali-ion batteries

Summary

This chapter provides a comprehensive overview of anode materials in alkali-ion batteries, focusing on lithium (Li), sodium (Na), and potassium (K) ions. It starts by exploring the fundamental requirements of anode materials, including high capacity, stability, rate capability, and safety. Focusing on anode design, the chapter reviews materials like graphite (intercalation), silicon/ tin (alloying), and phosphides/ sulfides (conversion), emphasizing their ion hosting capacities. Key challenges like volume expansion during ion intercalation are discussed alongside mitigation strategies such as nanostructuring and composite materials to improve performance and longevity. The critical role of electrolytes and the solid electrolyte interphase (SEI) is explored. Preparation methods for electrodes and electrolytes are analyzed for their impact on battery characteristics. The chapter concludes with the essential measurements and analyses to assess anode and electrolyte performance. This comprehensive understanding serves as an academic and concise resource, offering insights into current challenges and innovations in anode technology for alkali-ion batteries.

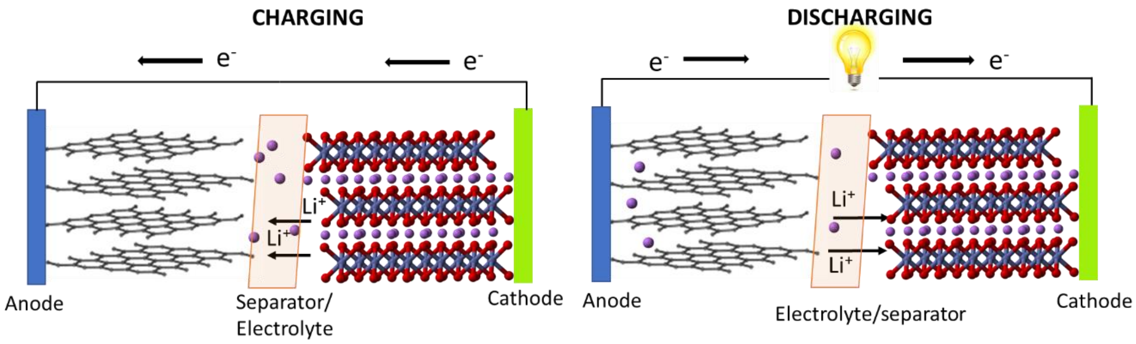

1.1.1 Relevance of energy storage

The global population has surpassed 8 billion, significantly impacting economic and technological advancement. [1]Consequently, this surge in population has spurred an immense worldwide demand for energy, primarily met by the rapidly depleting fossil fuel resources, resulting in severe environmental crises linked to accelerated climate change.[2] The imminent exhaustion of fossil fuels poses a grave threat, making it imperative to explore sustainable alternatives to meet our energy needs. Renewable energy sources, such as wind, solar, nuclear, and hydropower, emerge as the most viable solutions.[3] However, it is essential to acknowledge that wind and solar energy are intermittent, potentially lacking the reliability necessary to satisfy the surging global electricity demand.

To address this challenge, batteries have been introduced into the energy storage market. Batteries are crucial for load leveling in power distribution and storage for renewable energy sources.[4] Batteries dominate the energy market from small-scale products (pacemakers, smoke detectors, wristwatches) to large-scale products (electric motors, submarines, electronic devices). This year, the International Energy Agency (IEA) projects an investment of over USD 1.7 trillion in clean energy initiatives. [5]

1.1.2 History

Batteries have evolved over many years to become a high-performing energy storage solution. It all started around 150 BC and 223 AD with the discovery of the first battery, i.e., the Baghdad battery (**Figure 1**).[6] Although batteries progressed to the invention of the voltaic pile in 1748 by Alessandro Volta, followed by Daniel's cell (1836), they could not be recharged (primary battery). [7]Since then, there have been rapid advancements to achieve rechargeable batteries such as Ni-Cd (1899), Ni-MH (1989), Li-ion (1980), and finally Li-polymer battery (1997). In 2019, Goodenough, Whittingham, and Yoshino won the Nobel Prize for their significant contributions to the development of LIB, which dominates the entire electronic market.[8][9]

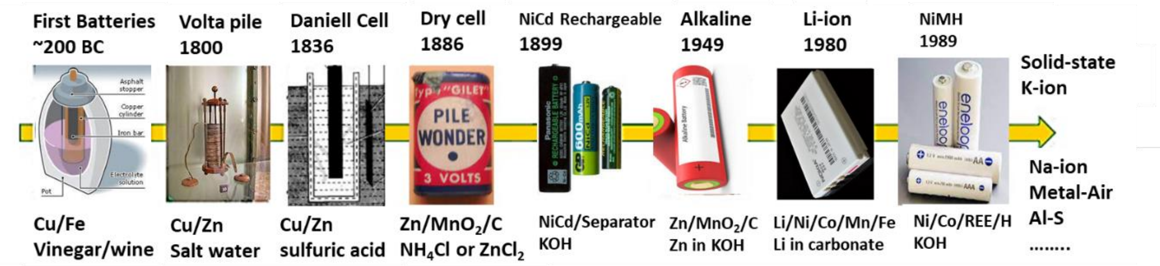

Figure 1. The development of battery.[10]

Li-ion batteries (LIBs), with their high energy density and good cycling stability, are used for various applications, from smartphones, laptops and plug-in hybrid EVs.[11] Such wide applications have convinced automakers and battery companies to commit nearly 300 billion USD to build a raft of gigafactories worldwide. Gigafactories started by Nissan (UK) and followed by Tesla (US) envision supplying Giga Watt hour (GWh) levels of battery manufacturing output with a 1GWh facility providing enough batteries for approximately 17,000 vehicles (**Figure 2**). Large-scale battery production is also used for pharmaceuticals/microchip manufacturing along with car manufacturing facilities.[12]

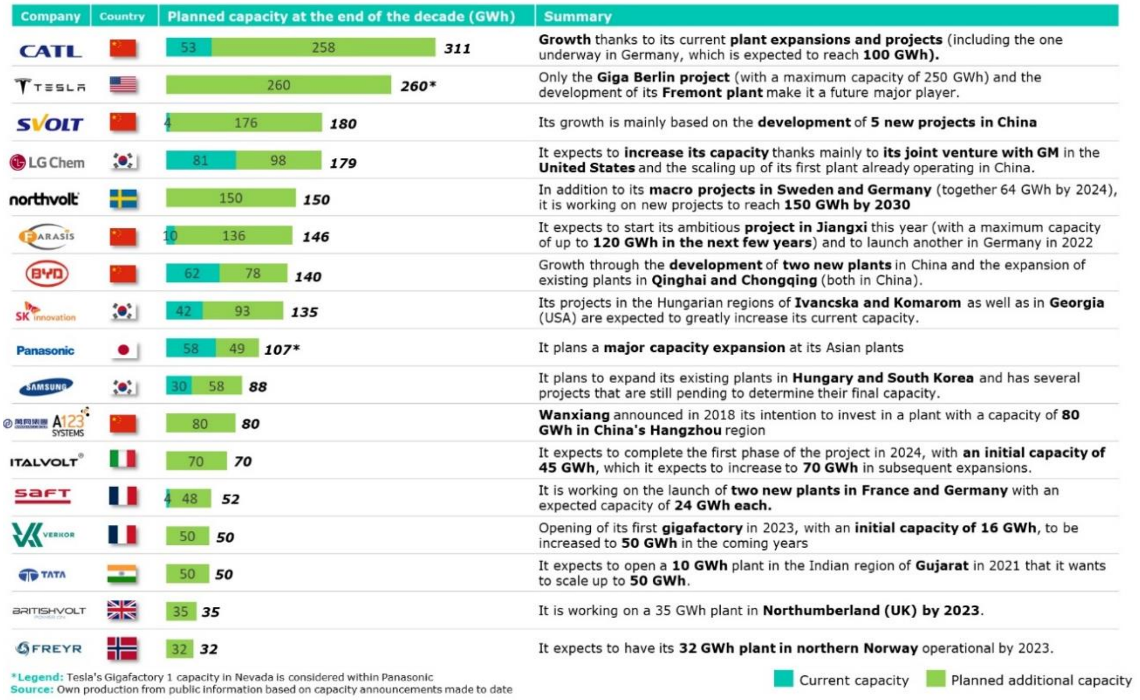

Company	Country	Planned capacity at the end of the decade (GWh)			Summary
		Current capacity	Planned additional capacity		
CATL	🇨🇳	53	258	311	**Growth** thanks to its current **plant expansions and projects** (including the one underway in Germany, which is expected to reach **100 GWh).**
TESLA	🇺🇸		260	260*	Only the **Giga Berlin project** (with a maximum capacity of 250 GWh) and the development of its **Fremont plant** make it a future major player.
SVOLT	🇨🇳	4	176	180	Its growth is mainly based on the **development** of **5 new projects in China**
LG Chem	🇰🇷	81	98	179	It expects to **increase its capacity** thanks mainly to **its joint venture with GM** in the **United States** and the scaling up of its first plant already operating in China.
northvolt	🇸🇪		150	150	In addition to its **macro projects in Sweden and Germany** (together 64 GWh by 2024), it is working on new projects to reach **150 GWh by 2030**
FARASIS	🇨🇳	10	136	146	It expects to start its ambitious **project in Jiangxi** this year (with a maximum capacity of up to **120 GWh in the next few years**) and to launch another in Germany in 2022
BYD	🇨🇳	62	78	140	Growth through the **development** of **two new plants** in China and the expansion of existing plants in **Qinghai and Chongqing** (both in China).
SK innovation	🇰🇷	42	93	135	Its projects in the Hungarian regions of **Ivancska and Komarom** as well as in **Georgia** (USA) are expected to greatly increase its current capacity.
Panasonic	🇯🇵	58	49	107*	It plans a **major capacity expansion** at its Asian plants
SAMSUNG	🇰🇷	30	58	88	It plans to expand its existing plants in **Hungary and South Korea** and has several projects that are still pending to determine their final capacity.
A123 SYSTEMS	🇨🇳		80	80	**Wanxiang** announced in 2018 its intention to invest in a plant with a capacity of **80 GWh in China's Hangzhou** region
ITALVOLT®	🇮🇹		70	70	It expects to complete the first phase of the project in 2024, with **an initial capacity of 45 GWh**, which it expects to increase to **70 GWh** in subsequent expansions.
saft	🇫🇷	4	48	52	It is working on the launch of **two new plants in France and Germany** with an expected capacity of **24 GWh each.**
VERKOR	🇫🇷		50	50	Opening of its first **gigafactory** in 2023, with an **initial capacity of 16 GWh**, to be increased to **50 GWh** in the coming years
TATA	🇮🇳		50	50	It expects to open a **10 GWh** plant in the Indian region of **Gujarat** in 2021 that it wants to scale up to **50 GWh**.
BRITISHVOLT	🇬🇧		35	35	It is working on a 35 GWh plant in **Northumberland (UK) by 2023**.
FREYR	🇳🇴		32	32	It expects to have its **32 GWh plant in northern Norway** operational by 2023.

*Legend: Tesla's Gigafactory 1 capacity in Nevada is considered within Panasonic
Source: Own production from public information based on capacity announcements made to date

🟦 Current capacity 🟩 Planned additional capacity

Figure 2. Evolution of significant companies with initiatives for establishing Gigafactories.[12]

Such a humongous leap in the development of the LIB industry has resulted in significant demand for mineral resources, thus challenging its sustainability. We now face lithium deficiency due to their limited reserve on the earth's crust with a total mass % of 0.0017.[13] Therefore, focussing on alternatives to Li metal to maintain sustainable development is a desperate need of the hour. Batteries with elements having high crustal abundances, such as Na-ion (SIB) (2.3 mass%), K-ion (PIB) (1.5 mass%), Metal-air, Al-S, and solid-state batteries can help reduce the burden on Li production.

LIB surpasses all rechargeable batteries, such as Ni-MH, Ni-Cd, and lead-acid batteries, in terms of their high energy and power density (**Figure 3a**.), as represented in the Energy density plot. [14]This superiority of LIBs makes them desirable for portable electronics, EVs, backup power supplies, and grid storage. With their low cost as a limiting factor for large-scale applications, PIB is a viable candidate with volumetric energy density (**Figure 3b**.) equivalent to LIBs.[15]

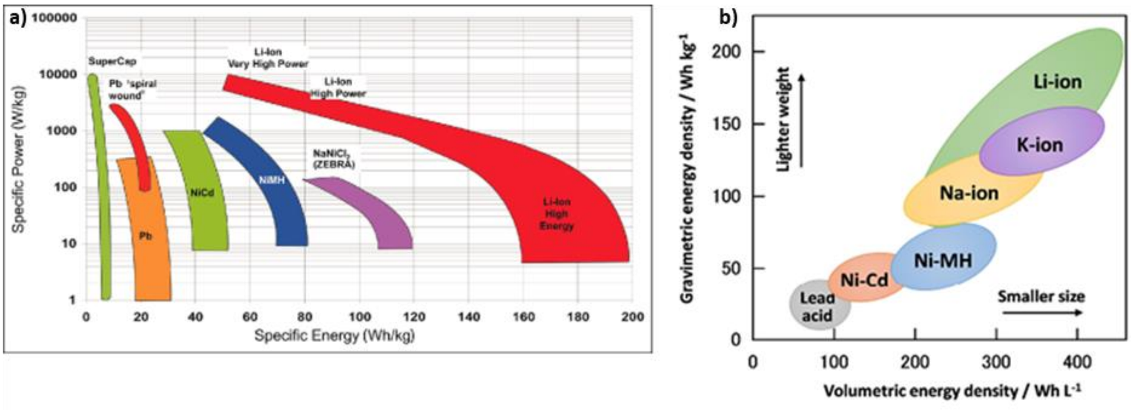

Figure 3. a) Ragone plot[14] and b) energy density for various rechargeable batteries where LIB outperforms. *Reproduced with permission from ref.* [15]

Current electrified vehicle types are targeting development towards low-cost, fast-charge, low cycle life fade (~20%) (reduced energy density with time).[16] So, the design, development, and optimization of electrode materials must be done to achieve the desired goals in the battery industry.

1.1.3 Configuration, principle, and evaluation parameters for Alkali-ion Batteries

To improve the performance of Li/Na/K-ion batteries, it is crucial to have a good understanding of the working mechanism. LIBs have been chosen as a simplified overview of the components of ion batteries and how they work.

The main components of the battery are (**Figure 4**)[17]:

- **Anode (Negative Electrode)**: The anode of a lithium-ion battery is typically made of carbon. During discharge, lithium ions are released from the anode and move towards the cathode.
- **Cathode (Positive Electrode)**: The cathode is usually made of a lithium metal oxide, such as lithium cobalt oxide ($LiCoO_2$) or lithium iron phosphate ($LiFePO_4$). When the battery is discharged, the cathode interacts with lithium ions, creating a flow of electrons.
- **Electrolyte**: A lithium salt dissolved in a solvent (commonly, a mixture of organic carbonates) separates the anode and cathode. It allows lithium ions to move between the two electrodes without electronic conductivity to avoid an internal short circuit.
- **Separator**: A porous separator material keeps the anode and cathode physically separated to prevent short circuits. It also allows the passage of lithium ions.

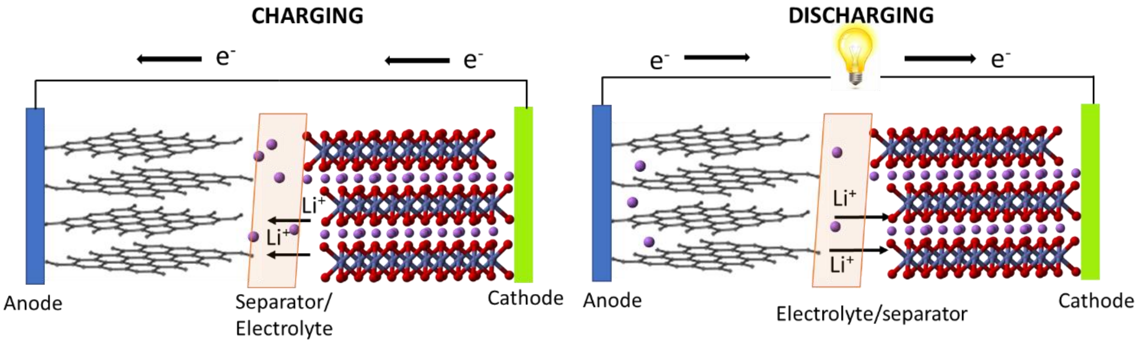

Figure 4. Schematic diagram of commercial rechargeable LIB.[17]

The basic working mechanism for discharge and charge cycles is a rocking-chair model and is as follows:

Discharge:

- When a battery is used to power a device, lithium ions move from the anode to the cathode through the electrolyte.
- As the lithium ions move, electrons are released at the anode and flow through an external circuit to the cathode, creating an electric current that can power a device.
- At the cathode, lithium ions combine with electrons and are stored in the cathode material.

Charge:

- On charging, the electrons are supplied to the anode, causing lithium ions to move back from the cathode to the anode through the electrolyte.
- This process stores energy in the battery by moving lithium ions back to the anode.

The evaluation parameters to understand the role of each alkali-ion have been highlighted below. To improve the performance of alkali-ion batteries, researchers and engineers focus on several key areas:

- **Capacity**: Electrode materials' theoretical gravimetric capacity [18]is dependent on number of reactive electrons (n) per formula unit and molar mass of active material (M) and can be expressed by[19],

$$C_t = n \text{ x } F/3.6\text{x}M \qquad (1)$$

Where F is the Faraday's constant. According to the equation, the lighter the element and the more the number of electrons provide high theoretical specific capacity. With a similar number of electrons for alkali ions, Li exhibits the highest theoretical gravimetric capacity compared to Na and K, respectively, as shown in **Table 1**. On replacing mass with volume of metal, volumetric capacity can be calculated.

Alkali metal	Gravimetric capacity (mAh g^{-1})	Volumetric capacity (mAh cm^{-3})
Li	3860	2062
Na	1165	1128
K	591	2047

Table 1. Comparison of theoretical capacity for Li/Na/K metal for battery.[20][21,22]

- **Energy Density**: Increasing the energy density of ion batteries allows them to store more energy in the same size or weight. The gravimetric energy density (Wh kg^{-1}) is the crucial parameter for lightweight electronics, and it is the product of operating voltage (V) and capacity (mAh g^{-1}). Li has a higher reduction potential vs. standard hydrogen electrode (SHE) (-3.04V) than Na (-2.71V) and is equivalent to K (-2.93V). Therefore, Li exhibits the highest gravimetric energy density, as seen in **Figure 3**, compared to Na and K batteries. The volumetric energy density of Li and K are equivalent and better than Na.[15] This makes Li the first choice for application in lightweight batteries for electronics (smartphones, EVs), while for large-scale application making, potassium is an ideal choice.[23]

- **Cycle Life**: Enhancing the number of charge-discharge cycles a battery can undergo before capacity significantly degrades is essential. This can be achieved through better electrode materials, electrolyte chemistry, and design.
- **Safety**: Safety is paramount, and efforts are made to reduce the risk of thermal runaway and fires, especially in high-performance applications like electric vehicles.
- **Charging Speed**: Faster charging without degrading battery life is a significant focus area to improve user convenience.
- **Environmental Impact**: Reducing the environmental impact of LIBs by using sustainable materials and recycling strategies is also a priority.

1.1.4 Thermodynamic consideration

To attain a high-performance battery, the thermodynamic evaluation of electrodes and electrolytes is crucial to understand. The spontaneity and energetics of battery can be clarified by Gibbs free energy.

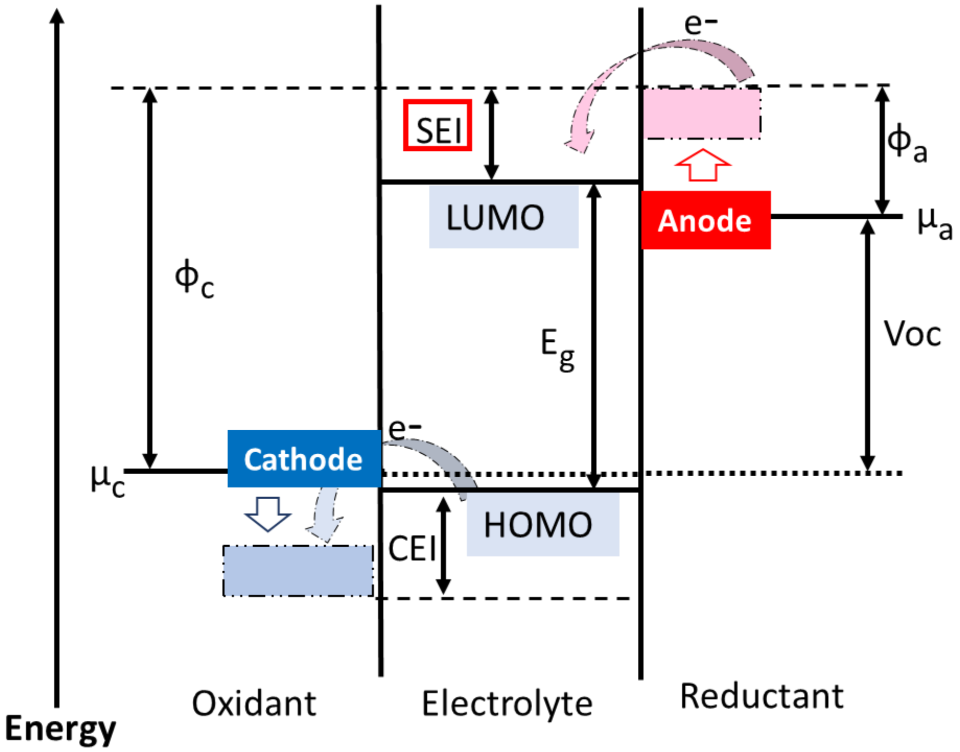

Figure 5. Schematic open circuit energy diagram with μ_A and μ_C for anode and cathode, respectively, and electrolyte degradation to form Solid Electrolyte Interphase (SEI).[17]

The free energy change ΔG is related to its electrochemical cell voltage (E) by

$\Delta G = -nFE$, (2)

Where n is the number of electrons involved in the reaction, and F is Faraday's constant (96487 C/mol). Cell voltage is determined by the anode, cathode, and electrolyte compatibility and can be understood by thermodynamics. The spontaneity of the process varies with the cell voltage.

The working voltage or open circuit voltage (V_{OC}) is the difference between the chemical potential of anode (μ_A) and cathode (μ_C)(**Figure 5**)[17]

$V_{OC} = \mu_A - \mu_C / e \leq Eg$ (3)

Where e is the magnitude of electronic charge, and Eg is the electrolyte's electrochemical stability window. Most importantly, Voc is limited by the thermodynamic stability of organic electrolytes used with anode and cathode. The choice of anode and cathode should be that μ_A lies below LUMO (lowest unoccupied molecular orbital) and μ_C lies above HOMO (highest occupied molecular orbital). Otherwise, the electrolyte is reduced on the anode (/ on the cathode) to form an irreversible solid electrolyte interphase (SEI) film. SEI formation is inevitable in alkali-ions due to their high reduction potential vs. SHE (Li: -3.04V, Na: -2.71V, and K: -2.93V). Notably, SEI allows Li^+ diffusion under a uniform electric field and prevents aggregation of electrochemically active materials.[24]Additionally, due to its electronically isolating nature, it acts as a barrier to avoid further electrolyte decomposition. SEI forms at both anode and cathode and is known as anode/electrolyte interphase (AEI) and cathode/electrolyte interphase (CEI), respectively.

1.1.5 Kinetic consideration

From the above commercial battery setup and thermodynamic understanding from the energy diagram, an elaborate discussion of Li^+ kinetics of battery components (**Figure 6a**) is of utmost importance.

During charging (**Figure 6b**) in LIB, the following steps are known to occur[25][26]:

1) Li^+ ion diffuses within the cathode;

2) Li^+ ion diffuses through the cathode electrolyte interface (CEI);

3) Li^+ ion is solvated by the solvation molecule at the CEI-electrolyte interface;

4) diffusion of solvated Li^+ in the bulk electrolyte;

5) De-solvation of solvated Li^+ at the electrolyte-AEI;

6) Li^+ ion diffuses through AEI and interacts with graphite interphase;

7) Li^+ ion diffusion in bulk graphite and lattice rearrangement.

Li^+ ion diffusion is driven by an electric field, concentration gradient, and convection (electrolyte movement).[27][28] The net flux density J_{Li} is:

$$J_{Li} = -z_{Li}u_{Li}Fc_{Li}\,\nabla\Phi - D_{Li}\nabla c_{Li} + c_{Li}v \qquad (4)$$

Where z_{Li} is the product of charge number, u_{Li} is mobility, F is Faraday constant, c_{Li} is Li^+ concentration, Φ is the gradient of electrolyte potential, and v is movement velocity. The first term represents migration kinetics, while the second and third terms represent diffusion and convection kinetics, respectively, where the convection term is ignorable due to lack of external force (such as stirring).

At nominal charging rates (<2C), the external electric field is mainly from solid-liquid interphase, and migration in the bulk electrolyte is negligible. Therefore, Li^+ transport kinetics can be described by Fick's law[28]:

$$\frac{\partial c(x,t)}{\partial t} = D\frac{\partial^2 c(x,t)}{\partial x^2} \qquad (5)$$

Where c(x.t) is the Li-ion concentration at specific position x (supposed one-dimensional diffusion for simplicity) at time t, and D is the corresponding diffusion coefficient.

At high charging rates (>2C), the migration rate of Li^+ conductivity and electronic conductivity across solid-liquid interphase is highly critical. [29]The diffusion coefficient D_i usually defines Li^+ conductivity in solid materials, which indicates diffusion flux per unit concentration gradient. The diffusion time (t) of Li^+ in electrode materials is:

$$t = \frac{x^2}{qD_i} \qquad (6)$$

Here, x represents the diffusion distance of Li^+ in anodes: q is the dimensionality constant, which is 2, 4, and 6 for 1D, 2D, and 3D diffusion, respectively. To attain a small t, nanomaterial synthesis can help tune diffusion distance (x) to achieve 3D diffusion (q). The electron mobility (σ)considering holes and free electrodes in solid anode materials can be expressed by:

$$\sigma = n_i e m_e + p_i e m_h \qquad (7)$$

Where n_i and p_i are the concentration of electrons and holes respectively and μ represent the mobility of electrons and holes respectively. For fast charging applications, high intrinsic electronic conductivity materials such as carbon, metals, and alloys with zero or negligible bandgap or materials can be modified externally by adding an optimum amount of conducting carbon to assist electronic movement.[26] Modifying the chosen material by tuning porosity, conductive networks can assist in Li^+ transport and electronic moment to facilitate capacity, rate capability, and stability.

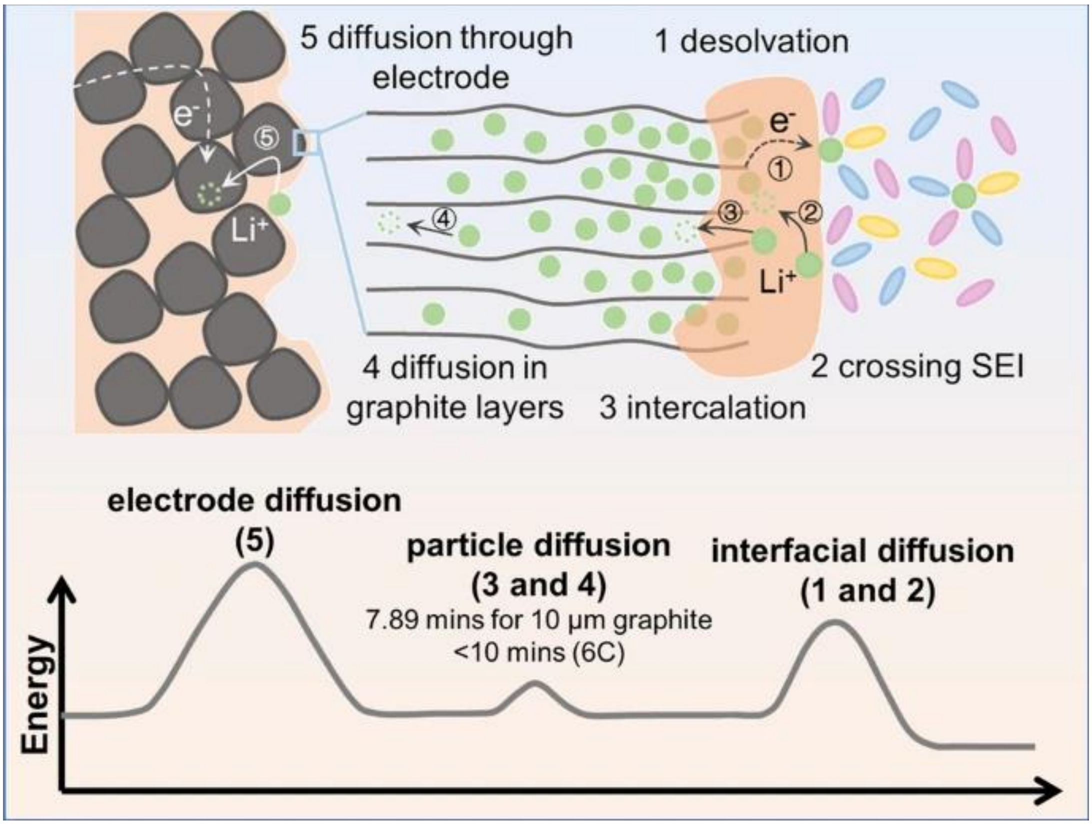

Figure 6. Schematically presented kinetic processes in LIB.[30] b) Three fundamental processes: anode, cathode, and electrolyte.

1.1.6 Criteria for element selection for anode/cathode

The choice of electrode materials depends on varying parameters, i.e., natural abundance and electrochemical performance. In the design of anode and cathode materials, lighter elements with low cost, low toxicity, and high alkali-ions storage are preferred.

1.1.6.1 Anode materials

The anode is a very crucial part of the rechargeable battery in terms of capacity and cyclability. Based on the choice of the element, the overall performance of the battery can be hugely affected. The elements from the periodic table (**Figure 7a**), which can be used as anode materials, have been highlighted. The commercially used anode for LIBs is graphite due to its low cost, nominal capacity, and stability.[31] In order to replace graphite with better-performing anodes, we need to understand the fundamental chemistry involved in various anode materials that have been exploited so far.

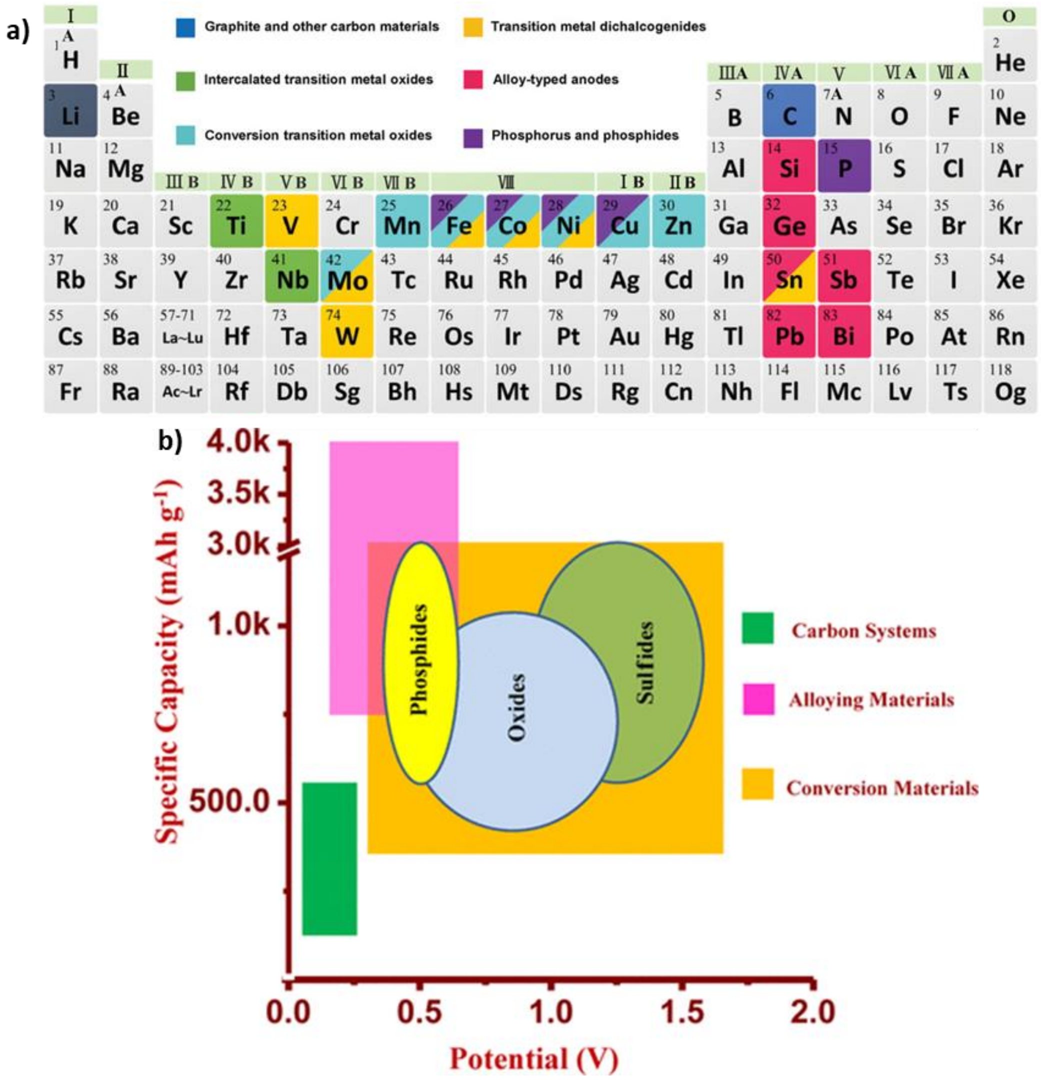

Figure 7. a)Elements in the periodic table that are suitable for interacting with Li for LIBs. [32]b) Different anode materials listed against the Li/Na system. [33]

Anodes follow three different types of reaction chemistries[34] (**Figure 7b**):

i) Intercalation-based anodes:

The mechanism of intercalation-type anode materials is mainly the reversible intercalation and extraction of alkali ions in the lattice of material with a layered structure. The intercalation depends on the crystal and interlayer spacing and the cation size ($Li^+/Na^+/K^+$). Graphite is the most commonly used example, along with titanium-based materials such as TiO_2, $Li_4Ti_5O_{12}$[35], $Na_2Ti_3O_7$,[36] and $NaTi_2(PO_4)_3$[37] have gained much attention in the past two decades, due to their natural abundance, nontoxicity, facile synthesis, and high chemical stability.

In order to understand charging and discharging in intercalation compounds, graphite is the best example, and the equation is as follows:

$$xLi^+ + xe^- + C_6 \longleftrightarrow LxC_6 \qquad (8)$$

The overall stoichiometry of LiC_6 is the highest possible lithium content at ambient conditions, attributing to the theoretical specific capacity of 372 mAh g^{-1} and volumetric capacity of 850 mAh cm^{-3}. To accommodate such high lithium content, the interlayer distance between the graphene layers increases by around 10.4% from 3.35 Å for lithium-free graphite to 3.7 Å for LiC_6. Depending on the content of Li, the de-/lithiation occurs as a staging mechanism, as shown in **Figure 8**. On lithiation, there are consecutive occurrences of the stages n= 1L, 4, 3, 2L, and 2 before eventually reaching stage 1 (completely lithiated). "L" indicates Li^+ arranged in a liquid-like manner and not perfectly ordered within layers.[38] Conclusively, graphite has been most widely studied because of its high stability and commercial relevance. However, certain drawbacks of graphite include low rate and specific capacity, and most importantly, safety risks have prompted further research into modifications of graphite.

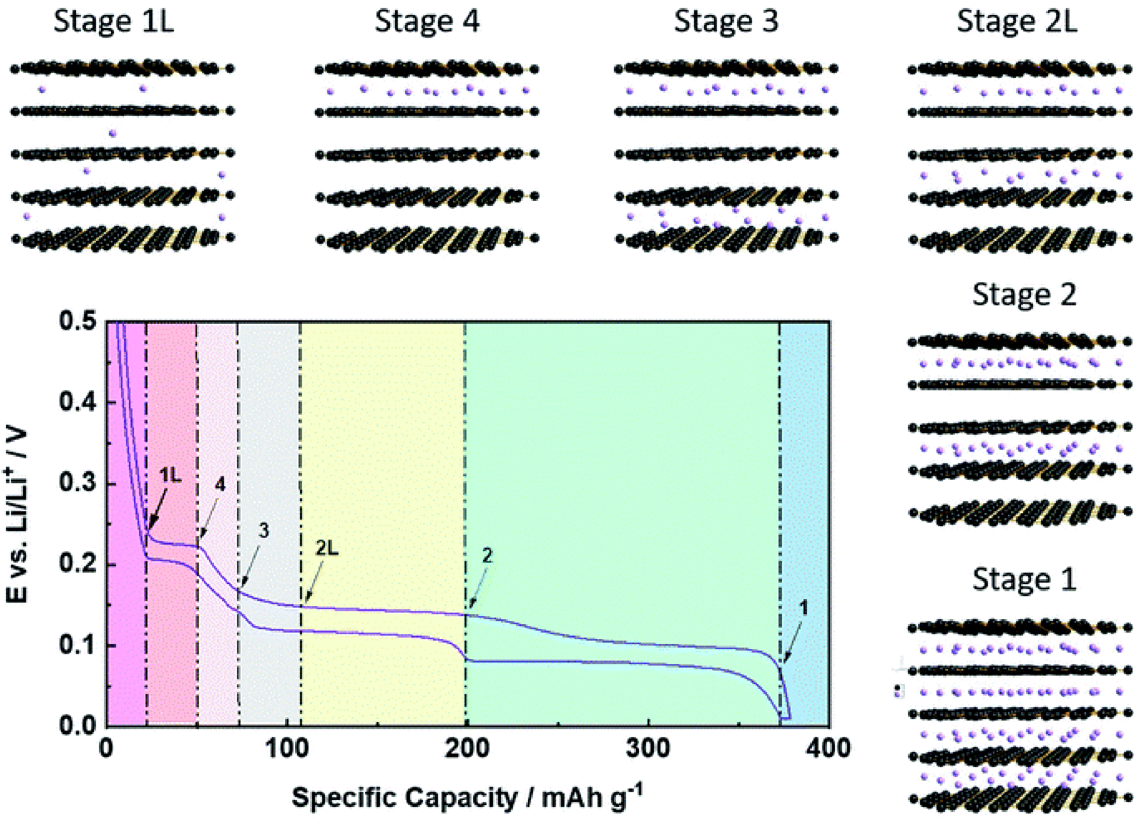

Figure 8. Illustration of staging mechanism on de-/lithitation into graphite with Li as a counter electrode. [38]

Graphite exhibits a capacity of 279 mAh g^{-1} (KC_8) for PIB but merely 30 mAh g^{-1} for SIB (NaC_{64}).[39] Sodium does not undergo intercalation in graphite due to unfavorable thermodynamics.[40] This is due to the positive formation energy of NaC_6, and it can be explained that as ion size decreases, the formation energy becomes less negative (less stable). But, in the trend, Li is an exception due to the formation of covalent interaction, which gives negative formation energy. Due to such limitations, various carbonaceous materials, such as graphene, CNT, SWCNT, hard carbon, etc., are being exploited nowadays (**Chapter 1.2a**).[41]

ii) Alloying-based anodes

In order to overcome the poor capacity of graphite, another class of materials explored is alloy-based materials, which include Si, Sn, Ge, Sb, P, etc. [42]Alloy anodes are known to have higher capacity than graphite, as shown in **Table 2**. Reported alloy materials are mainly composed of elements from Groups IV and V, in which Si and P are nonmetals while others are metals.[43]

Element	Gravimetric capacity (mAh g^{-1})	Lithiated phase	Volume change (LIB) (%)
Si	3579	$Li_{4.4}Si$	400
Sn	994	$Li_{4.4}Sn$	260
Al	993	LiAl	96
Ge	1384	$Li_{4.4}Ge$	370
Sb	660	Li_3Sb	147
P	2600	Li_3P	300

Table 2. Theoretical gravimetric capacity for alloy materials as anodes for Li-ion battery.[43][44]

Among various alloys, Si exhibits the highest capacity, is environmentally friendly, and has a high crustal abundance. The highest capacity of Si with LIB is attributed to $Li_{22}Si_5$ (Li-Si alloy) formation (**Figure 9**) and low molecular weight compared to any other alloy.

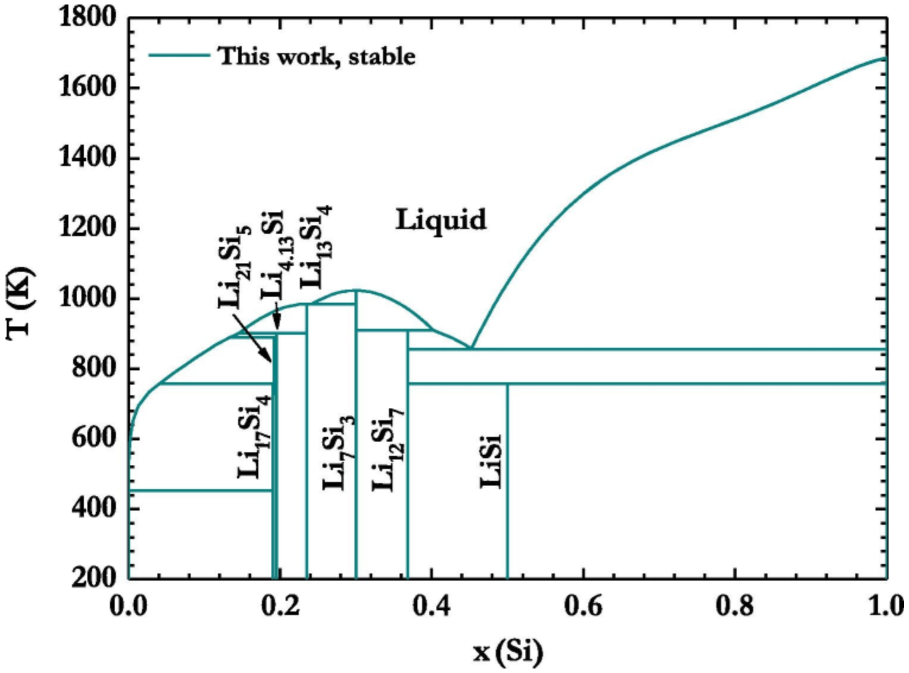

Figure 9. Li-Si phase diagram *was reproduced with permission from ref.* [45]

However, when Si, Sn, or P is used as the active material, its volume expands (**Figure 10**) and shrinks tremendously during Li^+ insertion and extraction.[46] On alloying, they undergo a volume expansion, and on dealloying, contraction occurs, eventually leading to severe degradation on numerous cycles.[47] Finally, this leads to a decline in performance and delamination, making the battery worthless. However, the irreversible SEI layer formation (SEI that forms from electrolyte degradation) on anode materials in the first cycles helps protect the electrode from further electrolyte degradation. Repetitive charge/discharge and volume expansion rupture the SEI at the electrode/electrolyte interface, thereby exposing the fresh electrode surface.[48] This increases electrode resistance due to the thickening of SEI, which also lowers the overall battery performance.

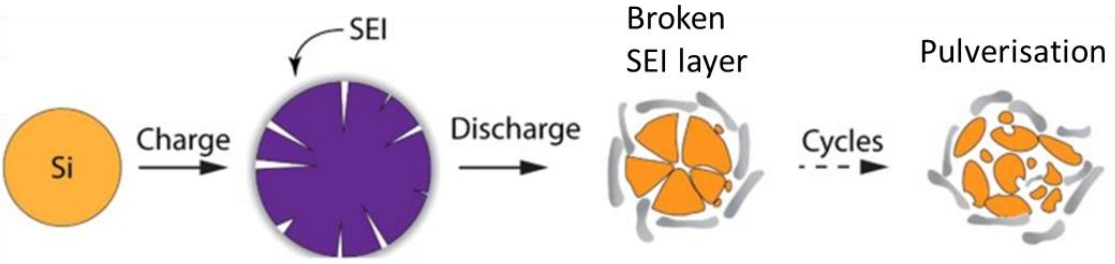

Figure10. Degradation mechanism of silicon particles and unstable SEI on continuous cycling with de-/lithitation.[49]

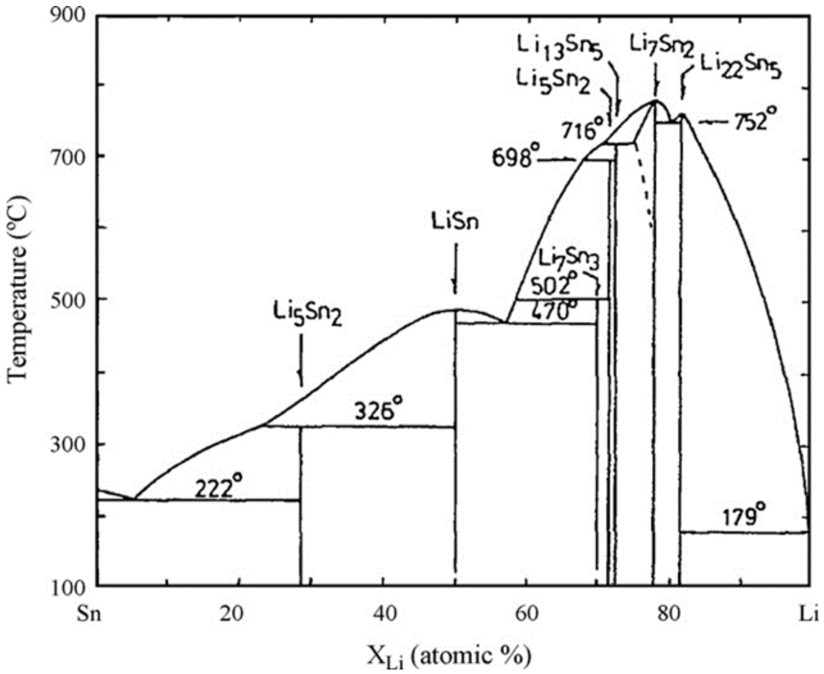

Figure 11. Li-Sn phase diagram with T (temperature) and varying Si and Li content in Sn.[50,51]

Since volume expansion is highest in the case of Si (400%) [52] (**Table 1**.), the attention has shifted to other alloy materials like Sn ($Li_{4.4}Sn$) (**Figure 11**) with a capacity of 991 mAh g^{-1}. (Chen et al. 2022) Sn has an electrical resistivity of $1.1 \times 10^{-7}\ \Omega$ m at room temperature, which is nearly an order of magnitude lower than that of graphite and, due to higher discharge voltage (0-400 mV), reduces safety concerns (**Chapter 1.3**). [53]Pulverization, continuous SEI formation, and delamination from current collectors are still the biggest challenges in alloy-based systems, drastically reducing battery performance. (Chen et al. 2022) In the case of Na, high theoretical capacities of 725 mAh g^{-1} for NaSi and 847 mAh g^{-1} for $Na_{15}Sn_4$ were observed. However, the practical capacity and increase in volume expansion (114% Na-Si, 420% in Na-Sn) with an increase in size from Li^+ to Na^+ reduces battery performance.[46] Such shortcoming, i.e., volume expansion, is mitigated by various morphologies (nanoparticles, nanotubes, etc.) of Sn, Si, and other alloys pairing with an inactive element (Fe, Co, Ni) or composites with carbon.[54]

iii) Conversion-based anodes

Transition metal compounds such as transition metal oxides, sulfides, fluorides, phosphides, and nitrides [55] undergo conversion reactions with Li to give a moderate theoretical capacity in the range of 500 to 1500 mAh g^{-1}.[56,57] The electrochemical reaction can be written in a generalized manner as follows:

$$TM_aX_b + (bxc)Li^+ + (bxc)e^- \longleftrightarrow aTM^0 + bLi_cX \qquad (9)$$

Where TM denotes a transition metal (Ni, Cu, Mn, Zn, Co) and X is oxide/sulfide/fluoride/phosphide. Among various conversion-based compounds, particular interest has been in sulfide and phosphides because of their high theoretical capacity of 1675 mAh g^{-1} and 2596 mAh $g^{-1,}$ respectively.[58] However, sulfide and phosphide have low electrical conductivities of elemental form and lithiated S/P, which results in low utilization (particularly at high current densities). [59,60]Additionally, polysulfide shuttle on recharging is known to cause severe self-discharge.[61] Selenides are another alternative with a lower capacity (675mAh g^{-1}), but due to their higher electrical conductivity than S, they are less prone to shuttling-based degradation.[62] The structure tunability by designing composites of conversion materials with carbonaceous materials assists in high structural stability and rate capability.[63]

It is worth mentioning that on increasing size from Li^+ to Na^+ to $K^{+,}$ volume expansion/ pulverization of electrodes increases immensely.[64] Therefore, morphological control and composites of conversion materials with carbonaceous materials assist in high structural stability and rate capability.

1.1.6.2 Electrolytes and Electrode/Electrolyte interface

State-of-the-art electrolytes for LIBs are based on organic solvents, i.e., carbonate esters solvent and lithium hexafluorophosphate ($LiPF_6$) salt.[65] Similarly, $NaPF_6$ and KPF_6 in carbonate esters-based solvents are commonly used. Commonly used carbonate esters are ethylene carbonate (EC) (crucial for all electrolytes), dimethyl carbonate (DMC), diethyl carbonate (DEC), and ethyl methyl carbonate (EMC) (**Figure 12)** Solvents are chosen on the basis of various factors such as melting point, boiling point and flash point (**Figure 12b**), permittivity, viscosity (**Figure 12c**), and dipole moments (**Figure 12d**).[66] Organic electrolytes with low melting point and high safety (flash point) are highly desired. EC is a typical carbonate ester used and exists in solid (mp: 36.4 °C), and due to the highest dielectric constant, it can be used with other solvents and dissolve metal salts easily. Ester-based solvents are considered better than ether-based solvents for real-time applications (full-cell ion batteries).[67]

In the case of salts, various salts such as $LiPF_6$, $LiClO_4$, $LiBF_4$, $LiN(SO_2F_2)_2$, $LiN(SO_2CF_3)_2$, etc. (**Figure 12e**) and their analogs for Na and K have been chosen. The criteria for choice are on the basis of their electrochemical stability, thermal stability, moisture sensitivity, and conductivity. $Li^+/Na^+/K^+$ are weakly coordinated to anions such $(ClO_4)^-$, $(BF_4)^-$, $(PF_6)^-$, $N(SO_2F_2)_2^-$, $N(SO_2CF_3)_2^-$.[68] The electron-withdrawing groups in anions delocalize the negative charges. Therefore, the interaction between cations and anions is significantly reduced.[69] Therefore, M^+ (M = Li/Na/K) can exist as an M^+-solvation sheath-like structure in bulk electrolytes.

The solvation sheath is understood by comparing the stoke's radii of metal ions. Li^+ (4.8 Å) is larger than Na^+ (4.6 Å) and K^+ (3.6Å) in the most commonly used propylene carbonate (PC)[70] due to the strong Lewis acidity of Li^+-solvent. Therefore, the bulkier size of K^+ exhibits higher ionic conductivity, unlike unfavorable for solid-state diffusion in electrode materials. [64]So far, there are no reports on any single solvent that has high dielectric permittivity (for salt dissolution), low viscosity (facilitate ion transport) as well as electrochemical stability with anode and cathode.

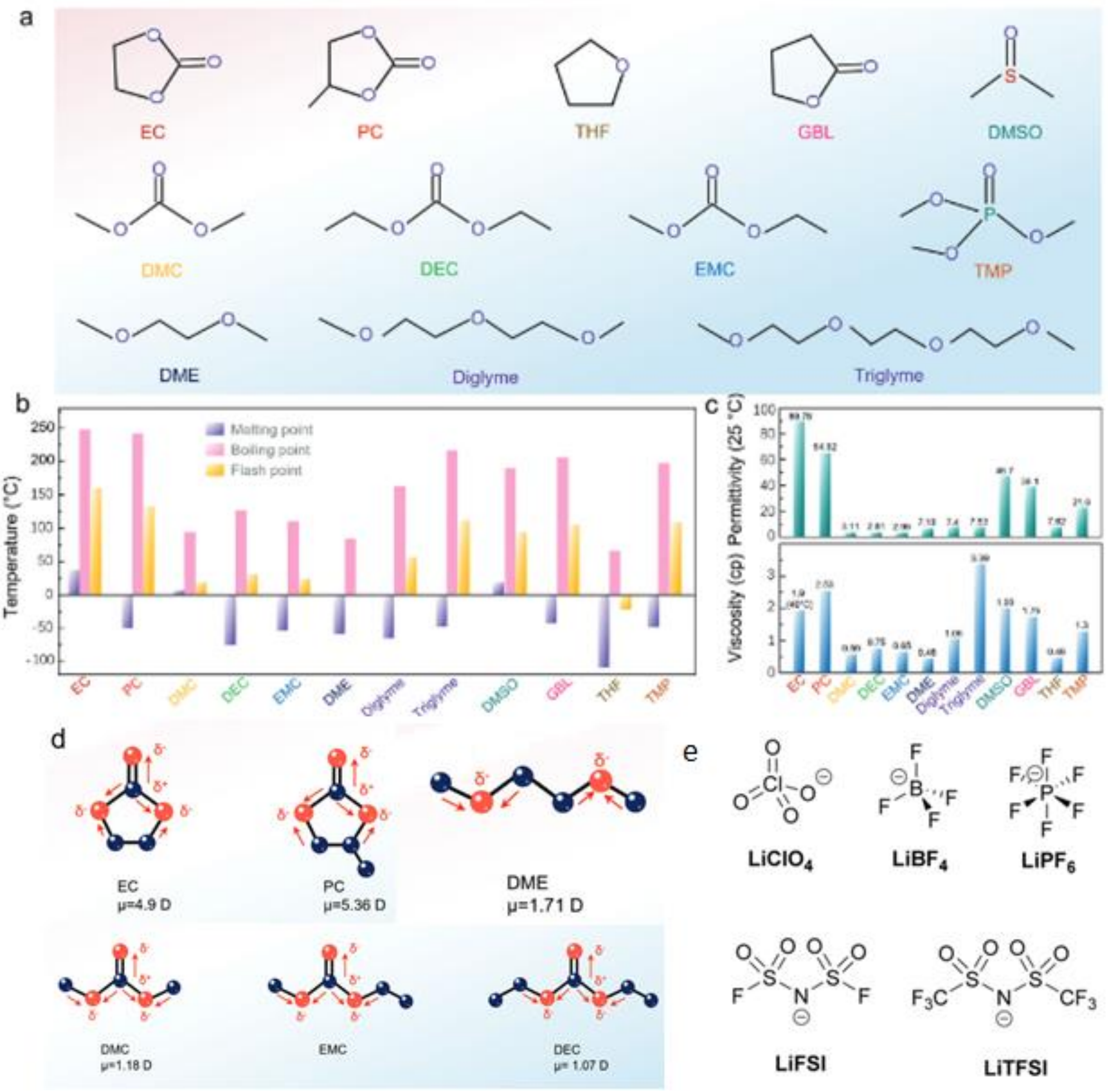

Figure 12. a) Geometrical structure of organic solvents used in ion batteries. The physical properties of a solvent are b) melting point, boiling point, and flash point, and c) permittivity and viscosity. [71] d) Geometric structure of salts used in electrolytes.*Reproduced with permission from reference* [72]

The inevitable instability of electrolytes with electrodes leads to the reduction of electrolytes on the interface and the formation of SEI. In 1979, Peled et al. coined the term SEI and claimed Li+ transport via SEI grain boundaries.[73][74] SEI formation takes place due to the electrochemical reduction of salt and solvent at electrode interphase. Since esters are prone to undergo electrochemical reduction on anode surfaces, SEI formed organic and inorganic moieties from electrolyte decomposition.[75] Solvents such as EC DEC degrade to give organic components such as Li_2CO_3, LiF, $LiOCH_2CH_2OCO_2Li$, ROH, CH_2=CH_2, etc. Salt such as $LiPF_6$ in solvents degrades to give LiF, Li2CO3, LiPxFy, LiPxOFy, etc. The layer close to the Li metal surface comprises low oxidation states, i.e., the inorganic layer, and the outer part of surface films comprises a higher oxidation state, i.e., the organic layer. Li^+ (**Figure 13**) desolvation occurs at the pore diffusion stage and is a rate-limiting step (50 kJ mol^{-1}), which is followed by migration of Li^+ (naked) through interfaces (only 20 kJ mol^{-1}). [76]

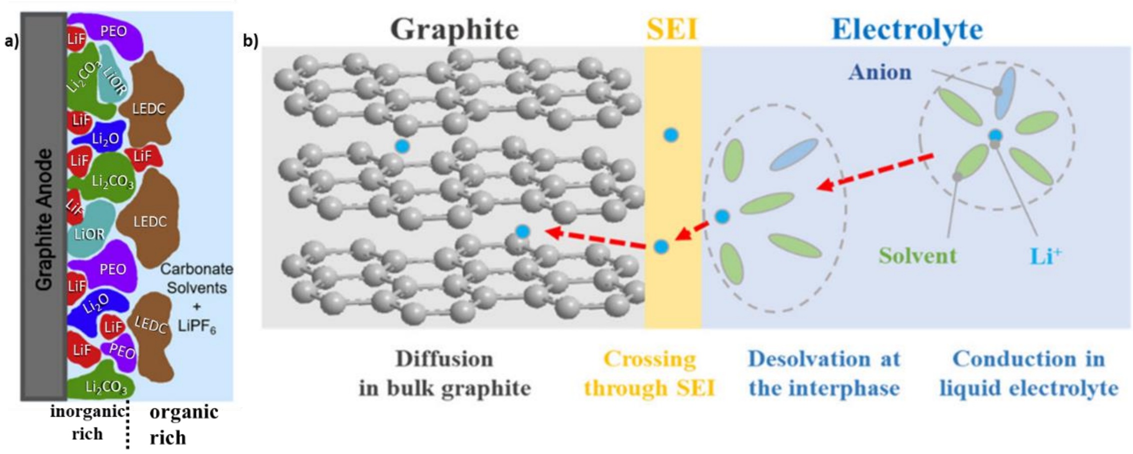

Figure 13. Schematic illustration of a) mosaic model of SEI structure *Reproduced with permission from ref*. [77]and b) Li^+ transfer and desolvation. *Reproduced with permission from ref* [78]

Such Li^+ solid-state flux helps in uniform electroreduction on the anode side. An ideal SEI layer has the following properties: high cation conductance, high electrical resistance (to control further electrolyte decomposition), and stable thickness (close to a few nanometers), high mechanical toughness (strength and ductility) so that it controls volume expansion in anodes on cycling.(Adenusi et al. 2023) Recent reports are now focussing on the use of inorganic rich-LiF in the interfacial layer (SEI), which can reduce SEI dissolution in organic electrolytes and keep it intact, thereby improving battery cyclability (**Chapter 1.2b**).[80][81,82]

1.1.6.3 Electrode preparation and Cell Assembly

1.1.6.3.1 Electrodes for Anode

To achieve consistency of active material to be tested for battery, a homogeneous and defect-free coating is required with uniform targeted weight throughout the layer. This enables uniform current density and $Li^+/Na^+/K^+$ ion transport between the anode and cathode. To maintain uniformity in cell cycling, additional conducting carbon (such as Vulcan carbon XC-72/ carbon black, etc.) and binders (such as polyvinylidene fluoride(PVDF), carboxymethyl cellulose (CMC), etc.) are used. The conducting carbon ensures electron movement from redox active sites in active material to the current collector (Cu or Al foil) on charging/discharging. Additive binder increases elasticity, viscidity, and mechanical strength. Ratios vary for active material: carbon: binder from 9:0.5:0.5 to 7:1.5:1.5, depending upon the electrical conducting nature of active material and its delamination tendency (volume expansion).

The coatings are dependent on slurry rheology and drying process. A consistent slurry is achieved by grinding the above mixture in a solvent that has high solubility for binder, i.e., N-Methyl-2-pyrrolidone (NMP) for PVDF. The homogeneous mixture is cast on the current collector, and with a doctor blade, a homogeneous coating can be attained. The optimization of the drying process is needed for every solvent, or else a higher drying rate will result in an uneven distribution of soluble and dispersible binder throughout the electrode, which can cause the binder to accumulate on the surface. This can lead to electrode delamination due to a reduction in adhesion strength.

On the laboratory scale, the assessment of battery chemistry generally starts with a half-cell/two-electrode configuration made up of a working electrode comprising active material (80% commonly) on the current collector and Li/Na/K as a counter electrode(/reference electrode).[83] They are physically separated by a separator soaked up in a nonaqueous electrolyte. This type of cell setup can help investigate some basic properties of electrode capacity and stability or electrolyte stability with electrodes.

1.1.6.3.2 Electrolytes

Symmetric cells have been intensively applied to investigate electrodes as well as various electrolytes (**Chapter 1.2b**).[83] Proper use of symmetric cells can provide information on electrode interfacial properties, electrode stability on long-term cycling, and electrolyte screening for batteries. The symmetric cell is a two-electrode system with the same electrode on both sides and provides the study of the evolution of electrolytes at the interface by charge-discharge and EIS study.

With cell assembly completed for electrodes and electrolytes, evaluation parameters are discussed.

1.1.6.4 Electrochemical Performance evaluation

1.1.6.4.1 Electrode materials

Different techniques with assembled cells are used to determine the battery performance.

i) Charge-discharge

A preliminary experiment to evaluate the performance of a new electrode material is a charge-discharge study. (**Figure 14a**) Charging and discharging are comprised of one cycle, and just discharging is considered a half cycle. It is carried out galvanostatically, and the potential is terminated after a certain potential (cut-off voltage in discharge) or else other side reactions occur, such as electrolyte decomposition at lower voltages. Due to polarization losses (IR drop), discharge potential decreases below OCV, and charging potential increases above OCV, creating a voltage hysteresis for most electrodes. [84] IR drop (**Figure 14b**) arises due to resistances from electrodes, electrolytes, and connectors and affects battery efficiency. So, capacity tends to fade with cycling, and to evaluate it, we use Coulombic efficiency(%) of each cycle, which is given by:

$100 \times Q_{dis}/Q_{ch}$

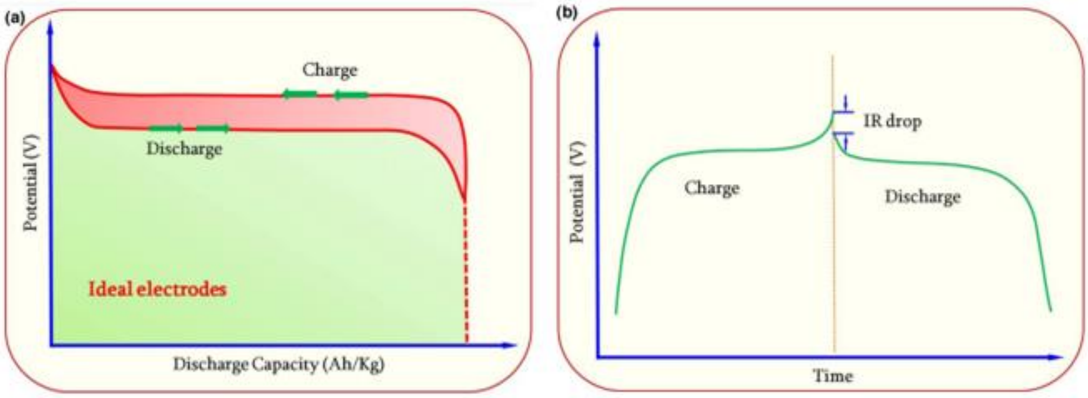

Figure 14. a) Schematic of charge/discharge plot for an electrode material. b) Illustration of potential drop (IR) from charge to discharge. [84].

ii) Cyclic Voltammetry

Cyclic voltammetry (CV) (**Figure 15a**) is a technique to measure current with changing potential with time. The voltage changes with time (dV/dt), which is the scan rate ($mV\ s^{-1}$). This study defines the rate of electron transfer depending on the electrochemical reactivity of electrode material under testing. The electrodes exhibit faradaic and non-faradaic reactions, and which process is dominant can understood from the power law between current and scan rate (**equation 6**). With varying scan rates, the current changes and is given by equation (**Figure 15b**)[83]:

$$I = a\nu^{b} \qquad (9)$$

I is the current (A), v is the scan rate (mV s^{-1}) and a and b are adjustable values (**Figure 15b**). b value is the sum of diffusion-controlled and capacitive current. $0<b<0.5$ implies capacitive dominant reaction and $0.5<b<1$ implies diffusion-controlled process. The contribution of current can be calculated by equation given by Bruce Dunn's (**Figure 15c**) group:

$$I = k_1 \nu + k_2 \nu^{1/2} \qquad (10)$$

Where $k_1\ \nu$ contributes to capacitive current and $k_2\ \nu^{1/2}$ contributes to faradaic current.

Which can be rearranged for analysis to:

$$I/\nu^{1/2}(V) = k_1\,\nu^{1/2} + k_2 \qquad (11)$$

On plotting $i/\nu^{1/2}$ vs. $\nu^{1/2}$, we can obtain k_1 (slope) and k_2 (intercept) values from linear fit and find the contribution of capacitive and faradaic behavior at a certain potential.

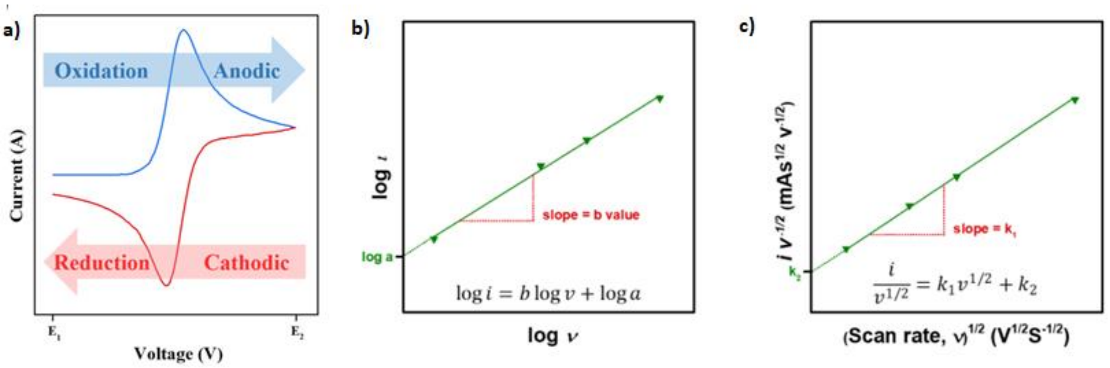

Figure 15. Scheme for a) cyclic voltammetry (CV) studies, b) and c) analysis from a change in scan rate of CV. [85]

iii) Electrochemical Impedance Spectroscopy (EIS)

A high impedance in LIBs comes from large overpotential (difference between the equilibrium and measured potentials), giving rise to low energy efficiency, low capacity, and rate capability and can cause thermal runaway.[86] So, it is paramount to observe the impedance of electrode materials over long-term cycling and each state of charge/discharge.[87] Overpotentials can arise from ohmic loss, charge transfer or activation polarization, and concentration polarization.

EIS is a very powerful technique to probe electrochemical processes in the system via a series of alternating oscillating voltage (/current). PEIS is a commonly used technique, and the current response to an applied potential at varying frequencies is recorded. Li-ion cells are very non-linear, and generally, a potentiostatic perturbation of voltage 1-10mV is applied with frequencies in the range of mHz to MHz at a certain controlled DC voltage or OCV of a cell. Nyquist plot (**Figure 16**) is commonly used in batteries when real and imaginary axes at different frequencies explain impedance associated with different processes.

The basic processes can be[88]:

1) transfer of electrons from current collector to active materials; (2) transfer of electrons across the electrode layer comprising of active material; (3) diffusion of ions through the electrolyte; (4) diffusion and migration of ions through the separator; (5) diffusion of ions in the porous electrode; (6) double-layer charging (C_{dl}) in the solid/electrolyte interface; (7) electrochemical insertion process in active material; and (8) coupled diffusion of ion and electron inside the active material particles. The limitation of EIS is that all interactions tend to overlap, which makes it difficult to convolute. Therefore, they are fitted with elements to clarify the processes occurring.

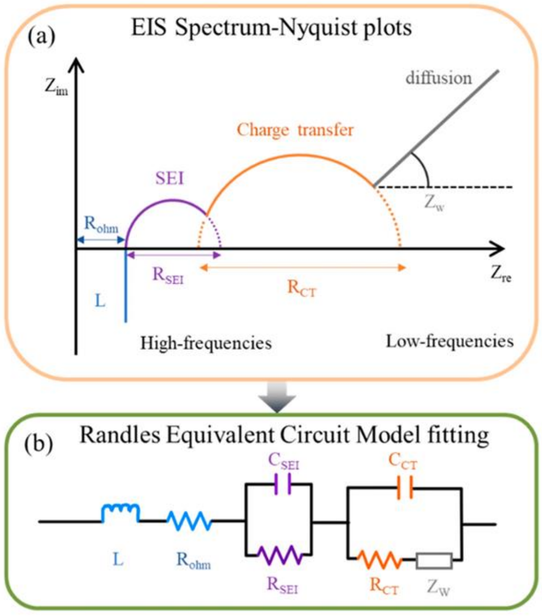

Figure 16. a) Schematic of Nyquist plot of LIBs through a wide frequency range with four components and b) Randles equivalent circuit.[89]

In order to deconvolute, the equivalent circuit model is used. It is based on prior knowledge and characteristics of Nyquist plots. Explanation of various elements (**Figures 16a and 16b**):

1) Inductor (L): Resistance associated with wound wires (high frequency) and specific adsorption or degradation processes (low frequency).
2) Resistor (R): Ionic resistance (electrolyte), SEI, charge transfer at electrode/electrolyte interface.
3) Constant phase element (CPE): With an electrode material in ion batteries, instead of pure capacitive behavior, CPE is used due to deviation in frequency.
4) Warburg element (W): It contributes to the diffusion process under the assumption of an infinite stagnant layer.
5) Randles circuit: (**Figure 16b**) This is the typical fitted model for the interfacial electrochemical process.

Other techniques like distribution of relaxation times (DRT) are also used to analyze electrochemical systems.

iv) Galvanostatic Intermittent Titration Technique (GITT)

The kinetic analysis of electrode materials can also be carried out by GITT at various state of charge (SOCs) simply by voltage change and resting the cell after specific time intervals. W. weppner and R.A. Huggins first developed the GITT method in 1977 for the kinetic investigation of Li_3Sb.[90] GITT is derived from Fick's law by calculating the number of mobile ions moving at the interface between the electrolyte and the electrode phase boundary, correlating with the transient and steady-state voltage measurements. In the experiment, a series of constant pulses, each followed by a relaxation period (no current applied).[91] As shown in **Figures 17b and 17c**.

1) The initial equilibrium state has a homogeneous distribution of ions (Li^+), and on applying a constant pulse (I_0) at time t_0, a sudden voltage step occurs from E_1 to E_2 owing to current flux in form or IR drop.
2) In case I_0 is positive/deintercalation of Li^+ occurs in the current duration time (τ) and voltage changes to E_3.
3) Then, on applying a constant current pulse, a voltage drop again shows up owing to IR drop, in which case, eventually, Li^+ diffusion is homogeneous in the material, and voltage reaches another equilibrium state (E_4). This state is now initial potential(E_1) for the next GITT step.

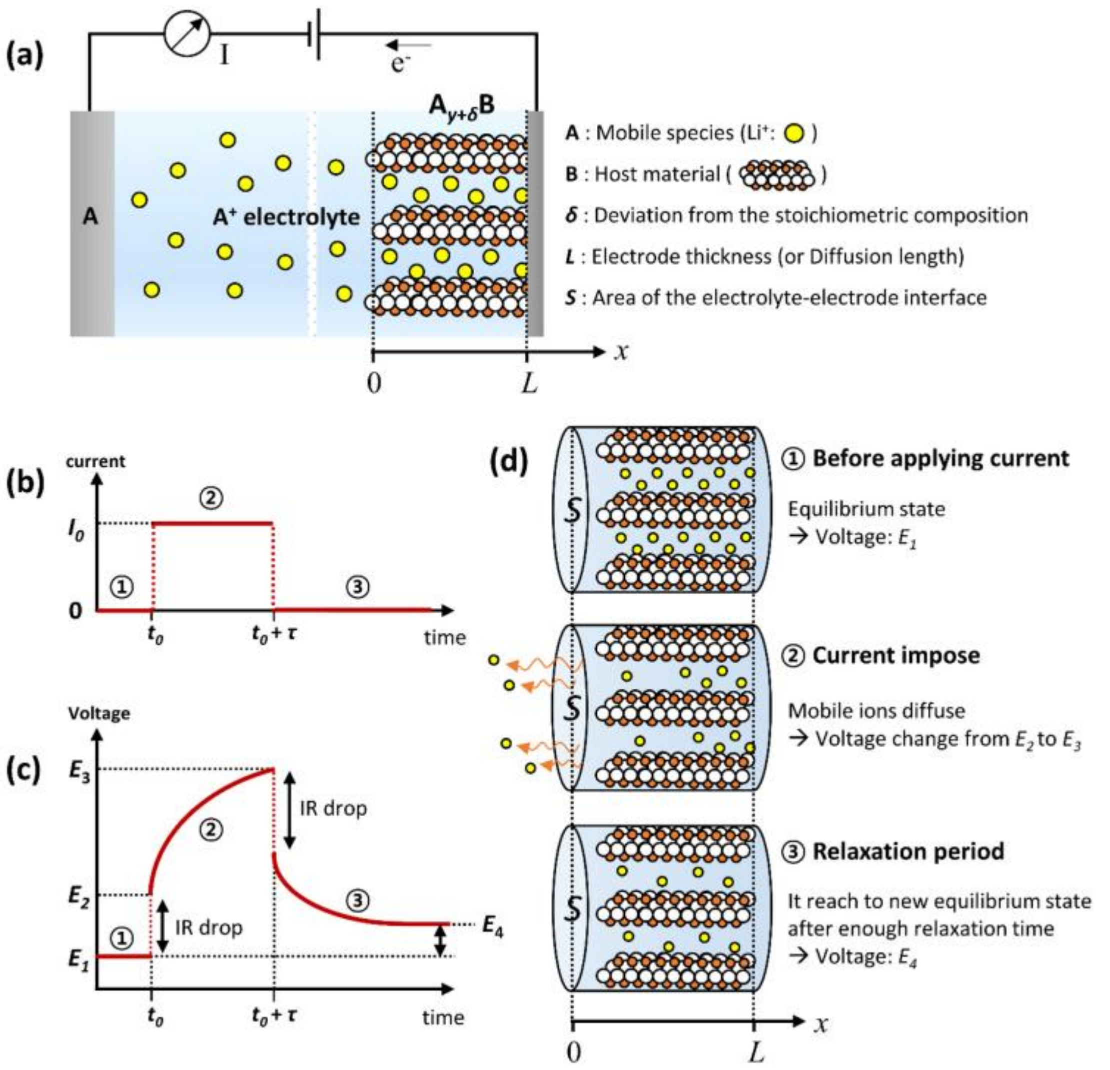

Figure 17. Schematic illustration of a) cell arrangement and components involved. GITT experiment with b) a constant current pulse (I_0) imposed for duration time (τ) at a time to and c) associated voltage changes. d) Stepwise mobile ions movement during GITT measurement.

To calculate the chemical diffusion coefficient:

$$D = \frac{4}{\pi\tau}\left(\frac{m_B V_M}{M_B S}\right)^2 \left(\frac{\Delta E_S}{\Delta E_t}\right)^2 \quad \left(t'' \frac{L^2}{D}\right) \qquad (12)$$

Where m_B is the mass of the host material in the electrode (g), M_B is the molecular weight of material (g mol^{-1}), S is the contact area of electrode/electrolyte interface (cm^2), V_M is the molar volume of the host material (cm^3 mol^{-1}), L is the electrode thickness (cm), $\Delta E_S = E_4 - E_1$ (steady-state voltage change) and $\Delta E\tau = E_3 - E_2$ (transient voltage change). The assumption is that the molar volume change is not large enough and that the current should be a low value with a short duration.

1.1.6.4.2 Electrochemical performance evaluation for electrolytes

Charge-discharge and EIS

Li-Li or metal-metal (M-M) symmetric cells provide an important platform for the quantitative evaluation of Li (/metal) without the need for electrode materials. Galvanostatic cycling of Li-Li (or M-M) showing voltage vs. time profiles helps in understanding electrode stability and failure with a certain electrolyte.[83] The voltage shape and polarization losses at a particular current density electrolyte composition can help in choosing an electrolyte for long cycling. The continuous electrodeposition/dissolution from Li-Li (/M-M) affects the cell polarization, which shows an increase in overpotential in voltage vs time plots. The change in thickness of SEI due to the electroreduction of electrolytes on both metal sides can be clearly recorded from the EIS study.

1.1.7 Conclusion:

This chapter highlights the evolution of energy storage systems, highlighted by the commercial success of lithium-ion batteries (LIBs) and the emerging interest in sodium-ion (SIB) and potassium-ion batteries (PIB). This chapter provided a comprehensive overview of anode materials in alkali-ion batteries, emphasizing design considerations for anode to attain desirable capacity. It delved into the limitations faced by anodes, such as volume expansion, and strategies to mitigate them. The intricate relationship between electrolytes and the solid electrolyte interphase (SEI) and their pivotal role in battery performance is of significant focus. Techniques for electrode and electrolyte preparation and essential measurements to evaluate anode and electrolyte performance were thoroughly discussed. This knowledge is integral to guiding future advancements in battery technology, marking a significant stride toward optimized energy storage solutions.

1.1.8 References:

1. As the global population hits 8 billion, here's what you need to know | World Economic Forum.
2. World Energy Outlook 2022 shows the global energy crisis can be a historic turning point towards a cleaner and more secure future - News - IEA.
3. Can renewable energy sources replace fossil fuels? | Prysmian Group.
4. Ati, M., Delacourt, C., Armand, M., -, al, Gubin, S.P., Koksharov, Y.A., Khomutov, G.B., Maurel, A., and Grugeon, S. The Li-Ion Battery: 25 Years of Exciting and Enriching Experiences You may also like Determination of the Diffusion Coefficient of Lithium in Li y FeSO 4 F Using Electrochemical Techniques Magnetic nanoparticles: preparation, structure and properties Overview on Lithium-Ion Battery 3D-Printing By Means of Material Extrusion.
5. Clean energy investment is extending its lead over fossil fuels, boosted by energy security strengths - News - IEA.
6. The Mystery of the Baghdad Battery - Discovery UK.
7. Zito, R. (2010) Appendix 1: A History of Batteries. *Energy Storage*, 265–282.
8. Royal Swedish Academy of Sciences, T. (2019) Nobel Prize ® and the Nobel Prize ® medal design mark are registrated trademarks of the Nobel Foundation.
9. Hu, Y.S., and Lu, Y. (2019) 2019 Nobel Prize for the Li-Ion Batteries and New Opportunities and Challenges in Na-Ion Batteries. *ACS Energy Lett*, **4** (11), 2689–2690.
10. The HELIOS perspective on batteries. Long history, powerful future.
11. Tarascon, J.-M., and Armand, M. (2001) Issues and challenges facing rechargeable lithium batteries.
12. Who are the big players in the gigafactories race? | CIC energiGUNE.
13. Liu, D., Qu, X., Zhang, B., Zhao, J., Xie, H., and Yin, H. (2021) Alkaline Roasting Approach to Reclaiming Lithium and Graphite from Spent Lithium-Ion Batteries. *ACS Sustain Chem Eng*.

14. Budde-Meiwes, H., Drillkens, J., Lunz, B., Muennix, J., Rothgang, S., Kowal, J., and Sauer, D.U. (2013) A review of current automotive battery technology and future prospects. *http://dx.doi.org/10.1177/0954407013485567*, **227** (5), 761–776.

15. Kubota, K., Dahbi, M., Hosaka, T., Kumakura, S., and Komaba, S. (2018) Towards K-Ion and Na-Ion Batteries as "Beyond Li-Ion." *The Chemical Record*, **18** (4), 459–479.

16. Masias, A., Marcicki, J., and Paxton, W.A. (2021) Opportunities and Challenges of Lithium Ion Batteries in Automotive Applications. *ACS Energy Lett*, **6** (2), 621–630.

17. Goodenough, J.B., and Kim, Y. (2010) Challenges for rechargeable Li batteries. *Chemistry of Materials*, **22** (3), 587–603.

18. Reddy, T.B. (2011) *Linden's Handbook of Batteries, Fourth Edition*, McGraw-Hill Education.

19. Cheng, X.B., Zhang, R., Zhao, C.Z., and Zhang, Q. (2017) Toward Safe Lithium Metal Anode in Rechargeable Batteries: A Review. *Chem Rev*, **117** (15), 10403–10473.

20. Xu, W., Wang, J., Ding, F., Chen, X., Nasybulin, E., Zhang, Y., and Zhang, J.-G. (2014) Lithium metal anodes for rechargeable batteries.

21. Zhang, W., Zhang, F., Ming, F., and Alshareef, H.N. (2019) Sodium-ion battery anodes: Status and future trends.

22. Wang, Q., Li, J., Jin, H., Xin, S., and Gao, H. (2022) Prussian-blue materials: Revealing new opportunities for rechargeable batteries. *InfoMat*, **4** (6).

23. Ge, S., Longchamps, R.S., Liu, T., Liao, J., Leng, Y., and Wang, C.-Y. ll OPEN ACCESS High safety and cycling stability of ultrahigh energy lithium ion batteries.

24. Liu, C., Neale, Z.G., and Cao, G. (2016) Understanding electrochemical potentials of cathode materials in rechargeable batteries. *Materials Today*, **19** (2).

25. Jow, T.R., Delp, S.A., Allen, J.L., Jones, J.-P., and Smart, M.C. (2018) Factors Limiting Li + Charge Transfer Kinetics in Li-Ion Batteries . *J Electrochem Soc*, **165** (2), A361–A367.

26. Tomaszewska, A., Chu, Z., Feng, X., O'kane, S., Liu, X., Chen, J., Ji, C., Endler, E., Li, R., Liu, L., Li, Y., Zheng, S., Vetterlein, S., Gao, M., Du, J., Parkes, M., Ouyang, M., Marinescu, M., Offer, G., and Wu, B. (2019) Lithium-ion battery fast charging: A review.

27. Xia, H., Zhang, W., Cao, S., and Chen, X. (2022) A Figure of Merit for Fast-Charging Li-ion Battery Materials. *ACS Nano*, **16** (6), 8525–8530.

28. ELECTROCHEMICAL SYSTEMS.

29. Li, S., Wang, K., Zhang, G., Li, S., Xu, Y., Zhang, X., Zhang, X., Zheng, S., Sun, X., and Ma, Y. (2022) Fast Charging Anode Materials for Lithium-Ion Batteries: Current Status and Perspectives. *Adv Funct Mater*, **32** (23).

30. Weng, S., Yang, G., Zhang, S., Liu, X., Zhang, X., Liu, Z., Cao, M., Ateş, M.N., Li, Y., Chen, L., Wang, Z., and Wang, X. (123AD) Kinetic Limits of Graphite Anode for Fast-Charging Lithium-Ion Batteries.

31. Li, R., Chen, Z., Bresser, D., Asenbauer, J., Eisenmann, T., Kuenzel, M., and Kazzazi, A. (2020) Sustainable Energy & Fuels Interdisciplinary research for the development of sustainable energy technologies The success story of graphite as a lithium-ion anode material-fundamentals, remaining challenges, and recent developments including silicon (oxide) composites The success story of graphite as a lithium-ion anode material-fundamentals, remaining challenges, and recent developments including silicon (oxide) composites. **4**, 5363–5870.

32. Li, S., Wang, K., Zhang, G., Li, S., Xu, Y., Zhang, X., Zhang, X., Zheng, S., Sun, X., and Ma, Y. (2022) Fast Charging Anode Materials for Lithium-Ion Batteries: Current Status and Perspectives. *Adv Funct Mater*, **32** (23).

33. Puthusseri, D., Wahid, M., and Ogale, S. (2018) Conversion-type Anode Materials for Alkali-Ion Batteries: State of the Art and Possible Research Directions. *ACS Omega*, **3** (4), 4591–4601.

34. Reddy, M. V., Subba Rao, G. V., and Chowdari, B.V.R. (2013) Metal oxides and oxysalts as anode materials for Li ion batteries. *Chem Rev*, **113** (7), 5364–5457.

35. Wang, S., Yang, Y., Quan, W., Hong, Y., Zhang, Z., Tang, Z., and Li, J. (2017) Communication Ti 3+-free three-phase Li 4 Ti 5 O 12 /TiO 2 for high-rate lithium ion batteries: Capacity and conductivity enhancement by phase boundaries Keywords: Li 4 Ti 5 O 12 /TiO 2 Phase boundaries High-rate Full pouch cell Lithium ion battery.

36. Rudola, A., Saravanan, K., Mason, C.W., and Balaya, P. Na 2 Ti 3 O 7 : an intercalation based anode for sodium-ion battery applications †.

37. Kitajou, A., Yamashita, M., Kobayashi, W., Okada, M., Nanami, T., and Muto, S. (2022) Anode Properties of NaTi2(PO4)3Prepared by Adding Excess Na2CO3for Aqueous Sodium-Ion Batteries. *ACS Appl Energy Mater*, **5** (8), 9587–9594.

38. Li, R., Chen, Z., Bresser, D., Asenbauer, J., Eisenmann, T., Kuenzel, M., and Kazzazi, A. (2020) Sustainable Energy & Fuels Interdisciplinary research for the development of sustainable energy technologies The success story of graphite as a lithium-ion anode material-fundamentals, remaining challenges, and recent developments including silicon (oxide) composites The success story of graphite as a lithium-ion anode material-fundamentals, remaining challenges, and recent developments including silicon (oxide) composites. **4**, 5363–5870.

39. John, B., Anoopkumar, V., and Mercy, T.D. (2020) Potassium-ion batteries: Key to future large-scale energy storage? *ACS Appl Energy Mater*, **3** (10), 9478–9492.

40. Park, J., Xu, Z.L., and Kang, K. (2020) Solvated Ion Intercalation in Graphite: Sodium and Beyond. *Front Chem*, **8**, 542849.

41. Adams, R.A., Varma, A., and Pol, V.G. (2019) Carbon Anodes for Nonaqueous Alkali Metal-Ion Batteries and Their Thermal Safety Aspects. *Adv Energy Mater*, **9** (35).

42. Obrovac, M.N., and Chevrier, V.L. (2014) Alloy negative electrodes for Li-ion batteries. *Chem Rev*, **114** (23), 11444–11502.

43. Liu, D., Liu, Z. jiao, Li, X., Xie, W., Wang, Q., Liu, Q., Fu, Y., and He, D. (2017) Group IVA Element (Si, Ge, Sn)-Based Alloying/Dealloying Anodes as Negative Electrodes for Full-Cell Lithium-Ion Batteries. *Small*, **13** (45).

44. Tian, H., Xin, F., Wang, X., He, W., and Han, W. (2015) High capacity group-IV elements (Si, Ge, Sn) based anodes for lithium-ion batteries-NC-ND license (http://creativecommons.org/licenses/by-nc-nd/4.0/).

45. Braga, M.H., Dębski, A., and Gąsior, W. (2014) Li–Si phase diagram: Enthalpy of mixing, thermodynamic stability, and coherent assessment. *J Alloys Compd*, **616**, 581–593.

46. Liang, S., Cheng, Y.J., Zhu, J., Xia, Y., and Müller-Buschbaum, P. (2020) A Chronicle Review of Nonsilicon (Sn, Sb, Ge)-Based Lithium/Sodium-Ion Battery Alloying Anodes. *Small Methods*, **4** (8).

47. Pender, J.P., Jha, G., Youn, D.H., Ziegler, J.M., Andoni, I., Choi, E.J., Heller, A., Dunn, B.S., Weiss, P.S., Penner, R.M., and Mullins, C.B. (2020) Electrode Degradation in Lithium-Ion Batteries. *ACS Nano*, **14** (2), 1243–1295.

48. Peled, E., and Menkin, S. (2017) Review—SEI: Past, Present and Future. *J Electrochem Soc*, **164** (7), A1703–A1719.

49. Zhang, S. (2017) Chemomechanical modeling of lithiation-induced failure in high-volume-change electrode materials for lithium ion batteries. *NPJ Comput Mater*, **3**, 7.

50. Morachevskii, A.G., and Demidov, A.I. (2015) Lithium-Silicon Alloys: Phase Diagram, Electrochemical Studies, Thermodynamic Properties, Application in Chemical Power Cells. *Russian Journal of Applied Chemistry*, **88** (4), 513–533.

51. Guidotti, R.A., and Masset, P.J. (2008) Thermally activated (“thermal”) battery technology: Part IV. Anode materials. *J Power Sources*, **183** (1), 388–398.

52. Chen, X., Zheng, J., Li, L., and Chu, W. (2022) Strategy for enhanced performance of silicon nanoparticle anodes for lithium-ion batteries †.

53. Kepler, K.D., Vaughey, J.T., and Thackeray, M.M. Copper-tin anodes for rechargeable lithium batteries: an example of the matrix effect in an intermetallic system. *J Power Sources*, **81**, 1999–383.

54. Yoon, S., and Manthiram, A. (2009) Superior capacity retention Sn-Ni-Fe-C composite anodes for lithium-ion batteries. *Electrochemical and Solid-State Letters*, **12** (9), A190.

55. Yu, S.H., Feng, X., Zhang, N., Seok, J., and Abruña, H.D. (2018) Understanding Conversion-Type Electrodes for Lithium Rechargeable Batteries. *Acc Chem Res*, **51** (2), 273–281.

56. Wang, F., Robert, R., Chernova, N.A., Pereira, N., Omenya, F., Badway, F., Hua, X., Ruotolo, M., Zhang, R., Wu, L., Volkov, V., Su, D., Key, B., Stanley Whittingham, M., Grey, C.P., Amatucci, G.G., Zhu, Y., and Graetz, J. (2011) Conversion reaction mechanisms in lithium ion batteries: Study of the binary metal fluoride electrodes. *J Am Chem Soc*, **133** (46), 18828–18836.

57. Yu, S.H., Feng, X., Zhang, N., Seok, J., and Abruña, H.D. (2018) Understanding Conversion-Type Electrodes for Lithium Rechargeable Batteries. *Acc Chem Res*, **51** (2), 273–281.

58. Ni, J., Li, L., and Lu, J. (2018) Phosphorus: An Anode of Choice for Sodium-Ion Batteries. *ACS Energy Lett*, **3** (5), 1137–1144.

59. Yu, S.H., Feng, X., Zhang, N., Seok, J., and Abruña, H.D. (2018) Understanding Conversion-Type Electrodes for Lithium Rechargeable Batteries. *Acc Chem Res*, **51** (2), 273–281.

60. Lin, L., Wang, K., Sarkar, A., Njel, C., Karkera, G., Wang, Q., Azmi, R., Fichtner, M., Hahn, H., Schweidler, S., and Breitung, B. (2022) High-Entropy Sulfides as Electrode Materials for Li-Ion Batteries. *Adv Energy Mater*, **12** (8).

61. Wang, L., Liu, J., Yuan, S., Wang, Y., and Xia, Y. (2016) To mitigate self-discharge of lithium-sulfur batteries by optimizing ionic liquid electrolytes †. | *Energy Environ. Sci*, **9**, 224.

62. Lei, Y., Liang, X., Yang, L., Chen, J., Qu, L., Xu, K., and Feng, J. (2022) LieSe batteries: Insights to the confined structure of selenium in hierarchical porous carbon and discharge mechanism in the carbonate electrolyte.

63. Li, X., Chen, L., Qu, Y., and Ma, Y. (2018) Carbon-assisted conversion reaction-based oxide nanomaterials for lithium-ion batteries.

64. Zhang, W., Liu, Y., and Guo, Z. (2019) Approaching high-performance potassium-ion batteries via advanced design strategies and engineering. *Sci Adv*, **5** (5), 7412–7422.

65. Kalhoff, J., Eshetu, G.G., Bresser, D., and Passerini, S. (2015) Safer electrolytes for lithium-ion batteries: State of the art and perspectives. *ChemSusChem*, **8** (13), 2154–2175.

66. Logan, E.R., Tonita, E.M., Gering, K.L., Li, J., Ma, X., Beaulieu, L.Y., and Dahn, J.R. (2018) A Study of the Physical Properties of Li-Ion Battery Electrolytes Containing Esters. *J Electrochem Soc*, **165** (2), A21–A30.

67. Yan, L., Zhang, G., Wang, J., Ren, Q., Fan, L., Liu, B., Wang, Y., Lei, W., Ruan, D., Zhang, Q., and Shi, Z. (2023) Revisiting Electrolyte Kinetics Differences in Sodium Ion Battery: Are Esters Really Inferior to Ethers? *Energy and Environmental Materials*, **6** (4).

68. Rajput, N.N., Seguin, T.J., Wood, B.M., Qu, X., and Persson, K.A. (2018) Elucidating Solvation Structures for Rational Design of Multivalent Electrolytes—A Review. *Topics in Current Chemistry 2018 376:3*, **376** (3), 1–46.

69. Tian, Z., Zou, Y., Liu, G., Wang, Y., Yin, J., Ming, J., and Alshareef, H.N. (2022) Electrolyte Solvation Structure Design for Sodium Ion Batteries. *Advanced Science*, **9** (22).

70. Zhang, W., Liu, Y., and Guo, Z. (2019) Approaching high-performance potassium-ion batteries via advanced design strategies and engineering. *Sci Adv*, **5** (5), 7412–7422.

71. Tian, Z., Zou, Y., Liu, G., Wang, Y., Yin, J., Ming, J., and Alshareef, H.N. (2022) Electrolyte Solvation Structure Design for Sodium Ion Batteries. *Advanced Science*, **9** (22).

72. Xue, Z., He, D., and Xie, X. (2015) Poly(ethylene oxide)-based electrolytes for lithium-ion batteries. *J Mater Chem A Mater*, **3** (38), 19218–19253.

73. Peled, E. (1979) The Electrochemical Behavior of Alkali and Alkaline Earth Metals in Nonaqueous Battery Systems—The Solid Electrolyte Interphase Model. *J Electrochem Soc*, **126** (12), 2047–2051.

74. Peled, E., Golodnitsky, D., and Ardel, G. (1997) Advanced Model for Solid Electrolyte Interphase Electrodes in Liquid and Polymer Electrolytes. *J Electrochem Soc*, **144** (8), L208–L210.

75. Parimalam, B.S., MacIntosh, A.D., Kadam, R., and Lucht, B.L. (2017) Decomposition Reactions of Anode Solid Electrolyte Interphase (SEI) Components with LiPF6. *Journal of Physical Chemistry C*, **121** (41), 22733–22738.

76. Cheng, X.B., Zhang, R., Zhao, C.Z., and Zhang, Q. (2017) Toward Safe Lithium Metal Anode in Rechargeable Batteries: A Review. *Chem Rev*, **117** (15), 10403–10473.

77. Kristiina Heiskanen, S., Kim, J., and Lucht, B.L. (2013) Generation and Evolution of the Solid Electrolyte Interphase of Lithium-Ion Batteries.

78. Yang, Y., Fang, Z., Yin, Y., Cao, Y., Wang, Y., Dong, X., and Xia, Y. (2022) Synergy of Weakly-Solvated Electrolyte and Optimized Interphase Enables Graphite Anode Charge at Low Temperature. *Angewandte Chemie - International Edition*, **61** (36).

79. Adenusi, H., Chass, G.A., Passerini, S., Tian, K. V., and Chen, G. (2023) Lithium Batteries and the Solid Electrolyte Interphase (SEI)—Progress and Outlook. *Adv Energy Mater*, **13** (10).

80. Chen, T., You, J., Li, R., Li, H., Wang, Y., Wu, C., Sun, Y., Yang, L., Ye, Z., Zhong, B., Wu, Z., and Guo, X. (2022) Ultra-Low Concentration Electrolyte Enabling LiF-Rich SEI and Dense Plating/Stripping Processes for Lithium Metal Batteries. *Advanced Science*, **9** (28).

81. Shi, P., Zheng, H., Liang, X., Sun, Y., Cheng, S., Chen, C., Xiang, H., Li, R., Chemcomm, /, and Communication, C. (2018) A highly concentrated phosphate-based electrolyte for high-safety rechargeable lithium batteries †. *Chem. Commun*, **54**, 4453.

82. Park, S., Kim, S., Lee, J.-A., Ue, M., and Choi, N.-S. (2023) Liquid electrolyte chemistries for solid electrolyte interphase construction on silicon and lithium-metal anodes †.

83. Nölle, R., Beltrop, K., Holtstiege, F., Kasnatscheew, J., Placke, T., and Winter, M. (2020) A reality check and tutorial on electrochemical characterization of battery cell materials: How to choose the appropriate cell setup. *Materials Today*, **32**, 131–146.

84. Liu, C., Neale, Z.G., and Cao, G. (2016) Understanding electrochemical potentials of cathode materials in rechargeable batteries. *Materials Today*, **19** (2).

85. Kim, T., Choi, W., Shin, H.-C., Choi, J.-Y., Man Kim, J., Park, M.-S., and Yoon, W.-S. (2012) 14-25 − 14 − Applications of Voltammetry in Lithium Ion Battery Research. *J. Electrochem. Sci. Technol*, **2020** (1).

86. Meddings, N., Heinrich, M., Overney, F., Lee, J.S., Ruiz, V., Napolitano, E., Seitz, S., Hinds, G., Raccichini, R., Gaberšček, M., and Park, J. (2020) Application of electrochemical impedance spectroscopy to commercial Li-ion cells: A review. *J Power Sources*, **480**, 228742.

87. Zhang, B., Wang, L., Zhang, Y., Wang, X., Qiao, Y., and Sun, S.G. (2023) Reliable impedance analysis of Li-ion battery half-cell by standardization on electrochemical impedance spectroscopy (EIS). *Journal of Chemical Physics*, **158** (5).

88. Gaberšček, M. (2021) Understanding Li-based battery materials via electrochemical impedance spectroscopy. *Nature Communications 2021 12:1*, **12** (1), 1–4.

89. Yang, K., Zhang, L., Zhang, Z., Yu, H., Wang, W., Ouyang, M., Zhang, C., Sun, Q., Yan, X., Yang, S., and Liu, X. (2023) Battery State of Health Estimate Strategies: From Data Analysis to End-Cloud Collaborative Framework. *Batteries*, **9** (7).

90. Weppner, W., and Huggins, R.A. (1977) Determination of the Kinetic Parameters of Mixed-Conducting Electrodes and Application to the System Li3Sb. *J Electrochem Soc*, **124** (10), 1569–1578.

91. Kim, J., Park, S., Hwang, S., and Yoon, W.-S. Principles and Applications of Galvanostatic Intermittent Titration Technique for Lithium-ion Batteries. *J. Electrochem. Sci. Technol*, **2022** (1), 19–31.

Chapter 1.2a

Boron-doped thermally exfoliated graphene as universal anode for alkali-ion batteries

Summary

In this chapter, we have established that BTEG carbon excels as an anode material in Lithium, Sodium, and Potassium ion batteries. It shows high reversible capacities (1014 mAh g^{-1} *for LIB, 295 mAh g*$^{-1}$ *for SIB, and 369 mAh g*$^{-1}$ *for PIB) at a current density of 25 mA g*$^{-1}$*. Notably, at 1 A g*$^{-1}$*, BTEG demonstrates remarkable capacity retention over 1000 cycles: 75% for LIB, 100% for SIB, and 87% for PIB. Our electrokinetic studies also underline that BTEG follows an intercalation-adsorption reaction, while SIB and PIB follow a dominant reaction.*

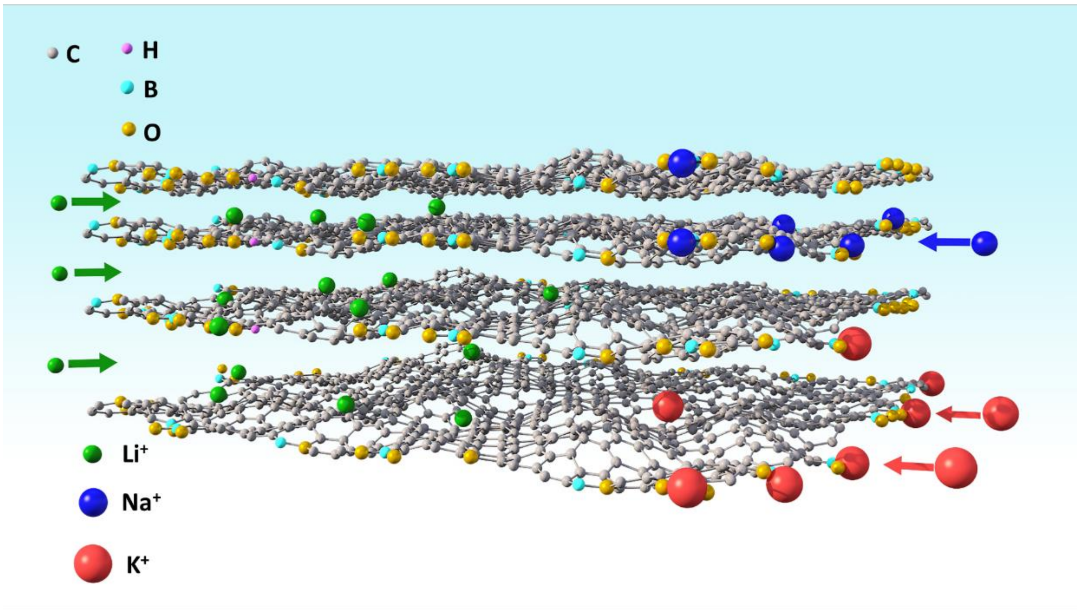

1.2a.1 Introduction

Lithium-ion batteries (LIBs) have significantly advanced battery technology, transforming portable electronics and electric vehicles.[1,2] However, lithium scarcity (only 0.0017% of Earth's crust) is causing a "lithium crisis" due to high demand.[3] This has sparked interest in sodium (Na) and potassium (K) as alternatives. Although Sodium and Potassium ion batteries have lower energy densities due to their higher reduction potentials compared to lithium, they remain significant for large-scale energy storage.[4] Their importance is emphasized in scenarios where the availability of materials is a priority over energy density, particularly in enhancing the incorporation of renewable energy sources into power grids.[5,6] Developing anodes with high specific capacity is critical for enhancing energy density in these batteries. The ionic size increases from Li^+ to Na^+ to K^+ ions, slowing reaction kinetics and causing volume expansion and electrolytic decomposition.[7]

Carbon-based anodes are crucial as they are abundant and economical and have been widely used in various forms in ion batteries.[8] Graphite electrodes, invented by Yazami in 1980, are anode materials for commercial LIBs, as they offer high capacity and stability.[9] Graphite faces challenges in Sodium and Potassium ion batteries due to poor intercalation thermodynamics and significant volume expansion, respectively.[9,10] Therefore, tailored carbon materials need to be prepared to attain high energy density in all alkali-ion battery types.[11]

Amorphous carbons, including hard (non-graphitizable) and soft (graphitizable) types, outperform graphite in Li/Na/K-ion batteries due to their defects, porosity, and better volume change accommodation (**Figure 1**).[12] Hard carbons show less volumetric expansion than graphite, but their capacity primarily comes from a low potential charge storage plateau (<0.2 V).[13] This leads to sodium plating at a fast cycling rate and thermal issues, making batteries unsafe. Soft carbons, like few-layer graphene nanosheets[14][15] and obtained from coal tar[16], provide sloping charge storage, offering a better alternative. Their tunability in pore size and surface defects create more adsorption sites for $Li^+/Na^+/K^+$.[17] Introducing heteroatoms like nitrogen, phosphorus, boron, and sulfur improves charge storage by altering carbon's electronic properties, adding defects, and creating optimal redox reaction sites.[18] This heteroatom doping enhances alkali ion binding and electron transfer, boosting storage capacity.

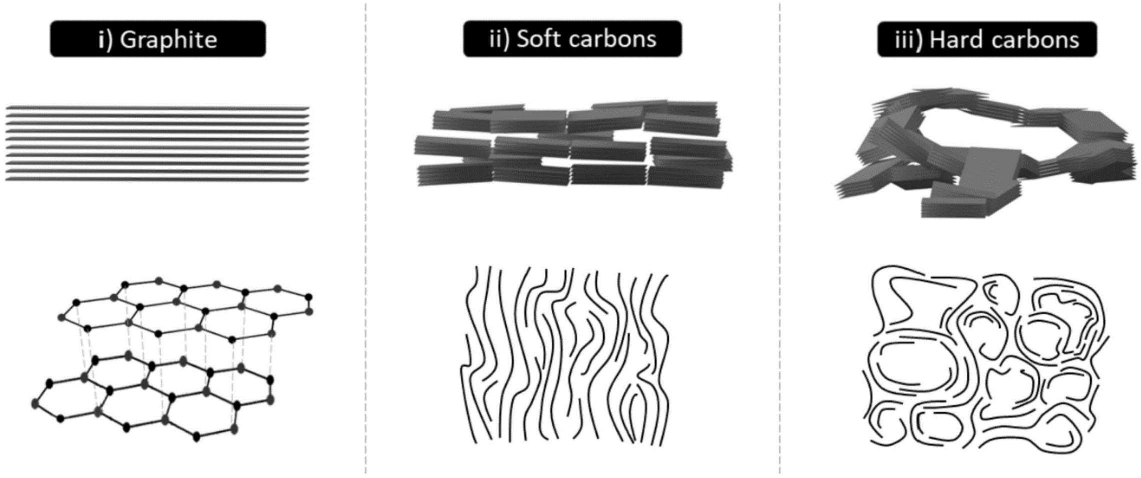

Figure 1. Schematic structure of graphite, soft carbon, and hard carbon.[19]

Boron, in particular, alters carbon's electronic and structural properties, thereby improving performance.[20] The lower electronegativity of boron can create an electron-rich environment on carbon, enhancing alkali-ion interactions. Theoretical studies show that boron-doped carbon, with BC_3 and B-C-O species, facilitates Na^+ movement by lowering diffusion energy barriers.[21] While boron-doped graphene (BDG) boosts lithium-ion battery performance[22], its impact on Na and K batteries remains unexplored.

1.2a.2 Scope of investigation

In this study, we introduce a novel boron-doped thermally exfoliated graphene (BTEG), showing enhanced performance in all three alkali-ion batteries for the first time. The BTEG demonstrates impressive reversible discharge capacities of 1014 mAh g^{-1} for LIBs, 295 mAh g^{-1} for SIBs, and 369 mAh g^{-1} for PIBs at a current density of 25 mA g^{-1}. Electrokinetic analysis using Dunn's equation, operando Raman spectroscopy, and the galvanostatic intermittent titration technique (GITT) reveal that the charge storage in LIBs is primarily through intercalation-adsorption. At the same time, it is predominantly adsorption-based for SIBs and PIBs, contributing to universally high capacities. Electrochemical impedance spectroscopy (EIS) is used to investigate the diffusion dynamics and reversibility of BTEG in relation to Li, Na, and K storage.

1.2a.3 Experimental section:

i. Materials and characterization techniques:

Graphite powder and sodium nitrate were supplied by Sigma Aldrich. Concentrated sulfuric acid (95-95%), hydrogen peroxide (30%), and boric acid were acquired from Emparta, Merck. Potassium permanganate was acquired from Thomas Baker. Lithium hexafluorophosphate in ethylene dicarbonate, diethyl carbonate (EC: DEC), sodium hexafluorophosphate, potassium hexafluorophosphate, EC, and DEC battery grade were procured from Sigma Aldrich. Potassium bisfluorosulfonylimide was sourced from TCI chemicals. Whatman glass fibre separator was procured from Sigma Aldrich.

ii. Synthesis of boron-doped thermally exfoliated graphene (BTEG):

The synthesis of BTEG involved thermal shock treatment of graphite oxide (GO), which was produced using the Modified Hummers method.[23] GO was placed in a preheated tube furnace at 350°C in the air for 5 minutes, yielding thermally exfoliated graphene (TEG-350). To create a homogeneous dispersion, 50 mg of TEG-350 was mixed with an equal amount of boric acid (50 mg) in 70 ml of water. This mixture was dried overnight at 70°C in an oil bath and ground into a fine powder. The powdered mixture was heated in an argon-atmosphere tube furnace at 800°C for 3 hours, with a temperature increase of 5°C per minute. The resulting product, which contained additional boron oxide residues, was rinsed with warm water at 70°C centrifuged three times at 10,000 rpm for 5 minutes. This was finally washed with ethanol before being dried at 60°C overnight to obtain BTEG.

iii. Control Experiments:

To evaluate the impact of boron doping, we compared the initial reversible capacity of TEG annealed at 800°C for 3 hours (without boric acid) to that of BTEG. Additionally, thermal shock treatment of GO (TEG-350) served as a control to understand the effects of pyrolysis and boron doping.

iv. Electrochemical Characterization:

The BTEG and TEG electrode was made by blade-coating a slurry (80wt% BTEG, 10wt% Vulcan carbon XC-72, 10wt% polyvinylidene fluoride) onto copper foil, followed by drying in a vacuum oven at 80°C for over 24 hours. TEG-350 was formed into pellets using a cold press, each weighing 17mg, as it does not adhere to Cu foil. BTEG had an active material loading of 1mg with a diameter of 10mm. Electrochemical testing was conducted in Swagelok cells, with BTEG as the working electrode and lithium, sodium, and potassium foils as the counter/reference electrodes (11mm diameter). Glass fibre separator was punched into 12 mm dimensions, and a single separator was used for LIB and SIB. For PIB, two separators were used to avoid any possible short circuit. Separator was soaked with the electrolytes 1M $LiPF_6$ (LIB), 1M $NaPF_6$ (SIB), 0.8M KPF_6 (PIB), 1M KFSI, and 5M KFSI in a 1:1 mixture of ethylene carbonate and diethyl carbonate, stirred for 24 hours. The cell used for electrochemical measurement is shown in **Figure 2**.

Figure 2. A homemade stainless steel cell is used for battery assembly.

Cyclic voltammetry (CV), galvanostatic charge-discharge (GCD), and electrochemical impedance spectroscopy (EIS) tests were performed using an electrochemical workstation (battery cycler). EIS measurements spanned from 600kHz to 10mHz at a 10mV amplitude. All tests were conducted at room temperature, with batteries equilibrated for 24 hours before CV, GCD, and EIS testing.

v. Operando Raman Cell:

An optical cell (El-Cell ECC-Opto-Std) was used to carry out operando Raman measurements. BTEG, the working electrode, was observed through the glass window.[24] The current collector used was copper mesh. The separator and alkali metal foils were pierced in the center to allow the laser to pass through and assess the BTEG electrode. A green laser (532nm) at 5% power with 30 seconds exposure and 3 accumulations provided data. The time duration for data recording was kept 20 minutes apart in order to prevent sample burning. Raman spectra were taken at a low current density of 15 mA g^{-1} to monitor gradual change in Raman active carbon peaks.

vi. Galvanostatic Intermittent Titration Technique (GITT):

This technique helps to analyze solid-state diffusion and kinetics of alkali ions. The GITT potential profiles (**Figure 3**) and corresponding diffusion coefficients for M^+ ions were calculated as follows[25]:

$$D = 4\pi\tau(n_m V_m/S)^2(\Delta Es/\Delta Et)^2 \quad (3)$$

In this formula, n_m, V_m, τ, and S represent the mole of the electrode material, molar volume, relaxation time, and electrode-electrolyte contact area, respectively.

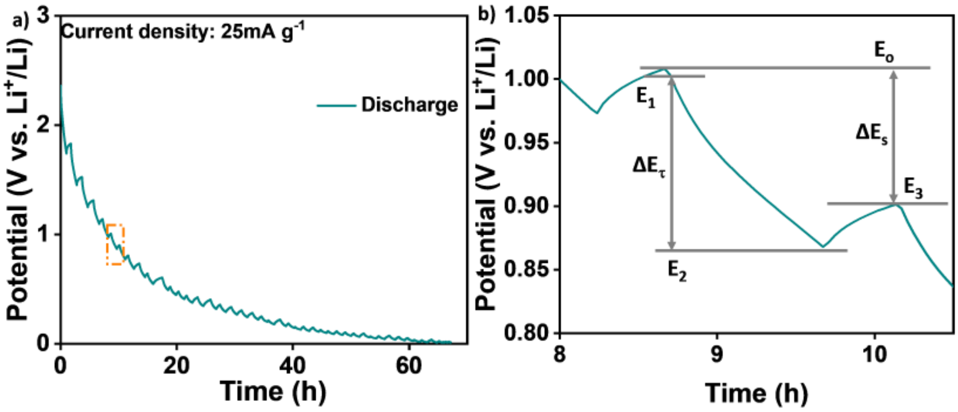

Figure 3. a) The GITT plot and b) enlarged version showing a change in the potential for discharge process on applying a constant current pulse of 25 mA g^{-1}, followed by relaxation. ΔEτ is the voltage change of constant current discharging, which is calculated by the equal E_1 -E_2; ΔEs is the voltage change caused by the pulse (relaxation), which is calculated by the equal E_0 -E_3.

vii. Characterization techniques

Powder X-ray diffraction (PXRD) analysis of the Cu foil was recorded with a PANalytical diffractometer (Empyrean) having monochromatic Cu $K_{\alpha 1}$ radiation ($\lambda = 1.5404$ Å) with an accelerating voltage of 40 kV and current of 40 mA. Thermogravimetric analysis (TGA) was done with a Mettler Toledo TGA-850 TG analyzer at the ramping rate of 5°C min^{-1} in an oxygen atmosphere. Raman spectra were obtained from Renishaw equipped with a green laser (532 nm). Brunauer–Emmett–Teller (BET) analysis for N_2 (ultra-high purity of 99.9995%) sorption studies were conducted at 77 K by Autosorb-iQ_2, and samples were degassed for 12 h at 423K. JEM 2100 PLUS electron microscope of 200 KV was used to acquire the samples' transmission electron microscope (TEM) images. ZEISS GEMINI 500 was used to procure field emission scanning electron microscopy (FESEM) images. X-ray photoelectron spectroscopy (XPS) measurements were carried out by an X-ray photoelectron spectrometer (Thermo

K-alpha+) using micro-focused and monochromated AlKα radiation with energy 1486.6 eV. The FESEM, TEM, and XPS samples were prepared by sonicating the powdered sample in 99.99% pure ethanol and uniformly drop casting on Cu foil, Cu grid, and Si wafer, respectively. Battery cycler Biologic BCS-810 was used for battery studies.

1.2a.4 Results and discussion

Physico-chemical analyses comparing BTEG, TEG, and TEG-350 were conducted using Powder X-ray Diffraction (PXRD), Raman spectroscopy, X-ray Photoelectron Spectroscopy (XPS), and nitrogen adsorption techniques. The PXRD pattern of graphite oxide in **Figure 4a** exhibits a low angle peak at 10.9° corresponding to the interlayer spacing of 0.81 nm attributed to the (002) plane of graphite. While on annealing, PXRD patterns for BTEG and TEG in **Figure 4b** display broad peaks between 23°-26°, indicating their poor crystallinity. Both materials exhibit an interlayer spacing of 0.36 nm, slightly larger than the typical graphite spacing of 0.336 nm. At the same time, the PXRD pattern of TEG-350 exhibited a vast peak, indicating the amorphous nature of carbon.

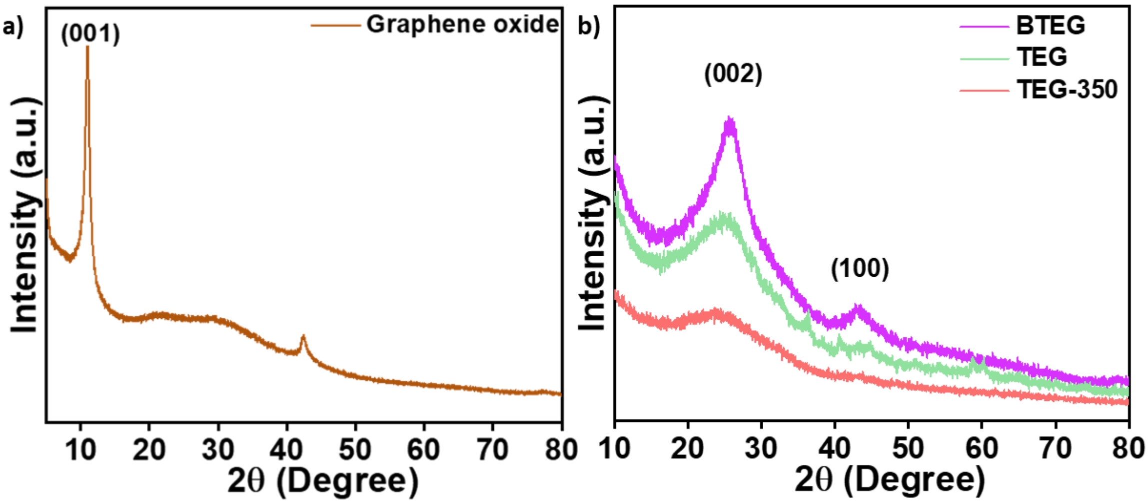

Figure 4. PXRD pattern of a) graphite oxide, b) BTEG, TEG, and TEG-350.

Figure 5 presents the Raman spectra of BTEG, highlighting its rich defect content with an I_D/I_G ratio of 0.95. This is marginally higher than the ratio observed for TEG and TEG-350, which have an I_D/I_G value of 0.93 and 0.87, respectively.

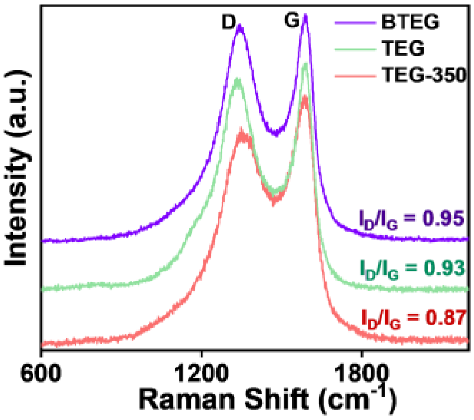

Figure 5. Raman spectra of BTEG, TEG, and TEG-350.

The nitrogen adsorption analysis reveals that the BET (Brunauer–Emmett–Teller) specific surface area, as depicted in **Figure 6a** (type I isotherm), is 312 m^2 g^{-1} for TEG-350, 203 m^2 g^{-1} for TEG and 129 m^2 g^{-1} for BTEG.

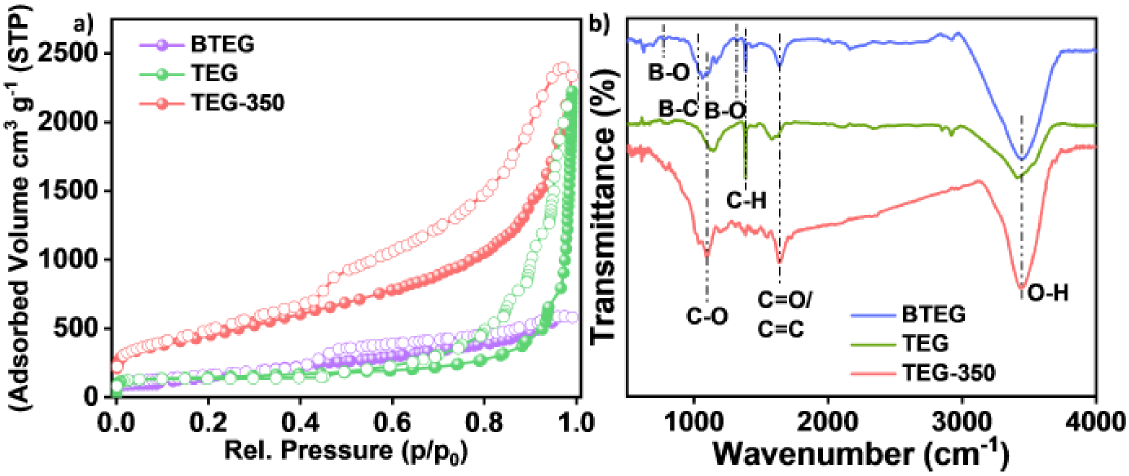

Figure 6. a) N_2 adsorption/ desorption isotherms and b) FT-IR spectra of BTEG, TEG, and TEG-350.

In the Fourier transform infrared (FTIR) spectra of BTEG, as illustrated in **Figure 6b** by Romanos et al. (2013), there are distinctive peaks that correlate with the vibrations of B-O at 781 cm^{-1} and 1321 cm^{-1} and B-C at 1100 cm^{-1}.

The X-ray photoelectron (XPS) analysis in Figure 7a of BTEG shows the C-C peak at 284.8 eV for C 1s spectra. **Figure 7b** shows O 1s spectra, which reveal C-O functionalities and weak signatures of the B-O functional group. **Figure 7c** shows B 1s spectra, revealing boron content to be 2.7 wt%. In **Figure 7d**, the B 1s peak of BTEG is resolved into four types of boron species: BC_3 (188 eV), BC_2O (190 eV), BCO_2 (191.5 eV), and B-OH (193.2 eV). Predominantly, boron species are found as BC_2O (41.1 wt%)

and BCO_2 (51.1 wt%), indicating boron's replacement of carbon atoms at the edges or defects in the graphene structure.[26,27] A minor presence of BC_3 species (4.4 wt%) suggests that the substitution of carbon by boron in the graphitic lattice is relatively limited.

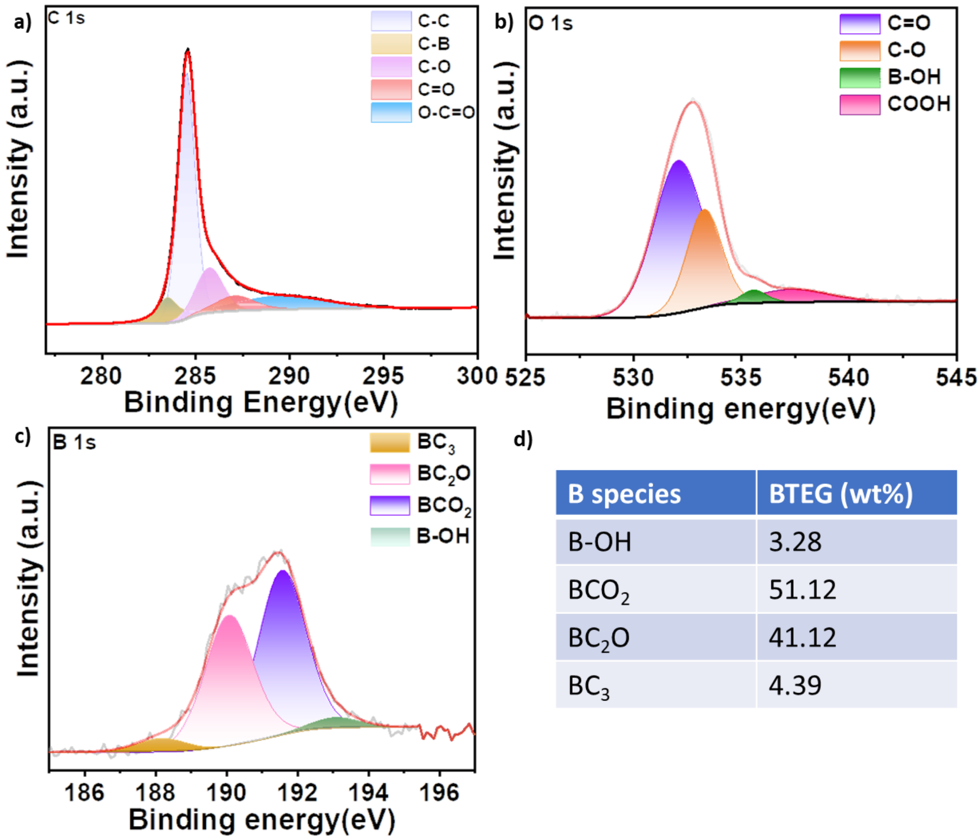

B species	BTEG (wt%)
B-OH	3.28
BCO_2	51.12
BC_2O	41.12
BC_3	4.39

Figure 7. High-resolution XPS spectra of a) C 1s, b) O 1s, and c) B 1s elements for BTEG. d) Weight percentage content of various boron species present.

Boron content was calculated from thermogravimetric analysis (TGA) (**Figure 8**).

Boron wt.% = (100-weight loss)% / molecular weight of boron * molecular weight of boric acid

= 12%/ 69.62 * 21.62

= 3.7wt.%

The boron content determined from TGA analysis is approximately 2.7 wt%, comparable to the boron content measured from XPS.

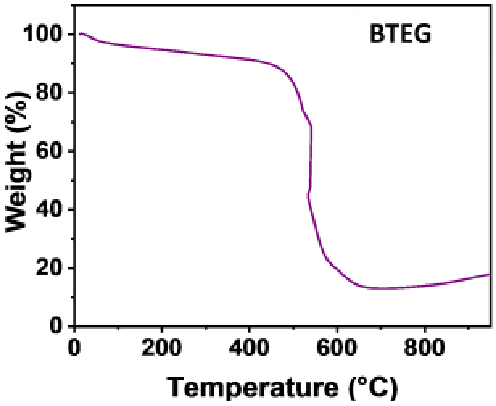

Figure 8. TGA curve of BTEG.

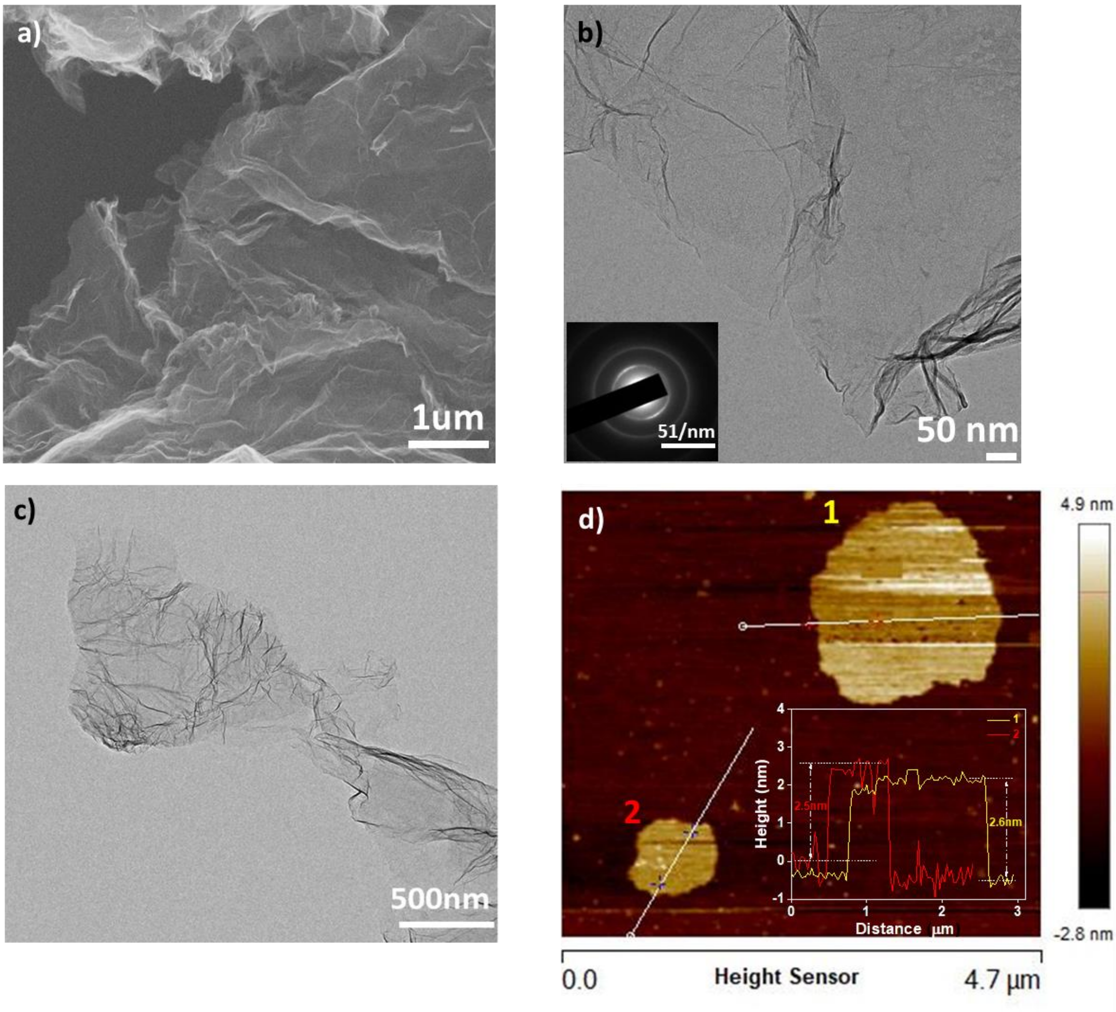

Figure 9. a) FESEM, b) TEM and d) AFM image of BTEG. d) TEM image of TEG.

The Field emission scanning electron microscopy (FESEM) and Transmission Electron Microscopy (TEM) image of BTEG, shown in **Figures 9a and 9b**, displays ultrathin, wrinkled nanosheets. The Selected Area Electron Diffraction (SAED) pattern reveals diffused diffraction rings for both TEG and BTEG, as shown in the inset of **Figure 9b**.

The TEM image of TEG is akin to that observed for BTEG, as shown in **Figure 9c**. The Atomic Force Microscopy (AFM) measurements, as seen in **Figure 9d**, indicate that the BTEG nanosheets are approximately 2.5 nm thick. Given that the standard thickness of a single graphene layer is about 0.4 nm, these 2.5 nm sheets are likely composed of around 7 graphene layers, as reported in [28]

Electrochemical Evaluations for alkali-ion batteries

Half-cell experiments were performed using BTEG/ TEG/ TEG-350 for LIB, SIB, and PIB to assess the impact of boron doping on TEG. For LIB, SIB, and PIB performance testing of BTEG, the selected electrolyte was 1M $LiPF_6$ (EC: DEC), 1M $NaPF_6$ (EC:DEC: FEC(10vol%)), and 5M KFSI (EC: DEC). Before initiating the electrochemical experiments, BTEG, when paired with Li/ Na/ K metal in a half-cell configuration, underwent a stabilization period of 24 hours, as depicted in **Figure 10**. During this phase, the open circuit voltage (OCV) for the LIB, SIB, and PIB showed a slight change of 92%, 98%, and 99%, respectively. All electrodes were equilibrated similarly, which was followed by battery studies.

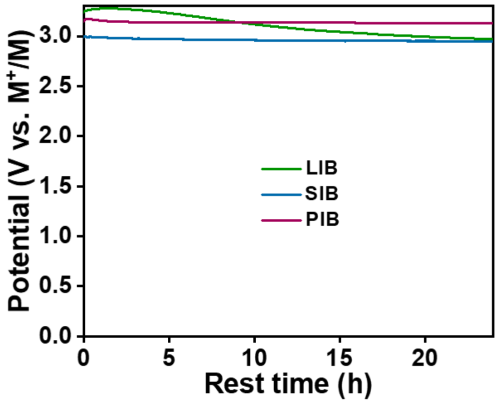

Figure 10. Comparison of open circuit voltage of BTEG for LIB, SIB, and PIB.

Firstly, the galvanostatic charge-discharge profile was studied for TEG-350 at a low current density of 25 mA g^{-1}. It exhibited poor reversibility through 5 cycles for LIB, SIB, and PIB, as shown in **Figure 11**. TEG-350 showed irreversibility with LIB and capacity value of 128 mAh g^{-1} and 83 mAh g^{-1} for SIB and PIB, respectively, after 5 cycles. Notably, TEG-350 exhibits poor reversibility on cycling at even low current density for LIB, SIB, and PIB.

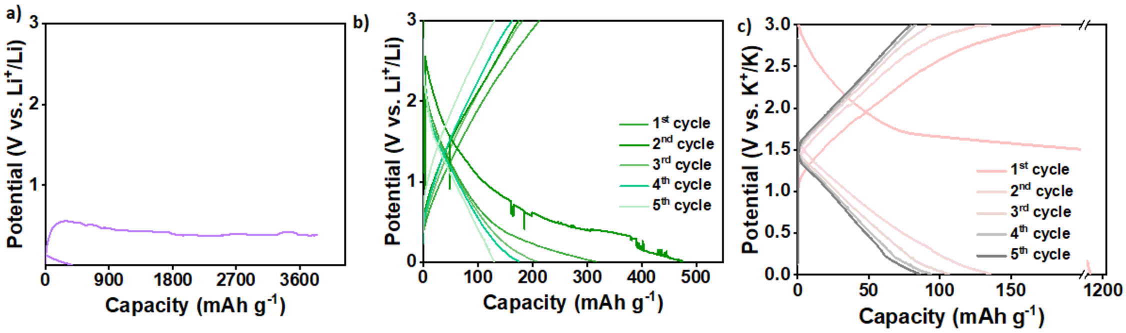

Figure 11. Galvanostatic charge-discharge (GCD) profiles of TEG-350 for a) LIB, b) SIB, and c) PIB at 25 mA g^{-1}.

After annealing TEG-350, the resulting TEG obtained showed reversible capacity values of 826 mAh g^{-1} for LIB, 83 mAh g^{-1} for SIB, and 225 mAh g^{-1} for PIB, seen in **Figure 12**.

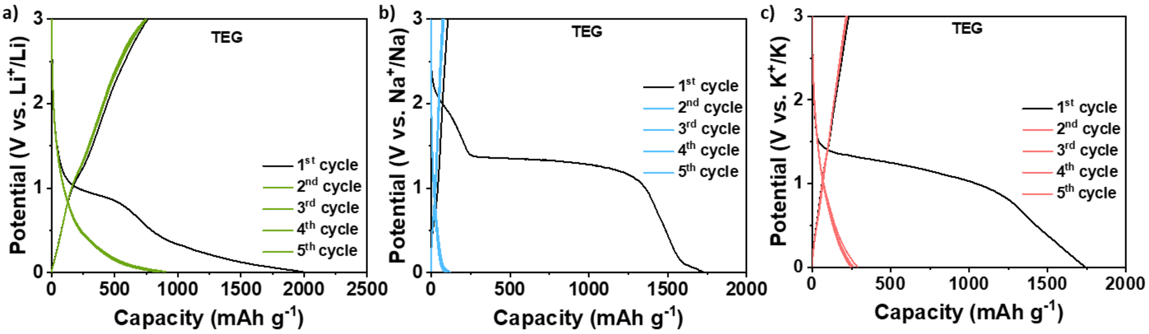

Figure 12. GCD profiles of TEG for a) LIB, b) SIB, and c) PIB at 25 mA g^{-1}.

Finally, after annealing with boron dopant, the resulting BTEG obtained (main sample) was tested thoroughly for electrochemical studies. The lithium storage behavior in BTEG was primarily analyzed using cyclic voltammetry (CV). Displayed in **Figure 13a** are the first five continuous CV curves ranging from 3.0 to 0.01 V (V vs. Li/Li$^+$) at a scan rate of 0.01 mV s^{-1}. The initial cycle revealed a significant cathodic peak between 1.2 and 0.6V, which is linked to the decomposition of the electrolyte and the consequent formation of a solid electrolyte interphase (SEI).[29] This peak diminishes in later cycles as the SEI becomes stable. The overlapping CV curves from the second cycle onwards indicate a highly reversible interaction of lithium ions with the boron-doped graphene layers in BTEG. These findings align with the galvanostatic charge-discharge (GCD) curves for the BTEG electrode, as seen in **Figure 13b**. BTEG demonstrates an initial Coulombic efficiency (ICE) of 51%, surpassing TEG's value of 35%. TEG exhibits lower ICE, likely due to its high surface area (203 m^2 g^{-1}) compared to BTEG (129 m^2 g^{-1}), leading to more electrolyte decomposition and irreversible Li$^+$ capture. After five cycles, BTEG showed a reversible charge storage capacity of 1014 mAh g^{-1} at 25 mA g^{-1}, exceeding TEG's capacity of 825 mAh g^{-1}, as illustrated in **Figures 14b and 13a**.

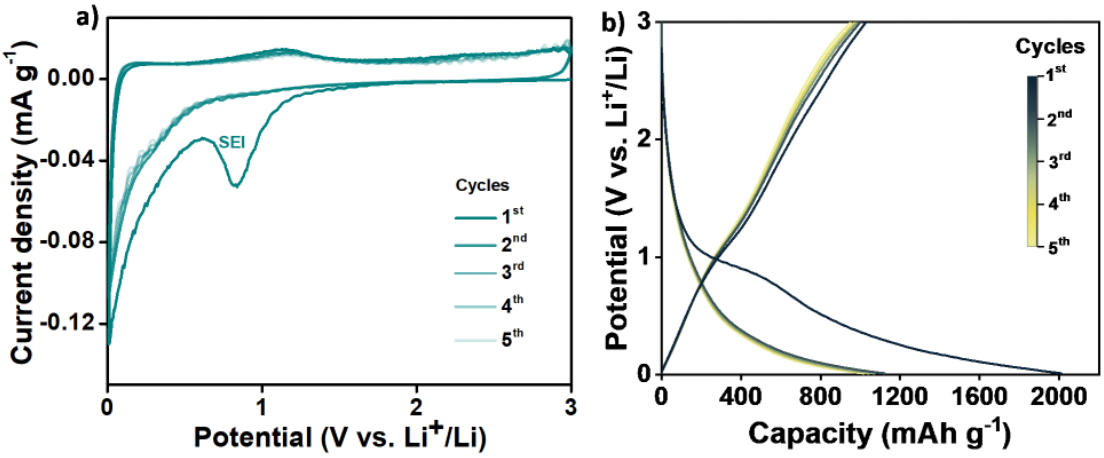

Figure 13. a) Cyclic voltammogram (0.01 mV s^{-1}) and b) GCD profile (25 mA g^{-1}) of BTEG electrode with Li-ion battery.

At a high current density of 1 A g^{-1}, BTEG and TEG exhibited an initial capacity of 276 mAh g^{-1} and 269 mAh g$^{-1,}$ respectively (**Figure 14a**). BTEG shows an average Coulombic efficiency of 99.7% and 75% capacity retention following 1000 lithiation/ delithiation cycles for long-term cycling.

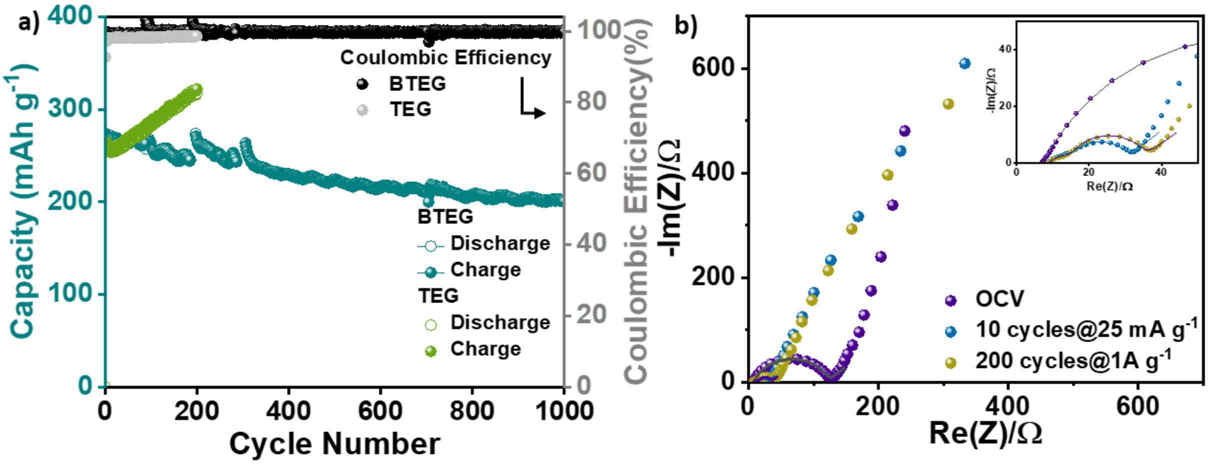

Figure 14. a) Comparison of long-term cycling for BTEG and TEG at 1 A g^{-1}. b) Comparison of Nyquist plots of BTEG before and after cycling and inset fitted data (solid line).

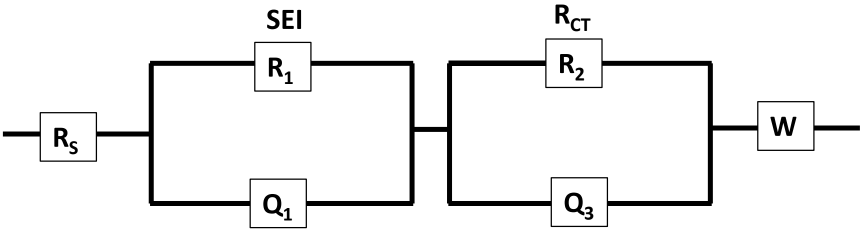

Figure 15. An equivalent circuit is used for fitting Nyquist plots for BTEG.[30]

To analyze the kinetics of lithium-ion reaction in BTEG before and after cycling at two different current densities (25 mA g^{-1} and 1 A g^{-1}), electrochemical impedance spectroscopy (EIS) measurements were conducted, as seen in **Figure 14b**. EIS typically encompasses three segments, each linked to a specific frequency range. The high-frequency range corresponds to the bulk resistance (R_S), whereas the medium-frequency range represents the solid electrolyte interface resistance (R_{SEI}) and the charge transfer resistance (R_{CT}) (**Figure 15**).[31][32] The low-frequency range's slope is associated with lithium ions' diffusional impedance (ZW) within the electrode. R_S, indicative of unstable ohmic impedance due to electrolyte resistance and often unchanged in battery aging, was not considered in this analysis. A notable decrease in R_{CT} was observed, from 107 Ω in the charged state at open circuit voltage to 12 Ω after 5 cycles at 25 mA g^{-1}, indicating electrode activation and stabilization due to gradual electrolyte penetration and SEI formation.[33] Additionally, the Z_W at open circuit voltage (OCV) initially exhibits capacitive-type behavior, likely due to the interaction of the electrolyte with graphene layers. This behavior shifts to a diffusive pattern after 5 cycles, post-SEI formation on the surface, at 25 mA g^{-1}. The stabilization of the R_{CT} value at 17 Ω, even after 200 cycles at 1 A g^{-1}, suggests that BTEG maintains robust performance over time.

The rate capability of BTEG was characterized by reversible capacities of 1014 mAh g^{-1}, 731 mAh g^{-1}, 615 mAh g^{-1}, 506 mAh g^{-1}, 342 mAh g^{-1}, and 261 mAh g^{-1} at current densities of 25 mA g^{-1}, 100 mA g^{-1}, 200 mA g^{-1}, 500 mA g^{-1}, 800 mA g^{-1}, and 1000 mA g^{-1} respectively, as depicted in **Figure 16**. In contrast, TEG displayed reversible capacities of 825 mAh g^{-1}, 665 mAh g^{-1}, 594 mAh g^{-1}, 484 mAh g^{-1}, 342 mAh g^{-1}, and 261 mAh g^{-1} at the same respective current densities (refer to **Figure 16**). BTEG and TEG retained over 80% of their initial capacity when the current density was reduced to 25 mA g^{-1}, with BTEG at 81% and TEG at 90%. Following the rate performance tests, long-term charge-discharge cycling at 100 mA g^{-1} was carried out with the BTEG electrode. This test further revealed an increase in BTEG's capacity from 735 mAh g^{-1} to

1042 mAh g^{-1}, indicating TEG material's stability and enhanced performance upon boron integration.

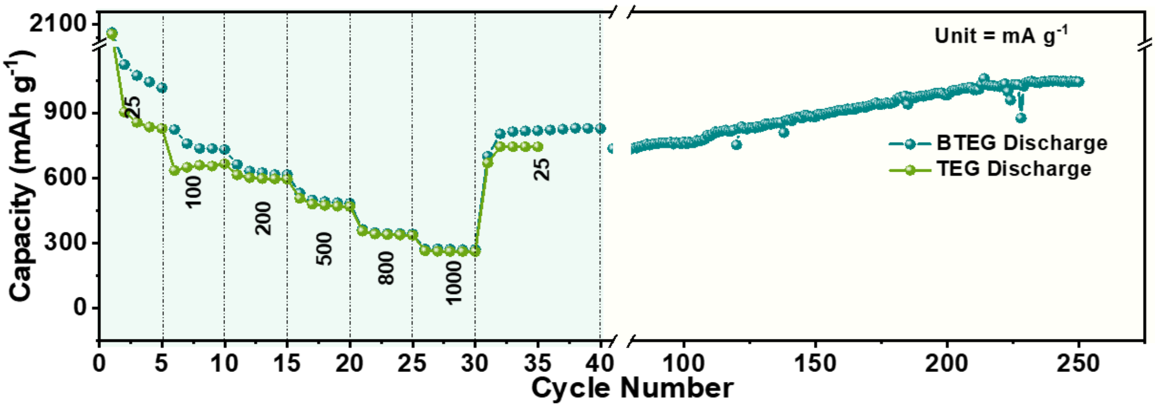

Figure 16. Comparison of rate performance of BTEG and TEG for LIB.

Cyclic voltammetry for BTEG shows a highly reversible battery with SIB and PIB at a low scan rate of 0.01 mV s^{-1}, as shown in **Figures 17a and 17b**.

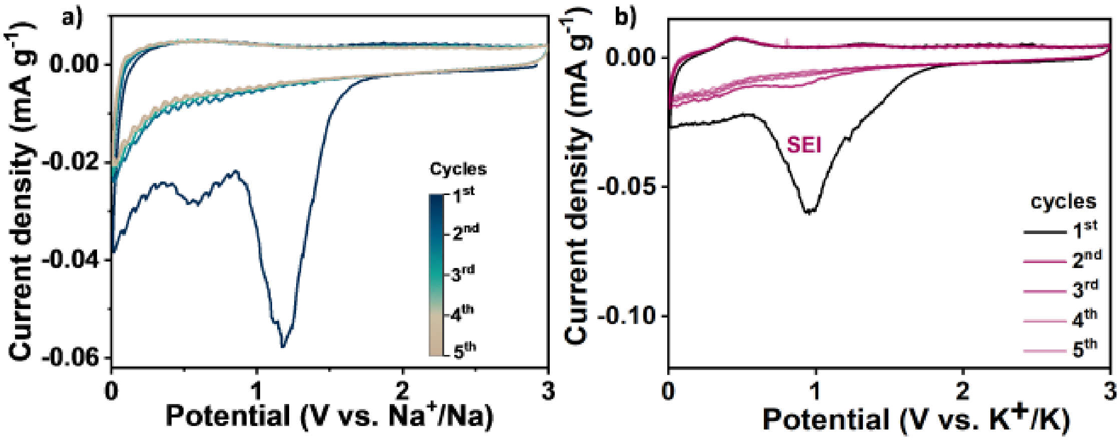

Figure 17. Cyclic voltammograms of BTEG with a) SIB and b) PIB at a scan rate of 0.01 mV s^{-1}.

The BTEG sample displays an initial Coulombic efficiency (ICE) of 27% for SIB and 29% for PIB, markedly surpassing the ICE values of TEG, which are 10% for SIB and 16% for PIB, as illustrated in **Figures 18a,b and 12b,c** respectively. Moreover, BTEG achieves a reversible discharge capacity of 295 mAh g^{-1} for Na^+ and 369 mAh g^{-1} for K^+ at a current density of 25 mA g^{-1}. The higher capacity value of BTEG for PIB, compared to SIB, is likely due to the employment of a highly concentrated 5M KFSI salt instead of the 1M $NaPF_6$.

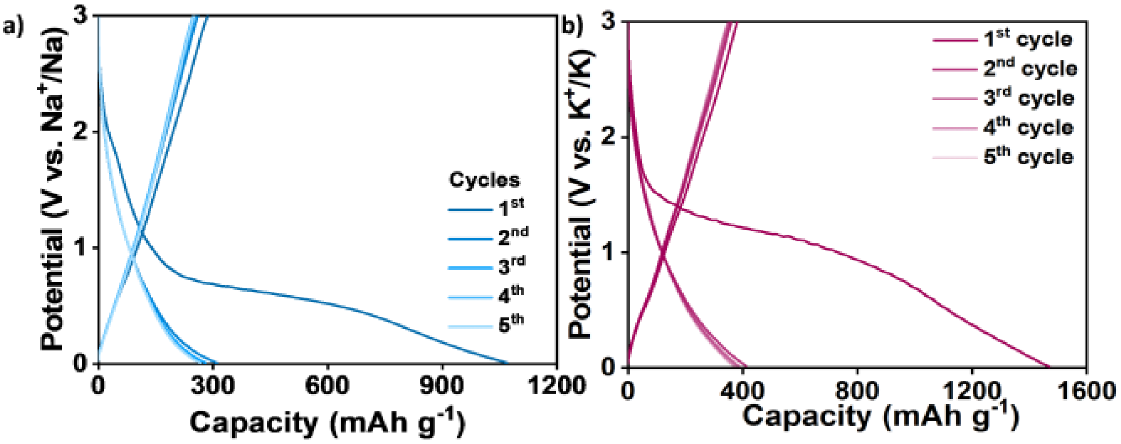

Figure 18. GCD profiles of BTEG with a) SIB and b) PIB at a low current density of 25 mA g^{-1}.

This claim is supported by the evidence that when BTEG is tested with a 1M KFSI electrolyte for charge-discharge cycles at 25 mA g^{-1}, it exhibits a discharge capacity value of 270 mAh g^{-1} (**Figure 19**).

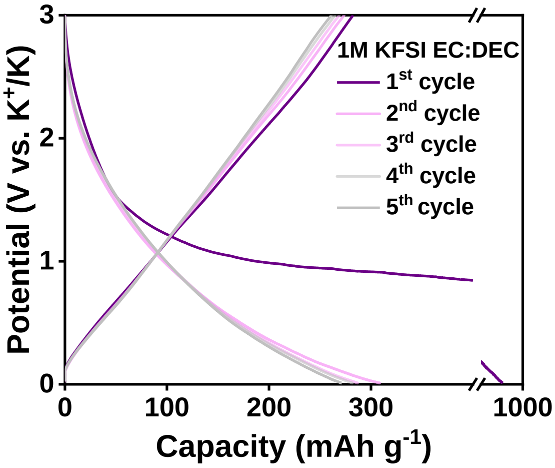

Figure 19. GCD profile of BTEG with PIB using electrolyte 1M KFSI at a low current density of 25 mA g^{-1}.

Conversely, TEG displayed significantly lower capacities of just 83 mAh g^{-1} for SIB and 225 mAh g^{-1} for PIB, as shown in **Figures 12b and 12c,** respectively.

At a high current density of 1 A g^{-1}, BTEG demonstrated a capacity of 147 mAh g^{-1} for SIB, which is approximately eight times greater than TEG's capacity of 21 mAh g^{-1}, as depicted in **Figure 20a**. For PIB, BTEG recorded a capacity of 184 mAh g^{-1}, approximately double the 84 mAh g^{-1} capacity achieved by TEG, shown in **Figure 20b**. This enhanced performance is likely due to increased surface defects associated with boron dopant species (primarily BCO_2 and BC_2O) in BTEG, as discussed in reference

[21]. BTEG exhibited impressive capacity retention in terms of long-term cycling, maintaining over 100% capacity for SIB and 87% for PIB after 1000 cycles (**Figures 20a and 20b**). Additionally, BTEG showed exceptionally high average Coulombic efficiencies of 99.9% for SIBs and 99.95% for PIBs.

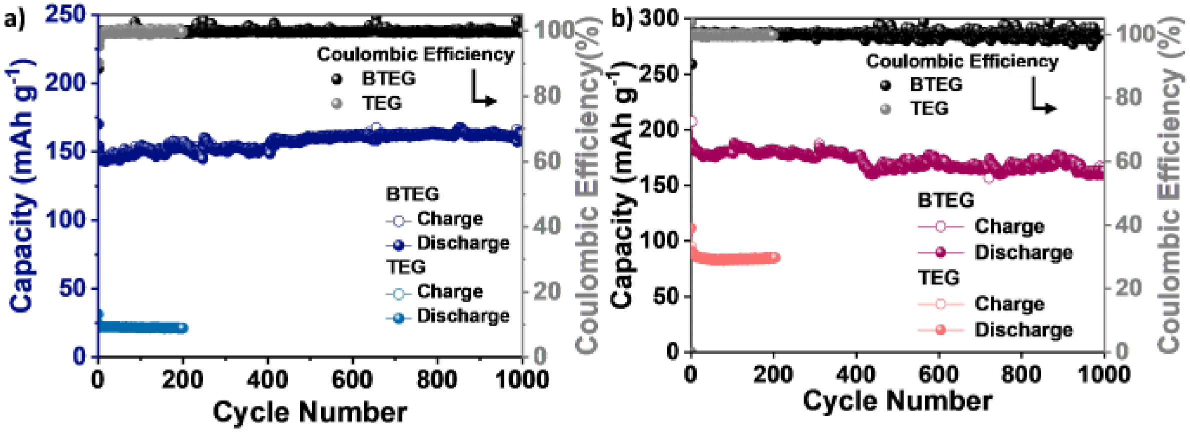

Figure 20. Comparison of long-term cycling for BTEG and TEG with a) SIB and b) PIB at 1 A g^{-1}.

Electrochemical Impedance Spectroscopy (EIS) analyses of BTEG reveal a modest rise in the charge transfer resistance (R_{CT}) value, increasing from 170 Ω to 215 Ω after 200 cycles at a current density of 1 A g^{-1} for SIB (**Figure 21a**). Conversely, for Potassium-Ion Batteries (PIB), there was a significant decrease in R_{CT}, from 721 Ω to 332 Ω, observed after the same 200 cycles at 1 A g^{-1} (**Figure 21b**). This reduction in PIB can be attributed to enhanced reaction kinetics resulting from continuous potassiation/depotassiation processes.[20]

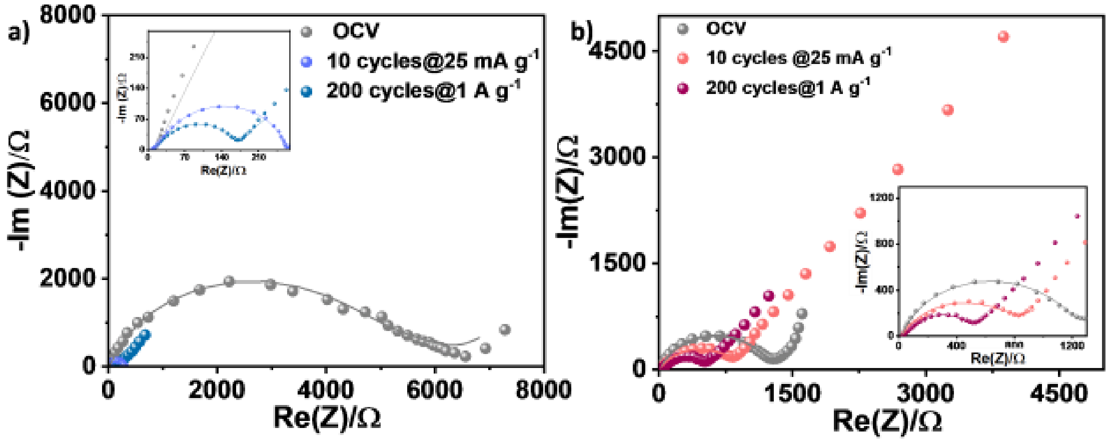

Figure 21. Comparison of Nyquist plots for BTEG with a) SIB and b) PIB with cycling.

BTEG showed enhanced rate performance compared to TEG for both SIB and PIB, as depicted in **Figures 22 and 23,** respectively. The reversible capacities at various current densities for SIB and PIB using TEG and BTEG are detailed in **Tables 1 and 2**. Specifically, BTEG retained 92% of its capacity with SIB when the current density returned to 25 mA g^{-1} after 40 cycles and maintained 95% at 100 mA g^{-1} after 300 cycles. For PIB, BTEG exhibited 96% capacity retention after 40 cycles when reverting to 25 mA g^{-1} and an impressive 100% retention at 100 mA g^{-1} after 284 cycles. This consistent and reversible charge storage capability of BTEG for both SIB and PIB can be ascribed to the electrolyte's role in forming a stable solid electrolyte interphase (SEI), which mitigates volume changes during the repetitive insertion and extraction of alkali ions.[34]

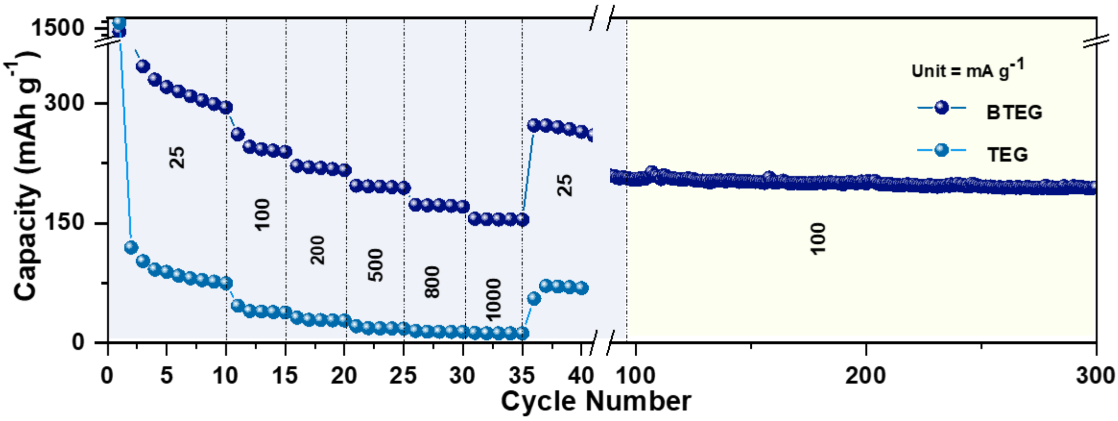

Figure 22. Comparison of rate performance for BTEG and TEG with SIB.

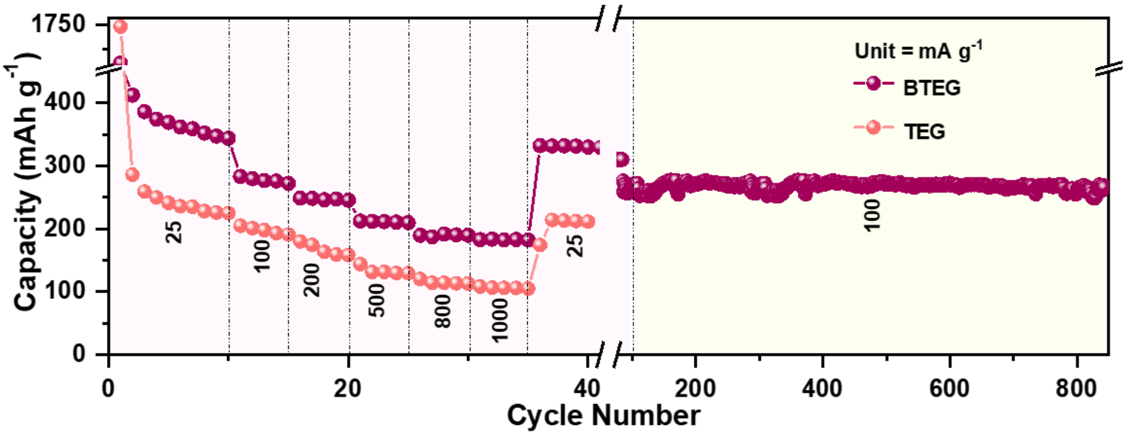

Figure 23. Comparison of rate performance for BTEG and TEG with PIB.

SIB **Current density (mA g^{-1})**	**BTEG** **(Capacity, mAh g^{-1})**	**TEG** **(Capacity, mAh g^{-1})**
25	295	75
100	246	38
200	220	27
500	195	18
800	172	13
1000	154	12
25	272	70

Table 1. Discharge capacity values were compared for BTEG and TEG at different densities from the rate performance plot with SIB.

PIB **Current density (mA g^{-1})**	**BTEG** **(Capacity, mAh g^{-1})**	**TEG** **(Capacity, mAh g^{-1})**
25	344	225
100	283	191
200	246	158
500	211	129
800	189	113
1000	182	105
25	331	211

Table 2. Discharge capacity values were compared for BTEG and TEG at different densities from the rate performance plot with PIB.

Electrochemical kinetic analysis for understanding alkali-ion storage mechanism in BTEG:

Detailed electrokinetic studies were conducted to understand further the enhanced electrochemical performance of the BTEG electrode in storing Li, Na, and K ions. Mechanistic investigations of the BTEG anode involved using electrolytes 1M $LiPF_6$ (EC: DEC) for LIB, 1M $NaPF_6$ (EC: DEC: FEC) for SIB, and 5M KFSI (EC: DEC) for PIB. The charge storage mechanism can be either diffusion-controlled or capacitive-controlled. The reaction kinetics were analyzed using cyclic voltammetry (CV) curves at various scan rates ranging from 0.01 mV s^{-1} to 0.7 mV s^{-1} for LIB, SIB, and PIB, as shown in **Figures 23a-c**. The relationship between the peak current (i) and the scan rate (ν) is expressed by a specific equation, indicating how the peak current changes with varying scan rates[35,36].

$$i = a\nu^{b} \tag{1}$$

In this equation, a and b are constants, where the value of b can be deduced from the slope of the plot between log(ν) and log(i).

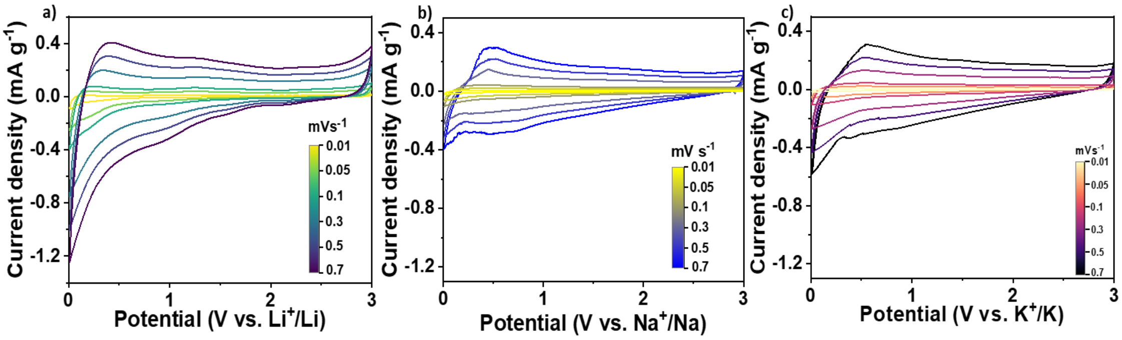

Figure 23. Cyclic voltammograms for BTEG at different scan rates from 0.01-0.7 mV s^{-1} in a) LIB, b) SIB, and c) PIB.

A b value of 0.5 suggests a diffusion-controlled process, whereas a value of 1 indicates a surface-controlled reaction. **Figure 24a** presents a log(ν) versus log(i) plot, demonstrating a linear correlation with an R^2 value of 0.99. For LIB using BTEG, a pseudocapacitive process is indicated, as evidenced by a b value of 0.57 for the anodic peak (close to 1) and 0.92 for the cathodic peak.[37] This suggests a diffusion-controlled process for the anodic reaction and a capacitive process for the cathodic reaction in LIB. The calculated b values for SIB are 0.77 (anodic) and 0.98 (cathodic), and for PIB, they are 0.84 (anodic) and 0.89 (cathodic). These higher b values point towards a capacitive-controlled process for both SIB and PIB, likely due to the larger size of Na$^+$ and K$^+$ than Li$^+$.

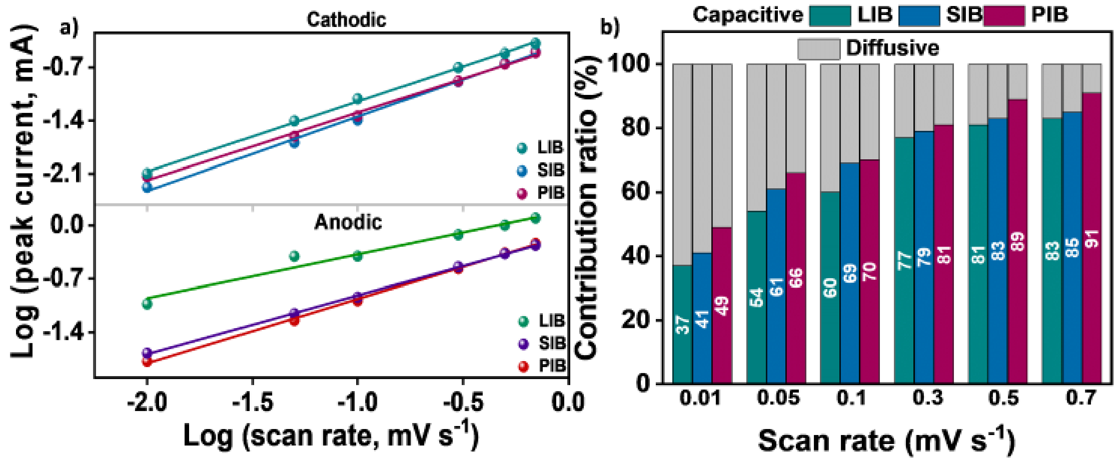

Figure 24. a) Comparison of b values for anodic and cathodic peaks in LIB, SIB, and PIB. B) Relative capacitive contribution histogram of BTEG for LIB, SIB, and PIB at different scan rates.

Additionally, to quantitatively assess the contributions from both capacitive-controlled and diffusion-controlled processes, the cyclic voltammetry (CV) curves were further examined using Dunn's equation[38]:

$$i(V) = k_1\nu + k_2\nu^{1/2} \qquad (2)$$

In this context, ν represents the scan rate, and the constants k_1 and k_2 are derived from the plot of $i(V)/\nu^{1/2}$ versus $\nu^{1/2}$. Here, $k_1\nu$ corresponds to the capacitive effect, while $k_2\nu^{1/2}$ is indicative of the diffusion-controlled insertion process. At a scan rate of 0.01 mV s^{-1}, the diffusion-controlled process accounted for 37% of the total current (charge-discharge) for LIB, 41% for SIB, and 49% for PIB, (**Figure 24b**) and as shown in the CV profiles (**Figures 25-27**). When the scan rate was increased to 0.7 mV s^{-1}, the contribution from capacitive-controlled processes rose to 83% for LIB, 85% for SIB, and 91% for PIB (**Figure 24b**). The pseudocapacitive mechanism, highlighted in the shaded areas of the cyclic voltammograms, is evident across all scan rates in **Figures 25-27** for LIB, SIB, and PIB. This dominant non-faradaic contribution at higher scan rates, which enhances the rate performance, is attributed to the B-O/C-O functionalities in BTEG.[39]

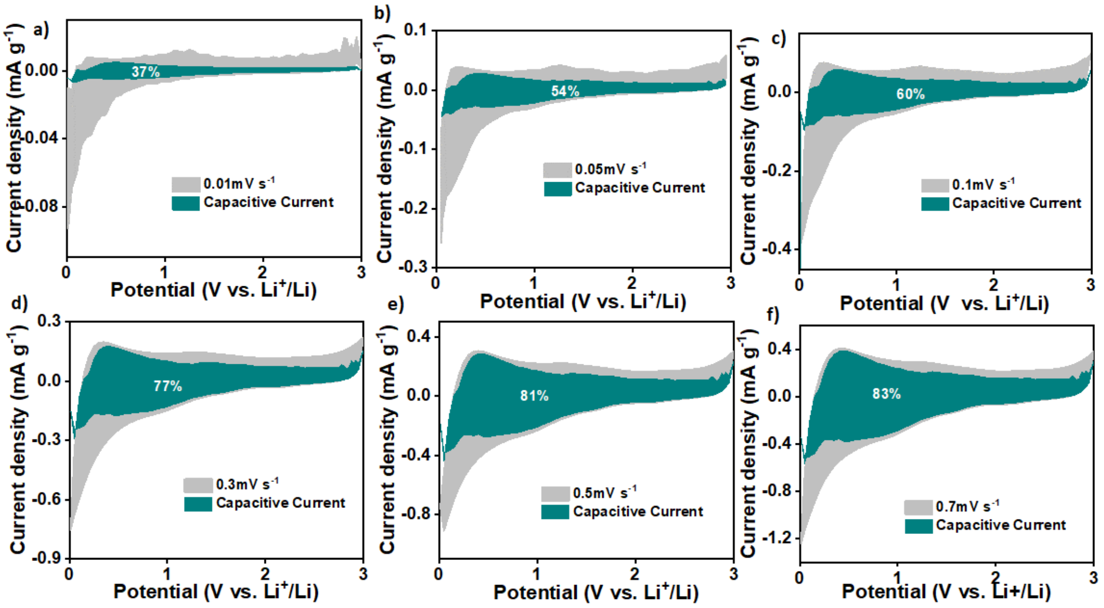

Figure 25. Pseudocapacitive contribution for BTEG a) 0.01mV s^{-1}, b) 0.05mV s^{-1}, c) 0.1mV s^{-1}, d) 0.3mV s^{-1}, e) 0.5mV s^{-1} and f) 0.7mv s^{-1} in LIB.

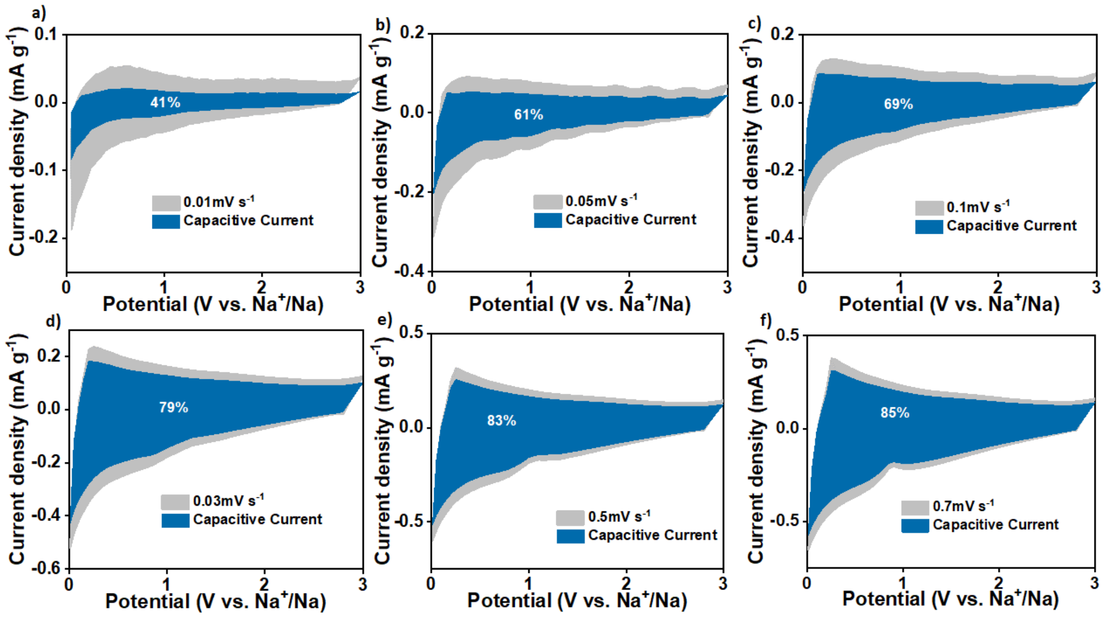

Figure 26. Pseudocapacitive contribution for BTEG a) 0.01mV s^{-1}, b) 0.05mV s^{-1}, c) 0.1mV s^{-1}, d) 0.3mV s^{-1}, e) 0.5mV s^{-1} and f) 0.7mv s^{-1} in SIB.

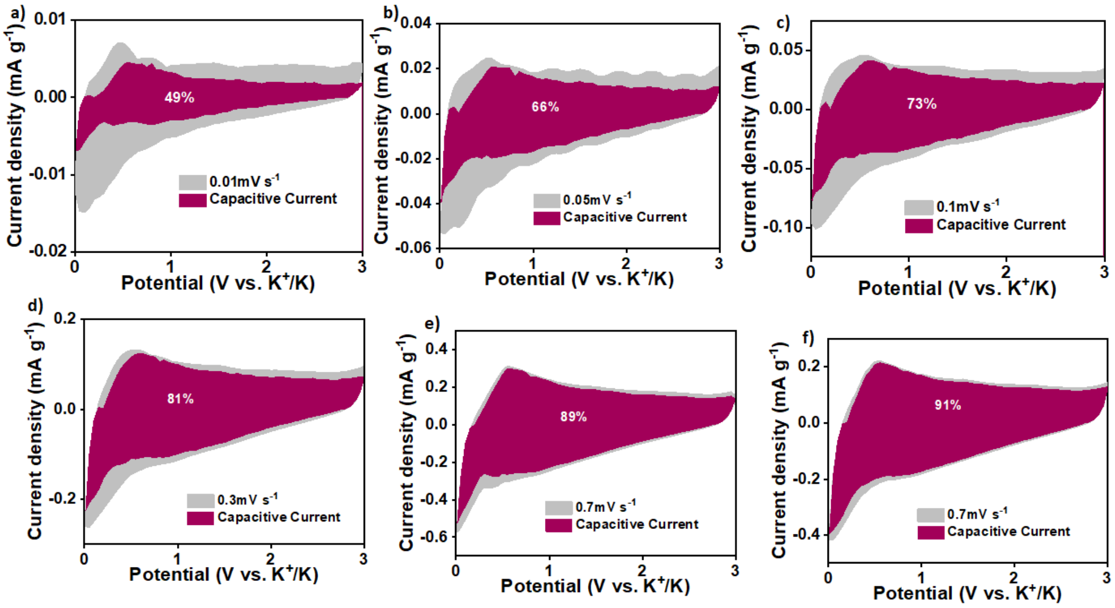

Figure 27. Pseudocapacitive contribution for BTEG a) 0.01mV s^{-1}, b) 0.05mV s^{-1}, c) 0.1mV s^{-1}, d) 0.3mV s^{-1}, e) 0.5mV s^{-1} and f) 0.7mv s^{-1} in PIB.

To investigate the charge storage sites in BTEG during charge/discharge for LIB, SIB, and PIB, operando Raman spectroscopy studies were performed. These measurements helped to track microstructural changes while discharging from 3 V (denoted as D3V) to 0.01 V (denoted as D0.01V) and recharging back to 3 V (denoted as C3V). The pristine BTEG comprises G and D peaks, as shown in **Figure 5**. G-peak in Raman spectra is associated with first-order scattering from sp^2-bonded carbon atoms in crystalline graphene (in-plane E_{2g} symmetry phonon).[24][40] Meanwhile, the D-peak indicates disorder scattering near the K-point in the graphene Brillouin zone.[41] D and G-peak energy and width are sensitive to charge transfer involving Li, Na, and K ions.

For LIB (**Figure 28**), lithiation broadens the D and G band peaks below 1.25 V, signifying Li^+ interaction with defect and graphitic sites in BTEG. As intercalation progresses, a downshift in the G peak energy occurs, indicating electron doping in graphene sheets. This downshift is caused by charge transfer from Li atoms to the π^* antibonding orbitals of carbon, elongating the C–C bonds.[42] Similarly, the D peak intensity changes due to alterations in phonon energies and lifetimes from electron doping.[43] The gradual effect on average phonon energy suggests a homogeneously delocalized charge transfer across BTEG. At 0.01V, the disappearance of G and D peaks is observed, likely due to the formation of highly conducting LiCx, reducing optical skin depth.[44]

Upon delithiation in LIB, a reverse trend is noticed with the gradual re-emergence of D and G peaks, supporting the intercalation-adsorption model and aligning with the dominant diffusion-controlled process observed in **Figure 24**.

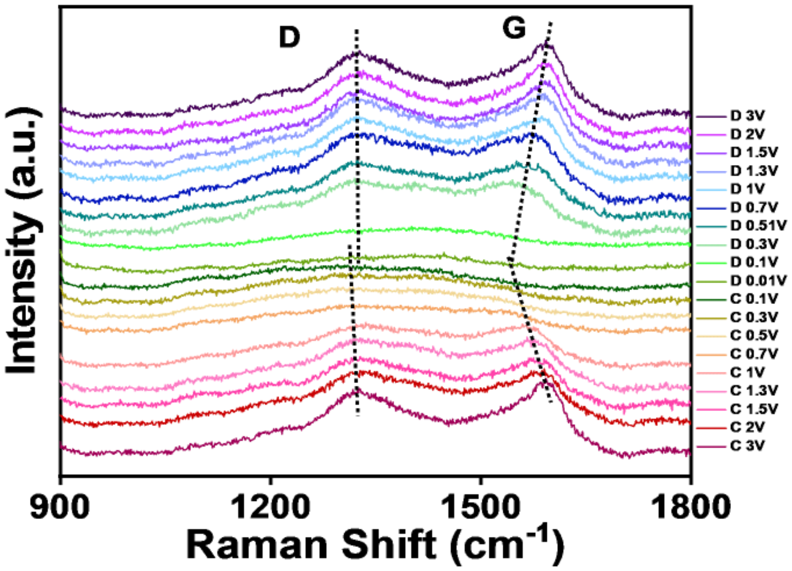

Figure 28. Operando Raman spectra of BTEG with charge/ discharge profile for LIB.

The G peak shows a redshift during SIB discharge, but its intensity stays intact even at full discharge (**Figure 29a**). In contrast, the D peak intensity significantly diminishes, and both D and G peaks are reversibly restored upon de-sodiation. **Figure 29b** shows PIB, which reveals a similar trend as seen for SIB in **Figure 29a**, and the Raman results for both SIB and PIB align with a capacitive controlled mechanism, suggesting dominant defect-related interaction with Na^+ and K^+ (**Figure 24**).

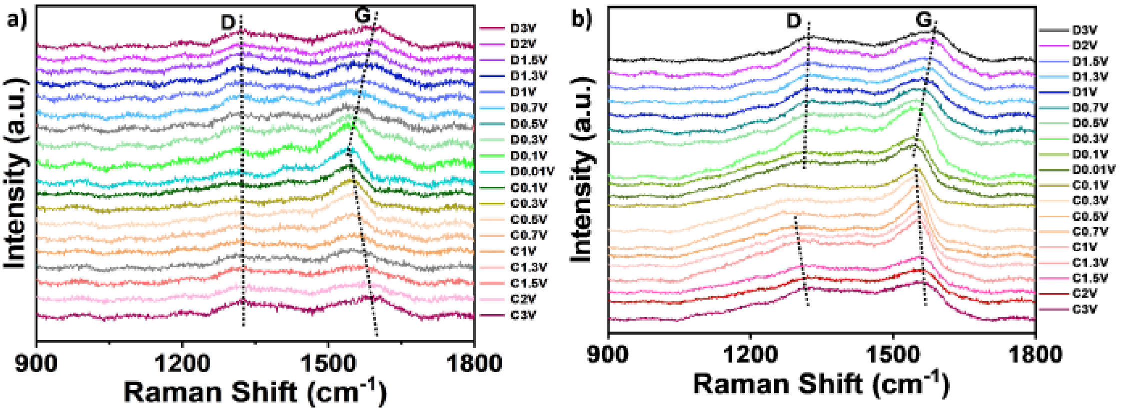

Figure 29. Operando Raman spectra of BTEG with charge/ discharge profile for a) SIB and b) PIB.

Additionally, LIB's I_D/I_G ratio shows the simultaneous disappearance of D and G peaks, while SIB and PIB display a reduced ratio (**Figure 30**), indicating different interaction mechanisms.[45] Notably, the I_D/I_G ratio for LIB (initial: 0.88; final: 0.91), SIB (initial: 0.85; final: 0.85), and PIB (initial: 0.88; final: 0.83) are restored after cycling, demonstrating the high reversibility of BTEG.

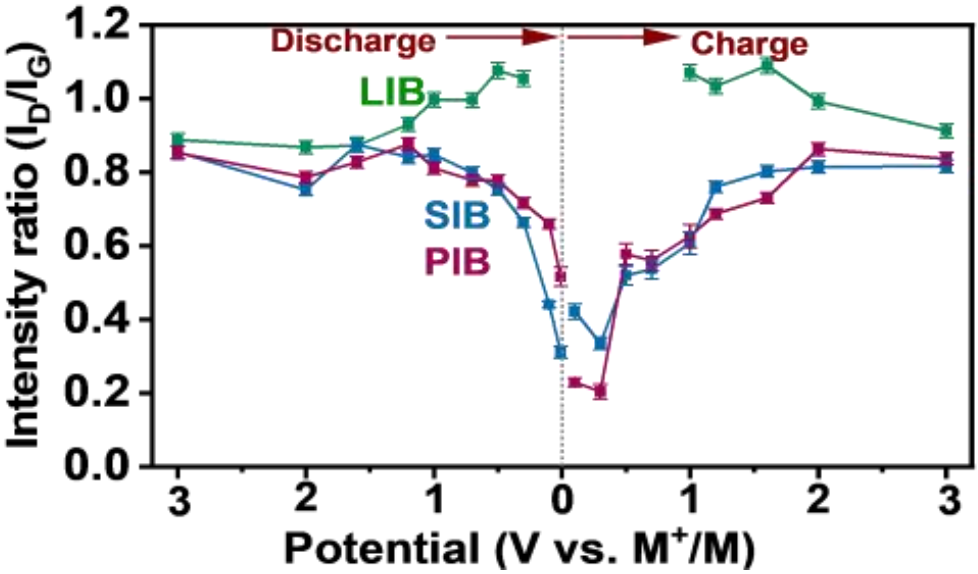

Figure 30. Comparison of I_D/I_G ratio of BTEG for LIB, SIB, and PIB obtained from operando Raman measurements.

The D and G peak positions in the Raman spectra for BTEG are reversible with both LIB and SIB, as demonstrated in **Figure 31**. However, for PIB, a slight variation in these peak positions is observed for BTEG when they are compared for discharge and charge at 3V. This discrepancy may be attributed to the use of 1M KFSI electrolyte for operando Raman measurements in PIB instead of the 5M KFSI. The decision to use 1M KFSI over 5M KFSI is due to the high concentration of the latter. Acquiring clear D and G peaks for BTEG electrodes is not easy. Therefore, 1M KFSI is preferred for operando Raman analysis in PIB.

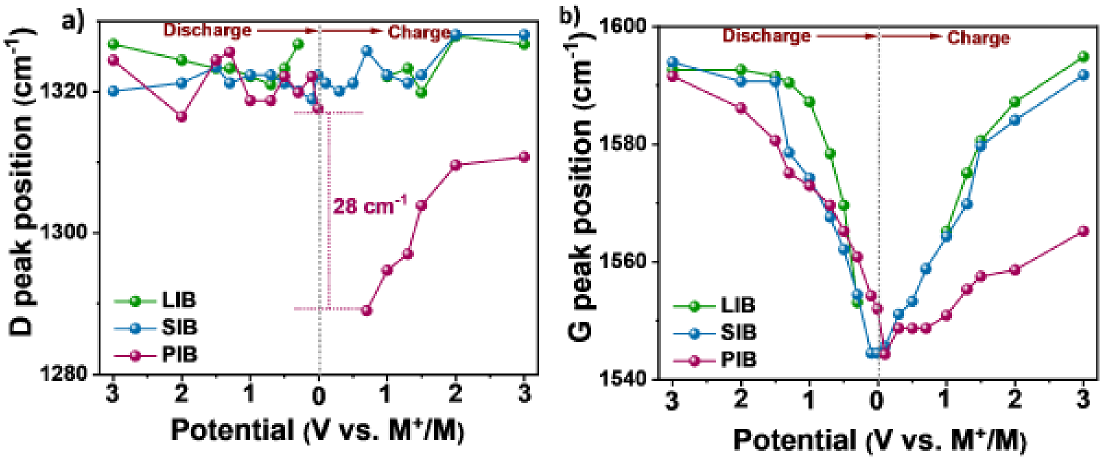

Figure 31. Comparison of a) D peak and b) G peak positions of BTEG for LIB, SIB, and PIB obtained from operando Raman measurements.

The diffusion kinetics of alkali metal ions at the charge storage sites in BTEG were evaluated using the Galvanostatic Intermittent Titration Technique (GITT). Here, a constant pulse current of 25 mA g^{-1} was applied, followed by a relaxation period for LIB, SIB, and PIB (**Figure 32**). Changes in potential during relaxation periods indicated overpotentials at various insertion/extraction stages. The diffusion coefficients were calculated at all stages except the first and last two due to significant voltage fluctuations.

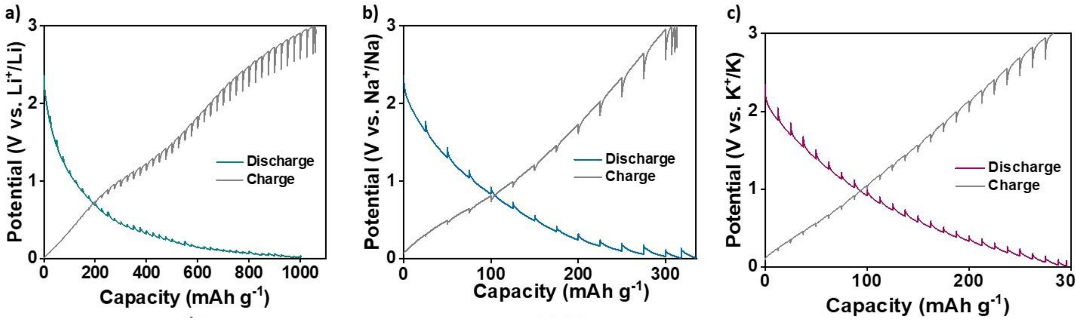

Figure 32. Charge discharge profile for GITT measurement for a) LIB, b) SIB, and c) PIB.

Figure 33 illustrates that the highest diffusion coefficient occurs at 2.5 V during discharging, after which the diffusion coefficient of alkali metal ions (D_{M+}) shows a sharp decline. This initial rapid diffusion is attributed to the availability of vacant sites in BTEG. However, diffusion slows as the sites progressively fill, and ions face a repulsive charge gradient created by the previously bound ions at defect sites, hindering further diffusion. The D_{M+} values above 1.25 V are associated with the adsorption of alkali metals on the surface of graphene layers. Below 1.25 V, the diffusion coefficient for lithium ions (D_{Li^+}) varies from 10^{-11} to $10x10^{-11}$, indicative of staging-type charge storage (dominant intercalation) into the graphitic layers.[46]

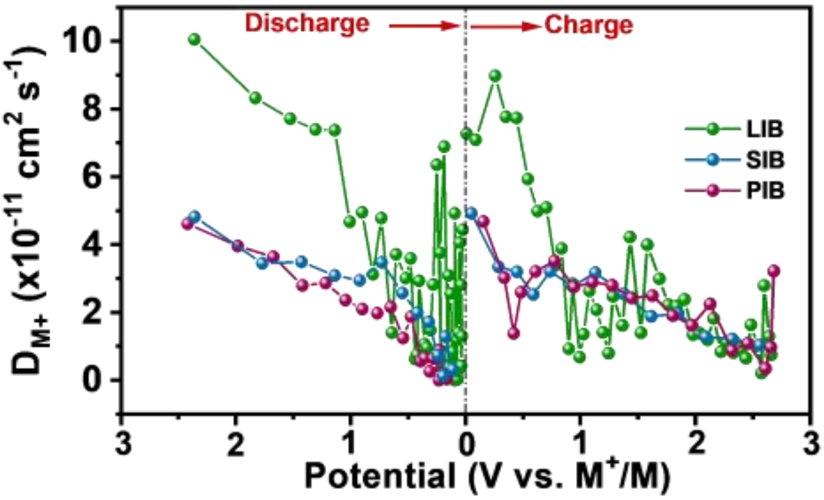

Figure 33. Comparison of diffusion coefficient values for BTEG in LIB, SIB, and PIB.

In contrast, there is a smoother decrease in the potential for SIB and PIB, reflecting the interaction of Na^+/K^+ with surface defects/ heteroatom dopants. LIB exhibits a higher diffusion coefficient than SIB and PIB (10^{-11} to $5x10^{-11}$). This is due to the full coverage of active sites in BTEG with Li^+ (intercalation-defect), in contrast to the predominantly defect-based coverage for Na^+/K^+. This finding aligns with the Raman analysis results in Figures **27 and 29**, suggesting different interaction mechanisms for Li^+, Na^+, and K^+ in BTEG. Also, on charging, expectedly, alkali ion diffusion is high initially and reduces with an increase in potential.

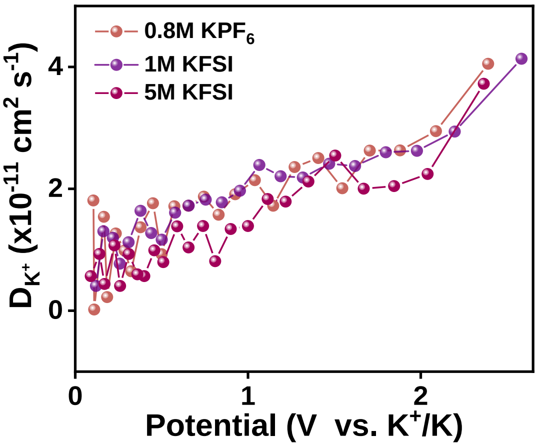

Figure 34. Comparison of diffusion coefficient value for BTEG in PIB utilizing 0.8M KPF_6, 1M KFSI, and 5M KFSI.

Additionally, BTEG exhibits similar diffusional coefficient values with electrolytes 0.8M KPF6, 1M KFSI, and 5M KFSI (**Figure 34**).

In-situ Potentiostatic Electrochemical Impedance Spectroscopy (PEIS) was employed to investigate the reaction dynamics of both the working electrode (BTEG) and the counter electrode (alkali metal) in a half-cell configuration during the charge/discharge process.[46] The EIS results, presented in **Figure 35**, were acquired after 10 cycles to ensure a stabilized Solid Electrolyte Interface (SEI). The Nyquist plots indicate that during discharging in BTEG, the charge transfer resistance (R_{CT}) for alkali metal ions (M^+) increases as the potential decreases, consistent with an increase in charge storage. This observation aligns with the findings from the Galvanostatic Intermittent Titration Technique (GITT) results, further supporting the electrochemical behavior of BTEG in the charge/discharge process. Unlike GITT, EIS considers the role of counter electrode in reaction kinetics.

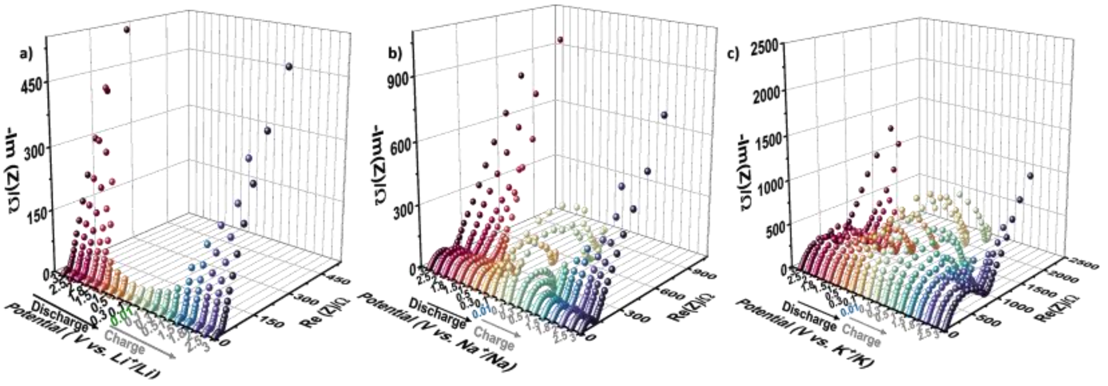

Figure 35. Comparison of Nyquist plots for BTEG during charge/ discharge with a) LIB, b) SIB, and c) PIB.

Nyquist plots were fitted for LIB, SIB, and PIB at different potentials and compared, as shown in **Figure 36**.

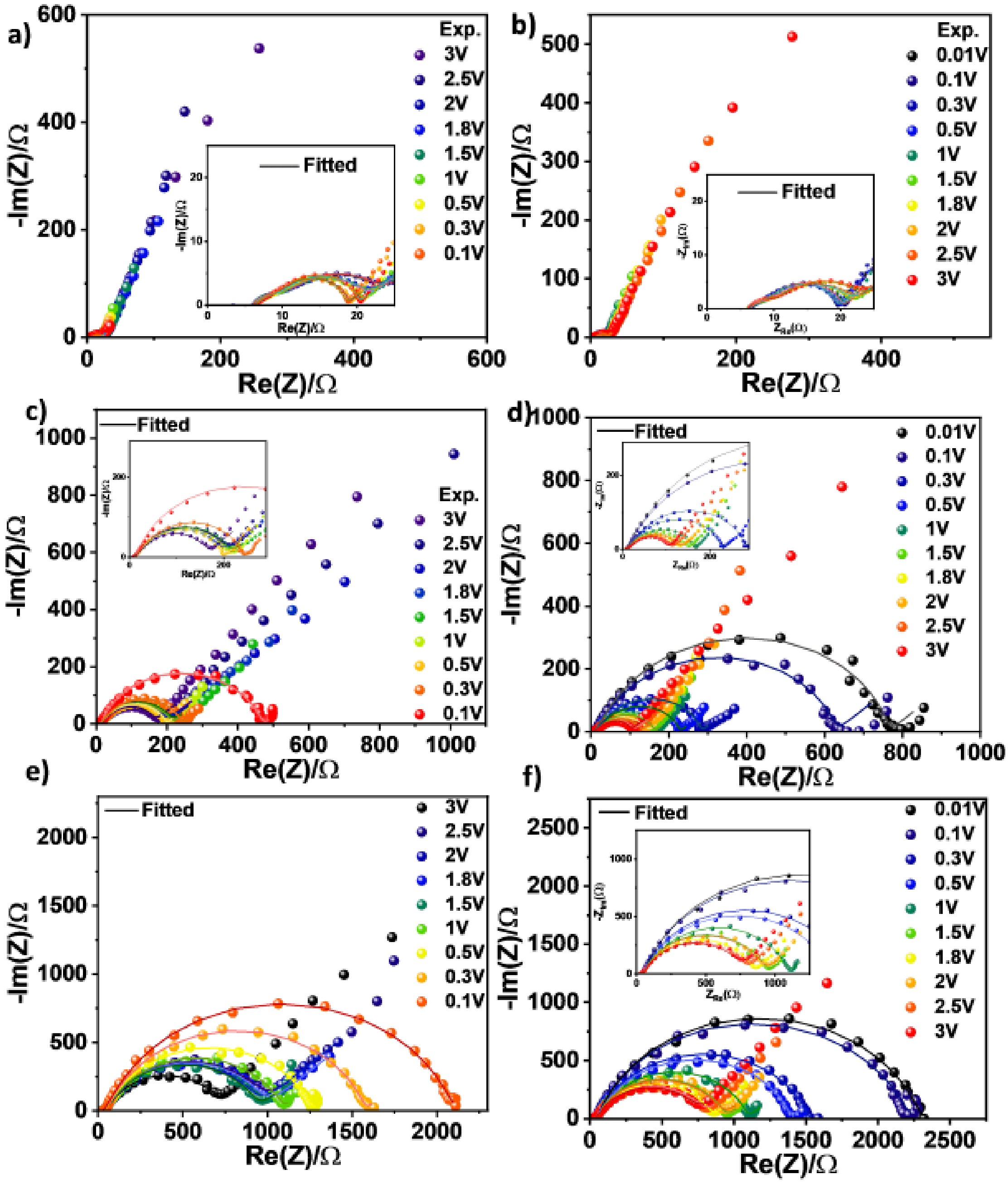

Figure 36. Fitted Nyquist plots with a solid line for BTEG with a) discharge and b) charge for LIB, c), d) SIB, and e), f) PIB, respectively.

Upon analyzing the fitting results (**Figure 37**), it was found that at 3V (initial state), the charge transfer resistance (R_{CT}) for LIB, SIB, and PIB was 10 Ω, 110 Ω, and 574 Ω, respectively. At full discharge (0.01 V), the R_{CT} for LIB, SIB, and PIB increased to 9 Ω, 717 Ω, and 2206 Ω, respectively. LIB showed minimal variation in R_{CT} during charging and discharging, indicating superior and more facile kinetics compared to SIB and PIB. The resistance tends to increase with the size of the alkali metal ion as it considers the resistance process of the alkali metal side (counter electrode) as well.

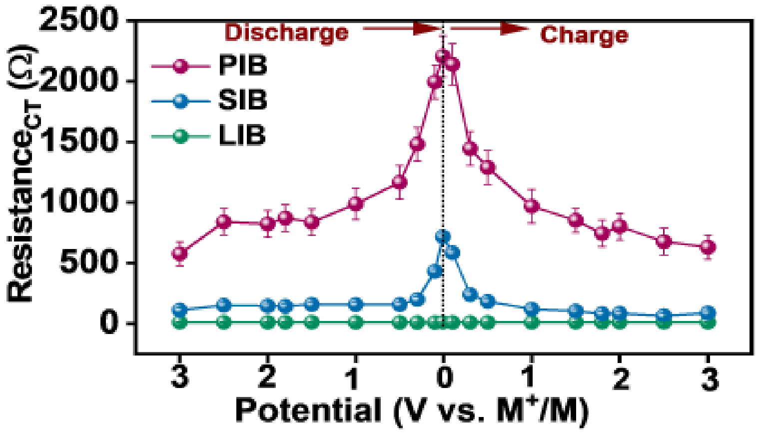

Figure 37. Comparison of charge transfer resistance values on charge/ discharge for LIB, SIB, and PIB.

Furthermore, **Figure 38b** shows that the bulk resistance (R_S) for LIB (6 Ω) and SIB (8 Ω) was similar, whereas PIB exhibited a much higher value of 30 Ω. This could be due to the increased viscosity associated with the higher concentration of electrolyte (5M KFSI) used for potassium. There was a negligible change in both R_S and R_{SEI} for LIB, SIB, and PIB during charging and discharging, indicating the excellent stability of BTEG (**Figure 38**). Additionally, the resistance values for LIB, SIB, and PIB demonstrate efficient charge transfer kinetics and a robust SEI, contributing to long-term cycling performance, as seen in **Figures 14b and 21**.

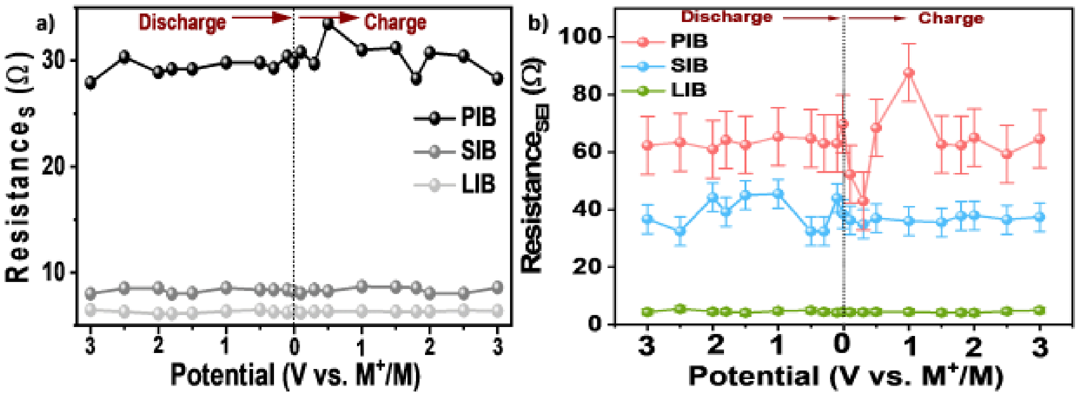

Figure 38. Comparison of a) solution resistance and b) solid electrolyte interphase resistance values on charge/ discharge for LIB, SIB, and PIB.

Despite K experiencing higher resistance than Li and Na, BTEG maintains stability for up to 1000 cycles. This stability is credited to using the 5M KFSI electrolyte, a deviation from the traditional 0.8M KPF_6 electrolyte system. The importance of selecting and optimizing an appropriate electrolyte for specific applications is further examined in the subsequent **chapter 1.2b**.

1.2a.5 Conclusion:

In this study, we have successfully demonstrated the superior performance of BTEG carbon as an anode material across alkali-ion batteries. BTEG carbon exhibited impressive reversible capacities of 1014 mAh g^{-1} for LIB, 295 mAh g^{-1} for SIB, and 369 mAh g^{-1} for PIB, all measured at a current density of 25 mA g^{-1}. Furthermore, at a higher current density of 1 A g^{-1}, BTEG maintained capacity retentions of 75% for LIB, 100% for SIB, and 87% for PIB over 1000 cycles. Our electrokinetic and in-situ analyses revealed that BTEG carbon is a universally effective anode material for alkali-ion batteries with a diffusion-dominated process for LIB and a capacitive-dominated process for SIB and PIB.

1.2a.6 References:

1. Assat, G., and Tarascon, J.M. (2018) Fundamental understanding and practical challenges of anionic redox activity in Li-ion batteries. *Nature Energy 2018 3:5*, **3** (5), 373–386.
2. Tarascon, J.M., and Armand, M. (2001) Issues and challenges facing rechargeable lithium batteries. *Nature 2001 414:6861*, **414** (6861), 359–367.
3. Wei, Z., Wang, A., Guan, X., Li, G., Yang, Z., Huang, C., Zhang, J., Ren, L., Luo, J., and Liu, X. (2022) Processable Potassium Metal Anode for Stable Batteries. *Energy & Environmental Materials*, **5** (4), 1278–1284.
4. Zhang, W., Liu, Y., and Guo, Z. (2019) Approaching high-performance potassium-ion batteries via advanced design strategies and engineering. *Sci Adv*, **5** (5), 7412–7422.
5. John, B., Anoopkumar, V., and Mercy, T.D. (2020) Potassium-ion batteries: Key to future large-scale energy storage? *ACS Appl Energy Mater*, **3** (10), 9478–9492.
6. Mousavi, S.M., Zarei, M., Hashemi, S.A., Lai, C.W., and Bahrani, S. (2020) K-Ion Battery Practical Application Toward Grid-Energy Storage. *Potassium-Ion Batteries*, 43–98.
7. Wang, H., Zhai, D., and Kang, F. (2020) Solid electrolyte interphase (SEI) in potassium ion batteries. *Energy Environ. Sci*, **13**, 4583.
8. Adams, R.A., Varma, A., Pol, V.G., Adams, R.A., Varma, A., and Pol, G. (2019) Carbon Anodes for Nonaqueous Alkali Metal-Ion Batteries and Their Thermal Safety Aspects. *Adv Energy Mater*, **9** (35), 1900550.
9. Yazami, R., and Touzain, P. (1983) A reversible graphite-lithium negative electrode for electrochemical generators. *J Power Sources*, **9** (3), 365–371.
10. Li, X., Li, J., Ma, L., Yu, C., Ji, Z., Pan, L., and Mai, W. (2022) Graphite Anode for Potassium Ion Batteries: Current Status and Perspective. *Energy & Environmental Materials*, **5** (2), 458–469.
11. Durmus, Y.E., Zhang, H., Baakes, F., Desmaizieres, G., Hayun, H., Yang, L., Kolek, M., Küpers, V., Janek, J., Mandler, D., Passerini, S., and Ein-Eli, Y. (2020)

Side by Side Battery Technologies with Lithium-Ion Based Batteries. *Adv Energy Mater*, **10** (24), 2000089.

12. Cheng, B., Li, X., Xu, H., Zhu, L., Zhang, Y., Yin, B., Ma, M., Kuang, Y., He, H., and Hu, D. (2022) Strengthen Synergistic Effect of Soft Carbon and Hard Carbon Toward High-Performance Anode for K-Ion Battery. *ACS Appl Mater Interfaces*, **14** (28), 31879–31888.

13. Luo, W., Jian, Z., Xing, Z., Wang, W., Bommier, C., Lerner, M.M., and Ji, X. (2015) Electrochemically expandable soft carbon as anodes for Na-ion batteries. *ACS Cent Sci*, **1** (9), 516–522.

14. Ali, G., Mehmood, A., Ha, H.Y., Kim, J., and Chung, K.Y. (2017) Reduced graphene oxide as a stable and high-capacity cathode material for Na-ion batteries. *Scientific Reports 2017 7:1*, **7** (1), 1–8.

15. Eom, W., Lee, E., Lee, S.H., Sung, T.H., Clancy, A.J., Lee, W.J., and Han, T.H. (2021) Carbon nanotube-reduced graphene oxide fiber with high torsional strength from rheological hierarchy control. *Nature Communications 2021 12:1*, **12** (1), 1–8.

16. Wu, S., Song, Y., Lu, C., Yang, T., Yuan, S., Tian, X., and Liu, Z. (2023) High-rate soft carbon anode in potassium ion batteries: The role of chemical structures of pitches. *Carbon N Y*, **203**, 211–220.

17. Zhang, S., Teck, A.A., Guo, Z., Xu, Z., and Titirici, M.M. (2021) Carbon Composite Anodes with Tunable Microstructures for Potassium-Ion Batteries. *Batter Supercaps*, **4** (4), 663–670.

18. Yuan, Y., Chen, Z., Yu, H., Zhang, X., Liu, T., Xia, M., Zheng, R., Shui, M., and Shu, J. (2020) Heteroatom-doped carbon-based materials for lithium and sodium ion batteries. *Energy Storage Mater*, **32**, 65–90.

19. Alvira, D., Antorán, D., and Manyà, J.J. (2022) Plant-derived hard carbon as anode for sodium-ion batteries: A comprehensive review to guide interdisciplinary research. *Chemical Engineering Journal*, **447**, 137468.

20. Lian, X., Sun, Z., Mei, Q., Yi, Y., Zhou, J., Rümmeli, M.H., and Sun, J. (2022) Biomass Template Derived Boron/Oxygen Co-Doped Carbon Particles as

Advanced Anodes for Potassium-Ion Batteries. *Energy & Environmental Materials*, **5** (1), 344–352.

21. Wu, D., Sun, F., Qu, Z., Wang, H., Lou, Z., Wu, B., and Zhao, G. (2022) Multi-scale structure optimization of boron-doped hard carbon nanospheres boosting the plateau capacity for high performance sodium ion batteries. *J Mater Chem A Mater*, **10** (33), 17225–17236.

22. Wu, Z.S., Ren, W., Xu, L., Li, F., and Cheng, H.M. (2011) Doped graphene sheets as anode materials with superhigh rate and large capacity for lithium ion batteries. *ACS Nano*, **5** (7), 5463–5471.

23. Biswas, S.S., Tandrapadu, M.S., Abinaya, E., and Eswaramoorthy, M. (2020) Deciphering the role of amine in amino silane-functionalized Pd/rGO catalyst for formic acid decomposition at room temperature. *Bulletin of Materials Science*, **43** (1), 1–6.

24. Weaving, J.S., Lim, A., Millichamp, J., Neville, T.P., Ledwoch, D., Kendrick, E., McMillan, P.F., Shearing, P.R., Howard, C.A., and Brett, D.J.L. (2020) Elucidating the sodiation mechanism in hard carbon by operando raman spectroscopy. *ACS Appl Energy Mater*, **3** (8), 7474–7484.

25. Weppner, W., and Huggins, R.A. (1977) Determination of the Kinetic Parameters of Mixed-Conducting Electrodes and Application to the System Li3Sb. *J Electrochem Soc*, **124** (10), 1569–1578.

26. Yu, X., Han, P., Wei, Z., Huang, L., Gu, Z., Peng, S., Ma, J., and Zheng, G. (2018) Boron-Doped Graphene for Electrocatalytic N2 Reduction. *Joule*, **2** (8), 1610–1622.

27. Wang, Q., Xie, Z., Liang, Y., Li, L., Liu, B., Li, X., Liu, C., Wu, X., and Huang, Q. (2019) Facile synthesis of boron-doped porous carbon as anode for lithium–ion batteries with excellent electrochemical performance. *Ionics (Kiel)*, **25** (5), 2111–2119.

28. Lin, P.C., Wu, J.Y., and Liu, W.R. (2018) Green and facile synthesis of few-layer graphene via liquid exfoliation process for Lithium-ion batteries. *Scientific Reports 2018 8:1*, **8** (1), 1–8.

29. Peled, E., and Menkin, S. (2017) Review—SEI: Past, Present and Future. *J Electrochem Soc*, **164** (7), A1703–A1719.

30. Pritzl, D., Solchenbach, S., Wetjen, M., and Gasteiger, H.A. (2017) Analysis of Vinylene Carbonate (VC) as Additive in Graphite/LiNi 0.5 Mn 1.5 O 4 Cells . *J Electrochem Soc*, **164** (12), A2625–A2635.

31. Choi, W., Shin, H.-C., Kim, J.M., Choi, J.-Y., and Yoon, W.-S. Modeling and Applications of Electrochemical Impedance Spectroscopy (EIS) for Lithium-ion Batteries. *J. Electrochem. Sci. Technol*, **2020** (1), 1–13.

32. Hu, W., Peng, Y., Wei, Y., and Yang, Y. (2023) Application of Electrochemical Impedance Spectroscopy to Degradation and Aging Research of Lithium-Ion Batteries. *Journal of Physical Chemistry C*, **127** (9), 4465–4495.

33. Yohannes, Y.B., Lin, S.D., and Wu, N.-L. (2017) In Situ DRIFTS Analysis of Solid Electrolyte Interphase of Si-Based Anode with and without Fluoroethylene Carbonate Additive. *J Electrochem Soc*, **164** (14), A3641–A3648.

34. An, S.J., Li, J., Daniel, C., Mohanty, D., Nagpure, S., and Wood, D.L. (2016) The state of understanding of the lithium-ion-battery graphite solid electrolyte interphase (SEI) and its relationship to formation cycling. *Carbon N Y*, **105**, 52–76.

35. Liu, J., Wang, J., Xu, C., Jiang, H., Li, C., Zhang, L., Lin, J., and Shen, Z.X. (2018) Advanced Energy Storage Devices: Basic Principles, Analytical Methods, and Rational Materials Design. *Advanced Science*, **5** (1), 1700322.

36. Sathiya, M., Prakash, A.S., Ramesha, K., Tarascon, J.M., and Shukla, A.K. (2011) V2O5-anchored carbon nanotubes for enhanced electrochemical energy storage. *J Am Chem Soc*, **133** (40), 16291–16299.

37. Jiang, Y., and Liu, J. (2019) Definitions of Pseudocapacitive Materials: A Brief Review. *Energy & Environmental Materials*, **2** (1), 30–37.

38. Wang, J., Polleux, J., Lim, J., and Dunn, B. (2007) Pseudocapacitive contributions to electrochemical energy storage in TiO 2 (anatase) nanoparticles. *Journal of Physical Chemistry C*, **111** (40), 14925–14931.

39. Wrogemann, J.M., Lüther, M.J., Bärmann, P., Lounasvuori, M., Javed, A., Tiemann, M., Golnak, R., Xiao, J., Petit, T., Placke, T., and Winter, M. (2023) Overcoming Diffusion Limitation of Faradaic Processes: Property-Performance Relationships of 2D Conductive Metal-Organic Framework Cu3(HHTP)2 for Reversible Lithium-Ion Storage. *Angewandte Chemie International Edition*, **62** (26), e202303111.

40. Ferrari, A.C. (2007) Raman spectroscopy of graphene and graphite: Disorder, electron–phonon coupling, doping and nonadiabatic effects. *Solid State Commun*, **143** (1–2), 47–57.

41. Ferrari, A., and Robertson, J. (2000) Interpretation of Raman spectra of disordered and amorphous carbon. *Phys Rev B*, **61** (20), 14095.

42. Dean, M.P.M., Howard, C.A., Saxena, S.S., and Ellerby, M. (2010) Nonadiabatic phonons within the doped graphene layers of X C6 compounds. *Phys Rev B Condens Matter Mater Phys*, **81** (4), 045405.

43. Yang, S.L., Sobota, J.A., Howard, C.A., Pickard, C.J., Hashimoto, M., Lu, D.H., Mo, S.K., Kirchmann, P.S., and Shen, Z.X. (2014) Superconducting graphene sheets in CaC6 enabled by phonon-mediated interband interactions. *Nature Communications 2014 5:1*, **5** (1), 1–5.

44. Mo, R., Rooney, D., Sun, K., and Yang, H.Y. (2017) 3D nitrogen-doped graphene foam with encapsulated germanium/nitrogen-doped graphene yolk-shell nanoarchitecture for high-performance flexible Li-ion battery. *Nature Communications 2017 8:1*, **8** (1), 1–9.

45. Yadav, R., Joshi, P., Hara, M., and Yoshimura, M. (2021) In situ electrochemical Raman investigation of charge storage in rGO and N-doped rGO. *Physical Chemistry Chemical Physics*, **23** (20), 11789–11796.

46. Schroeder, M., Menne, S., Ségalini, J., Saurel, D., Casas-Cabanas, M., Passerini, S., Winter, M., and Balducci, A. (2014) Considerations about the influence of the structural and electrochemical properties of carbonaceous materials on the behavior of lithium-ion capacitors. *J Power Sources*, **266**, 250–258.

Chapter 1.2b

Understanding of SEI formation on the performance of alkali-ion batteries

Summary

This chapter examines how the SEI formation and composition affect the stability and performance of alkali-ion batteries (AIBs). Compared to LIB and SIBs, potassium-ion batteries (PIBs) produce less stable SEIs, thus affecting their efficiency and longevity. This chapter highlights how the electrolyte concentration affects the SEI composition, influencing its performance. The findings underscore the importance of tailored SEI compositions for optimizing PIB stability.

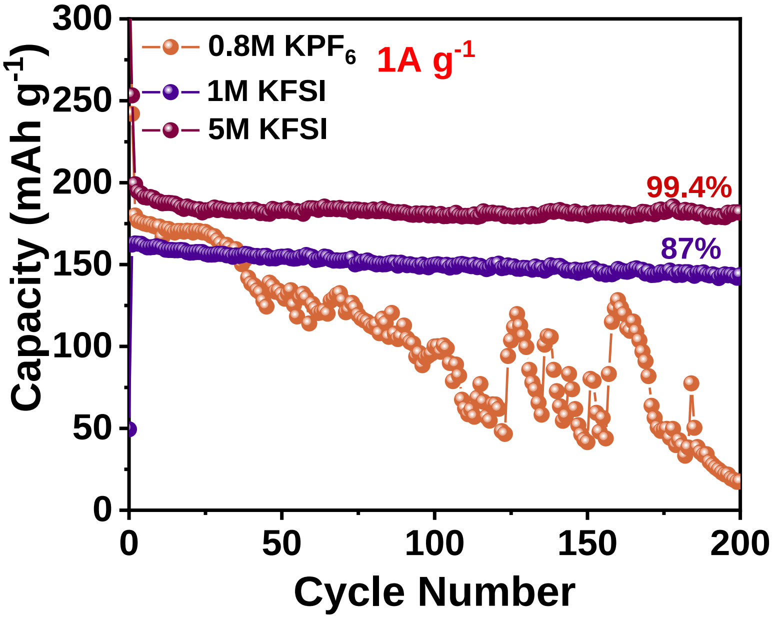

1.2b.1 Introduction:

To accelerate the commercialization of batteries, gaining an in-depth understanding of electrolytes is crucial, as they play a significant role in determining the capacity and stability of electrode materials.[1] Electrolytes, the essential medium for ionic movement, involve complex interactions among cations, anions, solvent molecules, and the solid electrolyte interphase (SEI).[2,3] Understanding these interactions is vital for assessing battery performance. The SEI, a key element in battery technology, primarily forms during the first cycle of battery use. It comprises various inorganic (like metal fluorides, oxides, and carbonates) and organic components that influence the stability of SEI.[4,5] Organic compounds, such as metal ethylene dicarbonates (MEDC) and polyolefins, provide flexibility but can reduce SEI stability due to their dissolution in the organic electrolytes they are used. Inorganic components such as metal fluorides, oxides, and carbonates are insoluble in organic electrolyte, mechanically stronger, and compact, enhancing SEI stability.[6–8] The stability and homogeneity of the SEI post-initial cycle play a pivotal role in promoting consistent ion diffusion throughout its structure. An effectively engineered SEI layer is crucial for inhibiting undesired side reactions and enhancing stability.[9] Consequently, tailored electrolyte formulations are essential to ensure optimal electrochemical and mechanical compatibility with various anode materials used for distinct alkali ions.

Due to each alkali ion's characteristic chemistry, extrapolating the SEI's physical and chemical behavior from lithium-ion systems to sodium and potassium-ion systems becomes a complex endeavor.[10] The conventional electrolytes used for anodes involve metal (M = Li, Na, K) hexafluorophosphate salt in a mixture of ethylene carbonate (EC) and diethyl carbonate (DEC) solvent.[11] Although alkali metal hexafluorophosphate salts work better for LIBs and SIBs, they significantly reduce the Coulombic efficiency in the case of PIBs due to the creation of an unstable SEI.[12][13] By carefully selecting the appropriate salts and solvents in the electrolyte composition, it is possible to significantly reduce unwanted side reactions, especially those leading to the deterioration of SEI during battery cycling.

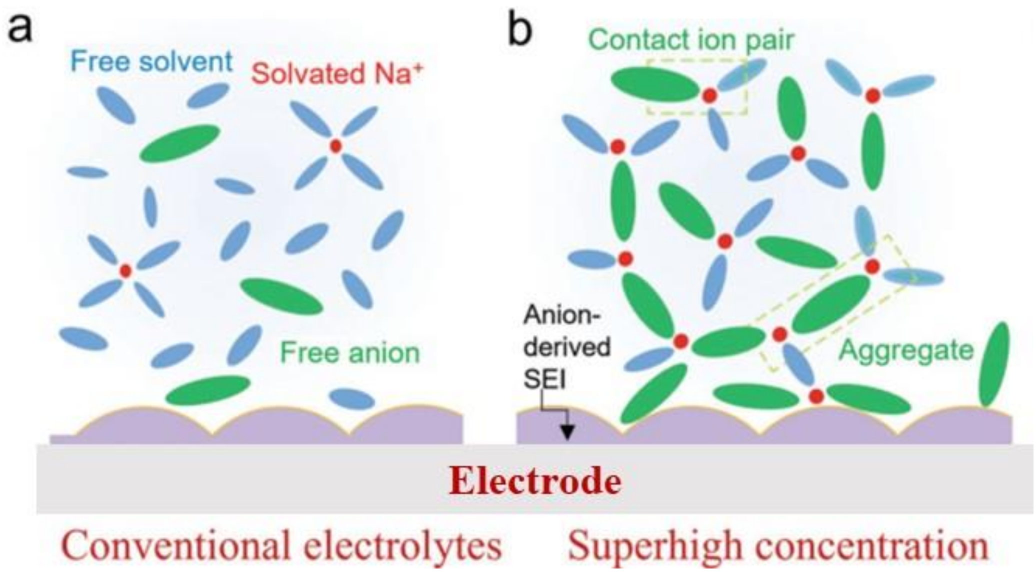

Figure 1. Illustration of solvation and interface model for different electrolyte concentrations. a) Conventional electrolytes (1M) and b) super high concentration (>3M)electrolytes.[14]

Modification in the choice of salts, solvents, and additives can refine the solvation structure that influences the SEI.[15,16] Use of electrolytes at high concentrations has yielded significant improvements in battery stability in recent years. In conventional electrolytes, typically at a concentration of around 1M, there is a balanced ratio of anions and solvent molecules, leading to the formation of the SEI predominantly through the decomposition of salts and solvent molecules (**Figure 1**). However, with an increase in electrolyte concentration, the reduced availability of solvent molecules results in the formation of ion pairs between cations and anions and anion aggregates.[17,18] The SEI primarily comprises decomposition products from anions in high-concentration electrolytes. This results in a higher proportion of inorganic components, typically more stable than the more soluble organic components.[19]

1.2b.2 Scope of the present investigation:

This chapter thoroughly assesses traditional electrolytes' chemical and electrochemical behavior for alkali-ion batteries. This analysis is instrumental in establishing a correlation between the SEI chemistry for different alkali ions and the corresponding stability of the anode material. Of particular significance is the investigation of a potassium bis(fluorosulfonyl)imide (KFSI) salt-based carbonate electrolyte with varying concentrations, compared with traditional electrolytes' performance.

1.2b.3 Experimental Procedure:

i. Materials and characterization techniques:

Lithium ribbons, sodium cubes (preserved in mineral oil), and potassium chunks (also in mineral oil) were obtained for the research. Additionally, 1M $LiPF_6$ in an EC: DEC (50/50 v/v) solution of battery grade, along with $NaPF_6$, KPF_6, ethylene carbonate (EC), and diethyl carbonate (DEC), were sourced from Sigma Aldrich. Potassium bis(fluorosulfonyl)imide (KFSI) with a purity greater than 95% was procured from TCI Chemicals. Glass microfiber filters required for the study were also acquired from Sigma Aldrich.

Renishaw Invia Reflex Raman spectrometer with a 785 nm laser, detector grating of 1200 l/mm, and spectral resolution of 0.5 cm^{-1} was used to characterize liquid electrolytes. Raman spectroscopy was performed on the electrolytes, which were placed in NMR tubes and sealed with parafilm. A red laser with 10% intensity was used, setting the exposure time to 50 seconds and carrying out two accumulations. X-ray photoelectron spectroscopy (XPS) analysis used a Thermo K-alpha+ spectrometer with a micro-focused and monochromated Al Kα radiation source at 1486.6 eV. This characterization was intended to determine the composition of the SEI. The pass energy set for capturing individual core-level spectra was 50 eV. Ar^+ sputter etching was performed for 120 seconds to analyze the SEI layers further. Polarization measurements were executed using an electrochemical workstation EC-Lab from Biologic Science Instruments-VSP.

ii. Preparation of Electrolytes:

The electrolytes for the experiments were meticulously prepared in a glovebox under an argon atmosphere, ensuring an environment with ultralow levels of contaminants: less than 0.1 ppm of H_2O and less than 0.1 ppm of O_2. This controlled setting is crucial to prevent any unwanted reactions or degradation of the electrolytes, which could be caused by exposure to moisture or oxygen, thereby ensuring the accuracy and reliability of the experimental results.

iii. Preparation of 1M $NaPF_6$, 0.8M KPF_6, 1M KFSI, and 5M KFSI in EC: DEC solvent

The preparation of the electrolytes was conducted as follows: A volume/volume (v/v) mixture of ethylene carbonate (EC) and diethyl carbonate (DEC) was stirred for two hours at room temperature to achieve a transparent and precise solution. It is important to note that while EC and DEC typically dissolve within thirty minutes, lingering small chunks of EC can hinder complete solubility, particularly in the case of $NaPF_6$ and KPF_6 salts. After the salts of the desired concentration were added, the electrolyte mixture was left to stir vigorously for 24 hours in a tightly sealed glass vial. While solutions of 1M $NaPF_6$ and 0.8M KPF_6 in EC: DEC appeared translucent, both 1M and 5M concentrations of KFSI in the same solvent system dissolved to form clear solutions.

For the Raman spectroscopy analysis, 500 μl of the freshly prepared electrolytes were transferred into NMR tubes, which were then adequately sealed to ensure the integrity of the samples during the spectroscopic examination.

iv. Preparation of symmetric cell

In fabricating symmetric cells, meticulous cleaning of metal surfaces constitutes the initial step. The lithium ribbon is carefully cleansed using a scalpel to eliminate any superficial lithium oxide layer. Sodium and potassium, preserved in mineral oil, are rid of oil residues via immersion in dry hexane. Subsequently, these metals are sliced and fashioned into discs of 11 mm diameter. To preclude short-circuiting, glass fiber separators, slightly larger at 12 mm diameter, are employed, ensuring they extend beyond the metal foils. Each cell incorporates two separators to ensure safety and reliability. Assembled in Swagelok cells with the chosen electrolytes, the cells are then allowed a 24-hour equilibration period prior to the commencement of electrochemical measurements.

v. Preparation of electrode for ex-situ XPS

The previously prepared BTEG electrode (chapter 1.2a), whose cell preparation details are outlined in the preceding chapter, was the working electrode and cycled with metal foils at a low current density. Post-cycling, the BTEG electrode was carefully removed and immersed in DEC solvent during disassembly. This step was crucial to dissolve and remove any residual salt deposits from the electrode's surface. Following this, the electrodes were dried overnight under vacuum conditions to ensure complete removal of the solvent. The dry electrodes were then transferred from the glovebox to the XPS system using a vacuum transfer module (VTM) to prevent exposure to air and moisture, thereby maintaining their integrity for accurate surface compositional analysis.

vi. Electrochemical studies:

- **Polarization and Impedance Studies:**

Galvanostatic charge-discharge testing at a current density of 1 mA cm^{-2} was conducted for 1 hour per cycle to study the metal plating and stripping behavior in symmetric metal-to-metal (M//M) cells containing various prepared electrolytes (120 µl each). An excess of electrolytes was intentionally added in the case of the Swagelok cells to compensate for the volume occupied by the spring, a critical cell component. This precaution helps in preventing the drying out of the cell during cycling. Following the cycling process, Potentiostatic Electrochemical Impedance Spectroscopy (PEIS) measurements were conducted over 800 kHz to 1 mHz. This analysis was crucial to elucidate the cells' electrochemical properties and interfacial characteristics.

- **Charge-discharge studies with BTEG**:

Galvanostatic charge-discharge experiments were performed using the BTEG electrode as the working electrode, complemented by metal foils serving as the counter and reference electrodes. The electrochemical experiments were conducted within a voltage window ranging from 3 V to 0.01 V.

1.2b.4 Results and Discussion:

Firstly, the solvation of cations in electrolytes was investigated by Raman spectroscopy, represented **in Figure 2**. As seen in **Figure 2a**, the Raman spectrum of the EC: DEC solution displays distinct peaks at 713 cm^{-1} and 887 cm^{-1}.[20] These peaks correspond to the vibrational modes of free EC molecules, denoting O-C-O ring breathing and C-C ring deformation vibrations. Upon the addition of salts to the solution, a new peak emerges in the Raman spectrum, indicative of metal ion solvation resulting from interactions with the carbonate solvent.[21] The peak area associated with K^+ solvation is weak compared to Li^+ and Na^+, as shown in **Figure 2b**.[22][23] Li^+ and Na^+ show stronger solvation compared to K^+, implying less parasitic reactions between Li/ Na and solvent molecules compared to K. With the substitution of KPF_6 salt by KFSI, an enhancement in the solvation of K ions is observed as shown from 1M KFSI in **Figure 2d**. Notably, at higher concentrations, such as 5M, the existence of contact ion pairs (CIP) and aggregates (AGG) was also detected (**Figure 2d)**.[24,25] The formation of CIP and AGG in 5M KFSI assists in alleviating parasitic reactions due to increased interaction with accessible solvents.[23]

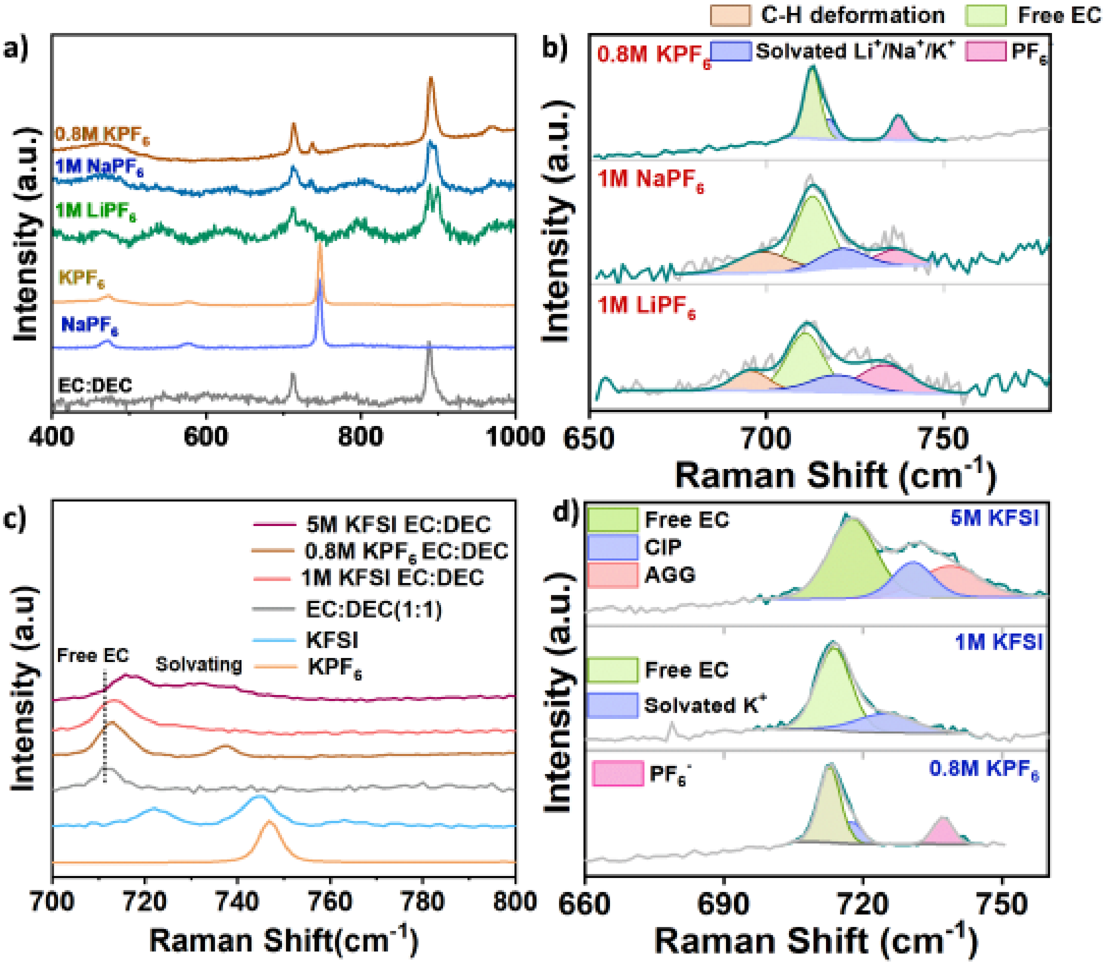

Figure 2. a) Raman spectra of solvent (EC: DEC), salt ($NaPF_6$, KPF_6), and solution (1M $LiPF_6$, 1M $NaPF_6$, and 0.8M KPF_6) and b) solvation structure compared. c) Raman spectra of salt (KPF_6 and KFSI) and solution (0.8M KPF_6, 1M KFSI, and 5M KFSI) and corresponding d) solvation structure compared.

Polarization behavior in symmetric cells was investigated to unveil the impacts of the electrolyte chemistry on alkali metals. **Figure 3a** illustrates the potential profiles of conventional electrolytes in symmetric cells (**Li//Li**, **Na//Na**, and **K//K**) across successive cycles for 120 hours at a current density of 1mA cm^{-2}. It was observed that polarization increased progressively in the order of Li, Na, and K (using 1M $LiPF_6$, 1M $NaPF_6$, and 0.8M KPF_6, respectively). This trend is attributed to the comparatively poorer conduction of Na and K ions within the solid electrolyte interphase (SEI). The polarization values of alkali metal symmetric cells were compared after SEI stabilization

(10 hours) and after 120 hours of long-duration cycling. For the **Li//Li** cells, the overpotential, initially at 5.0 mV (10 hours), escalated to 6.9 mV (120 hours). In **Na//Na** cells, initial stabilization of the SEI on the Na metal foil was noted, after which the overpotential altered from 14 mV (10 hours) to 22 mV (120 hours). For 0.8M KPF_6 electrolytes in **K//K** cells (**Figure 3b**), the polarization value of 42 mV (10 hours) increased to 103 mV (120 hours). In the case of 1M KFSI, higher polarization was observed than in 0.8M KPF_6 and 5M KFSI. The polarization values vary from 88 mV (at 10 hours) to 120 mV after 120 hours of cycling, which shows that 1M KFSI is more stable than 0.8M KPF_6. 5M KFSI overcomes the limitation of 0.8M KPF_6 and 1M KFSI and shows insignificant change on cycling from 53 mV to 56 mV at 10 and 120 hours, respectively.

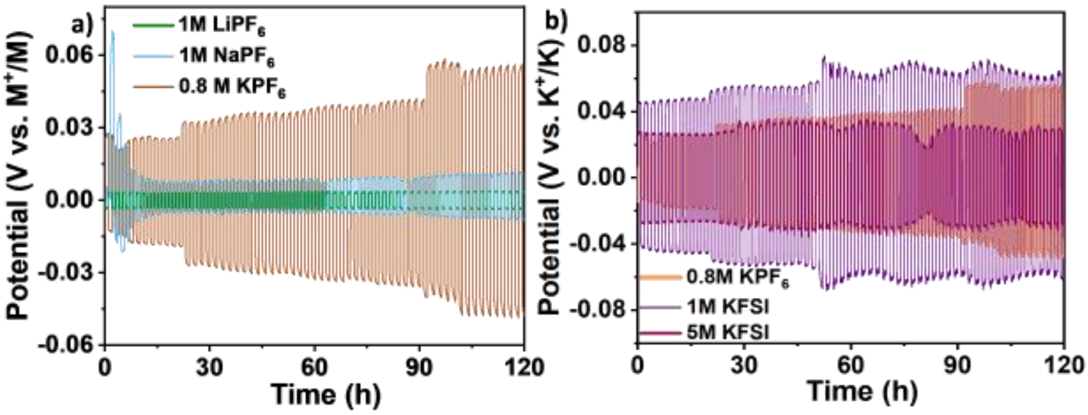

Figure 3. Comparison of symmetric cells with electrolyte a) 1M $LiPF_6$, 1M $NaPF_6$, and 0.8M KPF_6. b) Potassium metal plating-stripping behavior for 0.8M KPF_6, 1M KFSI, and 5M KFSI electrolyte.

Electrochemical impedance spectroscopy (EIS) measurements were taken for the **Li//Li**, **Na//Na**, and **K//K** symmetric cells to understand their polarization losses with long-term cycling.[23] The resistances are associated with the interfaces between the liquid electrolyte and the solid electrolyte interphase (RLE/SEI) and between the SEI and the anode (RSEI/A), as represented in **Figure 4f**. The EIS profiles exhibited solution resistance (R_S) and semicircular patterns indicative of solid electrolyte interface (R_{SEI}) and charge transfer resistance (R_{CT}). For the **Li//Li** and **Na//Na** cells, outlined in **Figures 4a and 4b**, the total interfacial resistance was within a spectrum of 40-1000 Ω. Meanwhile, the K//K cells (Figures 4c, 4d, and 4e) exhibited a markedly higher range of interfacial resistance, spanning from 1500 to 7500 Ω for various electrolytes.

Specifically, the R_S, R_{SEI}, and R_{CT} for the **K//K** cells using a 0.8M KPF_6 electrolyte (**Figure 4c and 5**) showed a significant increase throughout the cycling process. The rise in resistance (R_S) over cycles suggests the degradation of the electrolyte, leading to the formation of more solid electrolyte interphase (SEI) and increasing diffusion resistance of K^+ diffusion through SEI. An unstable SEI with potassium (K) metal contributes to a fluctuating interface, adversely affecting potassium plating and stripping, further elevating R_{CT}. The **K//K** cells with 1M KFSI electrolyte (**Figure 4e and 5b-c**) experienced the highest RSEI and RCT but showed lower cycling change than 0.8M KPF_6. In the case of cells with 5M KFSI electrolyte (**Figure 4d and 5b-c**), there was minimal change in the R_{SEI} and R_{CT} over successive cycling, indicating a stable charge transfer and SEI performance.

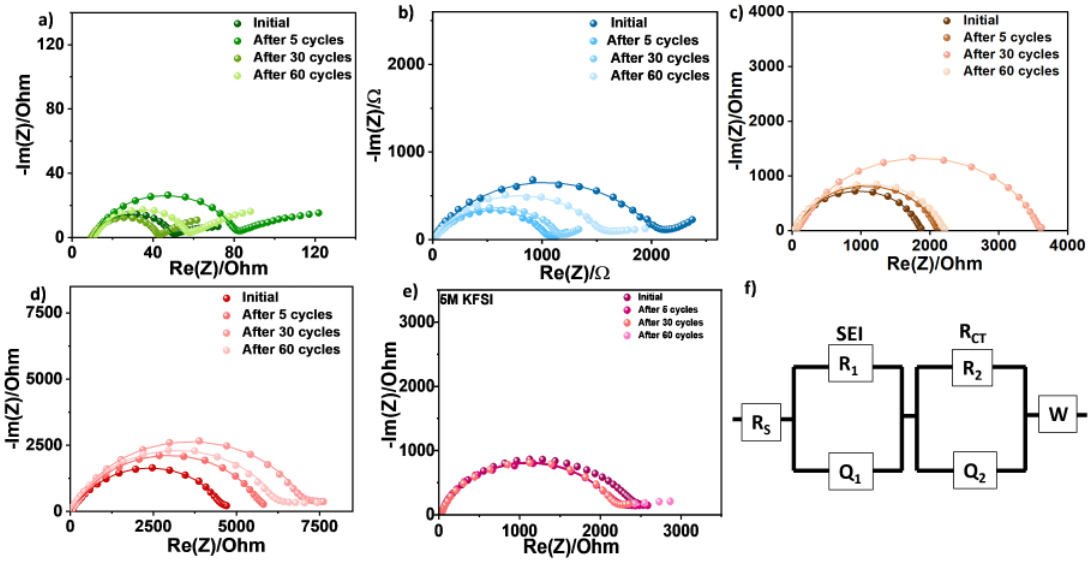

Figure 4. Nyquist plots for a) 1M $LiPF_6$, b) 1M $NaPF_6$, c) 0.8M KPF_6, d) 1M KFSI, and e) 5M KFSI before and after cycling. f) The electrical circuit was fitted for Nyquist plots.

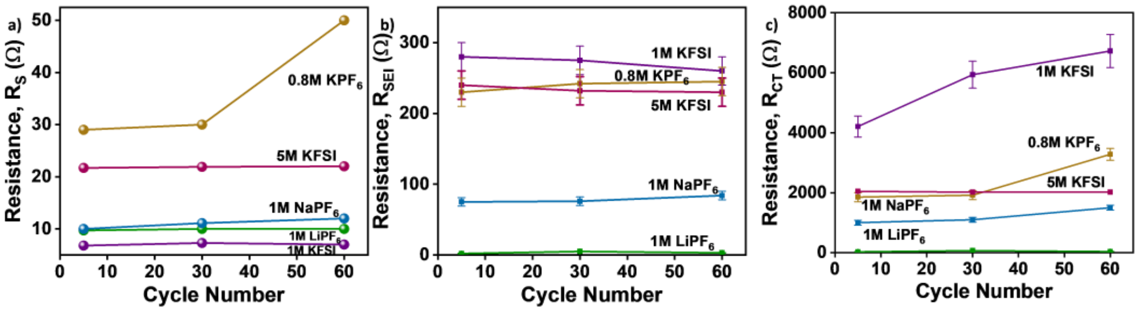

Figure 5. Comparison of fitted resistance from EIS associated with a) solution (R_S), b) SEI (R_{SEI}), and c) charge transfer (R_{CT}) for electrolyte 1M $LiPF_6$, 1M $NaPF_6$, 0.8M KPF_6, 1M KFSI and 5M KFSI electrolyte for symmetric cell.

Exploring the interaction between electrolytes and the metal surface and their effect on the performance of BTEG electrodes reveals significant insights for alkali-ion batteries in a half-cell configuration. BTEG was tested primarily by cyclic voltammetry (CV) studies at a low scan rate of 0.01 mV s^{-1} and a potential limitation of 3-0.01 V, as shown in **Figure 6**. After SEI stabilization, CV studies show curves overlap in the case of electrolytes 1M $LiPF_6$ and 1M $NaPF_6$, but a continuous change in current density in 0.8M KPF_6 (**Figure 6a-c**). The BTEG electrode shows unstable SEI with 0.8M KPF_6 compared to 1M $LiPF_6$ and 1M $NaPF_6$. This is overcome by 5M KFSI with high reversibility of BTEG electrode after SEI stabilization (**Figure 6d**).[26]

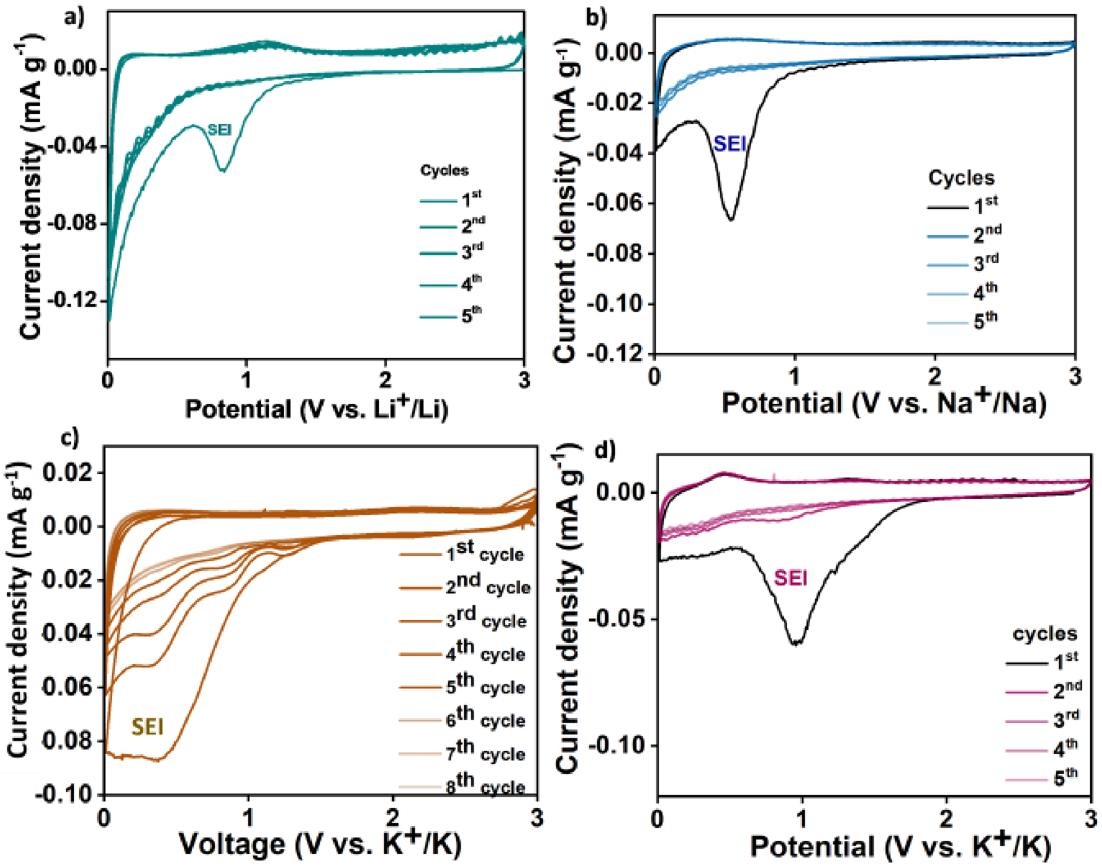

Figure 6. Cyclic voltammograms for BTEG electrode with a) 1M $LiPF_6$, b) 1M $NaPF_6$, c) 0.8M KPF_6, and d) 5M KFSI.

X-ray photoelectron spectroscopy (XPS) measurements were undertaken to assess the composition of the SEI layer stabilized on a BTEG anode following cycles of operation by CV in alkali-ion batteries. The XPS analysis focused on the BTEG surface interactions before (0 nm) and after etching (approximately 30 nm deep) with different electrolytes, i.e., 1M $LiPF_6$, 1M $NaPF_6$, and 0.8M KPF_6 in an EC: DEC solution.

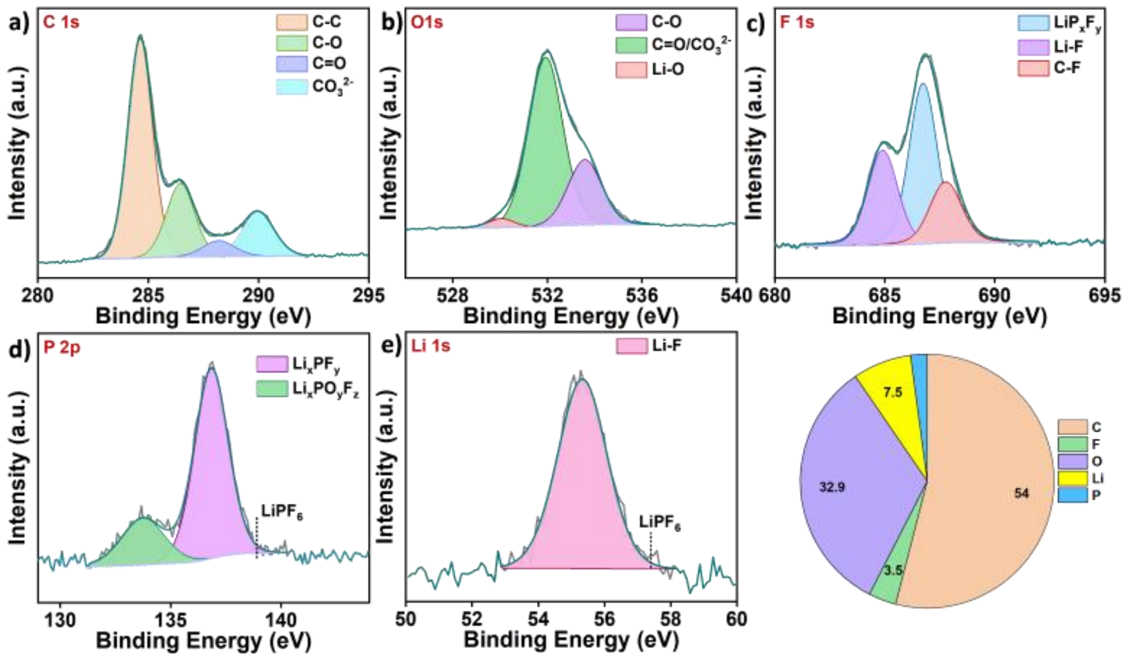

Figure 7. Deconvoluted XPS spectra of a) C 1s, b) O 1s, c) F 1s, d) P 2p, and e) Li 1s of surface of BTEG with 1M LiPF$_6$. f) The calculated percent composition of surface elements.

Elements	Species	Binding Energy (eV)
C 1s	C-C	284.8
	C-O	286.5
	C=O	288.4
	CO$_3^{2-}$	290
O 1s	C=O/CO$_3^{2-}$	532
	C-O	533.6
	Li-O	530
F 1s	Li-F	684.9
	Li$_x$PF$_y$	686.8
	C-F	687.8
P 1s	Li$_x$PF$_y$	136.9
	Li$_x$POF$_y$F$_z$	133.8
Li 1s	Li-F	55.3

Table 1. Binding energy values of S 2p and N 1s element for SEI in 1M LiPF$_6$ in EC: DEC.[27,28]

The XPS results reveal that the topmost layer of SEI comprises a mixture of organic (carbon-based decomposition products) and inorganic constituents. For SEI formed by

1M $LiPF_6$, the C1s spectra (**Figure 7a**), O1s spectra (**Figure 7b**), F1s spectra (**Figure 7c**), P 2p spectra (**Figure 7d**) and Li1s spectra (**Figure 7e**).

For a quantitative understanding of the elemental composition within the SEI layer, the areas of individual peaks were calculated and correlated with relative sensitivity factors (RSFs) for each element, as indicated in **equation 1**. This analysis provides deeper insight into the SEI layer's complex molecular structure and composition, shedding light on the interfacial chemistry and stability factors critical to battery performance.

$$\text{Atomic } \% = \frac{(\text{Area/RSF.})\,\text{element}}{\text{Total }(\text{Area/RSF})\,\text{all elements}} * 100\ \% \qquad (1)$$

The normalized content for each element is summarised in **Figure 7f**.

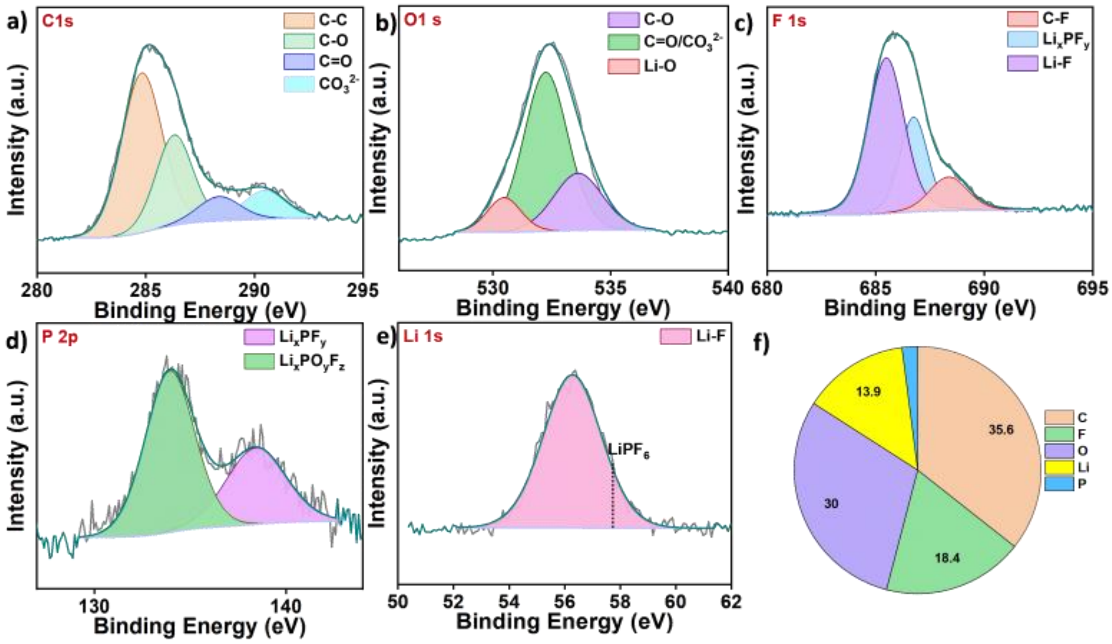

Figure 8. Deconvoluted XPS spectra of a) C 1s, b) O 1s, c) F 1s, d) P 2p, and e) Li 1s of surface of BTEG with 1M $LiPF_6$ after etching. f) The calculated percent composition of surface elements.

Similarly, after Ar^+ etching of the BTEG surface, SEI was evaluated to observe the change in elemental composition, as seen in **Figure 8a-f**. After sputtering, carbon content (indicative of organic content) decreases from 54 at% to 35 at%, with an increase in inorganic content (F species particularly).

In the case of the SEI surface formed by 1M $NaPF_6$, characteristic XPS peaks were observed similar to 1M $LiPF_6$, as shown in **Figure 9a-d**. O1s spectra exhibit an additional Na Auger peak at 536.2 eV, as seen in **Figure 9b,** and **Figure 9e** shows the Na signature with the existence of $NaPF_6$. **Figure 10a-f** shows XPS spectra after Ar^+ etching of SEI formed by 1M $NaPF_6$. Similar to 1M $LiPF_6$, the carbon content reduces after etching from 45% to 29%, as seen from the comparison between **Figure 9f and 10f**.

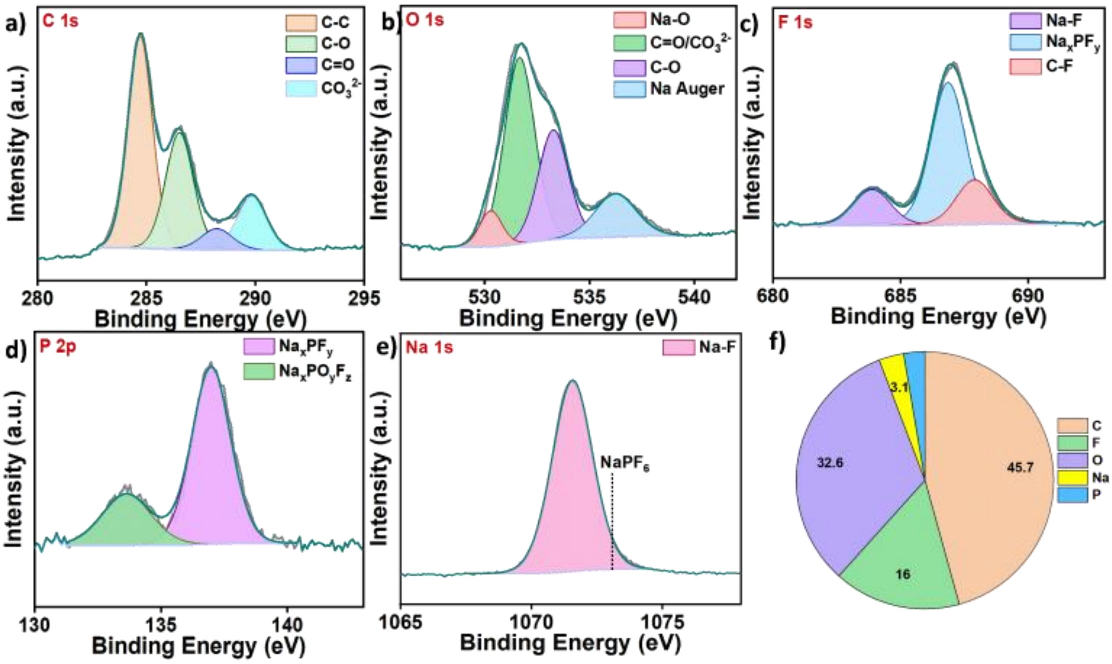

Figure 9. Deconvoluted XPS spectra of a) C 1s, b) O 1s, c) F 1s, d) P 2p, and e) Na 1s of surface of BTEG with 1M $NaPF_6$ before etching. f) The calculated percent composition of surface elements.

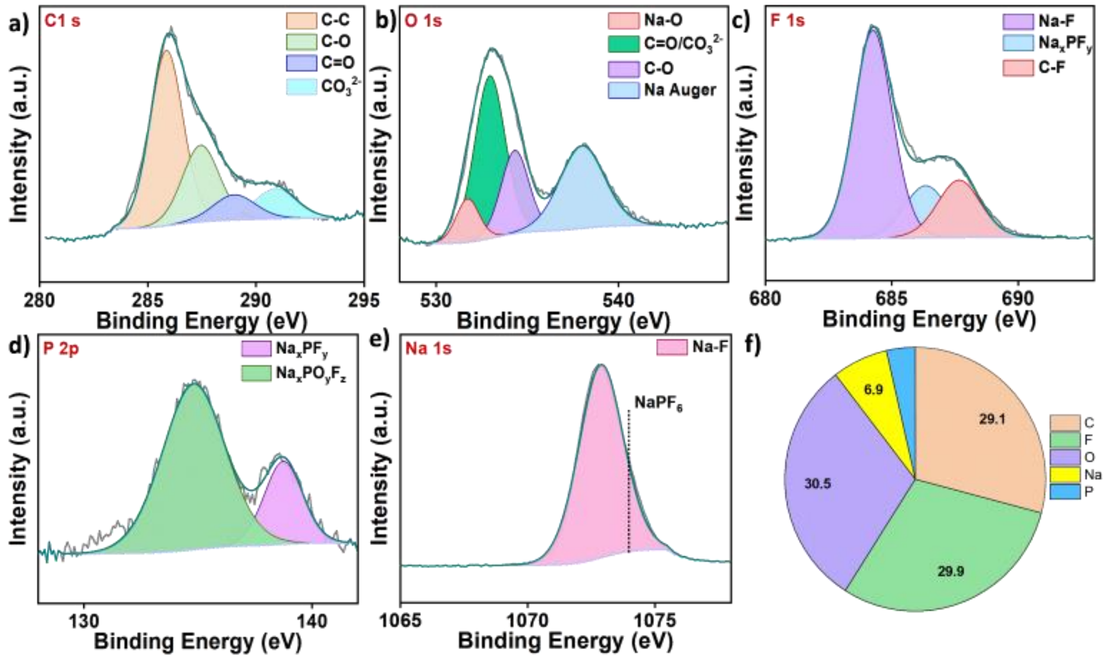

Figure 10. Deconvoluted XPS spectra of a) C 1s, b) O 1s, c) F 1s, d) P 2p, and e) Na 1s of surface of BTEG with 1M $NaPF_6$ after etching. f) The calculated percent composition of surface elements.

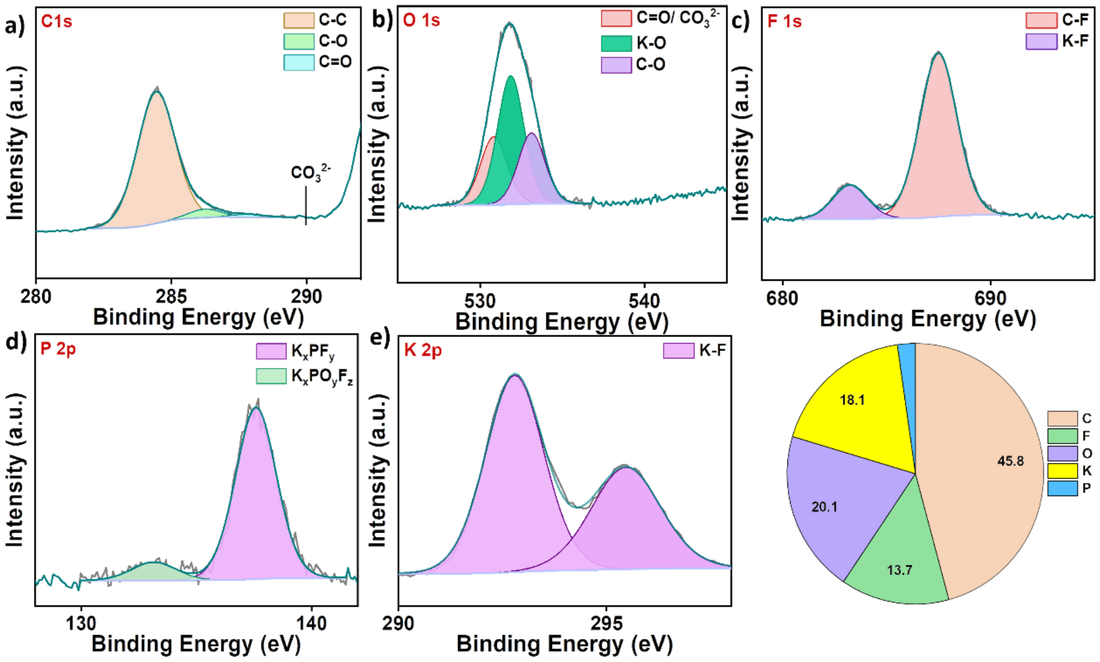

Figure 11. Deconvoluted XPS spectra of a) C 1s, b) O 1s, c) F 1s, d) P 2p, and e) K 2p of surface of BTEG with 0.8M KPF_6 before etching. f) The calculated percent composition of surface elements.

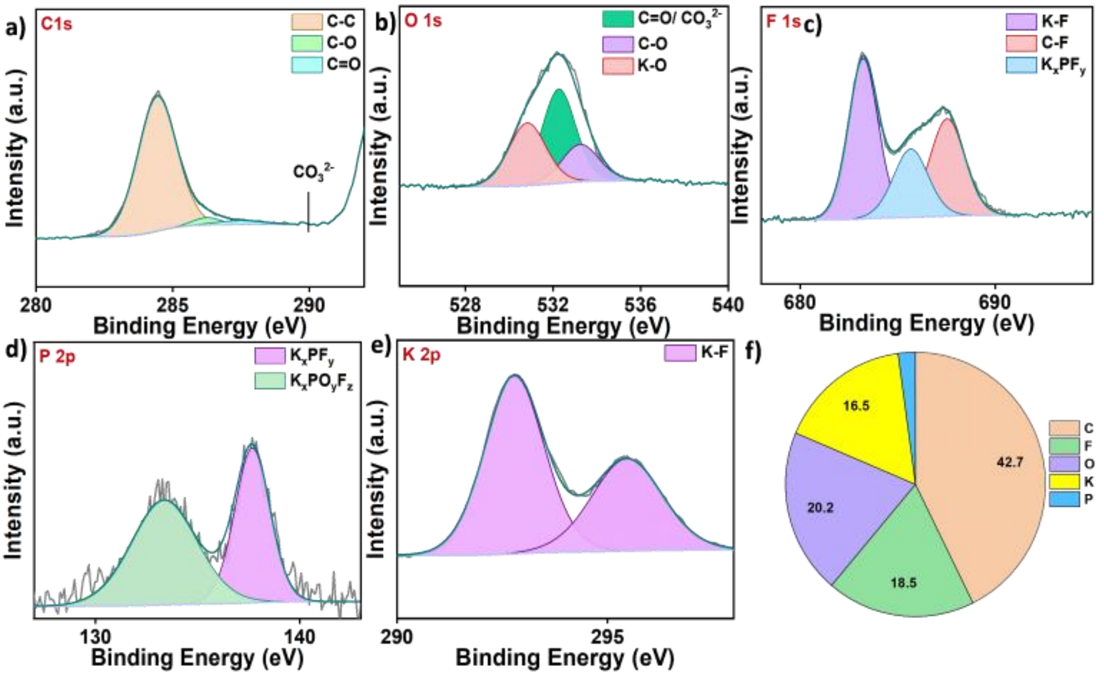

Figure 12. Deconvoluted XPS spectra of a) C 1s, b) O 1s, c) F 1s, d) P 2p, and e) K 2p of surface of BTEG with 0.8M KPF_6 after etching. f) The calculated percent composition of surface elements.

Surface XPS spectra formed by 0.8 M KPF_6 are presented in **Figure 11a-f**, and unlike $LiPF_6$ and $NaPF_6$, the carbonate peak disappeared (**Figure 11a**). Similar to Li and Na analogs, KPF_6-based SEI decreases organic content from 46% to 36% when comparing **Figures 11f and 12f**.

On comparing conventional electrolytes for alkali-ion batteries (**Figure 13a**), the surface XPS analysis (without etching) shows lesser carbon content for Na (~46 at%) and K (~46 at%) compared to Li (~54 at%). [29]This can be due to the dissolution of organic components by electrolyte, which is more for K and Na than Li on the surface.[30] On comparing the organic and inorganic species of SEI after etching (**Figures 13b and 14**), the content is similar with ~ 35 at% inorganic species. However, the stability of BTEG was observed to be poor with 0.8 M KPF_6 electrolyte, which implies that the SEI is fragile for bigger-sized K^+ conduction while is stable for smaller-sized Li^+ conduction, as shown in CV studies (**Figure 6a-c**).

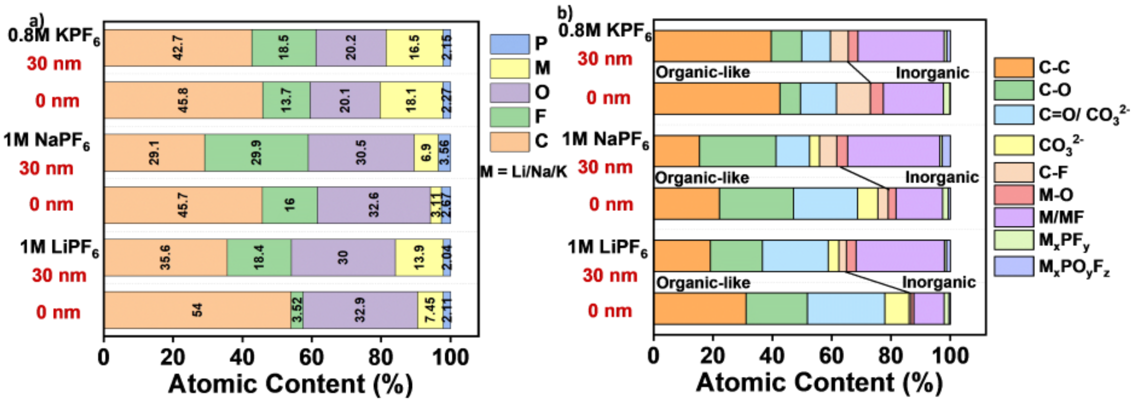

Figure 13. The elemental composition of conventional electrolytes compared for alkali ion batteries before (0 nm) and after etching (30 nm). b) The comparison of calculated percent composition of decomposed products of alkali-ion batteries after etching. M denotes Li, Na and K.

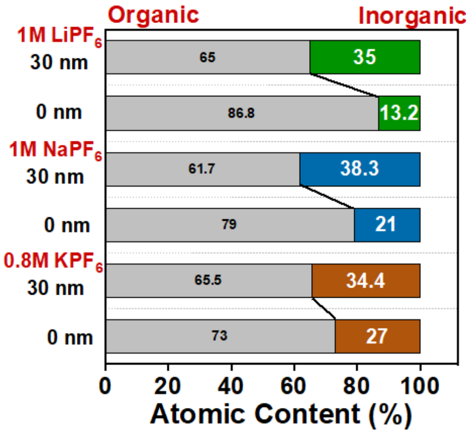

Figure 14. Comparison of organic-like and inorganic content percentage before (0 nm) and after etching(30 nm) for conventional electrolytes $LiPF_6$, $NaPF_6$, and KPF_6 in EC: DEC.

Figures 15 and 16 show species' content corresponding to individual elements for conventional electrolytes before and after etching compared to alkali-ion batteries. The individual species content of the elements C, P, O, and F show their distribution on heterogeneous SEI.

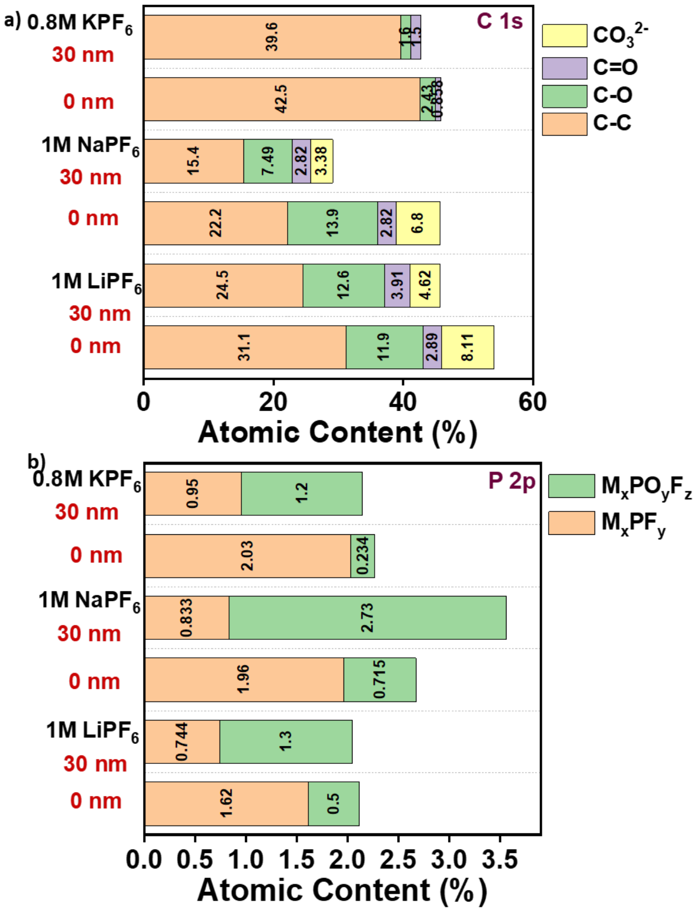

Figure 15. The composition of species for a) C 1s and b) P 2p on BTEG surface before and after etching for conventional electrolytes for alkali-ion batteries. M denotes Li, Na, and K metal.

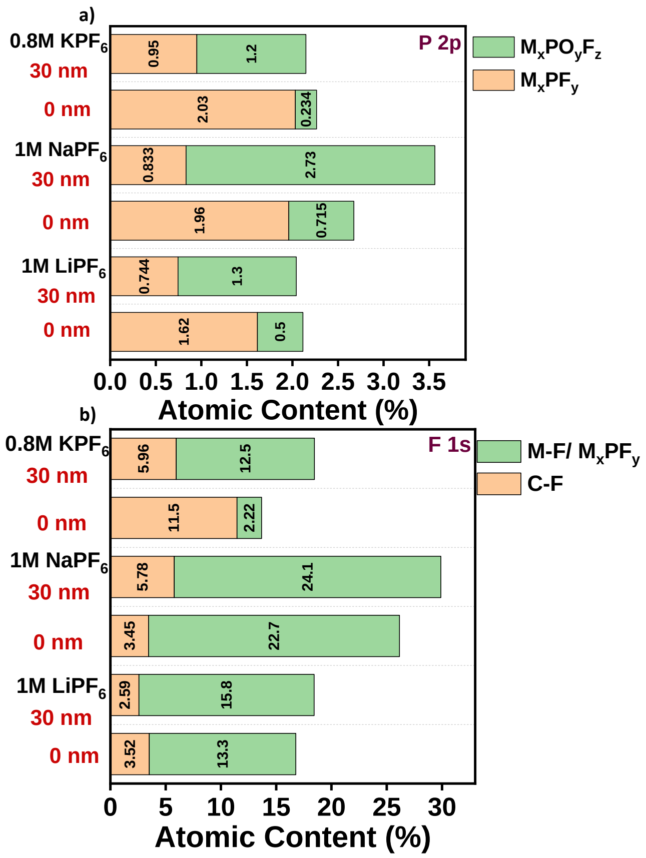

Figure 16. The species composition for a) O 1s and b) F 1s peak on BTEG surface before and after etching for conventional electrolytes for alkali-ion batteries. M denotes Li, Na, and K metal.

Therefore, optimizing SEI contents is essential and directly related to BTEG stability for PIBs (**Figures 17-20**).[31] On changing the electrolyte from 0.8M KPF6 to 1M KFSI, XPS deconvoluted spectra show additional deconvoluted peaks of S 2p and N 1s (**Table 1**).

Element	Species	Binding Energy (eV)
S 2p	R-S (R- alkyl)	167.8
	K_2SO_4	170
N 1s	=N-	398.3
	-N-	399.8

Table 2. Binding energy values of S 2p and N 1s element for SEI in 1M KFSI.

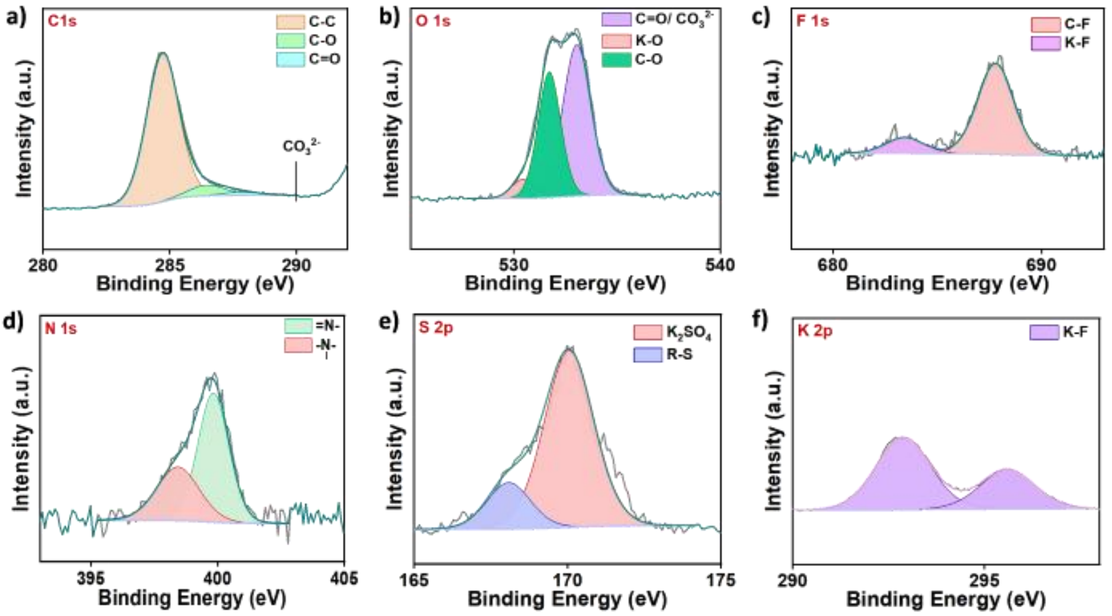

Figure 17. Deconvoluted XPS spectra of a) C 1s, b) O 1s, c) F 1s, d) N 1s, e) S 2p, and f) K 2p of surface of BTEG with 1M KFSI before etching.

Figure 18 shows XPS spectra after etching of SEI formed by 5M KFSI electrolyte. C 1s spectra (**Figure 18a**) show the presence of a C-C peak and complete elimination of C-O, C=O, and CO$_3^{2-}$ contrary to the before-etched surface (**Figure 17a**). **Figure 18c** shows the emergence of a new peak associated with K$_2$SO$_3$ after etching at 162.8 eV.

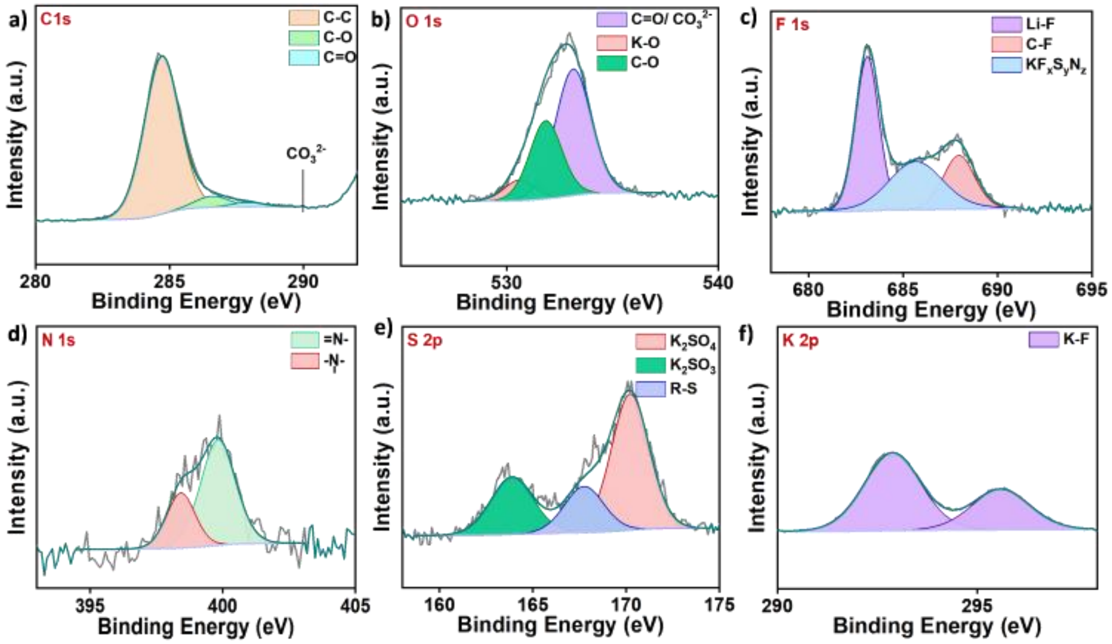

Figure 18. Deconvoluted XPS spectra of a) C 1s, b) O 1s, c) F 1s, d) N 1s, e) S 2p, and f) K 2p of surface of BTEG with 1M KFSI after etching.

5M KFSI-based SEI shows similar peaks to 1M KFSI before and after etching but with varying species composition, as seen in Figures **17-21**. Although C 1s spectra show the absence of all peaks C-O, C=O, and CO_3^{2-} after etching (**Figure 20a**).

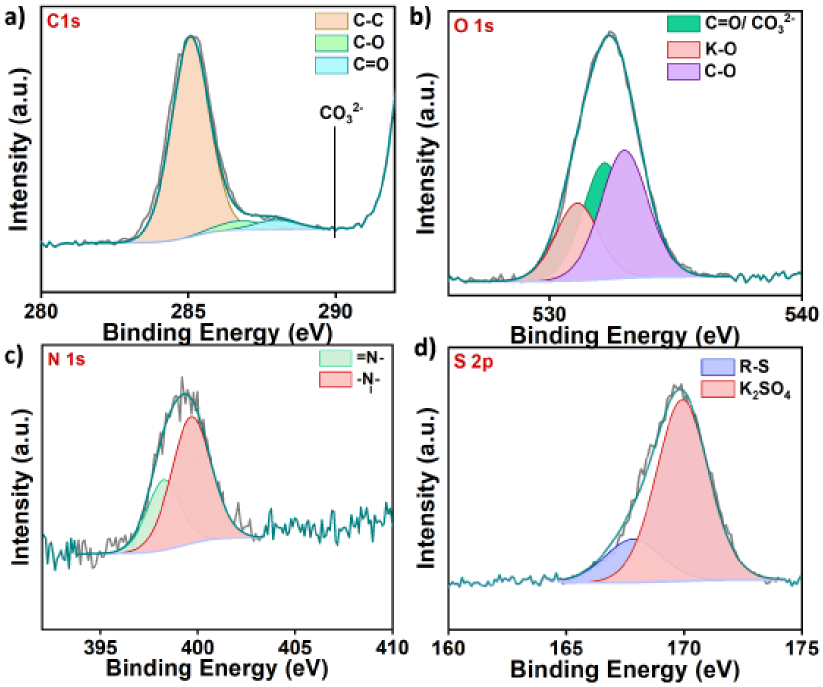

Figure 19. XPS spectra of a) C 1s, b) O 1s, c) S 2p, and d) N 1s peaks of BTEG with 5M KFSI electrolyte before etching.

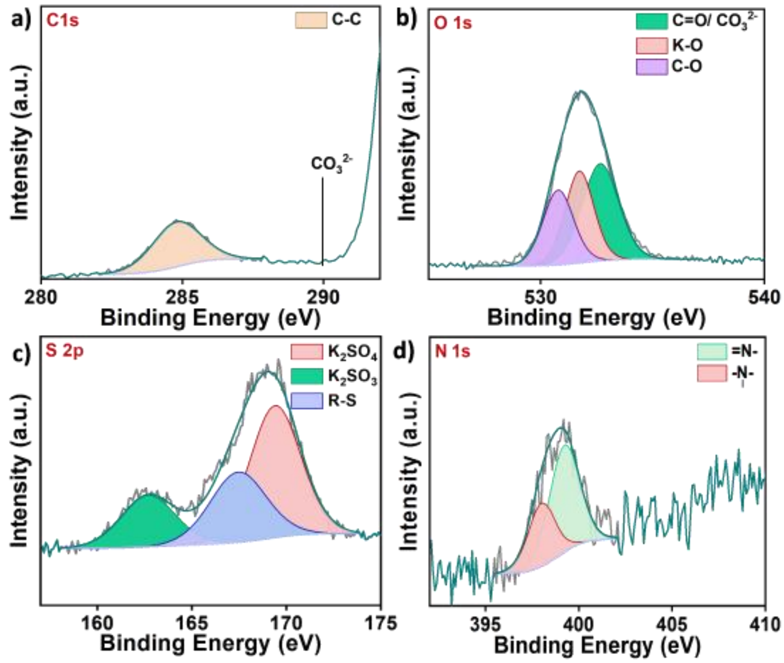

Figure 20. XPS spectra of a) C 1s, b) O 1s, c) S 2p, and d) N 1s peaks of BTEG with 5M KFSI electrolyte after etching.

Figure 21 compares the composition of SEI associated with 0.8 M KPF_6 and 5M KFSI, examining the differences before (0 nm) and after etching (30 nm). The nature of fluorine species dictates the stability of SEI in a battery. Figure 20a illustrates F 1s spectra, showing higher C-F species intensity in 0.8M KPF_6 and dominant K-F in 5M KFSI SEI. Post-etching, the complete disappearance of C-F species indicates SEI stability in PIB.[32] Correspondingly, C 1s spectra were analyzed (**Figure 21b**) to understand the organic species in SEI. It was observed that C-C content diminishes dramatically for 5M KFSI compared to 0.8M KPF_6, making SEI stable enough to allow bulkier-sized K^+ conduction for 5M KFSI.

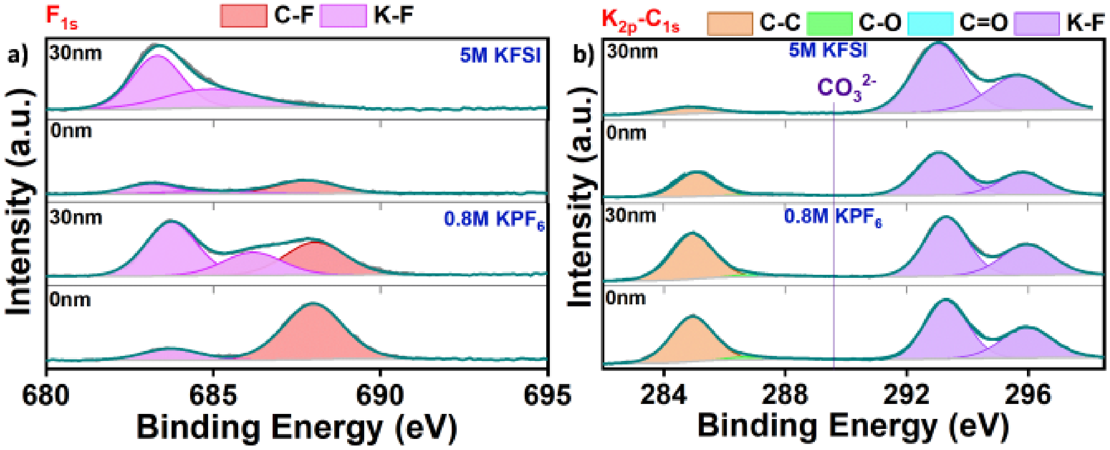

Figure 21. XPS spectra comparing the SEI post-formation on BTEG a) F 1s and b) K 2p-C 1s spectra for 0.8M KPF_6 and 5M KFSI electrolyte before (0 nm) and after etching (30 nm).

The quantitative analysis was performed with segregated organic and inorganic-like species, as shown in the histogram in **Figures 22a and 23**. 5M KFSI-based SEI exhibits highest inorganic content before (35 at%) and after etching (65 at%) compared to 0.8M KPF_6 (23 at%; 31 at%) and 1M KFSI (25 at%; 23.6 at%). These results indicate that KFSI decomposition is aggravated in the case of HCE, i.e., 5M KFSI. This can be correlated with stability and potential profiles obtained in symmetric cells shown in **Figure 3b-d**. Looking closely at species of interest, i.e., K-F, which is maximum up to 20 at% in case of 5M KFSI (after etching) compared to 12 at% in 0.8M KPF_6 (**Figure 22b**).

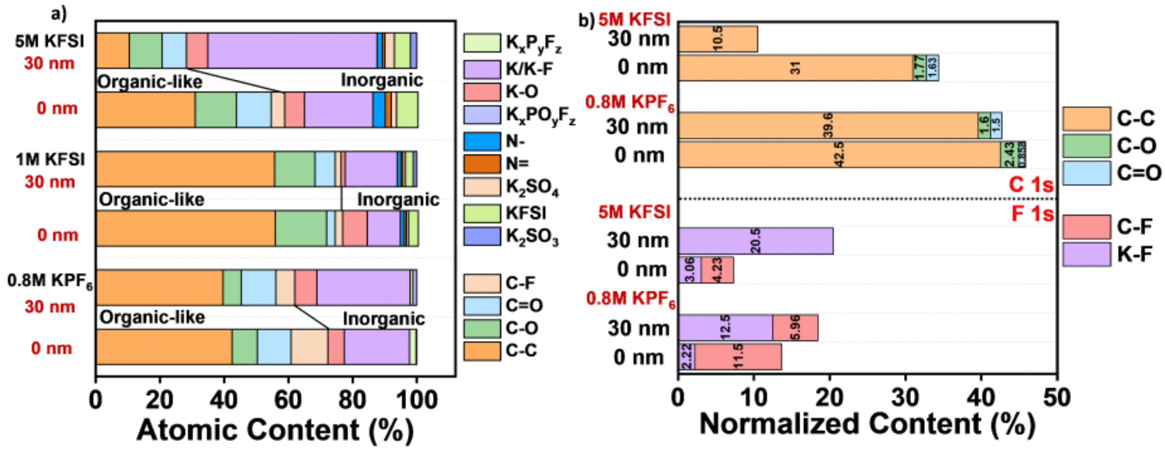

Figure 22. a) Bar charts showing the relative percentage of different species in the SEI of electrolyte 0.8M KPF_6, 1M KFSI, and 5M KFSI. b) Bar charts comparison of 0.8M KPF_6 and 5M KFSI electrolyte for C 1s and F 1s.

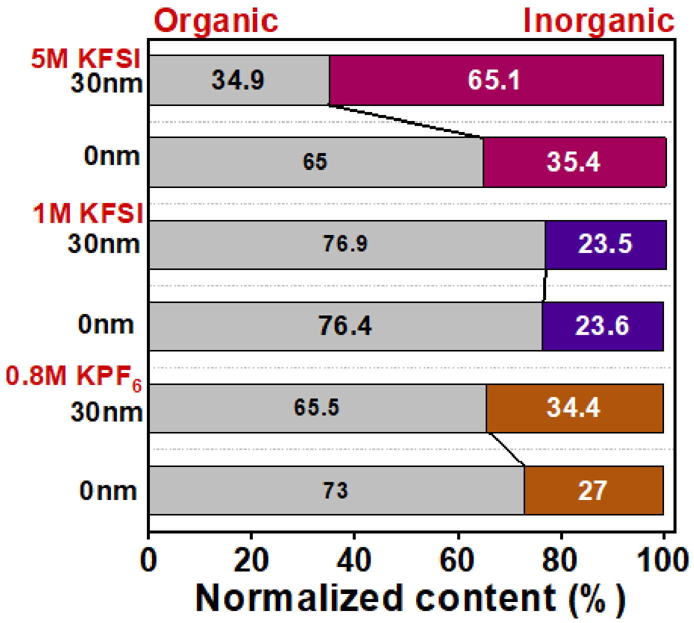

Figure 23. Comparison of organic-like and inorganic content percentage before (0 nm) and after etching(30 nm) for conventional electrolytes KPF_6, 1M KFSI, and 5M KFSI in EC: DEC.

When utilizing conventional electrolytes, the BTEG demonstrates varied capacity retentions for different battery types: 80% and 75% for LIBs and SIBs, respectively (**Figures 24a and 24b**). However, PIBs' capacity noticeably deteriorates, plunging drastically after 200 cycles at a current density of 1 A g^{-1}, as indicated in **Figure 24c.** In contrast, incorporating a 1M KFSI exhibits an impressive 87% capacity retention at a current density of 1 A g^{-1} over 200 cycles, as showcased in **Figure 24d**. Furthermore, 5M KFSI shows the highest capacity retention of 99.4% after 200 cycles, as shown in **Figure 25**. A plausible explanation for this enhanced performance could be the reduced presence of free solvent molecules in the HCE, as suggested by Raman spectroscopic analysis, and the highest inorganic content (particularly KF species) in SEI.

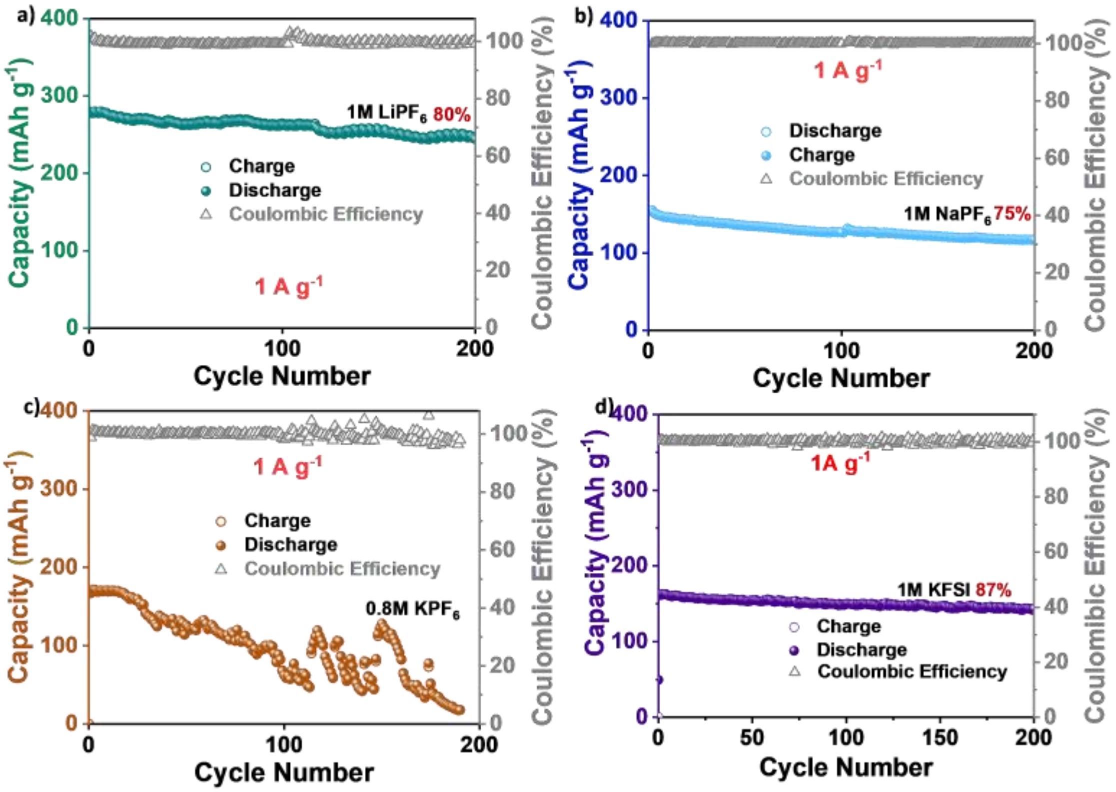

Figure 24. Long-term stability of BTEG electrodes with electrolytes a) 1M $LiPF_6$, b) 1M $NaPF_6$, c) 0.8M KPF_6, and d) 1M KFSI at 1 A g^{-1}.

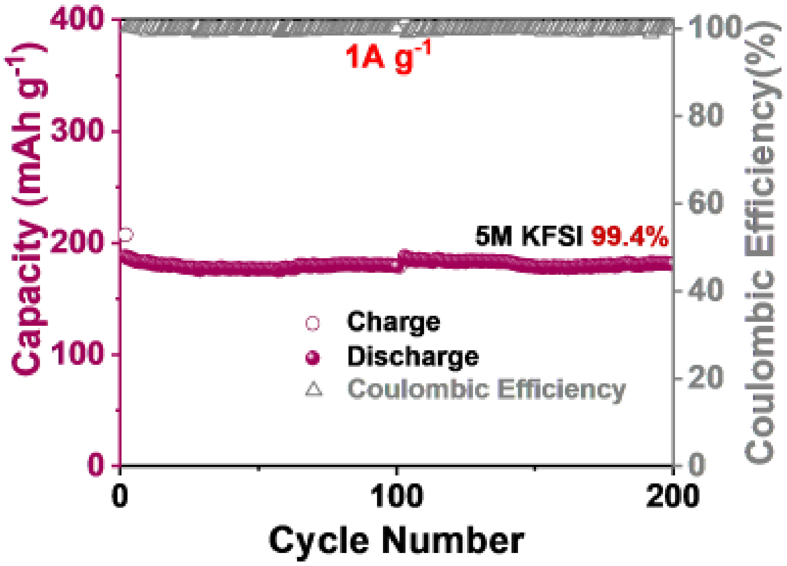

Figure 25. Long-term stability of BTEG electrode with electrolytes 5M KFSI at 1 A g^{-1}.

1.2b.5 Conclusion

The analysis of SEI layers in alkali-ion batteries reveals that electrolyte composition significantly influences SEI formation and, consequently, battery performance. Potassium-based electrolytes, especially at higher concentrations like 5M KFSI, produce an SEI layer rich in inorganic components, offering enhanced stability and performance in potassium-ion batteries (PIBs). This contrasts with the SEI formed from lithium and sodium-based electrolytes, which show similar compositions but less optimal performance in PIBs. The findings underline the importance of electrolyte and SEI chemistry in improving battery efficiency, stability, and longevity, with particular implications for advancing PIB technology.

1.2b.6 References:

1. Lim, J.J.N., Lim, G.J.H., Cai, Y., Chua, R., Guo, Y., Yan, Y., and Srinivasan, M. (2023) Electrolyte designs for safer lithium-ion and lithium-metal batteries. *J Mater Chem A Mater*, **11** (42), 22688–22717.

2. Chen, J., Zhang, Y., Lu, H., Ding, J., Wang, X., Huang, Y., Ma, H., and Wang, J. (2023) Electrolyte solvation chemistry to construct an anion-tuned interphase for stable high-temperature lithium metal batteries. *eScience*, **3** (4), 100135.

3. Tian, Z., Zou, Y., Liu, G., Wang, Y., Yin, J., Ming, J., and Alshareef, H.N. (2022) Electrolyte Solvation Structure Design for Sodium Ion Batteries. *Advanced Science*, **9** (22), 2201207.

4. Attia, P.M., Chueh, W.C., Harris, S.J., Guan, P., Liu, L., and Lin, X. You may also like Revisiting the t 0.5 Dependence of SEI Growth Simulation and Experiment on Solid Electrolyte Interphase (SEI) Morphology Evolution and Lithium-Ion Diffusion.

5. Liu, S., Ji, X., Piao, N., Chen, J., Eidson, N., Xu, J., Wang, P., Chen, L., Zhang, J., Deng, T., Hou, S., Jin, T., Wan, H., Li, J., Tu, J., and Wang, C. (2021) An Inorganic-Rich Solid Electrolyte Interphase for Advanced Lithium-Metal Batteries in Carbonate Electrolytes. *Angewandte Chemie International Edition*, **60** (7), 3661–3671.

6. Liu, X., Zheng, X., Dai, Y., Wu, W., Huang, Y., Fu, H., Huang, Y., and Luo, W. (2021) Fluoride-Rich Solid-Electrolyte-Interface Enabling Stable Sodium Metal Batteries in High-Safe Electrolytes. *Adv Funct Mater*, **31** (30), 2103522.

7. Jia, T., Zhong, G., Lu, S., Ren, X., Lv, Y., Li, N., Yin, R., Kang, G., Cai, K., Kang, F., and Cao, Y. (2023) Interfacial fluoride engineering enabled robust LiF-rich solid electrolyte interphase to reduce active lithium loss in rechargeable lithium battery. *Chemical Engineering Journal*, **454**, 140397.

8. McBrayer, J.D., Apblett, C.A., Harrison, K.L., Fenton, K.R., and Minteer, S.D. (2021) Mechanical studies of the solid electrolyte interphase on anodes in lithium and lithium ion batteries. *Nanotechnology*, **32** (50), 502005.

9. Wu, B., Chen, C., Danilov, D.L., Jiang, M., Raijmakers, L.H.J., Eichel, R.A., and Notten, P.H.L. (2022) Influence of the SEI Formation on the Stability and Lithium Diffusion in Si Electrodes. *ACS Omega*, **7** (36), 32740–32748.

10. Wang, H., Zhai, D., and Kang, F. (2020) Solid electrolyte interphase (SEI) in potassium ion batteries. *Energy Environ Sci*, **13** (12), 4583–4608.

11. Teng, W., Wu, J., Liang, Q., Deng, J., Xu, Y., Liu, Q., Wang, B., Ma, T., Nan, D., Liu, J., Li, B., Weng, Q., and Yu, X. (2023) Designing Advanced Liquid Electrolytes for Alkali Metal Batteries: Principles, Progress, and Perspectives. *Energy & Environmental Materials*, **6** (2), e12355.

12. Guéguen, A., Streich, D., He, M., Mendez, M., Chesneau, F.F., Novák, P., and Berg, E.J. (2016) Decomposition of LiPF 6 in High Energy Lithium-Ion Batteries Studied with Online Electrochemical Mass Spectrometry . *J Electrochem Soc*, **163** (6), A1095–A1100.

13. Zhang, W., Pang, W.K., Sencadas, V., and Guo, Z. (2018) Understanding High-Energy-Density Sn4P3 Anodes for Potassium-Ion Batteries. *Joule*, **2** (8), 1534–1547.

14. Horstmann, B., Shi, J., Amine, R., Werres, M., He, X., Jia, H., Hausen, F., Cekic-Laskovic, I., Wiemers-Meyer, S., Lopez, J., Galvez-Aranda, D., Baakes, F., Bresser, D., Su, C.C., Xu, Y., Xu, W., Jakes, P., Eichel, R.A., Figgemeier, E., Krewer, U., Seminario, J.M., Balbuena, P.B., Wang, C., Passerini, S., Shao-Horn, Y., Winter, M., Amine, K., Kostecki, R., and Latz, A. (2021) Strategies towards enabling lithium metal in batteries: interphases and electrodes. *Energy Environ Sci*, **14** (10), 5289–5314.

15. Xiao, P., Yun, X., Chen, Y., Guo, X., Gao, P., Zhou, G., and Zheng, C. (2023) Insights into the solvation chemistry in liquid electrolytes for lithium-based rechargeable batteries. *Chem Soc Rev*, **52** (15), 5255–5316.

16. Moharana, S., West, G., Menon, A.S., da Silva, W.L., Walker, M., and Loveridge, M.J. (2023) Combined Stabilizing of the Solid-Electrolyte Interphase with Suppression of Graphite Exfoliation via Additive-Solvent Optimization in Li-Ion Batteries. *ACS Appl Mater Interfaces*, **15** (43), 50185–50195.

17. Yu, Z., Balsara, N.P., Borodin, O., Gewirth, A.A., Hahn, N.T., Maginn, E.J., Persson, K.A., Srinivasan, V., Toney, M.F., Xu, K., Zavadil, K.R., Curtiss, L.A., and Cheng, L. (2022) Beyond Local Solvation Structure: Nanometric Aggregates in Battery Electrolytes and Their Effect on Electrolyte Properties. *ACS Energy Lett*, **7** (1), 461–470.

18. Yamada, Y., Wang, J., Ko, S., Watanabe, E., and Yamada, A. (2019) Advances and issues in developing salt-concentrated battery electrolytes. *Nature Energy 2019 4:4*, **4** (4), 269–280.

19. Wang, A., Kadam, S., Li, H., Shi, S., and Qi, Y. (2018) Review on modeling of the anode solid electrolyte interphase (SEI) for lithium-ion batteries. *npj Computational Materials 2018 4:1*, **4** (1), 1–26.

20. Yang, G., Sacci, R.L., Ivanov, I.N., Ruther, R.E., Hays, K.A., Zhang, Y., Cao, P.-F., Veith, G.M., Dudney, N.J., Saito, T., Hallinan, D.T., and Nanda, J. (2019) Probing Electrolyte Solvents at Solid/Liquid Interface Using Gap-Mode Surface-Enhanced Raman Spectroscopy. *J Electrochem Soc*, **166** (2), A178–A187.

21. Kock, L.D., Lekgoathi, M.D.S., Crouse, P.L., and Vilakazi, B.M. (2012) Solid state vibrational spectroscopy of anhydrous lithium hexafluorophosphate (LiPF6). *J Mol Struct*, **1026**, 145–149.

22. Matsumoto, K., Nakahara, K., Inoue, K., Iwasa, S., Nakano, K., Kaneko, S., Ishikawa, H., Utsugi, K., and Yuge, R. (2014) Performance Improvement of Li Ion Battery with Non-Flammable TMP Mixed Electrolyte by Optimization of Lithium Salt Concentration and SEI Preformation Technique on Graphite Anode. *J Electrochem Soc*, **161** (5), A831–A834.

23. Wang, H., Yu, D., Wang, X., Niu, Z., Chen, M., Cheng, L., Zhou, W., and Guo, L. (2019) Electrolyte Chemistry Enables Simultaneous Stabilization of Potassium Metal and Alloying Anode for Potassium-Ion Batteries. *Angewandte Chemie International Edition*, **58** (46), 16451–16455.

24. Ma, P., Mirmira, P., and Amanchukwu, C. V. (2021) Effect of Building Block Connectivity and Ion Solvation on Electrochemical Stability and Ionic Conductivity in Novel Fluoroether Electrolytes. *ACS Cent Sci*, **7** (7), 1232–1244.

25. Lewis, N.H.C., Zhang, Y., Dereka, B., Carino, E. V., Maginn, E.J., and Tokmakoff, A. (2020) Signatures of Ion Pairing and Aggregation in the Vibrational Spectroscopy of Super-Concentrated Aqueous Lithium Bistriflimide Solutions. *Journal of Physical Chemistry C*, **124** (6), 3470–3481.

26. Zhang, R., Bao, J., Wang, Y., and Sun, C.F. (2018) Concentrated electrolytes stabilize bismuth–potassium batteries. *Chem Sci*, **9** (29), 6193–6198.

27. Zhao, Y., Zhou, T., Mensi, M., Choi, J.W., and Coskun, A. (2023) Electrolyte engineering via ether solvent fluorination for developing stable non-aqueous lithium metal batteries. *Nature Communications 2023 14:1*, **14** (1), 1–10.

28. Arreaga-Salas, D.E., Sra, A.K., Roodenko, K., Chabal, Y.J., and Hinkle, C.L. (2012) Progression of solid electrolyte interphase formation on hydrogenated amorphous silicon anodes for lithium-ion batteries. *Journal of Physical Chemistry C*, **116** (16), 9072–9077.

29. Hosaka, T., Kubota, K., Hameed, A.S., and Komaba, S. (2020) Research Development on K-Ion Batteries. *Chem Rev*, **120** (14), 6358–6466.

30. Mogensen, R., Brandell, D., and Younesi, R. (2016) Solubility of the Solid Electrolyte Interphase (SEI) in Sodium Ion Batteries. *ACS Energy Lett*, **1** (6), 1173–1178.

31. Liu, Q., Rao, A.M., Han, X., and Lu, B. (2021) Artificial SEI for Superhigh-Performance K-Graphite Anode. *Advanced Science*, **8** (9).

32. Ye, M., Hwang, J.Y., and Sun, Y.K. (2019) A 4 v Class Potassium Metal Battery with Extremely Low Overpotential. *ACS Nano*, **13** (8), 9306–9314.

Chapter 1.3

Sn@C composite as an anode for Li-ion battery

Summary

The work presented herein details the development of a tin nanoparticle-embedded carbon composite synthesized through a single-step combustion process. This composite is noteworthy for its ability to endure the substantial volumetric changes typically associated with the alloying and dealloying processes in battery anodes. The carbon matrix, enriched with graphitic content, ensures a stable electrical connection to the tin nanoparticles, which is crucial for maintaining the structural integrity of the anode material. The batteries display a reversible 184 mA h g-1 capacity at a current density of 500 mA g^{-1}*, maintaining 94.6% of its capacity after 700 cycles. These findings suggest that the composite material has significant potential for use in batteries, providing a balance of capacity and longevity.*

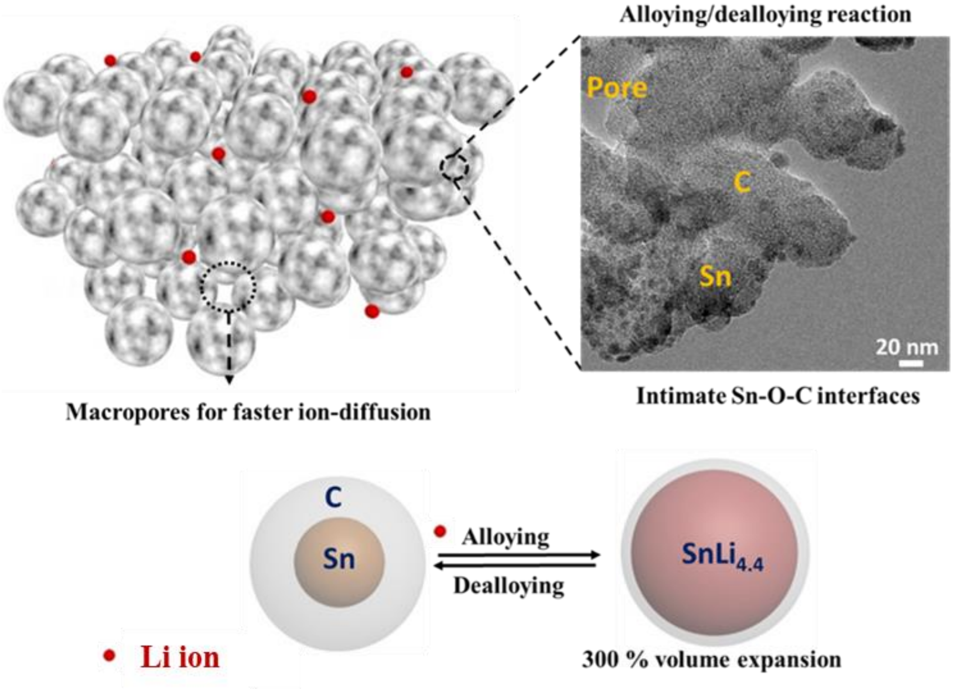

1.3.1 Introduction

The development of lithium-ion batteries (LIBs) has been paramount in powering a variety of portable electronic devices for over two decades, with the performance of these batteries heavily depending on the advancement of anode materials.[1] High capacity, high energy density, and lower potential against Li^+/Li[2,3] are critical benchmarks in anode selection. Despite their wide usage, traditional graphite anodes have a low theoretical capacity at 372 mA h g^{-1} due to their intercalation mechanism.[4]

To transcend these limitations, researchers have turned their attention to alternative elements such as Si[5][6], Ge[7,8], and Sn[9,10], which are theorized to offer vastly superior capacities through an alloying reaction.[11] Among these, tin-based materials are particularly noteworthy for their high theoretical capacities 994 mA h g^{-1} for Sn, 1244 mA h g^{-1} for SnO, and 1467 mA h g^{-1} for SnO_2 alongside their low environmental impact, natural abundance, and favorable thermodynamic stability.[12] Tin undergoes direct alloying upon lithiation, while SnO and SnO_2 first experience a reduction step (equation 1), followed by alloying (equation 2) reaction[2].

$SnO_2 + 4Li^+ + 2e \rightarrow Sn + 2Li_2O$ (1)

$Sn + 4.4Li^+ + 4.4e \rightarrow Li_{4.4}Sn$ (2)

In anode materials utilizing SnO_2 and SnO, the generation of Li_2O through the reduction step tends to be non-reversible due to the larger particle size of the oxides.[13] This reduces the theoretical reversible/ irreversible capacities of 846/ 398 mAh g^{-1} and 756/ 711 mAh g^{-1}. These values are calculated based on Li_2O and $Li_{4.4}Sn$ final phase.[14] However, this challenge can be mitigated by scaling down Sn/ SnO_x particle sizes to sub-5 nm dimensions, where enhanced kinetic properties can render the process reversible. Additionally, during the alloying phase, tin undergoes a dramatic volume expansion of approximately 300%[15], which inflicts significant mechanical strain, leading to material pulverization and loss of electrical connectivity after several cycles (**Figure 1**). This compromises the innate properties of tin, i.e., its ductility[16], malleability, and high crystallinity.

Figure 1. Illustration depicting the lithium-tin (Li-Sn) alloy formation process and the challenges during prolonged cycling.[17]

Developing intermetallics or composite anodes containing tin addresses these drawbacks and has been shown to improve structural stability. This approach was adopted in Sony's "Nexelion" battery,[18] which uses an amorphous Sn-Co-C composite, resulting in a 30% boost in volumetric capacity compared to traditional LIBs. However, cobalt's costly and potentially harmful nature, along with its limited lifespan, restricts widespread adoption.[19]

Recent advances suggest that tin-carbon hybrids, such as those with graphene,[20] carbon,[21,22] and carbon nanotubes,[23] hold potential. The performance of these materials largely depends on the characteristics of the carbon involved, the size of the Sn particles, and their interaction, which are all products of the chosen synthesis method. Maintaining the morphology of Sn nanoparticles on carbon substrates across multiple cycles poses a challenge, particularly when the composite is derived from Sn precursors and pre-existing carbon structures. Functionalized carbon could facilitate enhanced tin-carbon interactions but at the cost of electrical conductivity due to charge-transfer inefficiencies. Thus, a simplistic approach to developing a tin-carbon composite with nanoparticles of tin well-embedded in a graphite-rich matrix is highly sought after.

1.3.2 Scope of investigation:

A cost-effective method using fractal-like interconnected carbon nanoparticles from candle soot has been explored for Li-ion batteries.[24] In a previous study, we fabricated Co_3O_4@C composites via a liquid-fuel combustion method, an in-situ approach for the oxygen evolution reaction.[25] This in-situ fabrication process confers distinct advantages by enhancing the metal-carbon interfacial interaction, a challenge often encountered with conventional ex-situ synthesis methods.[26,27] In the current investigation, we have synthesized a composite embedding of tin nanoparticles within a turbostratic carb to achieve optimized battery performance. For comparison, carbon soot (CS)[28,29] was produced through the combustion of n-decane, serving as a reference material.

1.3.3 Experimental procedure:

i. Materials and characterization techniques:

Tetrabutyl tin was acquired from TCI Chemicals, and n-Decane was acquired from Spectrochem. HNO_3 (69%) was bought from Merck, and H_2O_2 (30%) from SD Fine Chemicals. $LiPF_6$ (1 M) in a 1:1 v/v mixture of ethylene carbonate (EC) and diethyl carbonate (DEC) liquid electrolyte, Li metal, and glass fiber (GF) separator were obtained from Sigma–Aldrich.

ii. Synthesis of Sn@C composite

Tetrabutyltin (5 wt%) was added to n-Decane (95 wt%) and collected in a 5 ml glass vial (3.6 ml of solution). On controlled combustion with a cotton wick, soot was accumulated on a glass slide (**Figure 2**) placed (at a height of 70%) parallelly above the flame (~1200-1300°C). The flame temperature, particle sizes, and chemical species depend on the height at which the glass slide is positioned from the flame. The glass slide's height was optimized to collect the maximum yield of highly porous interconnected carbon soot with maximum uptake of tin. Sn@C was collected on a glass slide and subjected to a heat treatment in a mixture of H_2 (5%) and Ar (95%) atmosphere at 700°C for 1 h with a ramp rate of 5°C/min from the room temperature. Control experiments were carried out with the as-prepared sample. Additionally, hydrogen-treated Sn@C with higher Sn loading is briefly mentioned.

iii. Material characterization

Powder X-ray diffraction (PXRD) analysis of the Cu foil was recorded with a PANalytical diffractometer (Empyrean) having monochromatic Cu $K_{\alpha 1}$ radiation ($\lambda = 1.5404$ Å) with an accelerating voltage of 40 kV and current of 40 mA. Thermogravimetric analysis (TGA) was done with a Mettler Toledo TGA-850 TG analyzer at the ramping rate of 5°C min^{-1} in an oxygen atmosphere. Raman spectra were obtained from Jobin Yvon LabRam HR spectrometer equipped with frequency-doubled Nd: YAG solid-state green laser (532 nm). Brunauer–Emmett–Teller (BET) analysis for N_2 (ultra-high purity of 99.9995%) sorption studies were conducted at 77 K by Autosorb-iQ$_2$, and samples were degassed for 12 h at 373K. JEM 2100 PLUS electron microscope of 200 KV was used to acquire the samples' transmission electron microscope (TEM) images. Technai F30 UHR electron microscope operating at an accelerating voltage of 200 kV was used for scanning transmission electron microscope (STEM) imaging. ZEISS GEMINI 500 was used to procure images for Field Emission Scanning Electron Microscopy (FESEM). X-ray photoelectron spectroscopy (XPS) measurements were carried out by an X-ray photoelectron spectrometer (Thermo K-alpha+) using micro-focused and monochromated AlKα radiation with energy 1486.6 eV. The pass energy was kept at 50 eV for individual core levels, and charge compensation was done using an electron flood gun. The FESEM, TEM, and XPS samples were prepared by sonicating the powdered sample in 99.99% pure ethanol and uniformly drop casting on Cu foil, Cu grid, and Si wafer, respectively.

iv. Sample preparation for ICP-OES analysis

Inductively coupled plasma optical emission spectroscopic (ICP-OES) analysis data was acquired from the Perkin Elmer Optima 7000DV instrument.

Four milligrams of hydrogen-treated Sn@C sample was taken in a 30 ml vial and dispersed in 2 ml of 30% hydrogen peroxide. Subsequently, heat treatment was carried out at 90°C, increasing to 120°C. This was carried out to eliminate carbon in the form of carbon dioxide. This step was repeated three times. It was observed that carbon residue was retained in the sample. So, HNO_3 (69%) was added to leach out Sn accompanied by heat treatment. Finally, only white residue adhered to the walls of the glass vial. Subsequently, the white residue was dissolved in 2 ml of aqua regia (HCl: HNO_3 = 3:1 (v/v)) and diluted up to 10 ml for sample analysis.

v. Electrode preparation and electrochemical measurement

The electrode was prepared by mechanically grinding Sn@C (85 wt%), Vulcan carbon (10 wt%), and PVDF (Polyvinylidene fluoride) (5 wt%) with NMP (N-methyl-2-pyrrolidone) for 3–4 h. The doctor blade applicator film-coated the slurry on copper foil (current collector), followed by drying it at 120°C overnight in a vacuum oven. After drying, the working electrode was punched to acquire an 11 mm diameter electrode. 1.0M $LiPF_6$ in EC and DEC was chosen as electrolytes with Li metal foil as the counter electrode. Half cells were fabricated in a high pure Ar (>99.999%) filled glove box.

Swagelok cells 316 were tested on BCS-810 BioLogic Science Instruments with cut off voltage range of 0.1 V-3.0 V. Cyclic voltammetry (CV) and Electrochemical Impedance Spectroscopy (EIS) was recorded on electrochemical workstation (760E, USA) obtained from CH Instruments, Inc. CV was carried out at a scan rate of 0.1 mV s^{-1} and EIS for a frequency range of 0.01 Hz to 100KHz with an amplitude of 5 mV.

1.3.4 Results and discussion

The Sn@C composite was synthesized using a homogenous mixture of tetrabutyltin and n-decane as the liquid fuel. The combustion process, facilitated by the wick action, yielded soot, which was then deposited onto a glass slide to form the Sn@C composite (**Figure 2**). This material was subjected to a hydrogen treatment at 700°C for an hour to achieve the final product.

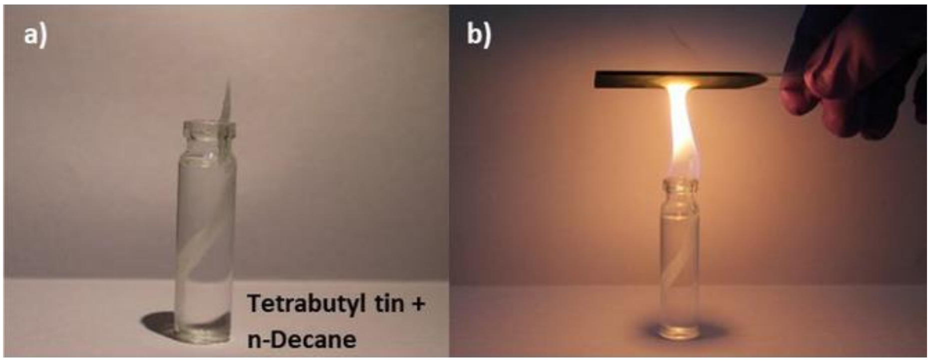

Figure 2. Digital images showing (a) the solubility of tetrabutyl tin in n-decane and (b) the accumulation of soot on a glass slide resulting from combustion.

Thermogravimetric analysis (TGA) was utilized to evaluate the thermal stability and tin content within the Sn@C composite. The hydrogen-treated composite demonstrated stability up to 500°C in an air atmosphere. Upon increasing the temperature beyond this point, complete combustion of carbon was observed at 675°C. The initial sample exhibited significant weight loss at around 400°C, attributed to the decomposition of oxygen-containing functional groups. The residual weight obtained from TGA measurement suggests a 20 wt% tin content in the Sn@C composite, further confirmed by inductively coupled plasma optical emission spectroscopy (ICP-OES), as depicted in **Figure 3.**

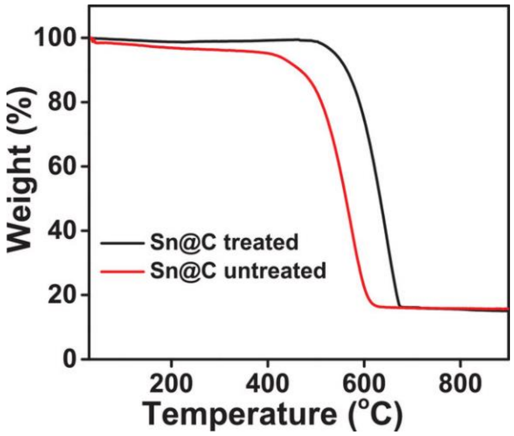

Figure 3. Thermogravimetric Analysis (TGA) was performed in an oxygen environment for both hydrogen-treated and untreated Sn@C samples.

The powder X-ray diffraction (PXRD) patterns of the Sn@C composite, presented in **Figures 4a and 4b**, reveal a pronounced peak at 29.7° (2θ), which can be ascribed to the (200) lattice plane of metallic tin (referenced from JCPDS Card No. 00-004-0673). Furthermore, there is a signature peak for tin dioxide (SnO_2)[30] at 26.6° (2θ), which corresponds to the (110) lattice plane, as per JCPDS Card No. 04-003-0649. The patterns shown in **Figure 4b** illustrate the partial reduction of SnO_2 to SnO after the hydrogen treatment process.

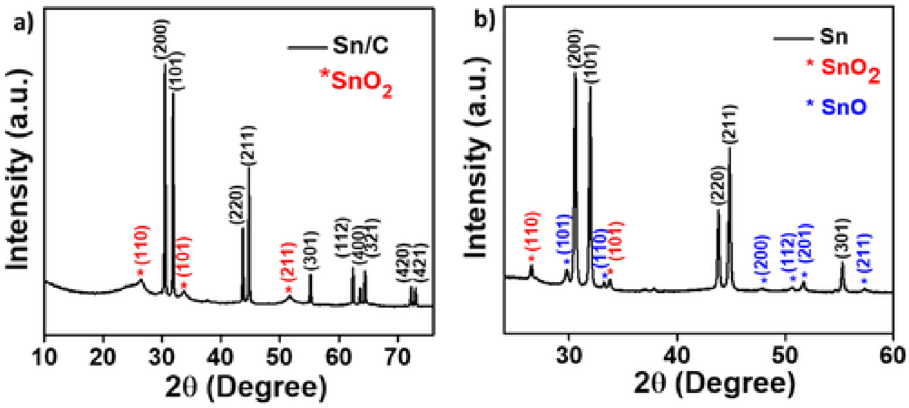

Figure 4. Powder X-ray Diffraction (PXRD) patterns of the Sn@C composite: (a) prior to hydrogen treatment and (b) following hydrogen treatment.

Field emission scanning electron microscopy (FESEM) reveals that Sn@C comprises an interconnected three-dimensional porous carbon network, as shown in **Figure 5c**. Morphological and microstructural analysis through transmission electron microscopy (TEM) and high-resolution transmission electron microscopy (HRTEM) demonstrate the evolution of Sn@C before and after hydrogen treatment. The TEM images (**Figures 5a and 5d**) indicate the distribution of tin nanoparticles, ranging from 5 to 20 nm in size, evenly encapsulated within the porous carbon matrix. The HRTEM images (**Figure 5b**) initially display tin oxide particles with an amorphous structure, which transform into a crystalline form post-hydrogen treatment (**Figure 5e and f**). The hydrogen treatment also visibly induces partial graphitization of carbon. The structural alterations, including the shedding of functional groups from tin and carbon leading to partial crystallinity, are evident from the HRTEM results. Notably, the HRTEM images of hydrogen-treated samples (**Figures 5e and 5f**) show nanoparticles of Sn and SnO_2 with interplanar spacings of 0.34 nm and 0.29 nm, respectively, corresponding to the lattice planes (200) and (110). These findings are congruent with the earlier PXRD results, affirming the consistency of the structural data obtained through different characterization techniques.

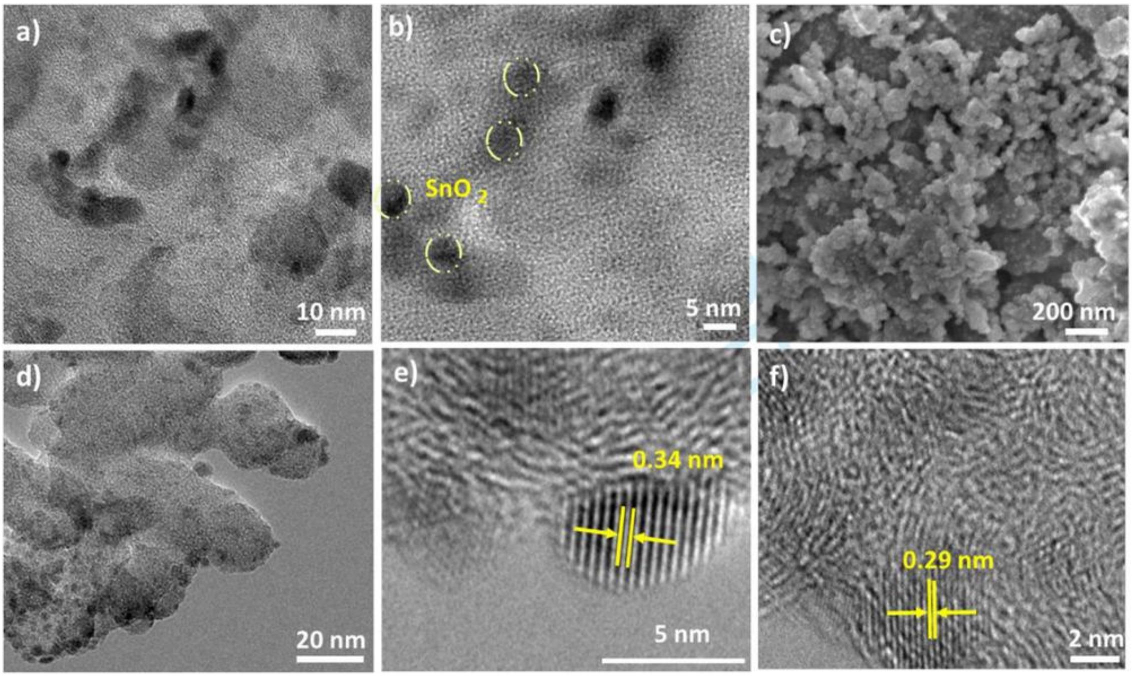

Figure 5. (a) TEM image before hydrogen treatment, illustrating uniformly distributed Sn particles within the carbon matrix in the as-prepared sample, and (b) HRTEM image displaying the amorphous structure of carbon. (c) FESEM image of hydrogen-treated Sn@C revealing an interconnected network, and (d) TEM image showing SnOx nanoparticles (5-20 nm) well dispersed in the carbon matrix. HRTEM images for (e) Sn and (f) SnO_2, respectively.

In some cases, the carbon support was found to have larger tin nanoparticles with a void, a core-shell-like morphology for Sn@C with and without hydrogen treatment, with Sn size approximately 50-70 nm, as depicted in **Figure 6**. Moreover, the HRTEM image of Sn@C hydrogen treated reveals a SnO layer on the surface of Sn (**Figure 7**).

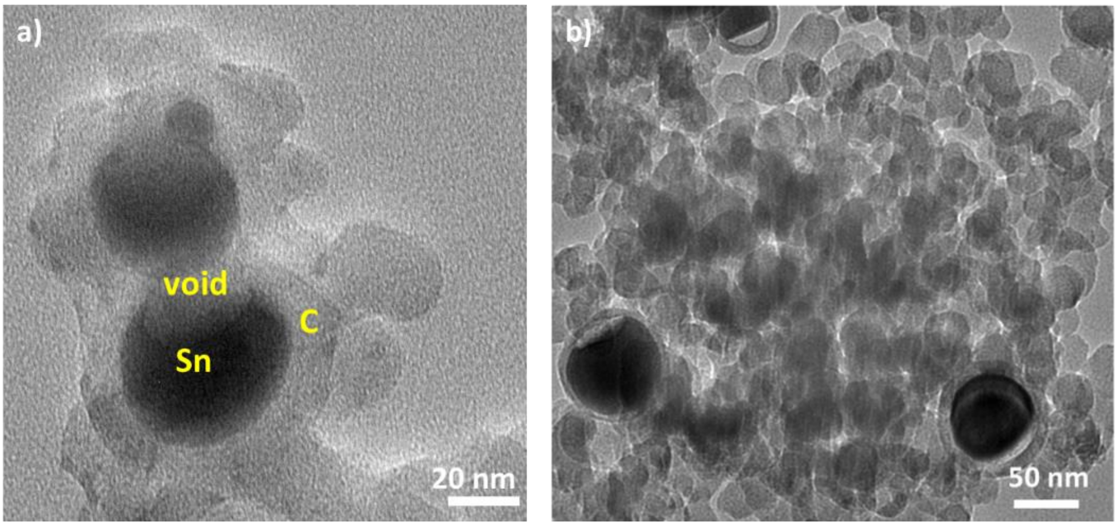

Figure 6. TEM image of the Sn@C composite a) before and b) after hydrogen annealing reveals 50 nm-sized hollow tin nanoparticles.

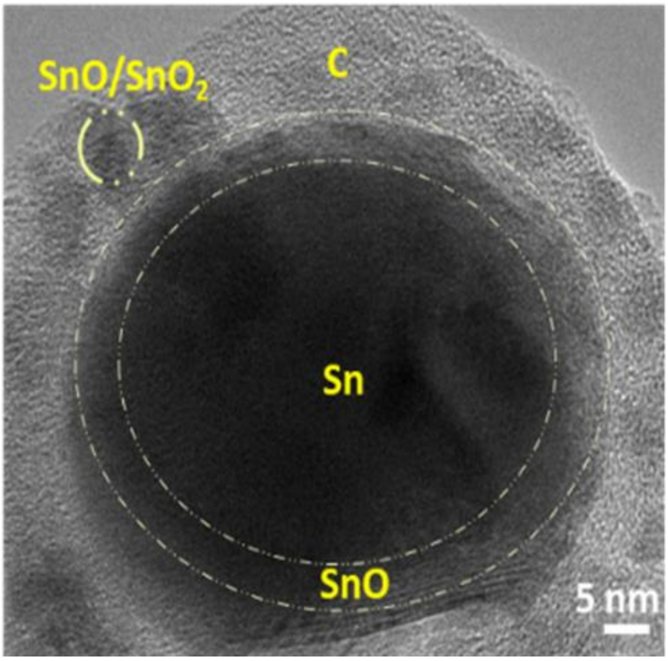

Figure 7. HRTEM image of Sn@C hydrogen treated.

The core-shell morphology of hydrogen annealed Sn@C was further explored through scanning transmission electron microscopy (STEM) imaging. Figure 8 shows larger Sn@C particles exhibit a core-shell structure, with an oxidized surface layer on the tin particles, which is clearly identified through elemental mapping.

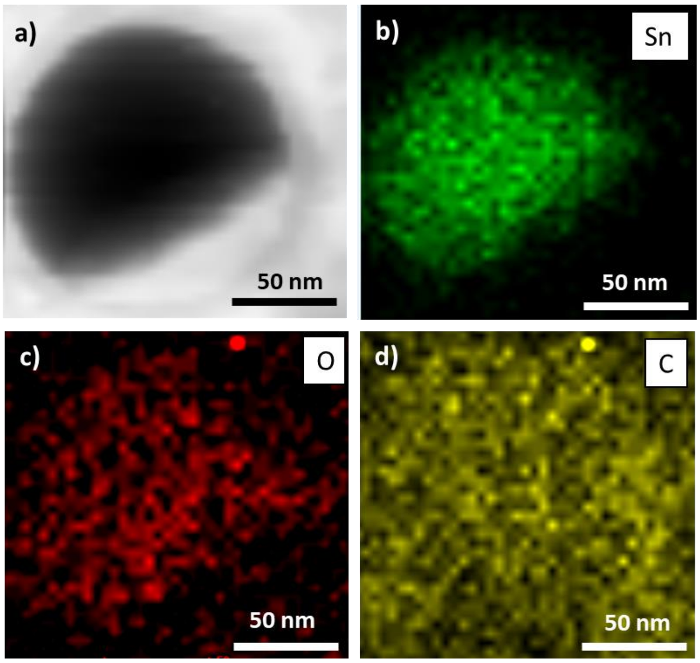

Figure 8. (a) STEM image of the Sn@C composite post hydrogen annealing, displaying a 60 nm hollow tin nanoparticle encased in carbon, accompanied by elemental mapping images for (b) tin (Sn), (c) oxygen (O), and (d) carbon (C).

Moreover, a hydrogen-treated Sn@C sample with a higher tin content of 30 wt% displayed Sn nanoparticles that were significantly larger, ranging from 50 to 100 nm in size, as observed in TEM images (**Figure 9**). This suggests that the hydrogen treatment process affects not only the crystallinity and distribution of the tin particles but also their size, potentially influencing the overall electrochemical performance of the material.

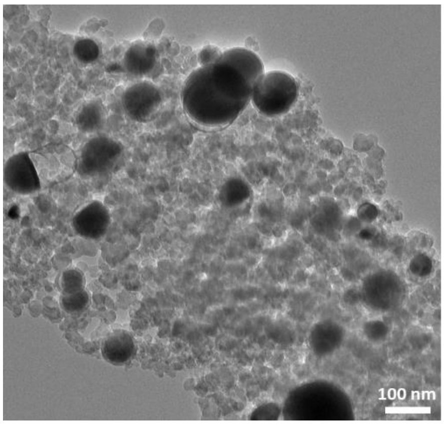

Figure 9. TEM image showing the Sn(30wt%)@C composite after hydrogen treatment, exhibiting a core-shell structure with an uneven distribution within the carbon matrix.

The high-resolution transmission electron microscopy (HRTEM) image showcases the turbostratic graphitic configuration of carbon encasing the tin nanoparticles. This graphitic arrangement is corroborated by Raman spectroscopy data presented in **Figure**

10, which features prominent peaks at 1345 cm^{-1} and 1580 cm^{-1}, representing the disordered (sp^3-hybridized) and graphitic (sp^2-hybridized) forms of carbon, respectively. Notably, the graphitic peak's intensity increases, denoted by an I_D/I_G ratio of 0.987 for the hydrogen-treated Sn@C, as opposed to a ratio of 1.020 for the carbon soot (CS).[31] This enhancement suggests that tin's presence promotes the in-situ conversion of carbon soot to a more graphitic form. Also, post-hydrogen treatment, the I_D/I_G ratio is lowered to 0.987 from 0.999, indicating a reduction in carbon defects or functional groups.

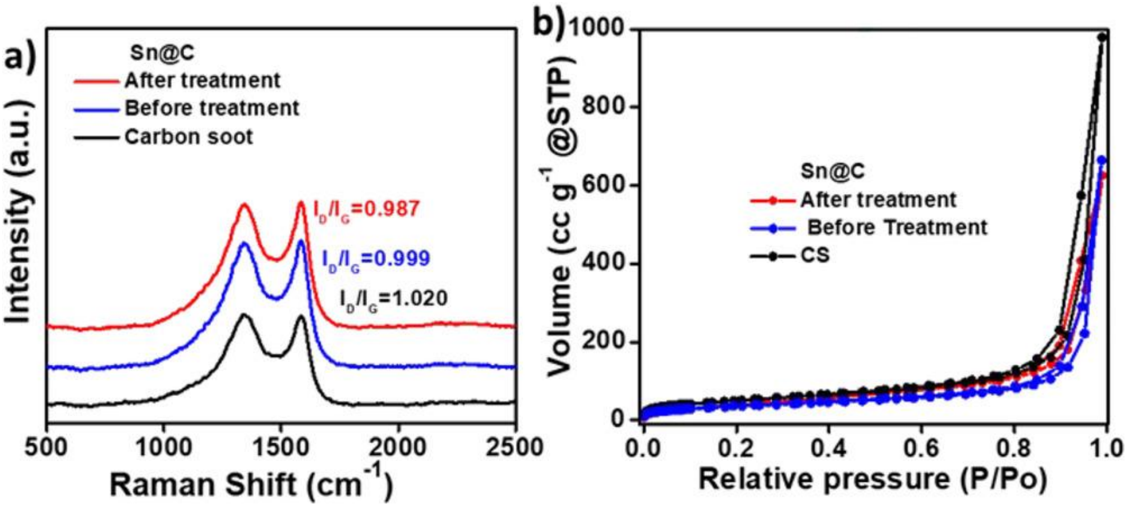

Figure 10. (a) Raman spectra display the distinctive D and G bands, and (b) BET (Brunauer–Emmett–Teller) plot contrasts the Sn@C samples before and after hydrogen treatment with CS.

Nitrogen adsorption-desorption analysis, performed at the temperature of liquid nitrogen (77K), reveals a type II isotherm, with hysteresis evident at elevated relative pressures (p/p_0), hinting at mesopore formation due to the aggregation of carbon nanoparticles, as depicted in **Figure 10b**. The pore size distribution, calculated using the quenched solid density functional theory (QSDFT)[32] and illustrated in **Figure 11**, indicates a broad range of meso and micropores. Surface area measurements via the Brunauer-Emmett-Teller (BET) method show that the as-prepared Sn@C possesses a surface area of 127 m^2 g^{-1}, which increases to 159 m^2 g^{-1} following hydrogen treatment, reflecting an augmentation in specific surface area consequent to structural modifications.

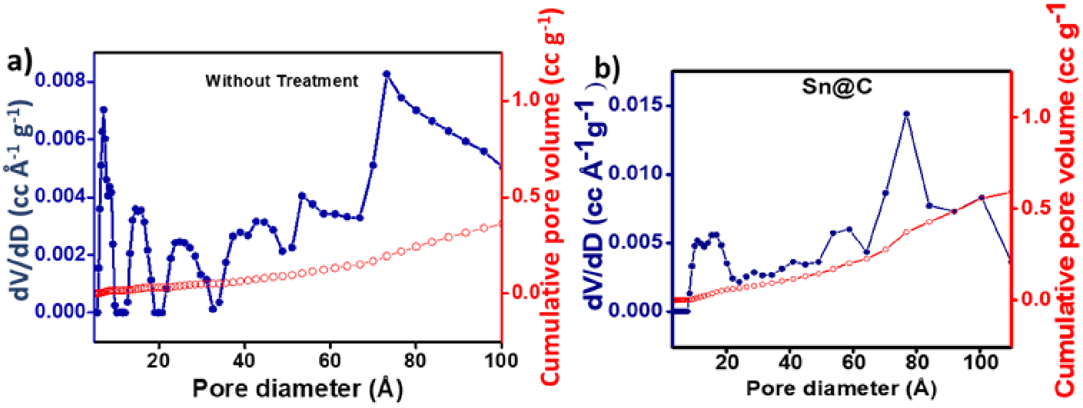

Figure 11. Distribution of pore sizes in the Sn@C composite: a) before and b) after hydrogen treatment.

The X-ray photoelectron spectroscopy (XPS) analyses helped to decipher the chemical states and the nature of oxygen bonds in the Sn@C composite before and after the hydrogen reduction treatment. The O1s XPS spectra (**Figures 12a and 12d**) delineate the peaks corresponding to oxygen bound within the Sn-O-C configurations. A notable decrease in the intensity of these linkages was observed after the reduction process, suggesting a decrease in the oxygenated species on the surface of the Sn nanoparticles.

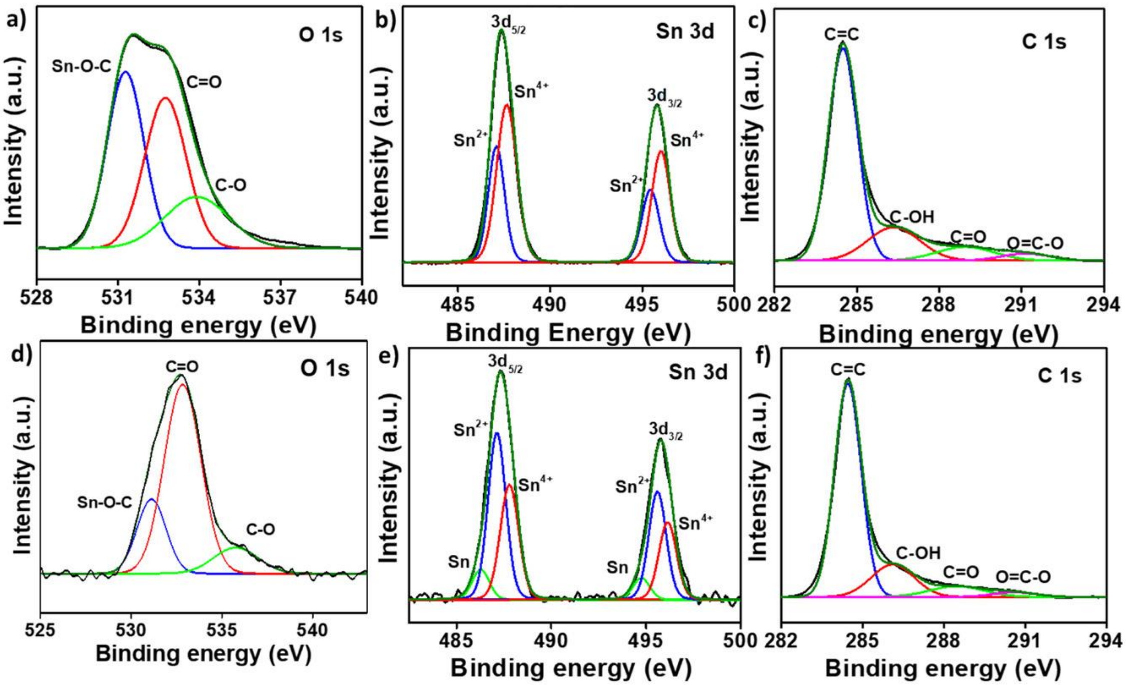

Figure 12. XPS spectra for the Sn@C composite: (a-c) as-prepared and (d-f) after hydrogen treatment, corresponding to (a, d) O 1s, (b, e) Sn 3d, and (c, f) C 1s.

In the Sn3d scans of the hydrogen-treated sample (**Figure 12e**), peaks are indicative of different tin oxidation states: metallic Sn (Sn^0), divalent tin (Sn^{2+}), and tetravalent tin

(Sn^{4+}). The untreated Sn@C sample (**Figure 12b**) lacks a Sn metallic peak. The binding energies at 487.1 eV and 495.6 eV for $Sn3d_{5/2}$ and $Sn3d_{3/2}$, respectively, are characteristic of Sn^{2+} species, while the slightly higher energies of 487.7 eV and 496.1 eV are for Sn^{4+} species (**Figure 12e**).[33] A decrease in the intensity of Sn^{4+}/Sn^{2+} from 0.71 to 0.58 was observed after hydrogen treatment.

Additionally, the C1s XPS spectra (**Figures 12c and 12f**) were deconvoluted to identify the carbon bonding environments. A distinct peak for sp^2 hybridized carbon (C=C) is visible at 284.8 eV, and there are peaks for various oxygen-carbon bonds (C-OH, C=O, and O-C=O). However, these appear at lower intensity after hydrogen is annealed, signifying a reduction of oxygenated functional groups on the carbon. This finding agrees with the Raman analysis, which indicated an increase in graphitization of the carbon material post-hydrogen treatment. This is another indicator that the hydrogen reduction treatment affects the tin particles and alters the carbon matrix, enhancing its graphitic nature and potentially its electrical conductivity.

The electrochemical performance of the hydrogen-treated Sn@C composite was thoroughly investigated using a series of tests in a half-cell configuration with a mass loading of 0.8 mg cm^{-2} at ambient temperature. Cyclic voltammetry (CV) at a scan rate of 0.1 mV s^{-1} was conducted within a voltage window of 0.01V to 3.0V, as shown in **Figure 13a**. The initial cycle revealed a broad, irreversible reduction peak around 1.2V, indicative of solid electrolyte interphase (SEI) formation or the generation of Li_2O.

Upon further cycling, the CV profiles began to overlap from the second cycle onward, indicating the stabilization of the SEI layer. On discharging, the reduction peak at 1.18V is consistent with lithium insertion into the graphitic structure of the carbon.[34] This is followed by additional peaks at 0.63V and 0.39V, attributed to the formation of different Li_xSn_y alloy phases. Charging revealed peaks at 0.54V, 0.62V, 0.72V, and 0.79V, aligning with the dealloying process of Li from different Li-Sn compounds back to Sn metal.[35] The overlap of peaks indicates a reversible electrochemical process for the lithiation and delithiation of Sn, a promising sign for the stability of the battery.

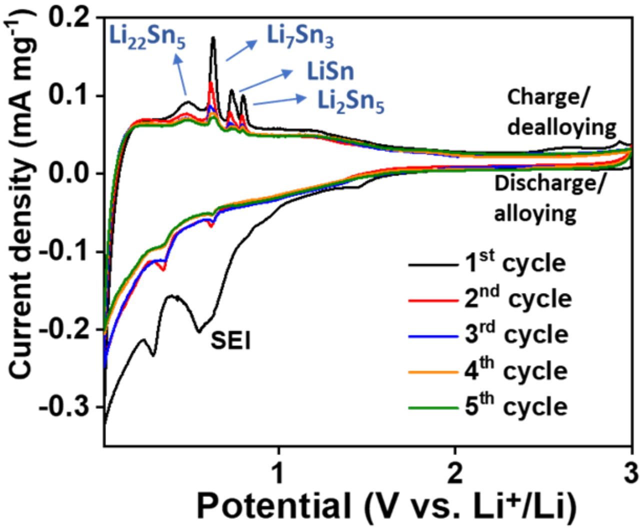

Figure 13. Electrochemical analysis of the hydrogen-treated Sn@C composite includes (a) Cyclic voltammograms at a scan rate of 0.1 mV s^{-1}.

Electrochemical Impedance Spectroscopy (EIS) was carried out to provide insights into the kinetic processes, as shown in **Figure 14**.

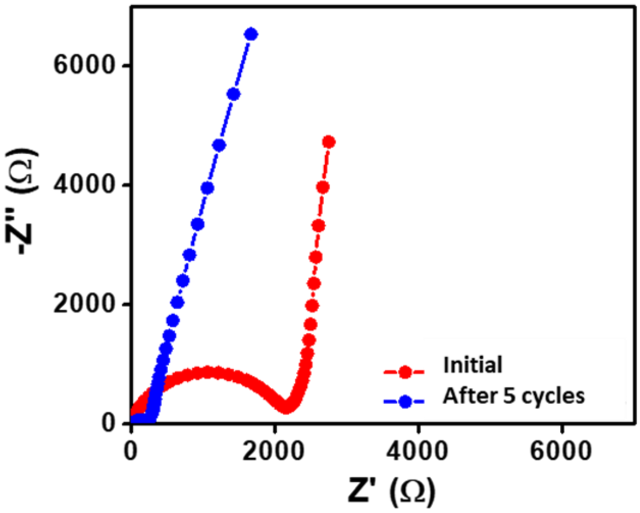

Figure 14. Nyquist plots before and after 5 cyclic voltammetry (CV) cycles.

An equivalent circuit fit (**Figure 15**) for Nyquist plots from different circuit element possibilities matches the impedance data. The fitted circuit involves ohmic resistance, charge transfer, and mass transfer processes at the interface. The ohmic resistance (Rs) is a contribution from the electrical connections, the cell connections, the current collector, etc. The SEI film formed at the interface of anode material and electrolyte (Sn@C/SEI and SEI/electrolyte, respectively) contributes to charge transfer resistance

(R_{SEI}) and capacitance (C_{SEI}). The charge transfer of Li^+ with Sn@C contributes to R_{CT}. Finally, the mass transfer limitation from the lithium-ion diffusion process is affected by the electronic conductivity of Sn@C (active material), diffusion pathways in Sn@C, and electrolyte resistance. An equivalent circuit fit model can define the combination of all these interfacial processes.

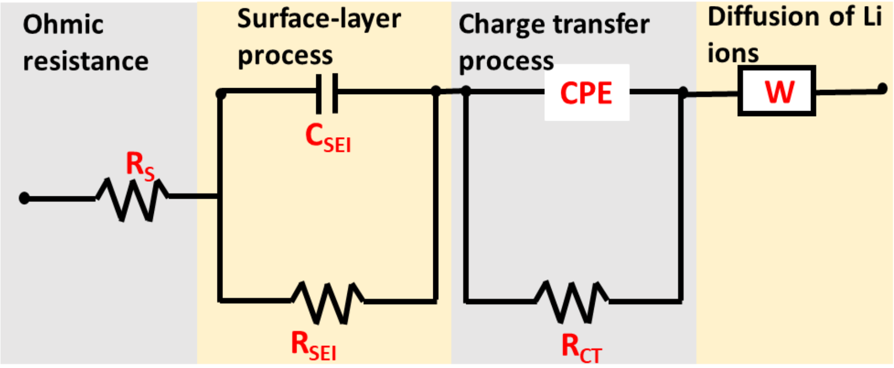

Figure 15. A schematic representation of an equivalent circuit for the hydrogen-annealed Sn@C.

The Nyquist plot shown in **Figure 14** depicts that a relatively high charge transfer resistance (RCT) of 2150 Ω was observed prior to cycling, which significantly reduces to 242 Ω after five cycles of CV. This substantial reduction in R_{CT} can be attributed to the formation and stabilization of the SEI layer. The low-frequency behavior indicated by EIS suggests that diffusion processes are the primary contributors to the electrochemical activity after cycling and changes from capacitive to diffusive behavior after SEI stabilization.

Subsequently, the galvanostatic cycling profile (**Figure 16b**) shows superior cycling stability at a current density of 300 mA g^{-1} for 300 cycles with 0.8 mg cm^{-2} mass loading. The initial discharge value is 305 mA h g^{-1}, and even after 300 cycles, discharge capacity is retained to a value of 281 mA h g^{-1} with an exceptional Coulombic efficiency of 98.6%. Sn@C composite achieves better capacity than graphite-based anodes.[36] Capacity retention of 92.1% was attained, showing superior structural stability upon cycling. The Nyquist plot better understands this cycling stability (**Figure 16c**). No significant change in R_{CT} values was observed from 200 to 300 cycles. This result suggests that on cycling, minimal polarization losses and facile charge transfer kinetics due to stabilized SEI and the highly graphitized carbon are observed.

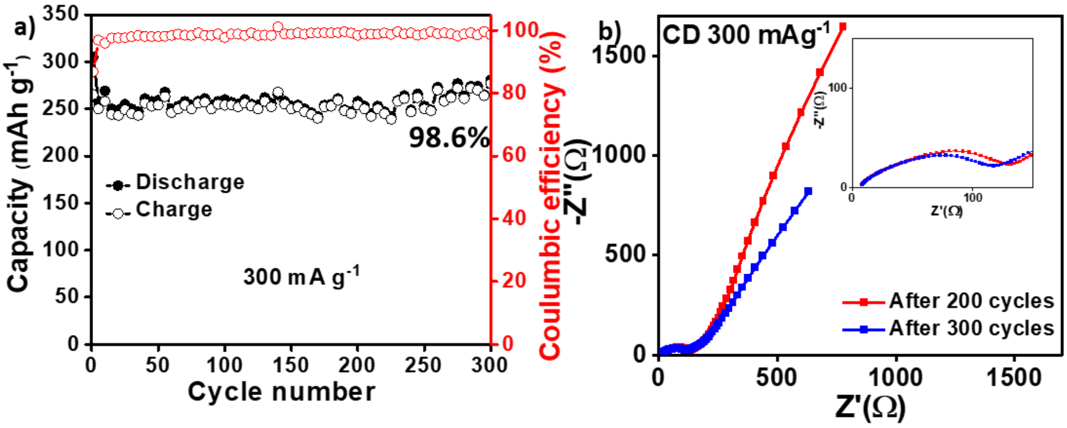

Figure 16. Charge-discharge profiles following CV activation at (c) 300 mA g^{-1}. (d) Nyquist plot demonstrating stable cyclability at 300 mA g^{-1}.

At a higher loading of 2 mg cm^{-2}, Sn@C hydrogen treated shows 77% capacity retention at 300 mA g^{-1}, as shown in **Figure 17**.

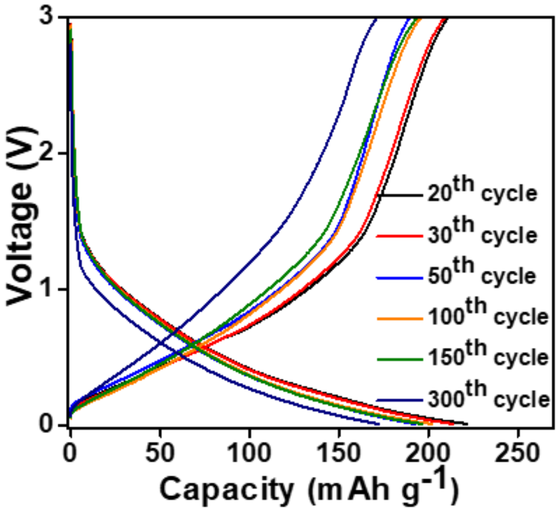

Figure 17. Galvanostatic charge-discharge at higher mass loading of 2mg cm^{-2} at 300mA g^{-1}.

After five cyclic voltammetry (CV) cycles, electrochemical analysis at a higher current density was carried out, as shown in **Figure 18**. The initial discharge capacity was observed at 184 mA h g^{-1}, and impressively, % capacity retention of 94% was maintained at 174 mA h g^{-1} even after 700 cycles. The increase in current density revealed the limitations in mass and charge transfer processes, which are affected by the limited electrochemical utilization of the tin within the composite.

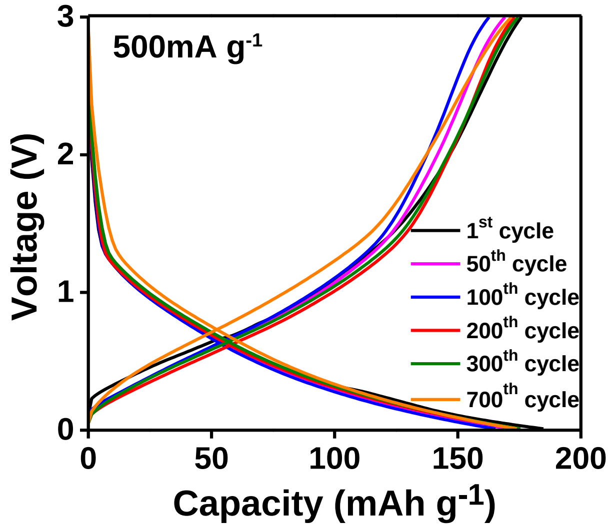

Figure 18. Galvanostatic charging and discharging at 500 mA g^{-1}, following 5 cyclic voltammetry cycles (CV).

Further examination after five CV cycles at an even higher current density of 1 A g^{-1}, as represented in **Figure 19**, demonstrated an initial discharge capacity of 273 mA h g^{-1}, maintaining 86.8% capacity after 100 cycles.

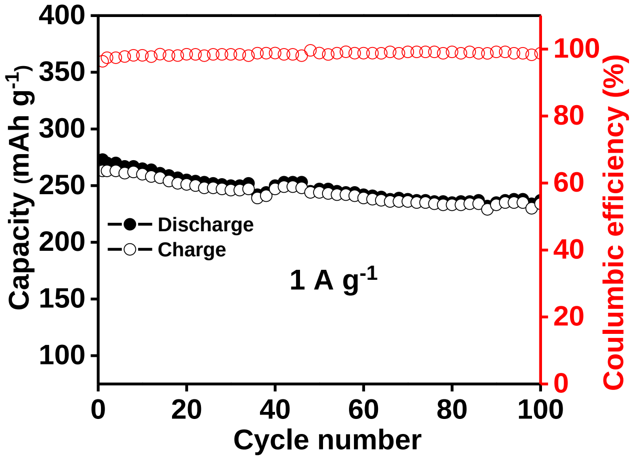

Figure 19. Charge discharge of hydrogen annealed Sn@C composite at a high current density of 1 A g^{-1}.

The rate capability, illustrated in **Figure 20**, indicated a high initial lithiation capacity of 1122 mA h g^{-1} at a current density of 20 mA g^{-1}, with a subsequent delithiation capacity of 842 mA h g^{-1}. The initial cycle's Coulombic efficiency of 75% was ascribed to SEI layer formation, a consequence of electrolyte decomposition, especially prevalent due to the high surface area of the hydrogen-treated Sn@C composite (159 m^2 g^{-1}). The rate performance of Sn@C after hydrogen treatment showed a high-capacity value of 706 mAh g^{-1} compared to the value (488 mAh g^{-1} at 20 mA g^{-1}) obtained for Sn@C before hydrogen treatment. When tested at a current density of 300 mA g^{-1}, the discharge capacity dropped to 392 mA h g^{-1}. The reduced SnO_2 content and the higher graphitized carbon (sp^2 hybridized C=C bonds) at 284.8 eV, as revealed by XPS analysis, enhanced the lithiation capacity.

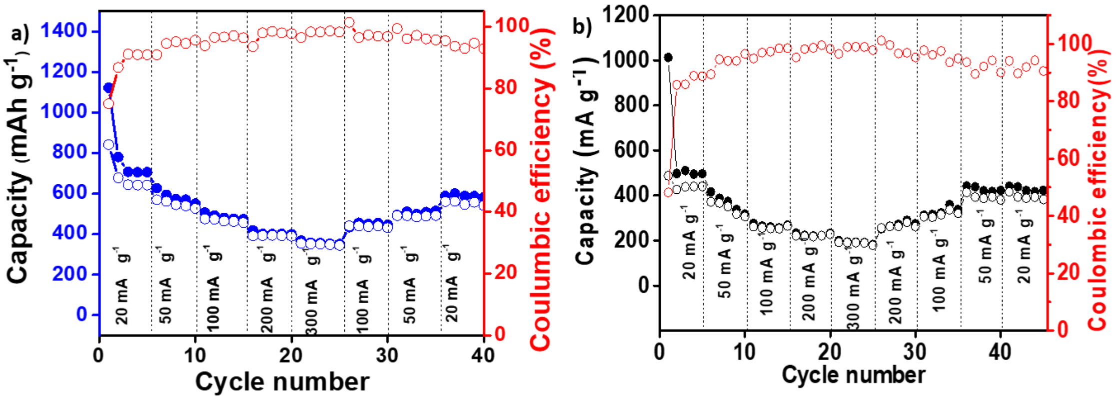

Figure 20. The rate capability of (b) hydrogen-treated and (c) as-prepared Sn@C samples.

Comparative analysis of lithiation capacities between the first and 40th cycles at the same current density indicated a capacity retention of 64%. A notable capacity retention of 82% was evident between the third and 40th cycles, after SEI layer formation, showcasing the long-term electrochemical stability of the system. The robust adherence of tin to the carbon matrix and hollow space between Sn and C (core-shell morphology) mitigated the volume expansion and prevented aggregation of the tin particles. This contributes to the structural integrity and operational stability of the battery.

Post-SEI stabilization, cycling at the current density of 20 mA g^{-1}, PXRD patterns were recorded and presented in **Figure 21**. The results corroborated the high reversibility of the electrode due to the intimate presence of tin nanoparticles in contact with carbon.

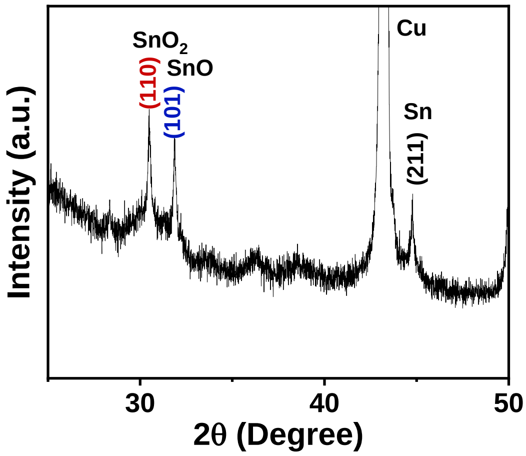

Figure 21. Powder X-ray diffraction pattern of hydrogen-annealed Sn@C, following 5 cycles at a current density of 20 mA g^{-1}.

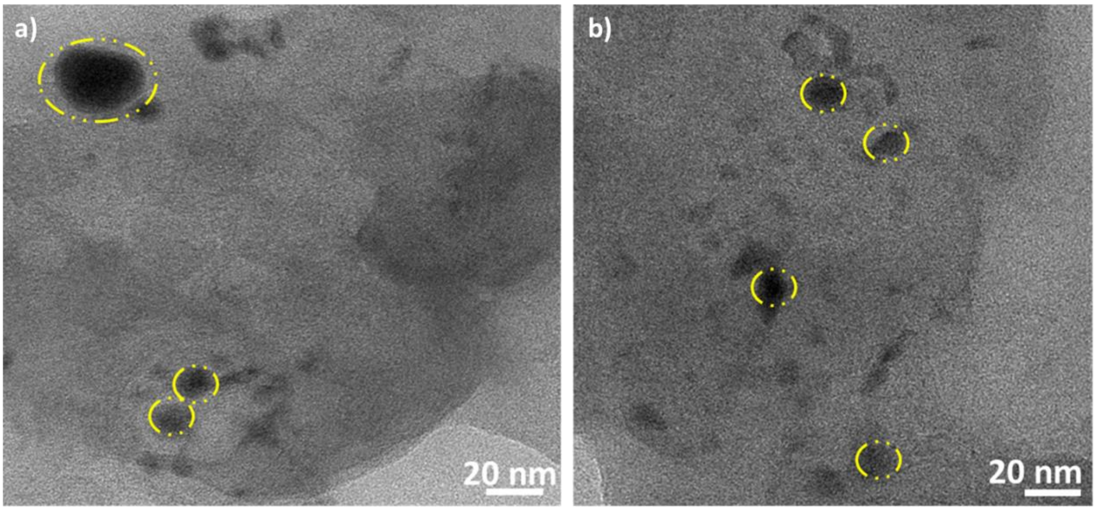

Figure 22. Post cycling TEM image of Sn@C hydrogen annealed.

The heightened structural stability conferred by the hydrogen treatment was observed by TEM after 50 cycles at a current density of 100 mA g^{-1}, displayed in **Figure 22**. The images are consistent with the pristine condition depicted in **Figures 5-7. T**he TEM images confirmed that tin nanoparticles remained well-integrated within the carbon matrix.

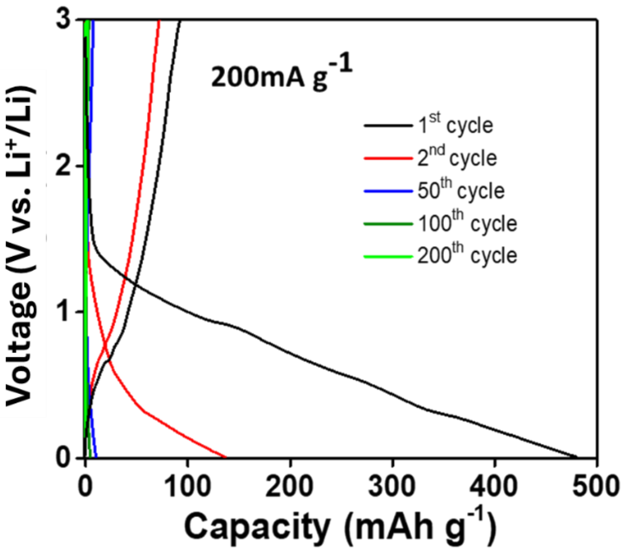

Figure 23. Charging and discharging at 200 mA g^{-1} leads to quick capacity loss in hydrogen-annealed Sn(30wt%)@C.

For the hydrogen-treated Sn(30 wt%)/C composite, characterized in **Figure 23**, charge-discharge cycles were performed at an increased current density of 200 mA g^{-1}. During these cycles, a pronounced capacity fading was observed. This decline in capacity can be attributed to the extended transport paths required for lithium ions (Li^+) and electrons to navigate through the crystal structure. Furthermore, the large tin particles, ranging from 50 to 100 nm as determined by transmission electron microscopy (TEM), are susceptible to mechanical pulverization under the stresses of lithiation and delithiation. The resultant volumetric changes from this process can lead to the fracturing the Sn@C composite's coating. Such cracking can cause the particles to lose their electrical connectivity with the carbonaceous substrate, effectively serving as the current collector. The physical disconnection impedes the efficient transfer of electrons, leading to a diminished capacity as the active material becomes electrochemically isolated. This phenomenon underlines the challenges in maintaining structural integrity and electrochemical performance in composite anodes with high active material content, especially under higher rate conditions.

1.3.5 Conclusion

The study presents a tin-carbon composite anode material with notable electrochemical stability and high-capacity retention, i.e., 98.6% over 300 cycles and 94.6% over 700 cycles at 300 mA g^{-1} and 500 mA g$^{-1,}$ respectively, for lithium-ion batteries. This performance is attributed to the efficient containment of tin nanoparticles within a conductive graphitic matrix, mitigating the usual volume expansion issues. The findings suggest significant potential for the Sn@C composite to enhance the durability and capacity of lithium-ion battery anodes.

1.3.6 References:

1. Manthiram, A. (2024) An Outlook on Lithium Ion Battery Technology. **22**, 49.

2. Lübke, M., Howard, D., Armer, C.F., Gardecka, A.J., Lowe, A., Reddy, M. V., Liu, Z., and Darr, J.A. (2017) High energy lithium ion battery electrode materials; enhanced charge storage via both alloying and insertion processes. *Electrochim Acta*, **231**, 247–254.

3. Heubner, C., Liebmann, T., Voigt, K., Weiser, M., Matthey, B., Junker, N., Lämmel, C., Schneider, M., and Michaelis, A. (2018) Scalable Fabrication of Nanostructured Tin Oxide Anodes for High-Energy Lithium-Ion Batteries. *ACS Appl Mater Interfaces*, **10** (32), 27019–27029.

4. Tian, H., Liang, Y., Repac, J., Zhang, S., Luo, C., Liou, S.C., Wang, G., Ehrman, S.H., and Han, W. (2018) Rational Design of Core-Shell-Structured Particles by a One-Step and Template-Free Process for High-Performance Lithium/Sodium-Ion Batteries. *Journal of Physical Chemistry C*, **122** (39), 22232–22240.

5. Roy, K., Wahid, M., Puthusseri, D., Patrike, A., Muduli, S., Vaidhyanathan, R., and Ogale, S. (2018) High capacity, power density and cycling stability of silicon Li-ion battery anodes with a few layer black phosphorus additive. *Sustain Energy Fuels*, **3** (1), 245–250.

6. Wang, B., Ryu, J., Choi, S., Zhang, X., Pribat, D., Li, X., Zhi, L., Park, S., and Ruoff, R.S. (2019) Ultrafast-charging silicon-based coral-like network anodes for lithium-ion batteries with high energy and power densities. *ACS Nano*, **13** (2), 2307–2315.

7. Kennedy, T., Brandon, M., Ryan, K.M., Kennedy, T., Brandon, M., and Ryan, K.M. (2016) Advances in the Application of Silicon and Germanium Nanowires for High-Performance Lithium-Ion Batteries. *Advanced Materials*, **28** (27), 5696–5704.

8. Mo, R., Lei, Z., Rooney, D., and Sun, K. (2019) Three-Dimensional Double-Walled Ultrathin Graphite Tube Conductive Scaffold with Encapsulated Germanium Nanoparticles as a High-Areal-Capacity and Cycle-Stable Anode for Lithium-Ion Batteries. *ACS Nano*, **13** (7), 7536–7544.

9. Nithyadharseni, P., Abhilash, K.P., Petnikota, S., Anilkumar, M.R., Jose, R., Ozoemena, K.I., Vijayaraghavan, R., Kulkarni, P., Balakrishna, G., Chowdari, B.V.R., Adams, S., and Reddy, M. V. (2017) Synthesis and Lithium Storage Properties of Zn, Co and Mg doped SnO2 Nano Materials. *Electrochim Acta*, **247**, 358–370.

10. Otero, M., Heim, C., Leiva, E.P.M., Wagner, N., and Friedrich, A. (2018) Design-Considerations regarding Silicon/Graphite and Tin/Graphite Composite Electrodes for Lithium-Ion Batteries. *Scientific Reports 2018 8:1*, **8** (1), 1–10.

11. Hau Seng, K., Park, M.-H., Ping Guo, Z., Kun Liu, H., Cho, J., Seng, K.H., Guo, Z.P., Liu, H.K., Park, M., and Cho, J. (2012) Self-Assembled Germanium/Carbon Nanostructures as High-Power Anode Material for the Lithium-Ion Battery. *Angewandte Chemie International Edition*, **51** (23), 5657–5661.

12. Vázquez-López, A., Maestre, D., Ramírez-Castellanos, J., González-Calbet, J.M., Píš, I., Nappini, S., Yuca, N., and Cremades, A. (2020) Influence of doping and controlled Sn charge state on the properties and performance of SnO2 nanoparticles as anodes in Li-ion batteries. *Journal of Physical Chemistry C*, **124** (34), 18490–18501.

13. Hu, R., Chen, D., Waller, G., Ouyang, Y., Chen, Y., Zhao, B., Rainwater, B., Yang, C., Zhu, M., and Liu, M. (2016) Dramatically enhanced reversibility of Li2O in SnO2-based electrodes: the effect of nanostructure on high initial reversible capacity. *Energy Environ Sci*, **9** (2), 595–603.

14. Shin, J.H., and Song, J.Y. (2016) Electrochemical properties of sn-decorated SnO nanobranches as an anode of Li-ion battery. *Nano Converg*, **3** (1), 1–7.

15. Im, H.S., Cho, Y.J., Lim, Y.R., Jung, C.S., Jang, D.M., Park, J., Shojaei, F., and Kang, H.S. (2013) Phase evolution of tin nanocrystals in lithium ion batteries. *ACS Nano*, **7** (12), 11103–11111.

16. Whiteley, J.M., Kim, J.W., Kang, C.S., Cho, J.S., Oh, K.H., and Lee, S.-H. (2015) Tin Networked Electrode Providing Enhanced Volumetric Capacity and Pressureless Operation for All-Solid-State Li-Ion Batteries. *J Electrochem Soc*, **162** (4), A711–A715.

17. Wang, J., Fan, F., Liu, Y., Jungjohann, K.L., Lee, S.W., Mao, S.X., Liu, X., and Zhu, T. (2014) Structural Evolution and Pulverization of Tin Nanoparticles during Lithiation-Delithiation Cycling. *J Electrochem Soc*, **161** (11), F3019–F3024.

18. Wolfenstine, J., Allen, J.L., Read, J., and Foster, D. (2006) Chemistry and Structure of Sony's Nexelion Li-ion Electrode Materials.

19. Bresser, D., Mueller, F., Buchholz, D., Paillard, E., and Passerini, S. (2014) Embedding tin nanoparticles in micron-sized disordered carbon for lithium- and sodium-ion anodes. *Electrochim Acta*, **128**, 163–171.

20. McCoy, D.E., Feo, T., Harvey, T.A., and Prum, R.O. (2018) Structural absorption by barbule microstructures of super black bird of paradise feathers. *Nature Communications 2017 9:1*, **9** (1), 1–8.

21. Weeks, J.A., Sun, H.H., Srinivasan, H.S., Burrow, J.N., Guerrera, J. V., Meyerson, M.L., Dolocan, A., Heller, A., and Mullins, C.B. (2019) Facile Synthesis of a Tin Oxide-Carbon Composite Lithium-Ion Battery Anode with High Capacity Retention. *ACS Appl Energy Mater*, **2** (10), 7244–7255.

22. Babu, B., Lashmi, P.G., and Shaijumon, M.M. (2016) Li-ion capacitor based on activated rice husk derived porous carbon with improved electrochemical performance. *Electrochim Acta*, **211**, 289–296.

23. Paul, R., Etacheri, V., Pol, V.G., Hu, J., and Fisher, T.S. (2016) Highly porous three-dimensional carbon nanotube foam as a freestanding anode for a lithium-ion battery. *RSC Adv*, **6** (83), 79734–79744.

24. Kakunuri, M., and Sharma, C.S. (2015) Candle Soot derived Fractal-like Carbon Nanoparticles Network as High-Rate Lithium Ion Battery Anode Material. *Electrochim Acta*, **180**, 353–359.

25. Singh, D.K., Chakraborty, S., Saha, A., Sampath, S., and Eswaramoorthy, M. (2018) Pick a Wick: A Simple, Ultrafast Combustion Synthesis of Co3O4 Dispersed Carbon for Enhanced Oxygen Evolution Kinetics. *ACS Appl Energy Mater*, **1** (9), 4448–4452.

26. Jahel, A., Ghimbeu, C.M., Monconduit, L., and Vix-Guterl, C. (2014) Confined Ultrasmall SnO2 Particles in Micro/Mesoporous Carbon as an Extremely Long

Cycle-Life Anode Material for Li-Ion Batteries. *Adv Energy Mater*, **4** (11), 1400025.

27. Liang, J., Yu, X.Y., Zhou, H., Wu, H. Bin, Ding, S., and Lou, X.W. (2014) Bowl-like SnO2@Carbon Hollow Particles as an Advanced Anode Material for Lithium-Ion Batteries. *Angewandte Chemie International Edition*, **53** (47), 12803–12807.

28. Al-Wakeel, H.B., Abdul Karim, Z.A., and Al-Kayiem, H.H. (2012) Soot reduction strategy: A review. *Journal of Applied Sciences*, **12** (23), 2338–2345.

29. Mulay, M.R., Chauhan, A., Patel, S., Balakrishnan, V., Halder, A., and Vaish, R. (2019) Candle soot: Journey from a pollutant to a functional material. *Carbon N Y*, **144**, 684–712.

30. Zhang, J., Ma, Z., Jiang, W., Zou, Y., Wang, Y., and Lu, C. (2016) Sandwich-like CNTs@SnO2/SnO/Sn anodes on three-dimensional Ni foam substrate for lithium ion batteries. *Journal of Electroanalytical Chemistry*, **767**, 49–55.

31. Hoekstra, J., Beale, A.M., Soulimani, F., Versluijs-Helder, M., Geus, J.W., and Jenneskens, L.W. (2015) Base metal catalyzed graphitization of cellulose: A combined Raman spectroscopy, temperature-dependent X-ray diffraction and high-resolution transmission electron microscopy study. *Journal of Physical Chemistry C*, **119** (19), 10653–10661.

32. Neimark, A. V., Lin, Y., Ravikovitch, P.I., and Thommes, M. (2009) Quenched solid density functional theory and pore size analysis of micro-mesoporous carbons. *Carbon N Y*, **47** (7), 1617–1628.

33. Paparazzo, E. (2013) On the interpretation of XPS spectra of metal (Pt, Pt–Sn) nanoparticle/graphene systems. *Carbon N Y*, **63**, 578–581.

34. An, W., Fu, J., Mei, S., Xia, L., Li, X., Gu, H., Zhang, X., Gao, B., Chu, P.K., and Huo, K. (2017) Dual carbon layer hybridized mesoporous tin hollow spheres for fast-rechargeable and highly-stable lithium-ion battery anodes. *J Mater Chem A Mater*, **5** (27), 14422–14429.

35. Zhao, L.-F., Hu, Z., Lai, W.-H., Tao, Y., Peng, J., Miao, Z.-C., Wang, Y.-X., Chou, S.-L., Liu, H.-K., Dou, S.-X., Zhao, L.-F.Z., Miao, -C, Zhao, L.-F., Hu, Z., Lai, W.-H., Tao, Y., Peng, J., Wang, Y.-X., Chou, S.-L.H., Liu, -K, and Dou, S.-X.

(2021) Hard Carbon Anodes: Fundamental Understanding and Commercial Perspectives for Na-Ion Batteries beyond Li-Ion and K-Ion Counterparts. *Adv Energy Mater*, **11** (1), 2002704.

36. Huang, X., Cui, S., Chang, J., Hallac, P.B., Fell, C.R., Luo, Y., Metz, B., Jiang, J., Hurley, P.T., Chen, J., Huang, X.K., Cui, S.M., Chang, J.B., Chen, J.H., Hallac, P.B., Fell, C.R., Luo, Y.T., Metz, B., Jiang, J.W., and Hurley, P.T. (2015) A Hierarchical Tin/Carbon Composite as an Anode for Lithium-Ion Batteries with a Long Cycle Life. *Angewandte Chemie International Edition*, **54** (5), 1490–1493.

Chapter – 2.1

Introduction to zinc-gas batteries

Summary

The scientific efforts in developing metal-gas batteries, especially Zn-air and Zn-CO_2 *types, integrate innovation with environmental care. It involves deep analysis of electrochemical reactions, materials science, and challenges like anode and cathode behavior, electrocatalyst design, and performance metrics. The shift from primary to rechargeable Zn-air batteries has advanced Zn-*CO_2 *batteries in sustainable energy storage and carbon capture. However, challenges like dendrite growth, electrode stability, and reaction kinetics persist in zinc-air/*CO_2 *batteries. Overcoming these challenges requires a multidisciplinary approach, focusing on material science and electrochemistry, aiming for better efficiency, scalability, and cost-effectiveness.*

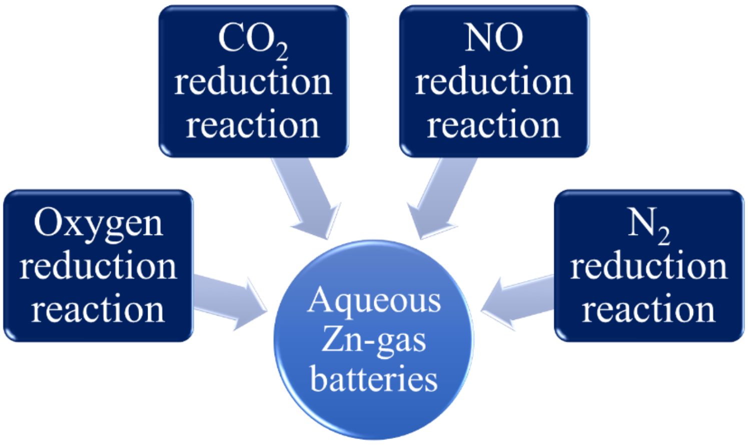

2.1.1 Introduction

Commercialized Li-ion batteries (LIBs) have long dominated the energy storage market, but they face challenges stemming from their high cost, limited energy density, and reliance on flammable organic electrolytes.[1] On the other hand, metal-gas batteries (MGBs) present a promising solution to meet the ever-growing demand for high-energy storage.[2] MGBs are known for their higher theoretical gravimetric energy density than LIBs due to their unique ability to utilize ambient atmospheric gases rather than relying on internal storage. For example, Li-O_2 battery shows an impressive energy density of approximately 3500 Wh kg^{-1}, nearly ten times greater than LIBs.[3] Despite having this apparent edge in gravimetric energy density, the potential for MGBs to outpace LIBs for future electric vehicles (EVs) remains uncertain. This is associated with the slow reduction/oxidation kinetics of gases and rapid catalyst degradation, which may not align with the power and longevity requirements essential for high-power and frequently utilized applications.[4] MGBs have demonstrated significant promise in consumer electronics, especially over the last five years.[2] [5] They are suitable for wearable electronic devices characterized by extended operational lifespans and minimal power consumption.

Various metal-gas couples have been explored extensively for MGBs, as depicted in **Figure 1** and **Table 1**. Metal anode selection for the MGBs is notably broad, encompassing alkali metals (such as Li, Na, and K), alkaline earth metals (including Mg and Al), and first-row transition metals (such as Zn and Fe).[2] Some of the unique features and limitations of various MGBs have been highlighted in **Table 1**.

Zinc-based anodes emerge as the preferred choice among various metal anodes, owing to their distinct advantages in energy storage systems. These advantages are underscored by their ease of handling, robust stability in aqueous environments, and a notably high energy density (1081 Wh kg^{-1}).[6][7] In stark contrast, alkali metal anodes possess drawbacks, primarily stemming from their reliance on aprotic organic electrolytes, which are susceptible to combustion risks, and their susceptibility to poor reversibility issues. The latter is attributed to the accumulation of discharge products on the cathode, leading to a discernible degradation in battery performance.[8] Regarding alkaline earth metal anodes, a noteworthy limitation pertains to their propensity for surface passivation when exposed to aqueous or alkaline media[9], a characteristic elucidated in **Table 1**. The amalgamation of these distinctive advantages of zinc-based anodes, coupled with the economic feasibility of zinc itself, has propelled the commercialization of Zn-air batteries.[10] These batteries have found application niches in medical and telecommunication devices, serving as power sources for miniature hearing aids, cardiac range finder monitors, Bluetooth headphones, and various other portable electronic systems.

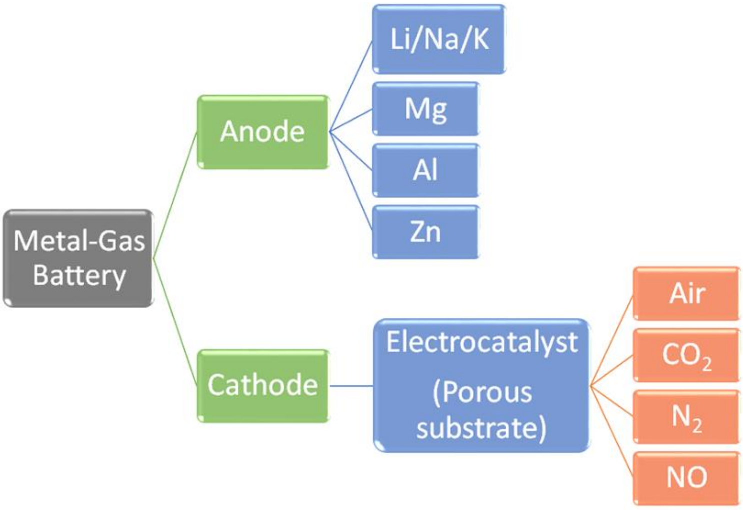

Figure 1. Combination of various metal anodes against gas cathodes for MGBs.[2][11]

Anode	**Electrolyte**	**Gas**	**Advantages**	**Disadvantages**	**Ref.**
Lithium	Organic Electrolyte/ Ionic liquid	Air	High theoretical energy density (11,429 Wh kg^{-1}); Volumetric energy density (2062 Ah L^{-1});	Pure O_2 has to be used (requires O_2 gas storage tank); Moisture sensitive; Instability of electrolyte due to superoxide (discharge product) formation; Formation of electronically insulating Li_2O_2/Li_2O reduces battery performance; High cost (\$400-800/kWh);	[12]
		CO_2	Energy density 1876 Wh kg^{-1}	Poor reversibility (Li_2CO_3+C discharge product accumulates on cathode); high overpotentials (organic electrolyte);	[13]
		N_2	Theoretical energy density (1248 Wh kg^{-1}); NH_3 production	N≡N difficult to break; Poor Faradaic efficiency.	[14]
Magnesium	Organic electrolyte/	Air	High theoretical volumetric energy density (3832 Ah L^{-1});	Self-corrosion of Mg anode (aqueous electrolyte)	[15]

	Aqueous electrolyte		Theoretical gravimetric energy density (2840Wh kg^{-1})		
		CO_2	Low overpotential	Insulating discharge products ($MgCO_3$, MgO/ MgC_2O_4) accumulate on electrode	[16]
Aluminium	Aqueous electrolyte/ Ionic liquid	Air	Low cost (1.9 USD kg^{-1}); Theoretical high energy density (4140 Wh kg^{-1})	Experimental energy density upto 1000Wh kg^{-1}; Very high corrosion (aqueous electrolyte);	[17]
		CO_2	Theoretical energy density: 1461 Wh kg^{-1}; Value added production (Formate; aqueous electrolyte); reversibility in ionic liquid	Reversibility of $Al_2(C_2O_4)_3$ over cycles is not still clear yet.	[18]
		N_2	NH_3 production	Poor Faradaic efficiency;	[19]
Zinc	Aqueous electrolyte	Air	Low cost (currently < $100 kW^{-1} h^{-1} and potential < 10 $ kW^{-1} h^{-1})	Increasing the practical energy density after cycling	[20]
		CO_2	Theoretical energy density (788 Wh kg^{-1}); Rechargeable battery; Value added product from CO_2RR (CO, CH_4, formate, alcohols)	Increasing rechargeability; reducing overpotential for CO_2 reduction and oxidation reaction; increasing energy density	[19]
		NO	NH_3 production; High faradaic efficiency	Primary battery	[21]
		N_2	NH_3 production	Low power and energy density	[22]

Table1. Comparison of metal-gas (gas = air (ambient atmosphere), CO_2, N_2, NO) batteries.

Recent research articles have shed light on a promising avenue within the field of metal-gas batteries, where the substitution of air with alternative gases, such as CO_2, NO, and N_2, offers the potential for concurrent fixation/utilization alongside energy storage. Notably, in the case of the Zn-CO_2 system, the fixation of CO_2 can yield value-added products, including CO, CH_4, HCOOH, and various alcohols.[23,24] Conversely, NO and N_2 gases have the potential to facilitate NH_3 production, a critical factor for applications in agriculture and the chemical industries.[25] This innovative approach of harnessing pollutants or underutilized gases to provide energy and power represents a noteworthy "two birds with one stone" strategy.[11] It is worth noting that the Zn-N_2 battery faces limitations associated with poor faradaic efficiency, and the Zn-NO battery has predominantly been employed in the form of primary batteries.[26] Therefore, the primary research focuses on comprehending the underlying principles of rechargeable zinc-air and zinc-CO_2 batteries.[27] These endeavors hold substantial promise in advancing both energy storage and environmental sustainability.

The rechargeable zinc-air batteries (ZABs) market is poised for significant growth, driven by escalating demand (**Figure 2a**) for electric automobiles and electronic devices.[28] Achieving a near zero-carbon footprint is anticipated to be a pivotal factor propelling the demand for ZABs.[29] In line with this trajectory, the Intergovernmental Panel on Climate Change (IPCC) underscores the substantial role of CO_2 as the primary contributor (76%) to greenhouse gas emissions, which have adverse consequences on climate, ecosystems, and human health (**Figure 2b**).[30] Consequently, the concept of CO_2 fixation, coupled with energy storage to yield value-added chemicals, emerges as a promising approach to attain carbon neutrality while simultaneously addressing the global energy storage requirements.[27] Furthermore, it is noteworthy that Zn-CO_2 batteries hold considerable appeal for research exploration and potential utilization in future missions to Mars, given that the Martian atmosphere comprises an impressive 95% CO_2.[31] This underscores the versatile and cross-disciplinary nature of ZABs, extending their relevance from earthly sustainability goals to extra-terrestrial exploration.

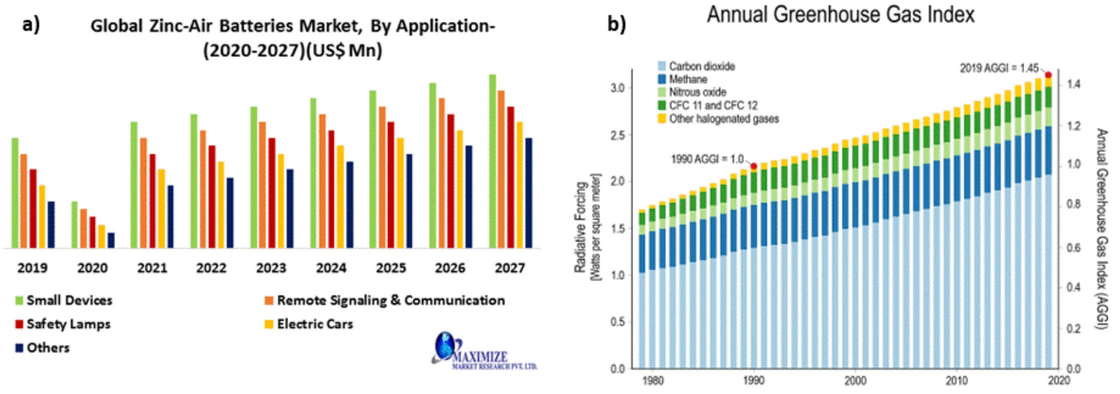

Figure 2. a) Global demand for ZAB[23]. b) Various pollutants contribute to greenhouse gases, CO_2 being the central part of it.

This chapter will delve into an extensive examination of **Zn-air and Zn-CO_2 batteries**, tracing their evolutionary development, elucidating the underlying mechanisms governing their operation, and critically assessing the fundamental challenges that must be surmounted to achieve the pinnacle of battery efficiency.

2.1.2 History

The history of zinc-air batteries (ZABs) is a journey that began in 1878 with Maiche's invention of the first primary ZAB, employing a porous platinized carbon cathode (**Figure 3**).[6] However, it was not until 1932 that commercial ZAB products debuted.[32] Rechargeable Zn-air batteries entered the commercial market in 2012, courtesy of NantEnergy (formerly Fluidic Energy).[33] These early models had a limited energy density, approximately 35 Wh kg^{-1}, as of 2017.

The reversible aqueous Zn-CO_2 battery emerged in 2018, offering a novel approach to reducing carbon emissions while simultaneously generating electricity [27]. Interestingly, until recently, CO_2 was predominantly regarded as a contaminant in Zn-air batteries. However, the use of low-cost metal-CO_2 batteries is poised to trigger a renewable energy revolution.

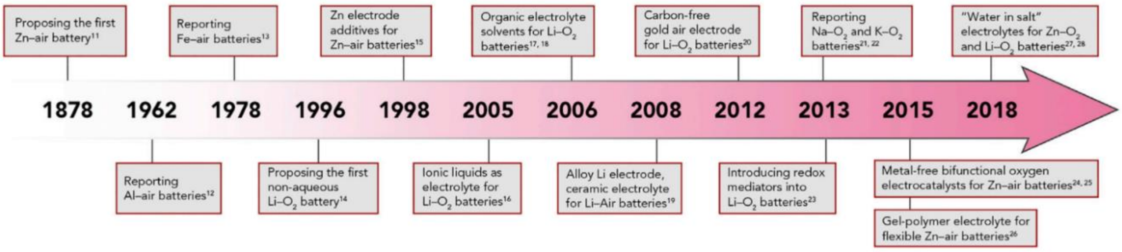

Figure 3. Timeline of scientific exploration in metal-air batteries.[34]

Despite these promising advancements, it is worth noting that neither ZABs nor Zn-CO_2 batteries have achieved commercial recognition for large-scale applications. Consequently, the next section will delve into a comprehensive exploration of the inherent shortcomings of both battery technologies, providing a foundational understanding of the areas that require attention and improvement.

2.1.3 Configuration and principle of Zinc-air and Zn-CO_2 battery

2.1.3.1 Zn-air battery

In zinc-air batteries, oxygen is selectively reduced at the air cathode during the battery's discharge cycle for several reasons.[33] In zinc-air batteries, oxygen from the air is the chosen reactant for the electrochemical reaction because it has a high reduction potential (1.23 V vs. standard hydrogen electrode, pH=7), meaning it readily gains electrons to complete the chemical process needed to generate electricity.[32][35] The catalysts used in these batteries are specifically designed to facilitate the reaction with oxygen while being less reactive to other gases, such as nitrogen, which is more abundant in air but less chemically reactive under standard conditions.[36]

The electrochemical reaction for the Zn-air battery is as follows (**Figure 4a**)[37][38]:

Discharge process:

Cathode (Air electrode): $O_2 + 4e^- + 2H_2O \rightarrow 4OH^-$ E = 0.40V vs. SHE (1)

Anode (Zn): $Zn + 4OH^- \rightarrow Zn(OH)_4^{2-} + 4e^-$ (2)

$Zn(OH)_4^{2-} \rightarrow ZnO + H_2O + 2OH^-$ E = -1.26 vs. SHE (3)

Overall reaction: $2Zn + O_2 \rightarrow 2ZnO$ E_{cell} = 1.65 V vs. SHE
(4)

Charging process:

Cathode: $4OH- \rightarrow O_2 + 4e^- + 2H_2O$ (5)

Anode: $ZnO + H_2O + 4e^- \rightarrow Zn + 2OH^-$ (6)

E is the reduction potential versus standard hydrogen electrode (SHE).

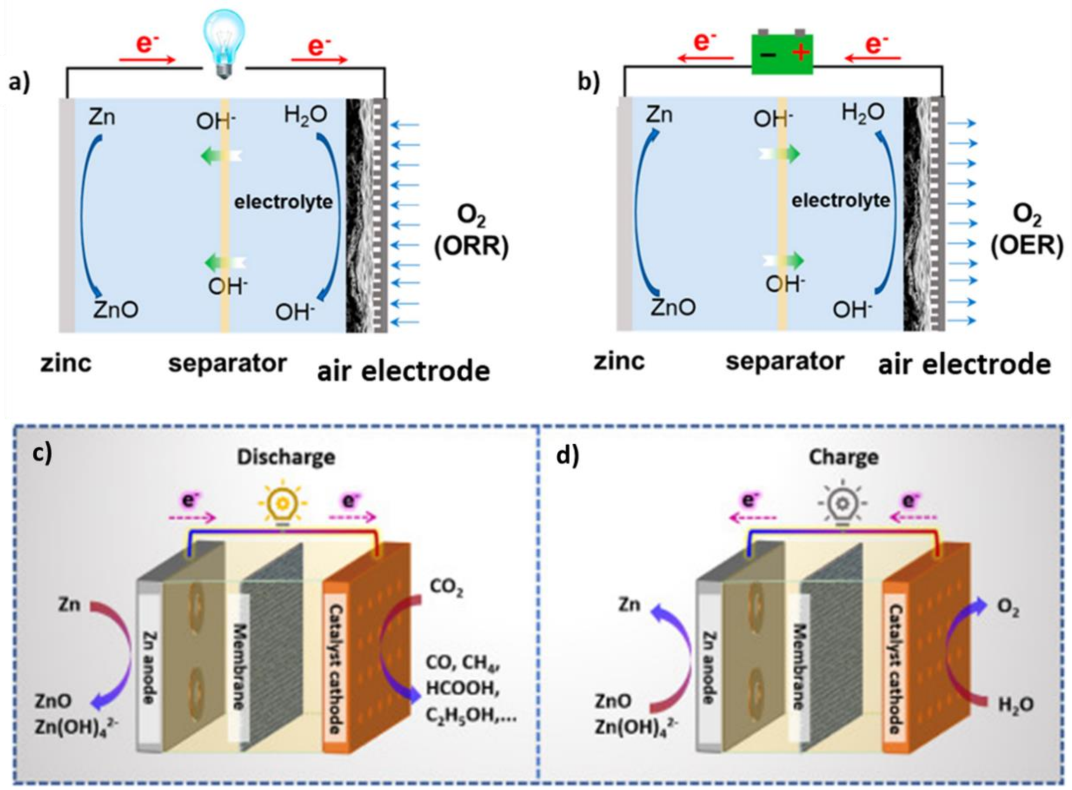

Figure 4. Schematic setup illustration for a) Zn-air battery[39] and b) Zn-CO_2 battery.[40]

During the discharge process, the Zn anode dissolves in a 6M KOH electrolyte and releases electrons to the external circuit. Meanwhile, O_2-to-OH^- conversion (oxygen reduction reaction) occurs on an electrocatalyst on a cathode with the help of electrons supplied from the external circuit.[41] On charging, OH^- converts to O_2, and an oxygen evolution reaction occurs. Therefore, in the reversible aqueous Zn-air battery, oxygen reduction and oxygen evolution reactions are equally important.

2.1.3.2 Zn-CO_2 battery

Although utilizing ambient air is desirable, CO_2 in the air acts as a contaminant that can hamper cathodic reactions by forming K_2CO_3 in 6M KOH, which accumulates on the cathode's surface.[42] To prevent the accumulation of K_2CO_3, CO_2 can be reduced to liquid or gaseous products using an appropriate electrocatalyst to achieve better stability and recyclability for ZABs.[27] This led to the concept of Zn-CO_2 batteries. Zn-CO_2 battery systems offer an intriguing solution that goes beyond merely capturing CO_2 and lowering atmospheric CO_2 concentrations; they can also harness CO_2 to generate valuable carbon-based compounds.

In a typical Zn-CO_2 battery system, the reaction on the anode side (Zn) stays the same, i.e., in 6M KOH (**equation 3**), while on the cathode (electrocatalyst) $KHCO_3$/ NaCl/ NaOH etc. can be used (**Figures 4c and 4d**).[27][43] CO_2 reduction reaction can generate different products such as CO, $HCOO^-$, alcohols, etc., leading to different E_{cell} values (**Table 2**).[44]

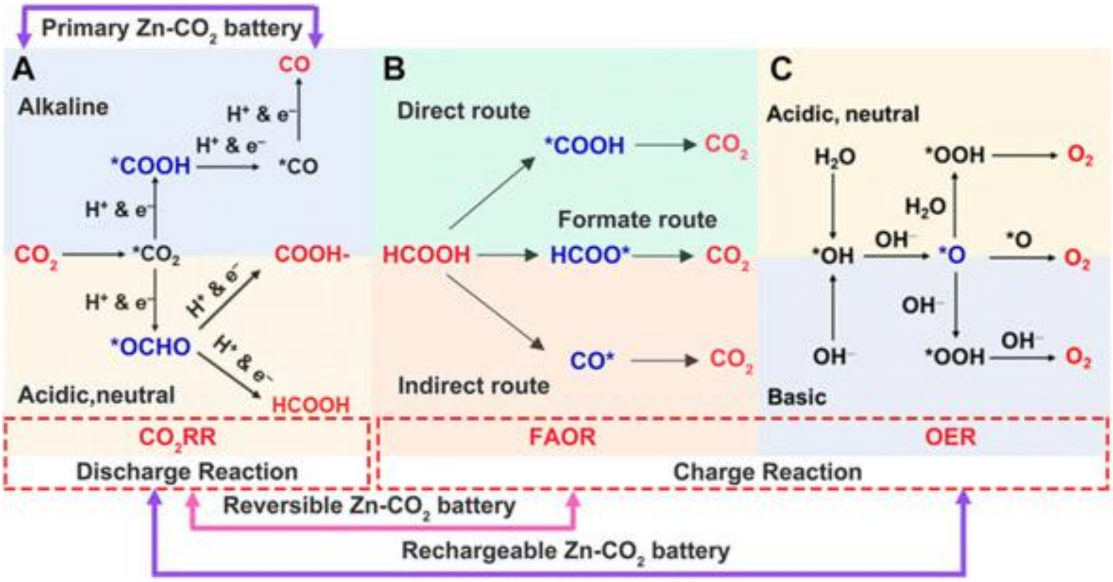

Figure 5. Schematic illustration of Zn-CO2 battery reactions. [45]*Reproduced with permission from reference* [46]

Product	Half-Cell Reaction for Cathode	Overall Reaction	E° (V) at 25°C
Carbon Monoxide (CO)	Discharge: $CO_2 + 2H^+ + 2e^- \rightarrow CO + H_2O$ E = -0.5 V Charge: $H_2O \rightarrow 1/2O_2 + 2H^+ + 2e^-$ E = 0.8 V vs. SHE	$Zn + CO_2 + 2H^+ + 4OH- \rightarrow Zn(OH)_4^{2-} + CO + H_2O$	E_{cell} = 0.74 V
Formic Acid (HCOOH)	Discharge: $CO_2 + 2H^+ + 2e- \rightarrow HCOOH$ E = -0.29V Charge: $HCOOH \rightarrow CO_2 + 2H^+ + 2e-$ E = 0.5 V	$Zn + CO_2 + 2H^+ + 4OH^- \rightarrow HCOOH + Zn(OH)_4^{2-}$	E_{cell}= 0.97 V
Hydrogen (H_2) (Side reaction)	Discharge: $2H^+ + 2e^- \rightarrow H_2$ E = -0.343 V	$Zn + 2H^+ + 2OH^- \rightarrow ZnO + H_2 + H_2O$	E_{cell}=0.91V

Table 2. E_{cell} values for CO_2RR and CO_2ER with Zn anode.[44]

i) HCOOH product[27]

The cathodic discharge process can be described as:

$$CO_2 + 2H^+ + 2e- \rightarrow HCOOH \quad (7)$$

Overall reaction:

$$Zn + CO_2 + 2H^+ + 4OH^- \rightarrow HCOOH + Zn(OH)_4^{2-} \qquad E_{cell} = 0.97\ V \quad (9)$$

ii) CO product

For CO_2 to CO conversion, the discharge reaction is as follows:

$$CO_2 + 2H^+ + 2e^- \rightarrow CO + H_2O \qquad E = -0.5\ V\ vs.\ SHE \quad (10)$$

Overall reaction:

$$Zn + CO_2 + 2H^+ + 4OH^- \rightarrow Zn(OH)_4^{2-} + CO + H_2O \qquad E_{cell} = 0.74\ V \quad (11)$$

On charging, in case of gaseous product formation (CO), cathodic reaction may lead to OER, where the reaction is:

$$H_2O \rightarrow 1/2O_2 + 2H^+ + 2e^- \qquad E = 0.8\ V\ vs.\ SHE \quad (12)$$

Overall reaction:

$Zn(OH)_4^{2-}$ + H_2O $\rightarrow$ $Zn + 1/2O_2 + 2H^+ + 4OH^-$ $E_{cell} = 2.06$ V vs. SHE (13)

iii) Side reaction (H_2)

In the discharge process, hydrogen evolution reaction (HER) competes with CO_2 to HCOOH/CO conversion. The side-reaction is as follows:

$2H^+ + 2e^- \rightarrow H_2$ E = -0.343 V vs. SHE (14)

Overall reaction:

$Zn + 2H^+ + 2OH^- \rightarrow ZnO + H_2 + H_2O$ $E_{cell} = 0.906$ V vs. SHE (15)

From the above theoretical E_{cell} values, on discharge, the Zn anode provides a driving force of 2.06 V and 0.906 V for CO_2 to $HCOO^-$ and CO, respectively. This enables a spontaneous discharge process for Zn anode dissolution and CO_2 reduction. On charging, HCOOH oxidation occurs, whereas in the case of CO (gaseous product), an oxygen evolution reaction occurs because of the low solubility of CO in an aqueous electrolyte. Additionally, CO_2 reduction to alcohols such as C_2H_5OH involves multiple elementary steps (>2 electrons transfer), each of which involves their individual overpotentials, and therefore, their selectivity is a huge problem.[44] Such multi-proton coupled electron transfer would complicate the discharge process and exhibit low discharge voltage value and low faradaic efficiency of products. Therefore, Zn-CO_2 batteries are mostly convenient for HCOOH formation due to their reversibility compared to CO, C_2H_5OH, and other products.

CO_2 reduction products compete with HER due to the use of aqueous electrolytes. Therefore, product selectivity can be an issue. On the other hand, H_2 is a clean energy source and can be utilized as a promising alternative to finite fossil fuels. Kim et al. proposed to utilize the acidity of CO_2 to produce electricity and H_2 driven by Zn electrooxidation.[47]

2.1.4 Detailed overview of Zn-air/CO_2 batteries

While the theoretical energy density of ZAB and Zn-CO_2 batteries is indeed high, the practical energy density achieved in real-world applications is often limited by various experimental constraints and challenges. These challenges can be attributed to specific limiting reactions occurring on both the anode and cathode sides. On the anode side, one notable instance is the generation of $Zn(OH_4)^{2-}$ (tetrahydroxozincate) when utilizing a 6M KOH electrolyte.[48][49] Concurrently, on the cathode side, substantial overpotentials arise during the ORR and OER, CO_2RR, and CO_2OR (CO_2 oxidation reaction).[49][27] These factors collectively contribute to the observed reduction in practical energy values within these battery systems. A successful reversible battery must have high active material utilization and high rechargeability (several hundred charge-discharge cycles) from the anode and cathode side to compete with existing Li-ion batteries. So, we need to understand individual anode and cathode side electrodes to achieve highly efficient rechargeable batteries.

2.1.4.1 Reversible anode: zinc electrode

The performance of Zn anode-based batteries is limited by four main processes, dendrite growth, shape change, passivation, internal resistance, and HER. These processes are explained in detail: [50]

(i) Dendrite growth

Zinc dendrite formation during the charging process is primarily a consequence of the concentration gradient of $Zn(OH)_4^{2-}$ ions (**Figure 5a**).[51] These dendrites can become brittle, potentially disconnecting from the electrode surface. Such detachment can result in several adverse effects, including capacity loss, potential damage to the separator, and the risk of causing a short circuit within the battery. [52,53]

ii) Shape change

The zinc material undergoes morphological changes due to dissolution while discharging and deposition at different locations during charging cycles.[54,55] As a result, over several charge-discharge cycles, the electrode can experience compaction, as depicted in **Figure 5a.** This densification leads to uneven distribution of the electrical current within the electrode, subsequently impacting the usable capacity of the battery.[56,57]

iii) Passivation and internal resistance

In the context of alkaline Zn-O_2/CO_2 batteries, a common choice is to employ a 6M KOH (or 25 wt.% KOH) electrolyte due to its optimal combination of electrolyte conductivity, as shown in **Figure 5b** and superior redox kinetics for the Zn/Zn^{2+} couple. However, it's essential to note that in long-duration reactions, $Zn(OH)_4^{2-}$ ions can reach a solubility limit, resulting in the formation of non-conductive ZnO on the surface of the zinc electrode.[58,59] This phenomenon increases the internal resistance of the battery, leading to voltage losses during discharge and voltage increases during charging. The dissolution of ZnO is influenced by the concentration of OH^- ions, as evidenced in **Figure 5b**. As the concentration of OH^- ions increases, the dissolution of ZnO becomes more pronounced, further affecting the battery's performance. [56,60]

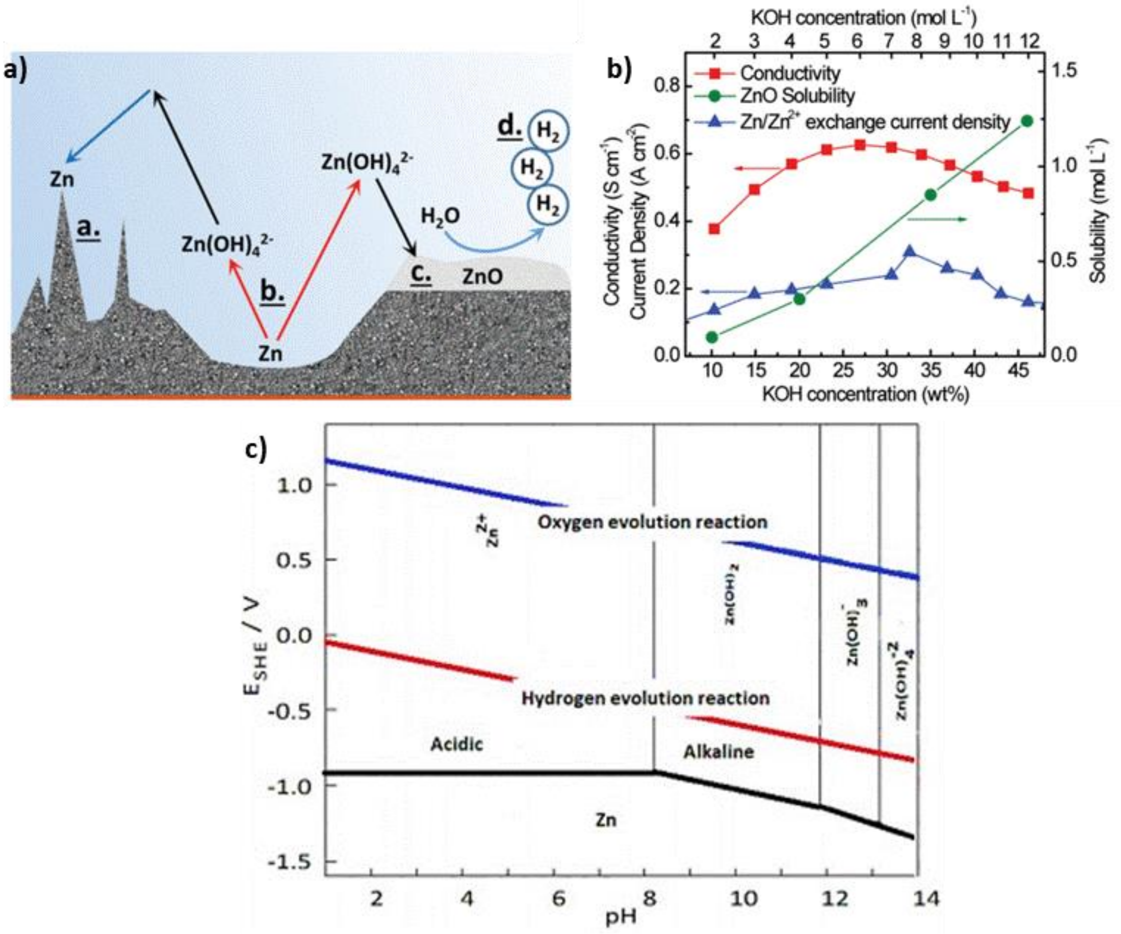

Figure 5. a) Limiting phenomenon on Zn anode/electrolyte interface a. dendrite growth, b. shape change, c. passivation, and d. hydrogen evolution reaction. *Reproduced with permission from reference* [50] b) Variation in conductivity, current density, and ZnO solubility with change in concentration of KOH electrolyte. [50] c) Pourbaix diagram of Zn in acidic and alkaline conditions. *Reproduced with permission from reference* [61]

iv) Hydrogen evolution

The pH conditions play a pivotal role in determining the occurrence of the hydrogen evolution reaction (HER) during the charging process, as illustrated in **Figure 5c**. Specifically, at a high pH of 14, the standard reduction potential of the Zn/ZnO couple (approximately -1.26 V vs. SHE) falls below that of the HER (-0.83 V vs. SHE). [62,63]Consequently, under such alkaline conditions, the HER becomes thermodynamically favorable. Zinc electrodes at rest will gradually undergo corrosion, i.e., self-discharge over time.[28] Consequently, achieving 100% Coulombic efficiency in a rechargeable Zn-based battery becomes challenging.[64]

To address these challenges and enhance the cycle life, capacity, and Coulombic efficiency of Zn-based batteries, various mitigation strategies involving modifications to the Zn electrode surface are being explored. Additionally, in cases where excessive Zn corrosion occurs, mechanical rechargeability can be considered as an option, allowing for the replacement of a spent Zn anode with a fresh one.[50]

2.1.4.2 Reversible Cathode Electrodes

Electrocatalyst-assisted ORR/OER and CO_2RR/CO_2ER reactions occur on the cathode side. The gas electrode consists of an electrocatalyst coated on a gas diffusion layer (GDL) and is connected to a current collector, typically made of stainless-steel mesh or titanium, to ensure efficient electronic connectivity.[65][66] It's important to note that catalyst support is a common feature shared by both ZAB and Zn-CO_2 batteries.

i. Support material for cathode

Heise and Schumacher pioneered the use of wax-treated carbon electrodes in 1932. Subsequently, the gas diffusion electrodes (GDE) with PTFE coating were employed as the air electrode in Zn-air batteries(this sentence is not clear) (**Figure 6**).[67,68] The GDE serves as a crucial triple-phase boundary interface between gas flow, electrocatalyst, and electrolyte.[69] It consists of two distinct layers: a macroporous layer and a microporous layer (MPL).[70] The properties of the GDE, including its mechanical characteristics such as compression, bending, and shear strength, as well as its thermal and electrical properties, are largely determined by the GDE substrate.[71] Meanwhile, the MPL plays a pivotal role in ensuring uniform electrocatalyst deposition and enhancing pore size distribution within the GDL structure.

To optimize its performance, a layer of polytetrafluoroethylene (PTFE) is applied to both sides of the GDE.[72][73] This PTFE coating serves to regulate the degree of hydrophobicity, thereby preventing issues like electrolyte flooding[74] (which can lead to clogged electrode pores) and, hence, facilitating efficient gas diffusion. The substrate side of the GDE is highly hydrophobic and features larger pores to facilitate the diffusion of gases such as O_2, air, and CO_2.[75] On the other hand, the MPL side exhibits mild hydrophobicity, with smaller pores and a thin catalyst layer, which helps facilitate interactions between the electrocatalyst and electrolyte.

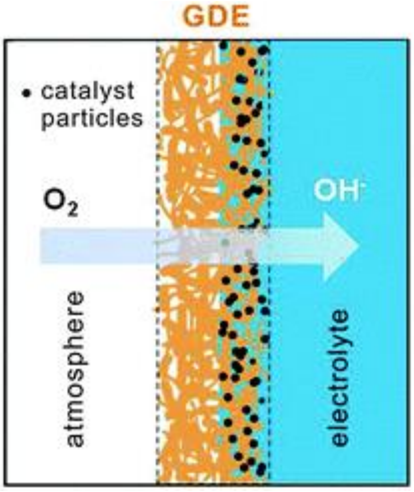

Figure 6. Illustration of three-phase reaction zone on gas diffusion electrode (GDE). Schematic showing catalyst particles loaded on GDE.[76]

GDEs play a crucial role in shortening the gas diffusion pathway to the electrode surface. This reduction in distance, coupled with the high concentration of the gas feed in close proximity, effectively mitigates mass transfer limitations associated with gas reactants.[77] In the case of Zn-CO_2 batteries with CO_2 gas feed, the concentration of the gas feed can be adjusted as needed, offering the potential to eliminate mass transfer limitations.

However, in the context of ZABs, the aim is often to utilize ambient atmosphere to achieve low-cost and commercial viability.[78] Consequently, at the laboratory scale, testing cells are typically operated under conditions where the cathode side is exposed to ambient air. This approach aligns with the practical considerations of using atmospheric air as the source of oxygen in ZABs for cost-effective and scalable applications.

ii. Air electrode

The air electrode plays a pivotal role in the overall performance of the system, as it involves the diffusion of oxygen from the atmosphere during discharge and OER during charging. Designing an effective cathode electrocatalyst is of paramount importance due to the sluggish kinetics associated with OER and ORR, primarily caused by the 4-electron transfer process, resulting in high overpotentials.[79]

Traditionally, noble metal catalysts like Pt-based (**Figure 7a**) and RuO_2 (**Figure 7b**) have been recognized as highly efficient catalysts for ORR and OER. However, Pt-based catalysts are susceptible to oxidation and exhibit subpar OER activity, while RuO_2 shows unsatisfactory performance for ORR. Moreover, both Pt and RuO_2 are prohibitively expensive and display poor stability, limiting their practical applications.[79,80] As a result, there is a pressing need to develop electrocatalysts that are cost-effective and exhibit exceptional stability, making them suitable for large-scale bifunctional applications.[81] It's worth noting that minimizing the overpotential between ORR and OER reactions is crucial for reducing energy losses.[82] Additionally, ORR and OER have distinct requirements for active sites due to the involvement of different intermediates in these reactions.

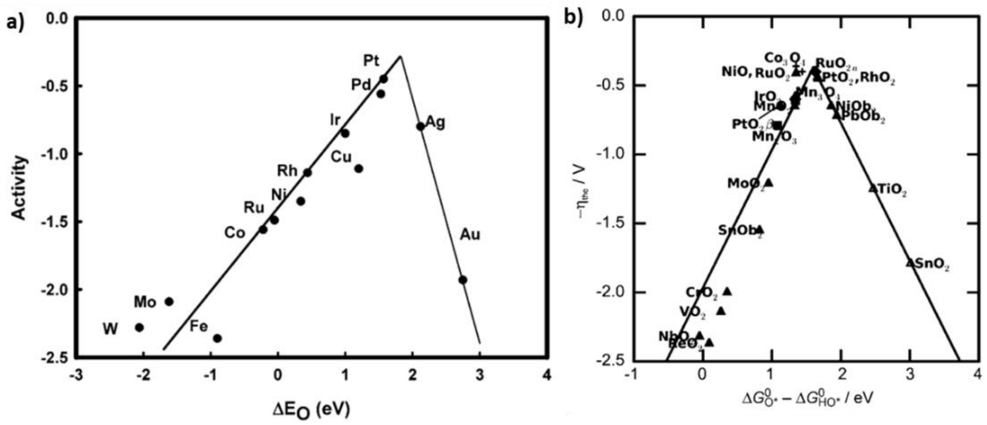

Figure 7. Volcano plot revealing overpotential (h) with a) standard free energy of intermediate (ΔG_{O^*}) for various metal-based catalyst (ORR) *Reproduced with permission from reference* [83]and b) standard free energy difference of two intermediates (ΔG_{MO^*}-ΔG_{MOH^*}) for various metal oxide catalysts. *Reproduced with permission from reference* [84]

The discussion on theoretical intermediates involved can help in understanding high-performance bifunctional OER/ORR catalysts. The reaction mechanism for ORR follows two main pathways, i.e., 4 electrons or 2 electrons to generate OH^- or H_2O_2, respectively. The 4 electrons' reaction mechanism is as follows[82,85]:

$$* + O_2 + H_2O + e^- \rightarrow *OOH + OH^- (aq) \tag{19}$$

$$*OOH + e- \rightarrow *O + OH^- (aq) \tag{20}$$

$$*O + H_2O(l) + e^- \rightarrow *OH + OH^- (aq) \tag{21}$$

$$*OH + e^- \rightarrow * + OH^- (aq) \tag{22}$$

The 2-electron reaction mechanism produces intermediate products of H_2O_2. ORR activity is poor when reduction follows this route:

$$O_2 + H_2O (l) + 2 e^- \rightarrow HO_2^- + OH^- (aq) \tag{23}$$

$HO_2^- + H_2O\ (l) + 2e^- \rightarrow 3OH^-\ (aq)$ (24)

ORR should follow the reduction of OOH* reduction to O* and OH*, while OER should follow the reverse process for bifunctional catalysts.

Sabatier's principle states that suitable adsorption energy, that is, neither too strong nor too weak binding of intermediates on catalyst active site dictates the high reaction rate.[86,87] The adsorption energy of ORR intermediates determines active sites on catalysts that affect reaction activity. Pt lies on top of the volcano plot for ORR and materials like RuO_2 and Co_3O_4 are positioned at the peak for OER.[88] However, it's important to note that electrocatalysts are susceptible to polarization and phase changes or amorphization in strong oxidizing environments, which can ultimately lead to poor catalyst stability.

Design of electrocatalyst for air electrode

Certain structural specifications can enhance the bifunctional OER/ORR nature of a catalyst. Structural modifications that can be made are as follows[89]:

- A porous structure with a high specific surface area can facilitate electrolyte contact and O_2 diffusion paths;[90,91]
- Interconnected networks with 3-D skeletons can enhance charge transfer and mass transfer, enhancing reaction kinetics [91]
- Tuning noble metal (ORR) with transition elements (OER) that lie on top of volcano plot to alter electronic properties;[92,93]
- For carbon-based materials, the high degree of graphitization can improve chemical resistance in harsh conditions (6M KOH) [94]
- Appropriate hydrophobicity of GDL for reactions at the gas-solid-liquid interface to promote adsorption-dissociation of reactants and transfer of electrons;[95]
- The binder-free catalysts grown directly on substrates such as Ni foam, carbon cloth, etc., as self-standing air cathodes can reduce impedance at the substrate/catalyst interface.[96,97]

By such structural optimizations, we can lower the overpotential and achieve high-durability ZABs. Before testing any material for ZAB, electrocatalyst has to be evaluated for ORR/OER (**Chapter 2.2**).

Evaluation parameters for ORR/OER

Onset potential, current density, tafel slope, turnover frequency, electrochemical surface area, electrochemical impedance spectroscopy, and potential gap.

- **Onset potential**

To make meaningful comparisons of electrochemical performance, it's important to consider the onset potential (E_{onset}).[98] E_{onset} is the potential at which a specific electrochemical reaction initiates. However, it's worth noting that E_{onset} can be somewhat arbitrary. It is typically defined as the potential at which the current deviates from the baseline and is determined by the intersection of tangents drawn between the baseline and the rising current in a linear sweep voltammogram (LSV).[99] In such cases, it's crucial to apply proper background correction techniques to avoid misinterpretation.

For the oxygen reduction reaction (ORR), the LSV can be defined as the potential at which a current density of -0.1 mA cm^{-2} is achieved.[100] This criterion helps provide a standardized reference point for comparing ORR performance across different systems.[101]

- **Current density**

The current density (j) is typically normalized by the geometric area or active mass of the catalyst.[88] This parameter is crucial for comparing electrocatalysts for practical applications such as ZAB.

- **Tafel slope**

The overpotential is logarithmically related to current density (j) and its linear portion as given by the Tafel equation:

$$h = a + b \log(j) \tag{25}$$

Where b is Tafel slope. b is an indicator of the reaction pathway and rate-determining step. Desirable bifunctional electrocatalysts must have a low b value.[102]

- **Electron transfer number**

ORR can take place via a 4-electron (OH^- formation) or by a 2-electron transfer pathway (peroxide formation). The number of electrons involved is determined by using the Koutecky-Levich (KL) technique on RDE. KL-plot establishes a relation between the current density and rotation speed by equation[103]:

$$1/j = 1/J_k + 1/j_L = 1/B \,.\, \omega^{-1/2} + 1/j_K \qquad (26)$$

Where j, $j_{K,}$ and j_L are the measured kinetic limited and mass transfer limited current densities, respectively. j_K is constant at a certain potential, and j_L is proportional to the square root of angular velocity (ω). RDE is rotated at different speeds from 400-2400 rpm. The proportionality coefficient (B) is,

$$B = 0.62D^{2/3} u^{-1/6} nFC^* \qquad (27)$$

Where D is the diffusion coefficient of the reactant, v is the kinematic viscosity of the electrolyte, *F* is the Faraday constant, and *C** is the concentration of the reactant in the bulk electrolyte. Thus, *n* can be deduced from the slope of the linear plot of j^{-1} versus $\omega^{-1/2}$.[103]

- **Turnover frequency (TOF)**

Turnover frequency can be given by:

$$TOF = j \times A / (n \times F \times m),$$

Where j is the current density at a given overpotential, A is the surface area of the electrode, n is the electron transfer number at a given overpotential, F is the Faraday constant, and m is the number of moles of metal on the electrode. Metal, in this case, is the active site of the catalyst and is typically estimated by inductively coupled plasma (ICP) technique or voltammetry techniques.[104] TOF represents the intrinsic activity of the catalyst, and a higher TOF value is desirable for a better bifunctional catalyst.

- **Electrochemical impedance spectroscopy (EIS)**

The most commonly used EIS is potentiostatic EIS and is recorded in the mixed transfer (charge and mass transfer) region. The various resistances in the OER/ORR system are associated with the solution, double layer capacitance, polarization resistance, pseudocapacitance, and resistance from the adsorption of reactants and intermediates. [105]

- **Potential gap**

The potential gap or ΔE (**Figure 8**) is the difference between potential at 10 mA cm^{-2} current density (OER) subtracted by half-wave potential (ORR).[88] The lower the voltage gap, the better bifunctional electrocatalyst is to be used for practical applications.

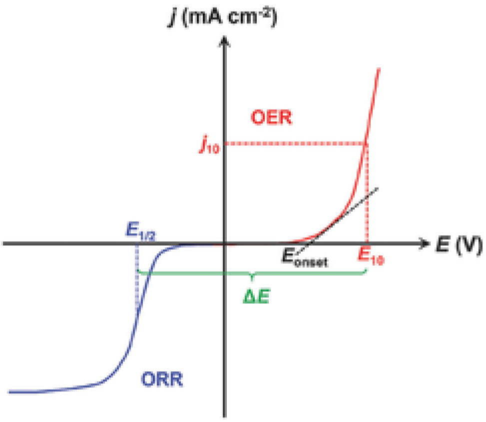

Figure 8. Illustration of the potential gap for OER/ ORR. *Reproduced with permission from reference* [106]

Evaluation parameters for Zn-air battery (ZAB)

The zinc-air battery is assembled in a two-electrode stack-type setting. It is acrylic made because of its resistance to harsh alkaline conditions. It has one side anode (Zn) and the other side cathode (electrocatalyst on GDE) with a current collector (**Figure 9**). Experimental testing techniques for the evaluation of ZAB are specific capacity (galvanostatic discharge), energy density, power density (galvanodynamic polarization), and cyclic stability (galvanostatic charge-discharge).

- **Specific Capacity (Discharge)**

During galvanostatic discharge, a constant discharge current is applied until a pre-determined cut-off voltage is reached (**Figure 9b**). The resulting capacity is normalized by the amount of zinc consumed (capacity limited by zinc). To calculate energy density in watt-hours per kilogram (Wh kg^{-1}), the $capacity_{Zn}$ is multiplied by the average voltage. The theoretical capacity of zinc is 820 milliampere-hours per gram (mAh g^{-1}).[107,108] Notably, the discharge curves exhibit a high degree of flatness, primarily due to minimal ohmic polarization, indicating efficient performance. The specific capacity is influenced by factors such as the mass loading of the electrocatalyst and the operating current density. An increase in electrocatalyst thickness can potentially lead to a decrease in specific capacity due to non-uniform wetting of the electrocatalyst.

Furthermore, when the current density is increased, the specific capacity may also decrease. This is attributed to the accelerated production of $Zn(OH)_4^{2-}$ ions, resulting in the early formation of ZnO-based passivation layers on the surface of the zinc electrode.[109] These passivation layers can impede the electrochemical reactions, leading to reduced specific capacity.

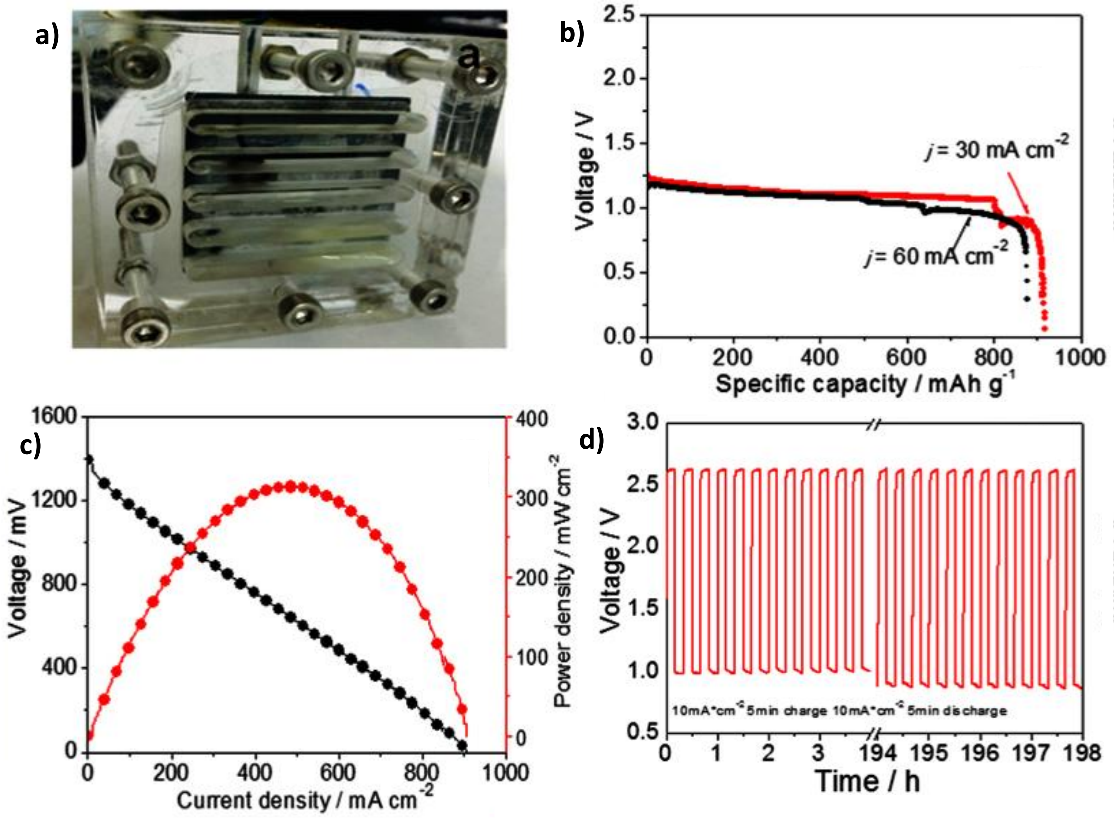

Figure 9. a) Zinc-air stack(the image needs to be enlarged two times) two electrode configuration. Measurements for ZAB are b) galvanostatic discharge, c) galvanodynamic discharge, and d) long-term charge-discharge profile.[110]

- **Power density**

The galvanodynamic polarization technique is used to obtain the power density value in ZAB (**Figure 9c**). In this technique, negative(discharging) or positive(charging) currents with progressive increases in magnitude and changes in voltage are recorded. The steep initial drop in potential is due to voltage losses from activation and mass-limited polarization.[50][111] On further increase in current, ohmic losses reduce the voltage, and the linear curve decreases. Sharp voltage drop is due to mass transfer limitation from O_2 and OH^-. Power density is multiplying voltage with current density.

- **Cycling stability**

Cycling stability is tested in galvanostatic conditions with charge-discharge for short time lengths (5 min or 10 min) and a large number of cycles (pulsing cycling test) (**Figure 9d**).[112] This stability study is for checking the performance of the cathode material (limiting factor here), as Zn is only discharged for a short fraction of its total capacity (5 min/ 10 min charge-discharge).

iii. CO_2 Electrode

The first report on Zn-CO_2 batteries was published in 2018 and was inspired by Zn-air batteries.[27] Like reversible ORR/OER bifunctional cathode in ZAB, aqueous Zn-CO_2 batteries with bifunctional cathode can also be designed in a stack-type setup.

- **Configuration**

In the initial report on Zn-CO_2 batteries [113], a cell constructed from Teflon material (**Figure 10a**) was utilized. This cell was designed in a configuration similar to the H-cell type (**Figure 10b**), which is commonly employed in electrochemical CO_2 reduction reactions. For the electrolytes, 1M KOH was used as the anolyte, and the catholyte consisted of 1M NaCl. In specific experiments, the catholyte contained 0.1M HCOONa, while others were conducted without HCOONa when measuring formate production.

To maintain the pH of the anolyte and catholyte while preventing cross-contamination between them, a bipolar membrane was incorporated into the setup.[114] This membrane played a crucial role in ensuring the integrity of the experimental conditions.

Recent reports have shifted towards the use of flow cell reactors with electrocatalysts coated on GDE.[115] The flow cell comprises gaseous flow through GDE and is collected on the same GDE side as gaseous feed.[116] The liquid products formed in the catholyte are collected from the opposite side of the gas feed. It is noteworthy that the gaseous feed supplied is humidified (contains water vapor) before entering the GDE.

Design of Electrode for Zn-CO_2 battery

Creating an effective electrocatalyst for Zn-CO_2 batteries is a complex task that demands careful consideration of various factors. Here's an original summary of the design principles involved:

- **Choice of Material:**

The catalyst should facilitate CO_2 reduction while maintaining a strong preference for the desired reaction pathway. This requires materials that can both activate CO_2 and avoid side reactions like hydrogen evolution.[117] High surface areas are crucial, so materials often take the form of nanoparticles or complex nanostructures. These structures increase the number of reactive sites and aid the diffusion of reactants and products.

- **Catalyst Supports:**

The support must conduct electricity well and should bolster the durability of the catalyst. It must also promote a good distribution of the active material, helping to maintain the catalyst's performance.[118]

- **Bimetallic and Hybrid Materials:**

Using two metals in conjunction can often enhance the catalyst's properties. Additionally, combining metals with carbon-based materials can boost stability and conductivity. Palladium-based materials with Ni, Cu, Co, and Ag can help selectively boost CO_2 reduction and eliminate side reactions (HER)[119] (**Chapter 2.3**).

- **Surface Chemistry:**

Modifying the surface with specific functional groups or atoms can adjust the electronic properties of the catalyst, thus enhancing its reactivity and selectivity towards a certain product.[120]

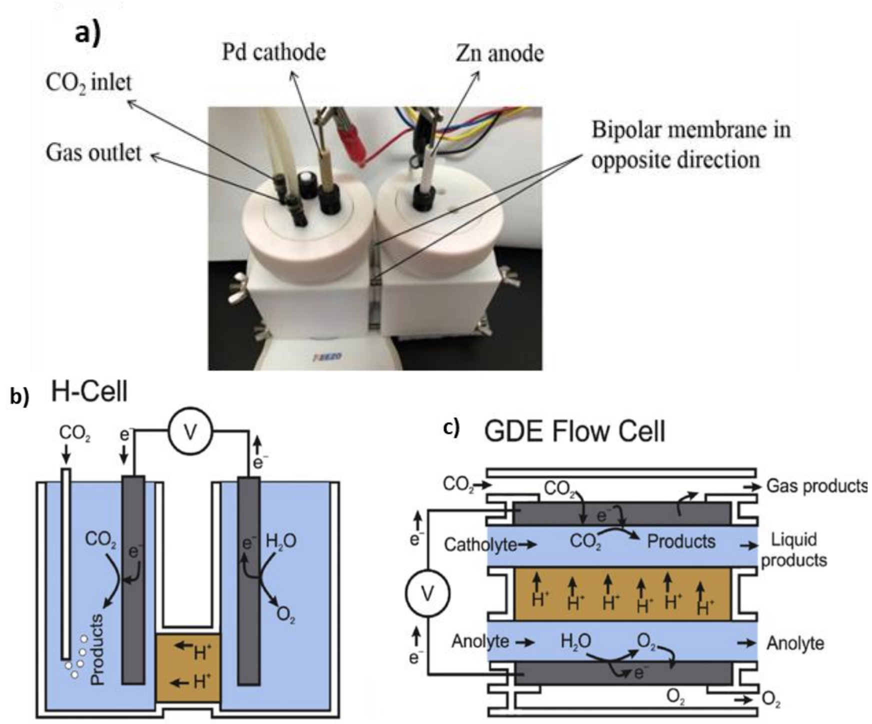

Figure 10. a) Setup used in the first report on Zn-CO_2 battery *Reproduced with permission from reference* [121]Schematic illustration of b) Laboratory electrochemical H-cell reactor for CO_2 (g) reduction at cathode and c) flow-cell reactor with gaseous reactant through GDE pores.[122]

- **Microenvironment Considerations:**

The local conditions around the active sites, such as pH, play a significant role in the efficiency of the reaction. The catalyst design should ensure optimal local conditions for CO_2 reduction.[123]

Analytical techniques are necessary to characterize the catalyst's performance in converting CO_2 into desired products, with a focus on achieving high Faradaic efficiency and stability under operational conditions.

Designing a catalyst is not just about the materials used; it's about how these materials are structured and interact with their environment. The ideal electrocatalyst will strike a balance between reactivity, selectivity, stability, and cost-efficiency, leading to a practical solution for Zn-CO_2 batteries.

Evaluation parameters for Zinc-CO_2 battery

The evaluation parameters for the Zn-CO_2 battery involve the detection and quantification of desirable products. It is tested at different galvanostatic discharge conditions to attain the optimum faradaic efficiency of a desired product (Formate/CO).

Faradaic efficiency is calculated by[124]:

$$\text{FE}\ (\%) = Q_{exp}/Q_{theo} = n.\ F.\ m\ /\ I.t \tag{28}$$

Where Q_{exp} and Q_{theo} are the charge for experimental and theoretical value, n is the number of electrons transferred (2 electrons for $HCOO^-$/CO), m is the moles of product formed, I is the current provided, and t is the reaction time. Generally, electrons can also be consumed by H_2 production, i.e., an undesirable product competes with the formation of value-added products.

Similar to ZAB, power density and charge-discharge studies can be carried out.

2.1.5 Conclusion

Zinc-air and zinc-CO_2 batteries present a promising frontier for advanced energy storage systems, balancing energy density, safety, and economic considerations. Their development centers on overcoming challenges like reaction kinetics, material stability, and longevity. Innovations in particular cathode materials, i.e., catalyst design and system integration, are key to enhancing their efficiency and lifecycle. These batteries not only offer energy storage solutions but also contribute to carbon capture and conversion, embodying a dual approach to environmental sustainability and technological advancement. Their evolution from laboratory curiosities to commercial products is pivotal for a future of renewable energy and reduced carbon emissions.

2.2.5 References

1. Li, Y., Gong, M., Liang, Y., Feng, J., Kim, J.-E., Wang, H., Hong, G., Zhang, B., and Dai, H. (2013) ARTICLE Advanced zinc-air batteries based on high-performance hybrid electrocatalysts.

2. Zhou, J., Cheng, J., Wang, B., Peng, H., and Lu, J. (2020) Flexible metal-gas batteries: a potential option for next-generation power accessories for wearable electronics, *Energy Environ. Sci*, **13**, 1933.

3. Amici, J., Marquez, P., Mangini, A., Torchio, C., Dessantis, D., Versaci, D., Francia, C., Aguirre, J., and Bodoardo, S. (2022) Sustainable, economic, and simple preparation of an efficient catalyst for Li-O 2 batteries. *J Power Sources*, **546**, 231942.

4. Younesi, R., Hahlin, M., Björefors, F., Johansson, P., and Edström, K. (2013) Li-O2 battery degradation by lithium peroxide (Li 2O2): A model study. *Chemistry of Materials*, **25** (1), 77–84.

5. Liu, H., Shi, S., Wang, Z., Han, Y., and Huang, W. (2022) Recent Advances in Metal–Gas Batteries with Carbon-Based Nonprecious Metal Catalysts. *Small*, **18** (10).

6. Zhang, J., Zhou, Q., Tang, Y., Zhang, L., and Li, Y. (2019) Zinc-air batteries: are they ready for prime time?

7. Lee, J.S., Kim, S.T., Cao, R., Choi, N.S., Liu, M., Lee, K.T., and Cho, J. (2011) Metal-air batteries with high energy density: Li-air versus Zn-air. *Adv Energy Mater*, **1** (1), 34–50.

8. Jenkins, M., Dewar, D., Nimmo, T., Chau, C., Gao, X., and Bruce, P.G. (2023) The accumulation of Li 2 CO 3 in a Li-O 2 battery with dual mediators †.

9. He, P., and Huang, J. (2022) Chemical Passivation Stabilizes Zn Anode. *Advanced Materials*, **34** (18).

10. Zhao, Z., Fan, X., Ding, J., Hu, W., Zhong, C., and Lu, J. (2019) Challenges in Zinc Electrodes for Alkaline Zinc-Air Batteries: Obstacles to Commercialization. *ACS Energy Lett*, **4** (9), 2259–2270.

11. Liu, W., Feng, J., Wei, T., Liu, Q., Zhang, S., Luo, Y., Luo, J., and Liu, X. (2022) Active-site and interface engineering of cathode materials for aqueous Zn—gas batteries. *Nano Research 2022 16:2*, **16** (2), 2325–2346.

12. Hou, J., Yang, M., Ellis, M.W., Moore, R.B., and Yi, B. (2012) This journal is c the Owner Societies. *Phys. Chem. Chem. Phys*, **14**, 13487–13501.

13. Lv, H., Xiang, A., Huang, L., Zhu, X., and Wang, B. (2022) Metal-related electrocatalysts for Li-CO 2 batteries: an overview of the fundamentals to explore future-oriented strategies.

14. Ma, J.L., Bao, D., Shi, M.M., Yan, J.M., and Zhang, X.B. (2017) Reversible Nitrogen Fixation Based on a Rechargeable Lithium-Nitrogen Battery for Energy Storage. *Chem*, **2** (4), 525–532.

15. Li, C.S., Sun, Y., Gebert, F., and Chou, S.L. (2017) Current Progress on Rechargeable Magnesium–Air Battery. *Adv Energy Mater*, **7** (24).

16. Jayan, R., and Islam, M.M. (2023) Advancing next-generation nonaqueous Mg-CO 2 batteries: insights into reaction mechanisms and catalyst design †.

17. Faegh, E., Ng, B., Hayman, D., and Mustain, W.E. (2020) Practical assessment of the performance of aluminium battery technologies. *Nature Energy 2020 6:1*, **6** (1), 21–29.

18. Fetrow, C.J., Carugati, C., Zhou, X.-D., and Wei, S. (2022) Electrochemistry of metal-CO 2 batteries: Opportunities and challenges. *Energy Storage Mater*, **45**, 911–933.

19. Guo, Y., Yang, Q., Wang, D., Li, H., Huang, Z., Li, X., Zhao, Y., Dong, B., and Zhi, C. (2020) A rechargeable Al-N 2 battery for energy storage and highly efficient N 2 fixation †. *2888 | Energy Environ. Sci*, **13**, 2888.

20. Zhang, J., Zhou, Q., Tang, Y., Zhang, L., and Li, Y. (2019) Zinc-air batteries: are they ready for prime time?

21. Zhang, R., Zhang, S., Guo, Y., Li, C., Liu, J., Huang, Z., Zhao, Y., Li, Y., and Zhi, C. (2022) A Zn-nitrite battery as an energy-output electrocatalytic system for high-efficiency ammonia synthesis using carbon-doped cobalt oxide nanotubes †, *Energy Environ. Sci*, **15**, 3024.

22. Ren, J.T., Chen, L., Wang, H.Y., and Yuan, Z.Y. (2021) Aqueous Rechargeable Zn-N2Battery Assembled by Bifunctional Cobalt Phosphate Nanocrystals-Loaded Carbon Nanosheets for Simultaneous NH3Production and Power Generation. *ACS Appl Mater Interfaces*, **13** (10), 12106–12117.

23. Global Zinc-Air Batteries Market: Global Industry Analysis (2020-2027).

24. Liu, W., Feng, J., Wei, T., Liu, Q., Zhang, S., Luo, Y., Luo, J., and Liu, X. (2022) Active-site and interface engineering of cathode materials for aqueous Zn—gas batteries. *Nano Research 2022 16:2*, **16** (2), 2325–2346.

25. Ren, J.T., Chen, L., Wang, H.Y., and Yuan, Z.Y. (2021) Aqueous Rechargeable Zn-N2Battery Assembled by Bifunctional Cobalt Phosphate Nanocrystals-Loaded Carbon Nanosheets for Simultaneous NH3Production and Power Generation. *ACS Appl Mater Interfaces*, **13** (10), 12106–12117.

26. Zhang, R., Zhang, S., Guo, Y., Li, C., Liu, J., Huang, Z., Zhao, Y., Li, Y., and Zhi, C. (2022) A Zn-nitrite battery as an energy-output electrocatalytic system for high-efficiency ammonia synthesis using carbon-doped cobalt oxide nanotubes †. *Energy Environ. Sci*, **15**, 3024.

27. Xie, J., Wang, X., Lv, J., Huang, Y., Wu, M., Wang, Y., and Yao, J. (2018) Reversible Aqueous Zinc–CO2 Batteries Based on CO2–HCOOH Interconversion. *Angewandte Chemie - International Edition*, **57** (52), 16996–17001.

28. Zhao, Z., Fan, X., Ding, J., Hu, W., Zhong, C., and Lu, J. (2019) Challenges in Zinc Electrodes for Alkaline Zinc-Air Batteries: Obstacles to Commercialization. *ACS Energy Lett*, **4** (9), 2259–2270.

29. Chang, J., Wang, G., and Yang, Y. (2021) Recent Advances in Electrode Design for Rechargeable Zinc–Air Batteries. *Small Science*, **1** (10), 2100044.

30. Pachauri, R.K., Meyer, L., Hallegatte France, S., Bank, W., Hegerl, G., Brinkman, S., van Kesteren, L., Leprince-Ringuet, N., and van Boxmeer, F. Ottmar Edenhofer (Germany), Ismail Elgizouli (Sudan), Christopher B. Field (USA), Piers), Mark Howden (Australia). *Kristin Seyboth (USA)*.

31. Fetrow, C.J., Carugati, C., Zhou, X.D., and Wei, S. (2022) Electrochemistry of metal-CO2 batteries: Opportunities and challenges. *Energy Storage Mater*, **45**, 911–933.

32. Cui, Y.-F., Zhu, Y.-H., Du, J.-Y., Liu, W.-Q., Huang, G., Zhang, X.-B., Zhang, Y.-L., and Li, K. (2022) A high-voltage and stable zinc-air battery enabled by dual-hydrophobic-induced proton shuttle shielding.

33. Liu, J.N., Zhao, C.X., Wang, J., Ren, D., Li, B.Q., and Zhang, Q. (2022) A brief history of zinc–air batteries: 140 years of epic adventures. *Energy Environ Sci*, **15** (11), 4542–4553.

34. Wang, H.-F., and Xu, Q. (2019) Materials Design for Rechargeable Metal-Air Batteries.

35. Wang, C., Li, J., Zhou, Z., Pan, Y., Yu, Z., Pei, Z., Zhao, S., Wei, L., and Chen, Y. (2021) EnergyChem Rechargeable zinc-air batteries with neutral electrolytes: Recent advances, challenges, and prospects.

36. Wang, H., Li, Z., Li, Y., Yang, B., Chen, J., Lei, L., Wang, S., and Hou, Y. (2021) An exfoliated iron phosphorus trisulfide nanosheet with rich sulfur vacancy for efficient dinitrogen fixation and Zn-N 2 battery. *Nano Energy*, **81**, 105613.

37. Iqbal, A., El-Kadri, O.M., and Hamdan, N.M. (2023) Insights into rechargeable Zn-air batteries for future advancements in energy storing technology. *J Energy Storage*, **62**, 106926.

38. Bard, A.J., and Faulkner, L.R. (2001) Basic Potential Step Methods. *Electrochemical Methods: Fundamentals and Applications*, 156–225.

39. Rebrov, E. V., and Gao, P.Z. (2023) Molecular Catalysts for OER/ORR in Zn–Air Batteries. *Catalysts 2023, Vol. 13, Page 1289*, **13** (9), 1289.

40. Guo, Y., Zhang, R., Zhang, S., and Zhi, C. (2022) Recent advances in Zn-CO 2 batteries for the co-production of electricity and carbonaceous fuels.

41. Schröder, D. (2016) Analysis of reaction and transport processes in zinc air batteries. *Analysis of Reaction and Transport Processes in Zinc Air Batteries*, 1–231.

42. Schröder, D., Sinai Borker, N.N., König, M., and Krewer, U. (2015) Performance of zinc air batteries with added K2CO3 in the alkaline electrolyte. *J Appl Electrochem*, **45** (5), 427–437.

43. Kaur, S., Kumar, M., Gupta, D., Mohanty, P., Das, T., Chakraborty, S., Ahuja, R., and Nagaiah, T.C. (2023) Efficient CO 2 utilization and sustainable energy conversion via aqueous Zn-CO 2 batteries. *Nano Energy*, **109**, 108242.

44. Xie, J., and Wang, Y. (2019) Recent Development of CO2 Electrochemistry from Li-CO2 Batteries to Zn-CO2 Batteries. *Acc Chem Res*, **52** (6), 1721–1729.

45. Guo, W., Wang, Y., Yi, Q., Devid, E., Li, X., Lei, P., Shan, W., Qi, K., Shi, L., and Gao, L. (2023) Research progress of aqueous Zn–CO2 battery: design principle and development strategy of a multifunctional catalyst. *Front Energy Res*, **11**, 1194674.

46. Xie, J., Huang, Y., Wu, M., and Wang, Y. (2019) Electrochemical Carbon Dioxide Splitting. *ChemElectroChem*, **6** (6), 1587–1604.

47. Kim, C., Kim, J., Joo, S., Yang, Y., Shin, J., Liu, M., Cho, J., and Kim, G. (2019) Highly Efficient CO2 Utilization via Aqueous Zinc– or Aluminum–CO2 Systems for Hydrogen Gas Evolution and Electricity Production. *Angewandte Chemie - International Edition*, **58** (28), 9506–9511.

48. See, D.M., and White, R.E. (1997) Temperature and Concentration Dependence of the Specific Conductivity of Concentrated Solutions of Potassium Hydroxide. *J Chem Eng Data*, **42** (6), 1266–1268.

49. Toussaint, G., Stevens, P., Moureau, F., Rouget, R., and Fourgeot, F. Development of a rechargeable zinc-air battery.

50. Fu, J., Paul Cano, Z., Gyu Park, M., Yu, A., Fowler, M., Chen, Z., Fu, J., Cano, Z.P., Park, M.G., Yu, A., Fowler, M., and Chen, Z. (2017) Electrically Rechargeable Zinc–Air Batteries: Progress, Challenges, and Perspectives. *Advanced Materials*, **29** (7), 1604685.

51. Diggle, J.W., Despic, A.R., and Bockris, J.O. (1969) The Mechanism of the Dendritic Electrocrystallization of Zinc. *J Electrochem Soc*, **116** (11), 1503.

52. Wranglén, G. (1960) Dendrites and growth layers in the electrocrystallization of metals. *Electrochim Acta*, **2** (1–3), 130–143.

53. Popov, K.I., Maksimović, M.D., Trnjančev, J.D., and Pavlović, M.G. (1981) Dendritic electrocrystallization and the mechanism of powder formation in the potentiostatic electrodeposition of metals. *J Appl Electrochem*, **11** (2), 239–246.

54. Huh, T., Savaskan, G., and Evans, J.W. (1992) Further studies of a zinc-air cell employing a packed bed anode part II: Regeneration of zinc particles and electrolyte by fluidized bed electrodeposition. *J Appl Electrochem*, **22** (10), 916–921.

55. Savaskan, G., Huh, T., and Evans, J.W. (1992) Further studies of a zinc-air cell employing a packed bed anode part I: Discharge. *J Appl Electrochem*, **22** (10), 909–915.

56. Gagnon, E.G. (1986) Effects of KOH Concentration on the Shape Change and Cycle Life of Zn / NiOOH Cells. *J Electrochem Soc*, **133** (10), 1989.

57. McBreen, J. (1972) Zinc Electrode Shape Change in Secondary Cells. *J Electrochem Soc*, **119** (12), 1620.

58. Baugh, L.M., and Baikie, A.R. (1985) Passivation of zinc in concentrated alkaline solution—II. Role of various experimental factors and the distinction between the solid-state and dissolution—precipitation mechanisms. *Electrochim Acta*, **30** (9), 1173–1183.

59. Lee, C.W., Eom, S.W., Sathiyanarayanan, K., and Yun, M.S. (2006) Preliminary comparative studies of zinc and zinc oxide electrodes on corrosion reaction and reversible reaction for zinc/air fuel cells. *Electrochim Acta*, **52** (4), 1588–1591.

60. Lee, J., Hwang, B., Park, M.S., and Kim, K. (2016) Improved reversibility of Zn anodes for rechargeable Zn-air batteries by using alkoxide and acetate ions. *Electrochim Acta*, **199**, 164–171.

61. Hosseini, S., Masoudi Soltani, S., and Li, Y.Y. (2021) Current status and technical challenges of electrolytes in zinc–air batteries: An in-depth review. *Chemical Engineering Journal*, **408**, 127241.

62. Zhang, Y., Wu, Y., You, W., Tian, M., Huang, P.W., Zhang, Y., Sun, Z., Ma, Y., Hao, T., and Liu, N. (2020) Deeply Rechargeable and Hydrogen-Evolution-Suppressing Zinc Anode in Alkaline Aqueous Electrolyte. *Nano Lett*, **20** (6), 4700–4707.

63. Bayaguud, A., Fu, Y., and Zhu, C. (2022) Interfacial parasitic reactions of zinc anodes in zinc ion batteries: Underestimated corrosion and hydrogen evolution reactions and their suppression strategies. *Journal of Energy Chemistry*, **64**, 246–262.

64. Jeong, J., and Shin, H.C. (2020) In-Depth Analysis of Coulombic Efficiency of Zinc-Air Secondary Batteries. *Journal of Electrochemical Science and Technology*, **11** (1), 26–32.

65. Shinde, S.S., Wagh, N.K., Lee, C.H., Kim, D.H., Kim, S.H., Um, H.D., Lee, S.U., and Lee, J.H. (2023) Scaling-Up Insights for Zinc–Air Battery Technologies Realizing Reversible Zinc Anodes. *Advanced Materials*.

66. Lee, D.U., Choi, J.-Y., Feng, K., Park, H.W., and Chen, Z. (2013) Advanced Extremely Durable 3D Bifunctional Air Electrodes for Rechargeable Zinc-Air Batteries.

67. Neburchilov, V., Wang, H., Martin, J.J., and Qu, W. (2010) A review on air cathodes for zinc–air fuel cells. *J Power Sources*, **195** (5), 1271–1291.

68. Kinoshita, K. (Kim), and Electrochemical Society. (1992) Electrochemical oxygen technology. 431.

69. Atiq Khan, Z., Angel Garcia Salaberri, P., M Heenan, T.M., -, al, Jung, S., Sabharwal, M., and Jarauta, A. (2022) Investigating the Role of the Triple-Phase Boundary in Zinc-Air Cathodes Using Pore Network Modeling. *J Electrochem Soc*, **169** (10), 100549.

70. Davari, E., and Ivey, D.G. (2017) Bifunctional electrocatalysts for Zn–air batteries. *Sustain Energy Fuels*, **2** (1), 39–67.

71. Zhang, W., Guo, F., Zhou, Y., Yu, S., Chen, A., Jiang, H., Jiang, H., and Li, C. (2022) Gas Diffusion Layer with a Regular Hydrophilic Structure Boosts the

Power Density of Proton Exchange Membrane Fuel Cells via the Construction of Water Highways. *ACS Appl Mater Interfaces*, **14** (15), 17578–17584.

72. Mortazavi, M., and Tajiri, K. (2014) Effect of the PTFE content in the gas diffusion layer on water transport in polymer electrolyte fuel cells (PEFCs). *J Power Sources*, **245**, 236–244.

73. Wan, L., Xu, Z., Cao, Q., Liao, Y., Wang, B., and Liu, K. (2022) Nanoemulsion-Coated Ni-Fe Hydroxide Self-Supported Electrode as an Air-Breathing Cathode for High-Performance Zinc-Air Batteries. *Nano Lett*, **22** (11), 4535–4543.

74. Yang, K., Kas, R., Smith, W.A., and Burdyny, T. (2021) Role of the Carbon-Based Gas Diffusion Layer on Flooding in a Gas Diffusion Electrode Cell for Electrochemical CO2Reduction. *ACS Energy Lett*, **6** (1), 33–40.

75. Lin, G., Liu, S., Yu, B., Wang, H., Yu, K., and Hu, Y. (2020) Preparation of graded microporous layers for enhanced water management in fuel cells. *J Appl Polym Sci*, **137** (47).

76. Li, Y., and Dai, H. (2014) Chem Soc Rev Chemical Society Reviews Recent advances in zinc-air batteries. *Chem. Soc. Rev*, **43**, 5257.

77. Wang, X., Tomon, C., Bobrowski, T., Wilde, P., Junqueira, J.R.C., Quast, T., He, W., Sikdar, N., Weidner, J., and Schuhmann, W. (2022) Gaining the Freedom of Scalable Gas Diffusion Electrodes for the CO2 Reduction Reaction. *ChemElectroChem*, **9** (21).

78. Anju, V.G., Manjunatha, R., Austeria, P.M., and Sampath, S. (2016) Primary and rechargeable zinc-air batteries using ceramic and highly stable TiCN as an oxygen reduction reaction electrocatalyst †.

79. Galán-Mascarós, J.R. (2015) Water Oxidation at Electrodes Modified with Earth-Abundant Transition-Metal Catalysts. *ChemElectroChem*, **2** (1), 37–50.

80. Nørskov, J.K., Rossmeisl, J., Logadottir, A., Lindqvist, L., Kitchin, J.R., Bligaard, T., and Jónsson, H. (2004) Origin of the Overpotential for Oxygen Reduction at a Fuel-Cell Cathode. *Journal of Physical Chemistry B*, **108** (46), 17886–17892.

81. Huang, Z.F., Wang, J., Peng, Y., Jung, C.Y., Fisher, A., and Wang, X. (2017) Design of Efficient Bifunctional Oxygen Reduction/Evolution Electrocatalyst: Recent Advances and Perspectives. *Adv Energy Mater*, **7** (23), 1700544.

82. Huang, Z.F., Song, J., Dou, S., Li, X., Wang, J., and Wang, X. (2019) Strategies to Break the Scaling Relation toward Enhanced Oxygen Electrocatalysis. *Matter*, **1** (6), 1494–1518.

83. Nørskov, J.K., Rossmeisl, J., Logadottir, A., Lindqvist, L., Kitchin, J.R., Bligaard, T., and Jónsson, H. (2004) Origin of the overpotential for oxygen reduction at a fuel-cell cathode. *Journal of Physical Chemistry B*, **108** (46), 17886–17892.

84. Man, I.C., Su, H.Y., Calle-Vallejo, F., Hansen, H.A., Martínez, J.I., Inoglu, N.G., Kitchin, J., Jaramillo, T.F., Nørskov, J.K., and Rossmeisl, J. (2011) Universality in Oxygen Evolution Electrocatalysis on Oxide Surfaces. *ChemCatChem*, **3** (7), 1159–1165.

85. Kim, H.W., Bukas, V.J., Park, H., Park, S., Diederichsen, K.M., Lim, J., Cho, Y.H., Kim, J., Kim, W., Han, T.H., Voss, J., Luntz, A.C., and McCloskey, B.D. (2020) Mechanisms of two-electron and four-electron electrochemical oxygen reduction reactions at nitrogen-doped reduced graphene oxide. *ACS Catal*, **10** (1), 852–863.

86. Sabatier, P. (1854-1941). A. du texte (1913) La Catalyse en chimie organique, par Paul Sabatier,...

87. Kheawhom, S., Luo, M., Ooka hideshiooka, H., Kai Exner, rikenjp S., Ooka, H., Huang, J., and Exner, K.S. (2021) The Sabatier Principle in Electrocatalysis: Basics, Limitations, and Extensions.

88. Huang, Z.F., Wang, J., Peng, Y., Jung, C.Y., Fisher, A., and Wang, X. (2017) Design of Efficient Bifunctional Oxygen Reduction/Evolution Electrocatalyst: Recent Advances and Perspectives. *Adv Energy Mater*, **7** (23), 1700544.

89. Liu, X., Zhang, G., Wang, L., and Fu, H. (2021) Structural Design Strategy and Active Site Regulation of High-Efficient Bifunctional Oxygen Reaction Electrocatalysts for Zn–Air Battery. *Small*, **17** (48).

90. Wang, X., Liu, T., Li, H., Han, C., Su, P., Ta, N., Jiang, S.P., Kong, B., Liu, J., and Huang, Z. (2023) Balancing Mass Transfer and Active Sites to Improve Electrocatalytic Oxygen Reduction by B,N Codoped C Nanoreactors. *Nano Lett*, **23** (11), 4699–4707.

91. Zhang, J., Zhang, M., Qiu, L., Zeng, Y., Chen, J., Zhu, C., Yu, Y., and Zhu, Z. (2019) Three-dimensional interconnected core–shell networks with Ni(Fe)OOH and M–N–C active species together as high-efficiency oxygen catalysts for rechargeable Zn–air batteries. *J Mater Chem A Mater*, **7** (32), 19045–19059.

92. Shi, Q., Zhu, C., Du, D., and Lin, Y. (2019) Robust noble metal-based electrocatalysts for oxygen evolution reaction. *Chem Soc Rev*, **48** (12), 3181–3192.

93. Wang, X., Li, Z., Qu, Y., Yuan, T., Wang, W., Wu, Y., and Li, Y. (2019) Review of Metal Catalysts for Oxygen Reduction Reaction: From Nanoscale Engineering to Atomic Design. *Chem*, **5** (6), 1486–1511.

94. Yu, Q., Li, H., Li, R., Zeng, S., Li, R., Yao, Q., Chen, H., Qu, K., and Zheng, Y. (2022) Natural DNA-assisted ultrafine FeP embedded in N, P-codoped carbons for efficient oxygen reduction, hydrogen evolution and rechargeable zinc-air battery. *Carbon N Y*, **186**, 171–179.

95. Inoue, T., Sakai, D., Hirota, K., -, al, Simon, C., Hasché, F., Gasteiger -, H.A., Bum Park, S., Kim, S., Park, Y., and Oh, M.-H. (2009) Fabrication of GDL microporous layer using PVDF for PEMFCs. *J Phys Conf Ser*, **165** (1), 012046.

96. Wang, P., Wan, L., Lin, Y., and Wang, B. (2019) Construction of mass-transfer channel in air electrode with bifunctional catalyst for rechargeable zinc-air battery. *Electrochim Acta*, **320**, 134564.

97. Cai, X., Lai, L., Zhou, L., and Shen, Z. (2019) Durable Freestanding Hierarchical Porous Electrode for Rechargeable Zinc-Air Batteries. *ACS Appl Energy Mater*, **2** (2), 1505–1516.

98. Loichet Torres, P.A., Li, Y.-S., Grön, C., -, al, Shinozaki, K., Zack, J.W., Pylypenko, S., Yeob Choi, E., Lee, S., and Kim, C.K. (2015) Oxygen Reduction Reaction Measurements on Platinum Electrocatalysts Utilizing Rotating Disk

Electrode Technique: I. Impact of Impurities, Measurement Protocols and Applied Corrections. *J Electrochem Soc*, **162** (10), F1144.

99. Huang, Z.F., Wang, J., Peng, Y., Jung, C.Y., Fisher, A., and Wang, X. (2017) Design of efficient bifunctional oxygen reduction/evolution electrocatalyst: Recent advances and perspectives. *Adv Energy Mater*, **7** (23).

100. Bouleau, L., Pérez-Rodríguez, S., Quílez-Bermejo, J., Izquierdo, M.T., Xu, F., Fierro, V., and Celzard, A. (2022) Best practices for ORR performance evaluation of metal-free porous carbon electrocatalysts. *Carbon N Y*, **189**, 349–361.

101. Yuan, Y., Li, H., Jiang, Z., Lin, Z., Tang, Y., Wang, H., and Liang, Y. (2022) Deciphering the selectivity descriptors of heterogeneous metal phthalocyanine electrocatalysts for hydrogen peroxide production †.

102. Shinagawa, T., Garcia-Esparza, A.T., and Takanabe, K. (2015) Insight on Tafel slopes from a microkinetic analysis of aqueous electrocatalysis for energy conversion. *Scientific Reports 2015 5:1*, **5** (1), 1–21.

103. Zhou, R., Zheng, Y., Jaroniec, M., and Qiao, S.Z. (2016) Determination of the Electron Transfer Number for the Oxygen Reduction Reaction: From Theory to Experiment. *ACS Catal*, **6** (7), 4720–4728.

104. Sun, Y., Silvioli, L., Sahraie, N.R., Ju, W., Li, J., Zitolo, A., Li, S., Bagger, A., Arnarson, L., Wang, X., Moeller, T., Bernsmeier, D., Rossmeisl, J., Jaouen, F., and Strasser, P. (2019) Activity-Selectivity Trends in the Electrochemical Production of Hydrogen Peroxide over Single-Site Metal-Nitrogen-Carbon Catalysts. *J Am Chem Soc*, **141** (31), 12372–12381.

105. Chakraborty, S., Marappa, S., Agarwal, S., Bagchi, D., Rao, A., Vinod, C.P., Peter, S.C., Singh, A., and Eswaramoorthy, M. (2022) Improvement in Oxygen Evolution Performance of NiFe Layered Double Hydroxide Grown in the Presence of 1T-Rich MoS2. *ACS Appl Mater Interfaces*, **14** (28), 31951–31961.

106. Huang, Z.F., Wang, J., Peng, Y., Jung, C.Y., Fisher, A., and Wang, X. (2017) Design of efficient bifunctional oxygen reduction/evolution electrocatalyst: Recent advances and perspectives. *Adv Energy Mater*, **7** (23).

107. Deckenbach, D., and Schneider, J.J. (2023) A Long-Overlooked Pitfall in Rechargeable Zinc–Air Batteries: Proper Electrode Balancing. *Adv Mater Interfaces*, **10** (15).

108. Zhong, X., Shao, Y., Chen, B., Li, C., Sheng, J., Xiao, X., Xu, B., Li, J., Cheng, H.M., and Zhou, G. (2023) Rechargeable Zinc–Air Batteries with an Ultralarge Discharge Capacity per Cycle and an Ultralong Cycle Life. *Advanced Materials*, **35** (30).

109. Stamm, J., Varzi, A., Latz, A., and Horstmann, B. (2017) Modeling nucleation and growth of zinc oxide during discharge of primary zinc-air batteries.

110. Xu, N., Liu, Y., Zhang, X., Li, X., Li, A., Qiao, J., and Zhang, J. (2016) Self-assembly formation of Bi-functional Co3O4/MnO2-CNTs hybrid catalysts for achieving both high energy/power density and cyclic ability of rechargeable zinc-air battery. *Scientific Reports 2016 6:1*, **6** (1), 1–10.

111. He, Y., Cui, Y., Shang, W., Zhao, Z., and Tan, P. (2022) Insight into the bubble-induced overpotential towards high-rate charging of Zn-air batteries. *Chemical Engineering Journal*, **448**, 137782.

112. Liu, X., Fan, X., Liu, B., Ding, J., Deng, Y., Han, X., Zhong, C., Hu Liu, W.X., Fan, X., Liu, B., Ding, J., Zhong, C., Hu, W., Deng, Y., and Han, X. (2021) Mapping the Design of Electrolyte Materials for Electrically Rechargeable Zinc–Air Batteries. *Advanced Materials*, **33** (31), 2006461.

113. Xie, J., Wang, X., Lv, J., Huang, Y., Wu, M., Wang, Y., and Yao, J. (2018) Reversible Aqueous Zinc–CO2 Batteries Based on CO2–HCOOH Interconversion. *Angewandte Chemie - International Edition*, **57** (52), 16996–17001.

114. Zhao, Y., Pei, Z., Lu, X.F., Luan, D., Wang, X., and Lou, X.W. (David) (2022) Rationally designed nitrogen-doped carbon macroporous fibers with loading of single cobalt sites for efficient aqueous Zn-CO2 batteries. *Chem Catalysis*, **2** (6), 1480–1493.

115. Liu, K., Smith, W.A., and Burdyny, T. (2019) Introductory Guide to Assembling and Operating Gas Diffusion Electrodes for Electrochemical CO 2 Reduction. *ACS Energy Lett*, **4** (3), 639–643.

116. Burdyny, T., and Smith, W.A. (2019) CO2 reduction on gas-diffusion electrodes and why catalytic performance must be assessed at commercially-relevant conditions. *Energy Environ Sci*, **12** (5), 1442–1453.

117. Guo, Y., Zhang, R., Zhang, S., and Zhi, C. (2022) Recent advances in Zn–CO2 batteries for the co-production of electricity and carbonaceous fuels. *Nano Materials Science*.

118. Gao, S., Wei, T., Sun, J., Liu, Q., Ma, D., Liu, W., Zhang, S., Luo, J., and Liu, X. (2022) Atomically Dispersed Metal-Based Catalysts for Zn–CO2 Batteries. *Small Struct*, **3** (12), 2200086.

119. Chatterjee, S., Griego, C., Hart, J.L., Li, Y., Taheri, M.L., Keith, J., and Snyder, J.D. (2019) Free Standing Nanoporous Palladium Alloys as CO Poisoning Tolerant Electrocatalysts for the Electrochemical Reduction of CO2 to Formate. *ACS Catal*, **9** (6), 5290–5301.

120. Nitopi, S., Bertheussen, E., Scott, S.B., Liu, X., Engstfeld, A.K., Horch, S., Seger, B., Stephens, I.E.L., Chan, K., Hahn, C., Nørskov, J.K., Jaramillo, T.F., and Chorkendorff, I. (2019) Progress and Perspectives of Electrochemical CO2 Reduction on Copper in Aqueous Electrolyte. *Chem Rev*, **119** (12), 7610–7672.

121. Xie, J., Wang, X., Lv, J., Huang, Y., Wu, M., Wang, Y., and Yao, J. (2018) Reversible Aqueous Zinc–CO2 Batteries Based on CO2–HCOOH Interconversion. *Angewandte Chemie - International Edition*, **57** (52), 16996–17001.

122. Tufa, R.A., Chanda, D., Ma, M., Aili, D., Demissie, T.B., Vaes, J., Li, Q., Liu, S., and Pant, D. (2020) Towards highly efficient electrochemical CO2 reduction: Cell designs, membranes and electrocatalysts. *Appl Energy*, **277**, 115557.

123. Xiao, H., Cheng, T., Goddard, W.A., and Sundararaman, R. (2016) Mechanistic Explanation of the pH Dependence and Onset Potentials for Hydrocarbon

Products from Electrochemical Reduction of CO on Cu (111). *J Am Chem Soc*, **138** (2), 483–486.

124. Dutta, N., Bagchi, D., Chawla, G., and Peter, S.C. (2024) A Guideline to Determine Faradaic Efficiency in Electrochemical CO2 Reduction. *ACS Energy Lett*, 323–328.

Chapter 2.2

Pd/Co_3O_4 incorporated BCN composite for Zn-air battery

Summary:

The increasing demand for clean energy has steered research towards developing efficient technologies like zinc-air batteries, thus focusing on improved oxygen evolution/reduction reaction (OER/ORR) to enhance the overall performance of the Zn-air batteries. Efforts are being made to reduce the use of noble metals and metal oxide catalysts such as platinum and iridium/ruthenium oxides in high loading. One approach is to incorporate these noble metals with non-noble metal/metal oxides to alter their electronic properties, thereby enhancing their performance. Our study presents a composite, boron carbon nitride (BCN) matrix incorporated with Pd nanoparticles and Co_3O_4 *nanosheets (Pd-*Co_3O_4*@BCN), offering a remarkable OER/ORR performance to be explored in rechargeable zinc-air batteries.*

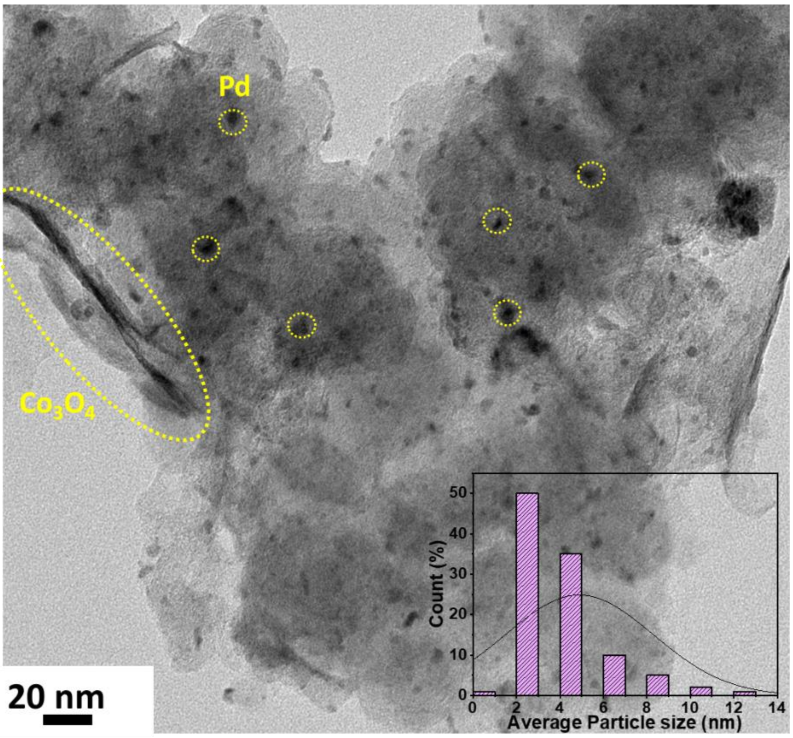

2.2.1 Introduction:

The escalating global energy demand and pressing environmental issues have spurred substantial research in advanced clean energy technologies, focusing on eco-friendly power sources like zinc-air batteries, electrolyzers, and fuel cells.[1,2] These devices heavily rely on oxygen evolution reaction/oxygen reduction reaction (OER/ORR) mechanisms, which traditionally depend on precious metals such as platinum (Pt) for ORR and iridium/ruthenium oxides (IrO_x/RuO_2) for OER as catalysts.[1,3] However, the scarcity and cost of these materials pose significant challenges, necessitating the exploration of low-cost, high-performance alternative materials capable of catalyzing both OER and ORR.[4,5]

Palladium (Pd), akin to Pt in redox properties, emerges as a potential substitute for Pt in ORR, as shown in the volcano plot (**Figure 1a**).[6] The alloying of Pd with non-noble metals like nickel (Ni), cobalt (Co), or copper (Cu) is a common strategy to mitigate its high oxygen-binding strength, thereby optimizing its electrocatalytic performance.[7] Co_3O_4, for instance, exhibits mixed valences and functions effectively in OER due to its chemisorption on octahedral sites (**Figure 1b**).[8] Yet, palladium-incorporated catalysts like PdO_x/Co_3O_4 face challenges like a significant voltage gap and high noble metal loading, which are attributed to insufficient electronic conductivity and suboptimal noble metal utilization.[9]

To enhance the efficiency of noble metals, single-atom catalysts (SAC) anchored on conductive supports like graphene or N-doped carbon have been explored[12,13], although they often suffer from deactivation due to low density of noble metal sites and high accumulation of intermediates on noble metal sites in long term reactions.[14]

Consequently, nanoparticle-based catalysts are increasingly favored over SACs due to their stability and efficiency in prolonged operations.

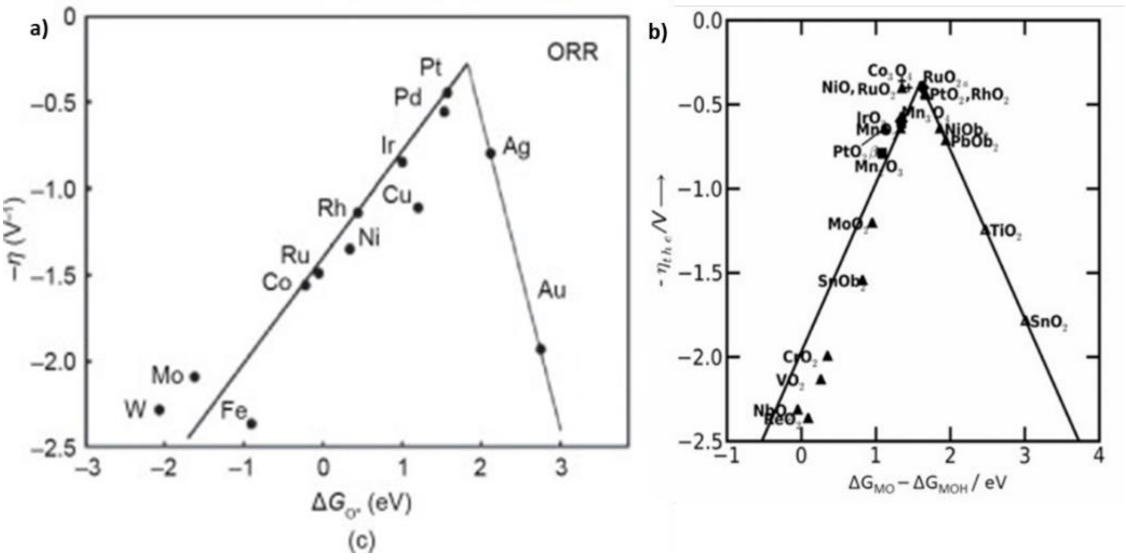

Figure 1. Volcano plots for a) oxygen reduction and b) evolution reaction. *Reproduced with permission from reference* [10,11]

The choice of conductive support is critical in boosting interfacial electron transfer and catalytic efficiency.[15] Carbon-based supports, particularly when doped with heteroatoms like boron (B), nitrogen (N), sulfur (S), or phosphorus (P), have shown promise due to their abundance, low cost, and high surface area.[16][17] Boron carbon nitride (BCN) nanosheets, combining the properties of hexagonal boron nitride (h-BN) and graphene, have emerged as effective supports, facilitating electron transfer in ORR[18,19] and enabling active interaction in OER[20]. Theory suggests that for ORR, B@pyridinic-N pairs exhibit more electron transfer on carbon sites around B than (charge deficient) near pyridinic-N.[21] Meanwhile, for OER, electron-deficient carbon atoms adjacent to N sites can be active for OH^- interaction. Hence, carbon, nitrogen, and boron can synergistically take part in electrochemical processes for OER/ORR.

2.2.2 Scope of Investigation:

We have utilized a bifunctional BCN matrix to anchor Pd nanoparticles and Co_3O_4 nanosheets Pd-Co_3O_4@BCN through a facile wet chemical process. The composite catalyst thus obtained shows a very high mass activity as well as stability for both OER and ORR. The ultra-low Pd loading (1 wt%), coupled with its synergistic interaction with Co_3O_4 and BCN, results in significantly reduced overpotentials, achieving a remarkably low voltage gap of 0.58 V. In the case of ORR, Pd-Co_3O_4@BCN exhibited $E_{1/2}$ at 0.87V and stability up to 15,000 cycles. More importantly, mass activity was 20 times (730 A g^{-1}_{Pd}) that of Pt/C (27 A g^{-1}_{Pt}) at 0.9V. In the case of OER, Pd-Co_3O_4@BCN shows η_{10} of 220 mV, which is far better than RuO_2 (300 mV). Pd-Co_3O_4@BCN also shows high mass activity of 217 A g_{Pd}^{-1} (1.68V), which is 2086 times that of RuO_2, respectively. Additionally, we were able to achieve long-term stability of 270 h at 20 $mAcm^{-2}$, suggesting good adherence of Co_3O_4 and Pd on BCN. The operando Fourier transform infrared spectroscopy, and Raman spectroscopy shows the formation of superoxide radicals, the rate-determining intermediate species, during the reaction. Exploiting this bifunctional electrocatalytic performance, a rechargeable zinc-air battery showing a high capacity of 905 mAh g^{-1}_{Zn} at 50 mA cm^{-2} and long-term stability of 330 h was fabricated.

2.2.3 Experimental Procedure:

i. Materials and Methods:

$CoNO_3.6H_2O$ was procured from SD Fine Chemical Limited, and $PdCl_2$ and $NaBH_4$ were procured from Sigma Aldrich. Vulcan carbon was procured from the Fuel cell store. Boric acid was procured from Emparta, and dicyanamide was purchased from Alfa Aeser. Pt/C, i.e., a state-of-the-art catalyst, was procured from Alfa Aeser. Milli-Q water was used for all experiments.

The synthesized materials were characterized through various established methods. Powder X-ray diffraction (PXRD) patterns were acquired using a Rigaku diffractometer, which employs a copper anode generating X-rays at a wavelength of 1.54 Å, under 30 mA and 40 kV. Transmission electron microscopy (TEM) images were captured using a JEOL JEM 2100 Plus, which was used for the microscopic analysis. Field emission scanning electron microscope (FESEM) images were captured using the Thermo Fisher (FEI) Apreo 2S. (rewrite the sentences). X-ray photoelectron spectroscopy (XPS) data were collected using a Thermo K-alpha+ spectrometer, which utilized micro-focused and monochromated Al Kα radiation of 146.6 eV energy, and the pass energy for recording core-level spectra was maintained at 50 eV. The composition of the elements within the samples was ascertained using Inductively coupled plasma optical emission spectroscopy (ICP-OES) through a PerkinElmer Optima 700DV.

ii. Protocol for Zn-air battery studies:

A two-electrode configuration was employed for battery studies, as delineated in Figure 2. The construction of a homemade cell using acrylic sheets is a practical choice, particularly when dealing with a 6M KOH (potassium hydroxide) solution.[22] Acrylic is chemically inert to the corrosive nature of KOH, ensuring durability and chemical resistance in the cell's structure. The use of an o-ring to seal the cell is a crucial aspect of the design. The o-ring acts as a mechanical gasket, creating a tight seal that prevents leakage of the KOH solution. The selected working electrode, the cathode, was a gas diffusion electrode (GDE) comprising both micro- and macroporous carbon layers.[23] This configuration allowed for the deposition of the catalyst ink onto the microstructured carbon layer. A stainless-steel (SS) mesh was incorporated as the current collector.[24] A zinc foil was utilized as an anode for the counter and reference electrode. The electrodes were coated to an effective surface area of 1.6 cm^2. The electrolyte was formulated from a mixture of 6M KOH and 0.2M zinc acetate solution.

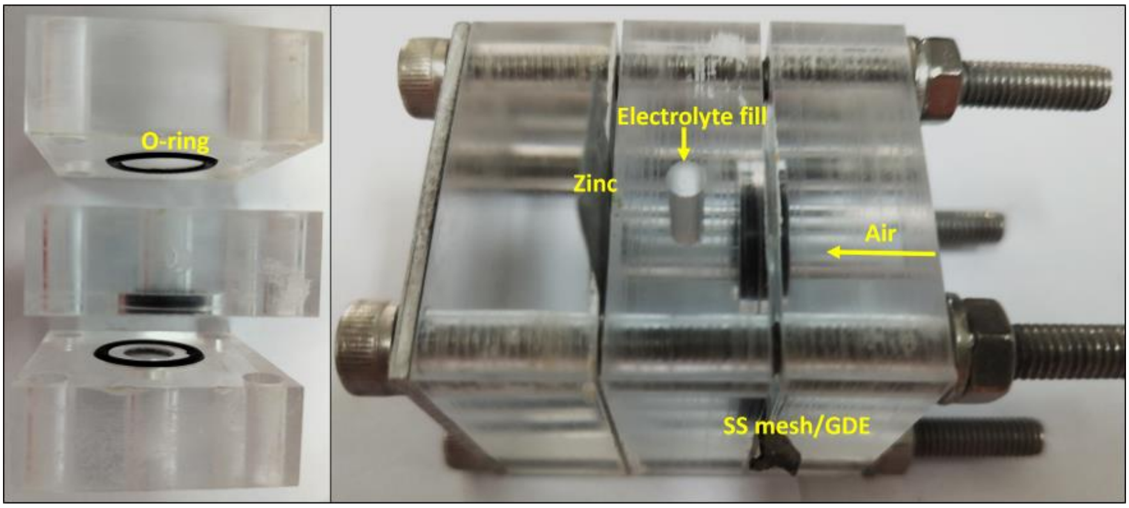

Figure 2. a) Setup for Zinc-air battery with b) Zn foil (anode) and gas diffusion electrode (GDE) with stainless steel (SS) mesh (cathode). The cathode side of the setup is designed with a hollow section to allow air inlet.

iii. Synthesis protocols of electrocatalysts

a. Synthesis of cobalt oxide nanosheets (Co_3O_4):

Cobalt oxide nanosheets wet chemical synthesis was opted. The initial setup involved the dissolution of 0.1M $CoNO_3$, $6H_2O$ in 5 mL water. $NaBH_4$ was added in excess volume (5 times the metal salt solution). 0.1M solution of $NaBH_4$ was added quickly to the metal salt solution and kept under stirring. A huge amount of effervescence was observed, and it settled down within a few seconds of stirring. The stirring was sustained for an additional 30 minute post-addition. This reaction resulted in the precipitation of a black residue, which was subsequently collected. Purification procedures included washing the precipitate with milli-Q water to remove unreacted species or side products. Following this, the precipitate was dried at a temperature of 60°C, extending over an overnight period. The final, brown-coloured product, designated as Co_3O_4, was thoroughly characterized to ascertain its properties and confirm its structure.

b. Synthesis of palladium nanosponges (Pd):

In the synthesis of Pd nanosponges, the initial step involved the preparation of 50 mL of a 0.1M H_2PdCl_4 solution. This solution was prepared by dispersing 0.88 g of $PdCl_2$ in 50 mL of distilled water (H_2O), to which 0.2M HCl was subsequently added. This mixture underwent continuous stirring for 24 hours, ensuring a complete dissolution of the salt.

In the second step, 16 mL of a 0.1M $NaBH_4$ solution was rapidly mixed with a 4 mL aliquot of the H_2PdCl_4 solution (0.1 M concentration) while maintaining vigorous stirring. The stirring was sustained for an additional 30 minutes post-addition. This reaction resulted in the precipitation of a black residue, which was subsequently collected. The precipitate was washed well with milli-Q water to remove any unreacted species or side products and dried at a temperature of 60°C for an overnight period. The final product, designated as Pd, was thoroughly characterized to ascertain its properties and confirm its structure.

c. Synthesis of Pd-Co_3O_4:

0.1M $CoNO_3.6H_2O$ was first dissolved in 3.225 mL of H_2O, followed by the addition of 0.679 mL of 0.1M H_2PdCl_4. Subsequently, 0.1M $NaBH_4$, in a quantity six times the volume of the solution (19.35 mL), was introduced. This process was conducted following a methodology similar to the aforementioned synthesis.

d. Synthesis of Borocarbonitride (BCN):

The synthesis of BCN was carried out using a straightforward thermal annealing method. Initially, 1 gram of Vulcan carbon was combined with 0.31 grams of boric acid and 1.26 grams of dicyandiamide. This mixture was uniformly integrated through wet impregnation in 70 mL of H_2O, followed by stirring at 70°C in an oil bath. After drying completely, the mixture was annealed at 900°C for 10 h under a nitrogen atmosphere.

This step was followed by a subsequent annealing at 930°C for 4 h in an ammonia atmosphere. For further purification, the black-colored powder was washed in warm water (70°C) twice to remove the borates, followed by a final wash in ethanol. The precipitate was dried in the oven at 60°C for an overnight duration.

e. Synthesis of Co_3O_4@BCN:

The synthesized BCN, weighing 64 mg, was dispersed in 3.225 mL of H_2O, to which $CoNO_3.6H_2O$ (93 mg) was added to achieve a concentration of 0.1M. The mixture of BCN and cobalt metal salt solution was then sonicated for 15 minutes to ensure a uniform dispersion. To this, 0.1M $NaBH_4$ was added (19.35 mL), and the subsequent steps were performed in a manner similar to the previous Pd-Co_3O_4 synthesis, resulting in the formation of Co_3O_4@BCN.

f. Synthesis of Pd@BCN:

The synthesized BCN, weighing 64 mg, was dispersed in 3.225 mL of H_2O, to which 0.679 mL of 0.1M of H_2PdCl_4 was added and sonicated for 15 minutes, followed by the addition of 19.35 mL of 0.1M $NaBH_4$ solution. The stirring was sustained for an additional 30 minutes post-addition. This reaction resulted in the precipitation of a black residue, which was subsequently collected. The precipitate was washed well with milli-Q water to remove any unreacted species or side products and dried at a temperature of 60°C for an overnight period. The final product, designated as Pd@BCN, was thoroughly characterized to ascertain its properties and confirm its structure.

g. Synthesis of Pd-Co_3O_4@BCN:

The synthesized BCN, weighing 64 mg, was dispersed in 3.225 mL of H_2O, to which 0.679 mL of 0.1M of H_2PdCl_4 and 93 mg of $Co(NO)_3.6H_2O$ (0.1M) was added and sonicated for 15 minutes followed by the addition of 19.35 mL of 0.1M $NaBH_4$ solution.

The stirring was sustained for an additional 30 minutes post-addition. This reaction resulted in the precipitation of a black residue, which was subsequently collected. The precipitate was washed well with milli-Q water to remove any unreacted species or side products and dried at a temperature of 60°C for an overnight period. The final product, designated as Pd-Co_3O_4@BCN, was thoroughly characterized to ascertain its properties and confirm its structure.

h. Synthesis of Pd-Co_3O_4@VC:

Vulcan carbon was taken instead of BCN, and Co and Pd, metal salt solutions, were reduced following a procedure similar to that of Pd-Co_3O_4@BCN.

iv. Electrochemical studies:

The electrodes, i.e., RDE, GCE, and carbon paper, were used as working electrodes. Mercury/ mercuric oxide (MMO) electrode was employed as a reference electrode in a basic medium, i.e., 0.1M KOH and 1M KOH for ORR and OER, respectively. Counter electrodes used for ORR and OER reactions are graphite rod and Pt wire, respectively. Pt wire was avoided in case of ORR reaction as they might oxidize and get deposited on our catalyst (working electrode) and may provide false positive results.

v. Working electrode preparation:

Rotating disk electrode (RDE) was utilized for ORR studies, while glassy carbon electrode (GCE) and carbon were utilized for OER studies. The effective area of GCE and RDE was 0.07068 $cm^{2,}$ and the carbon paper was 0.25 cm^2.

a. Coating ink of Pd-Co_3O_4@BCN, Pd@BCN, Co_3O_4@BCN, Pd-Co_3O_4@VC, BCN, VC, Pt/C and RuO_2 catalysts for RDE and GCE was prepared as follows:

In the procedure, 2 mg of the catalyst was thoroughly dispersed in a mixture of 700 µl of H_2O and 300 µl of isopropyl alcohol. This dispersion was then sonicated for 1 h, after which 10 µl of a 5 wt% Nafion solution was added. To ensure uniform distribution of the Nafion within the catalyst mixture, the solution was bath sonicated for 1 h. Subsequently, 7 µl of this catalyst ink was applied onto the surfaces of both a rotating disk electrode (RDE) and a glassy carbon electrode (GCE). The electrodes were then left to dry at room temperature for 12 h before being subjected to testing.

b. Coating ink for Pd-Co_3O_4@BCN, Pd@BCN, Co_3O_4@BCN, Pd-Co_3O_4@VC, and RuO_2 electrocatalysts to be coated on carbon paper was prepared as follows:

In the procedure, 2 mg of the catalyst was thoroughly dispersed in a mixture of 1 mL of isopropyl alcohol. This dispersion was then sonicated for 1 h, after which 50 µl of a 5 wt% Nafion solution was added. To ensure uniform distribution of the Nafion within the catalyst mixture, the solution was bath-sonicated for an hour. Subsequently, 50 µl of catalyst ink was drop cast on both sides of carbon paper. The electrodes were then left to dry at room temperature for 12 h before being subjected to testing for ORR/OER.

c. Coating ink for Co_3O_4, Pd, Pd-Co_3O_4 and RuO_2 electrocatalysts was prepared as follows:

~0.4 mg of Co_3O_4, ~0.05 mg of Pd, 0.4 mg of Pd-Co_3O_4, 1.6 mg BCN/ VC, and 2 mg of RuO_2 of catalyst was thoroughly dispersed in a mixture of 700 µl of H_2O and 300 µl of isopropyl alcohol. This dispersion was then sonicated for 1 h, after which 10 µl of a 5 wt% Nafion solution was added. To ensure uniform distribution of the Nafion within the catalyst mixture, the solution was bath sonicated for 1 h. Subsequently, 7 µl of this catalyst ink was applied onto the surfaces of both a rotating disk electrode (RDE) and a glassy carbon electrode (GCE). The electrodes were then left to dry at room temperature for 12 h before being subjected to testing.

d. Coating ink of ~0.4 mg of Co_3O_4, ~0.05 mg of Pd, 0.4 mg of Pd-Co_3O_4, 1.6 mg BCN/ VC, and 2 mg of RuO_2 of catalyst was prepared as follows:

Catalysts were thoroughly dispersed in a mixture of 1 mL of isopropyl alcohol. This dispersion was then sonicated for 1 h, after which 50 µl of a 5 wt% Nafion solution was added. To ensure uniform distribution of the Nafion within the catalyst mixture, the solution was bath-sonicated for an hour. Subsequently, 50 µl of catalyst ink was drop cast on both sides of carbon paper.

It is to be noted that the metal loading of Co and Pd on GCE, RDE, and carbon paper are kept Constant in all samples constituting of Co_3O_4, Pd, Pd-Co_3O_4, Co_3O_4@BCN, Pd@BCN, and Pd-Co_3O_4@BCN.

vi. Linear sweep Voltammetry (LSV) and stability studies:

For ORR and OER, LSV was carried out at a scan rate of 5 mV s^{-1}. Three consecutive LSVs are acquired to attain overlapping curves finally, and the final one is plotted for comparison and further analysis.

vii. Calculation of number of electrons in ORR:

It is calculated by Kouteck Levich equation[25][26]:

$$\frac{1}{i_L} = \frac{1}{i_K} + \left(\frac{1}{0.620nFAD^{\frac{2}{3}}v^{\frac{-1}{6}}C}\right)\omega^{\frac{-1}{2}} \quad (1)$$

Where J is the measured current density, J_K and J_L are the kinetic- and diffusion-limiting current densities, ω is the angular velocity of the disk (ω=2pN, N is the linear rotation speed), n is the overall number of electrons transferred in oxygen reduction, F is the

Faraday constant (F=96485 C·mol^{-1}), C_0 is the bulk concentration of O_2, (C_0 =1.2×10^{-6}mol·cm^{-3}),ν is the kinematic viscosity of the electrolyte (ν=0.01 cm^2 ·s $^{-1}$), D_0 is the diffusion coefficient of O_2 in 0.1 M KOH (1.9 × 10^{-5} cm^2 ·s^{-1}).

viii. **ECSA Calculation** [27]:

$C_{dl} = \Delta j\ (j_a - j_c)/\ 2\nu$ (2)

Where j_a and j_c are anodic and cathodic current density and ν is the scan rate (mV s^{-1}).

$ECSA = C_{dl}/\ C_S$

C_{dl} is double-layer capacitance, and C_S is specific capacitance.

2.2.4 Results and discussion:

a. Spectroscopic and Microscopic Characterizations

The composition of Pd and Co in Pd-Co_3O_4@BCN was found to be 1.0 and 15wt% for Pd and Co, respectively. The composition of Pd and Co in Pd-Co_3O_4@BCN was determined using inductively coupled plasma optical emission spectroscopy (ICP-OES) and was found to be 1.0 wt% for Pd and 15 wt% for Co, respectively. X-ray diffraction (XRD) patterns (**Figure 3a and 3b)** for BCN, Co_3O_4@BCN, Pd@BCN, and Pd-Co_3O_4@BCN show broad peak at 25.6°, which indicate poor crystallinity of carbon in BCN. A weak peak at two theta 40° corresponds to the (111) crystal plane of the face-centered cubic structure of metallic palladium (Pd) was observed in Pd, Pd-Co_3O_4, Pd@BCN and Pd-Co_3O_4@BCN.[28] Notably, there were no signature peaks for Co_3O_4 in the XRD patterns of Co_3O_4, Pd-Co_3O_4, Pd-Co_3O_4@BCN, and Co_3O_4@BCN.

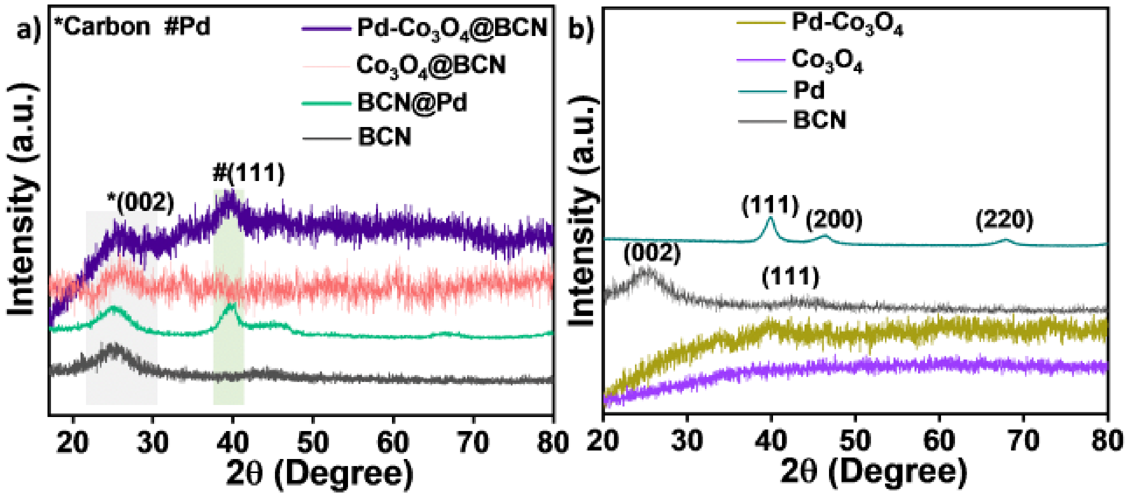

Figure 3. PXRD pattern of a) Pd-Co_3O_4@BCN, Co_3O_4@BCN, Pd@BCN, and BCN. PXRD pattern of control samples b) Pd-Co_3O_4, Co_3O_4, Pd and BCN.

However, the presence of Co_3O_4 was confirmed using Raman spectroscopy (**Figure 4a and b).** It shows three characteristic Raman-active modes identified at 691 cm^{-1} (A_{1g}), 482 cm^{-1} (E_g), and 522 cm^{-1} (F_{2g}) corresponding to Co_3O_4 in Co_3O_4@BCN and Pd-Co_3O_4@BCN.[29] Additionally, the D (defect) and G (graphitic) bands, indicative of the out-of-plane and in-plane vibrations of BCN, were observed at 1340 cm^{-1} and 1590 cm^{-1}, respectively (**Figure 4a**). No peak associated with Pd was detected in the Raman spectrum, which confirms the metallic nature of Pd in Pd@BCN and Pd-Co_3O_4@BCN (**Figure 4a and b**).[30]

The combined XRD and Raman analyses suggest that in Pd-Co_3O_4@BCN, Co_3O_4 is amorphous, and Pd is in its metallic form.

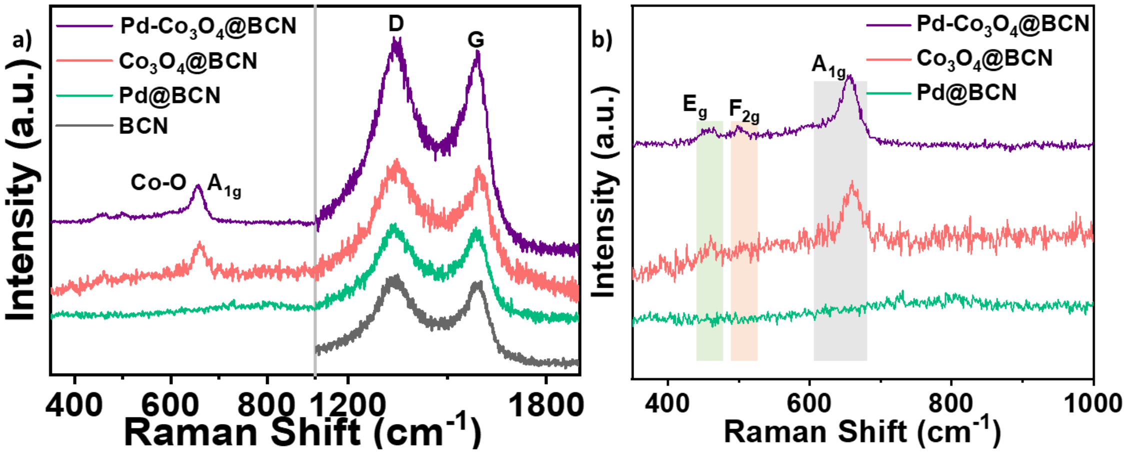

Figure 4. Raman spectra of Pd-Co_3O_4@BCN, Co_3O_4@BCN, Pd@BCN and BCN.

Fourier Transform Infrared (FT-IR) spectroscopy further confirmed the presence of BCN in Pd-Co_3O_4@BCN (**Figure 5**). The strong bending vibrational signals for B-N were observed at 801 cm^{-1} (in-plane) and 1422 cm^{-1} (out-of-plane), while the peaks at 1554, 1193, and 1087 cm^{-1} could be assigned to C=C stretching, C-N stretching, and B-C vibrations, respectively (**Figure 5a and b**).[31] **Figure 5b** shows weak signatures of metal-O stretching, i.e., Co-O (Co_3O_4) and Pd-O (Pd) at 660 cm^{-1} and 682 cm^{-1} respectively.[32,33]

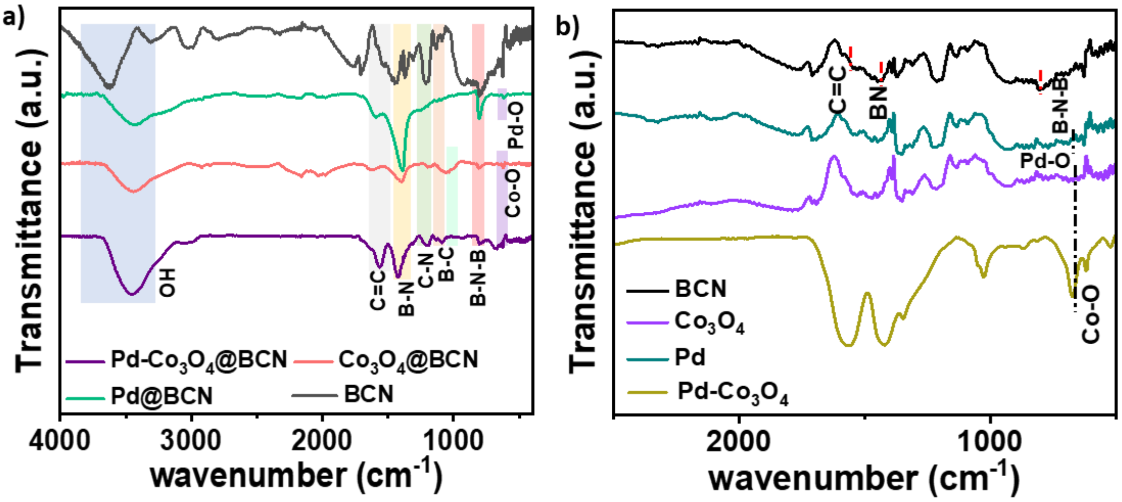

Figure 5. FTIR spectra of a) Pd-Co_3O_4@BCN, Co_3O_4@BCN, Pd@BCN, and BCN. FT-IR spectra of control samples b) Co_3O_4, Pd, Pd-Co_3O_4 and BCN.

Nitrogen adsorption/desorption analysis (**Figure 6**) indicated a change in surface area upon the introduction of metal onto BCN. Brunauer-Emmett-Teller (BET) analysis showed the surface area of BCN decreasing from 344 m^2 g^{-1} to 137 m^2 g^{-1} after incorporation of Pd-Co_3O_4. This reduction in surface area is likely due to the occupation of BCN pores and surface by Pd and Co_3O_4 particles. The calculated surface area for all samples is tabulated in **Table 1**.

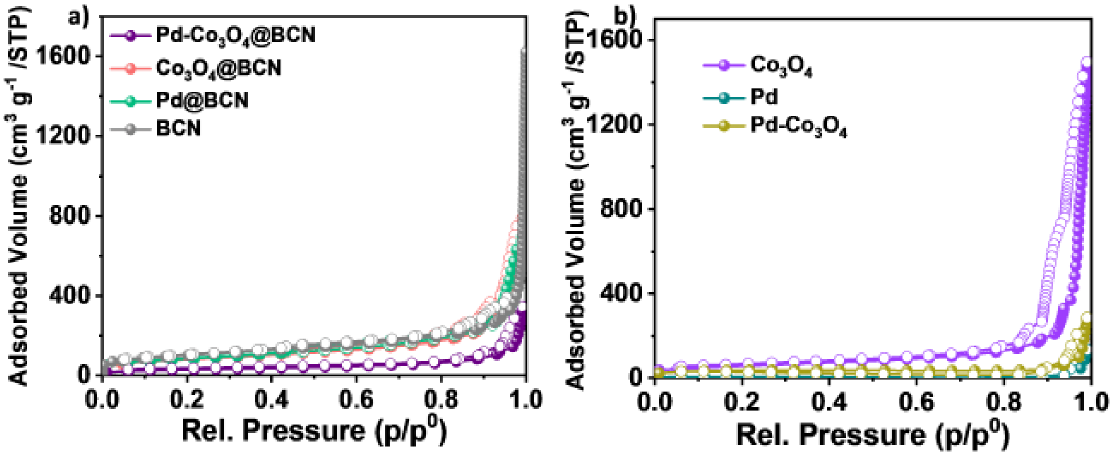

Figure 6. N_2 adsorption/ desorption of a) Pd-Co_3O_4@BCN, Co_3O_4@BCN, Pd@BCN, and BCN. N_2 adsorption/ desorption of control samples b) Co_3O_4, Pd and Pd-Co_3O_4.

Samples	**Surface area** (**m^2 g^{-1}**)
Co_3O_4	209
Pd	20
Pd-Co_3O_4	154
BCN	344
Co_3O_4@BCN	288
Pd@BCN	207
Pd-Co_3O_4@BCN	137

Table 1. Comparison of surface area of Co_3O_4, Pd, Pd-Co_3O_4, BCN, Co_3O_4@BCN, Pd@BCN and Pd-Co_3O_4@BCN.

The interaction and chemical composition of Pd, Co_3O_4, and BCN in Pd-Co_3O_4@BCN were explored using X-ray Photoelectron Spectroscopy (XPS) (**Figures 7-9**). The Co 2p spectra from XPS analysis of Pd-Co_3O_4@BCN show a significant negative shift in the electronic structure of cobalt species (Co^{3+}/Co^{2+}) compared to Co_3O_4@BCN, as indicated in **Figure 7a and Table 2**. Additionally, a negative shift was observed in Pd-Co_3O_4 and Co_3O_4@BCN compared to Co_3O_4 (**Figures 8 and 9**). On comparing all binding energies for Co 2p (Co^{2+} and Co^{3+}), the order is as follows: Co_3O_4 > Co_3O_4@BCN > Pd-Co_3O_4 > Pd-Co_3O_4@BCN as shown in **table 2**. This indicates the direction of charge transfer is from BCN and Pd towards Co_3O_4.

Furthermore, the high-resolution Pd-3d core level XPS spectra[34] of Pd-Co_3O_4@BCN and Pd@BCN (**Figure 7b**) reveal that in Pd-Co_3O_4@BCN, Pd $3d_{5/2}$ exhibits a positive shift of 0.3 eV for Pd^0 and Pd^{2+} peak, compared to Pd@BCN (refer **table 3**). This positive shift indicates charge transfer from Pd to Co_3O_4. In Pd-Co_3O_4@BCN, Pd^0 is negatively shifted compared to Pd-Co_3O_4, implying charge transfer from BCN to Pd (**Figure 7b and 8b**).

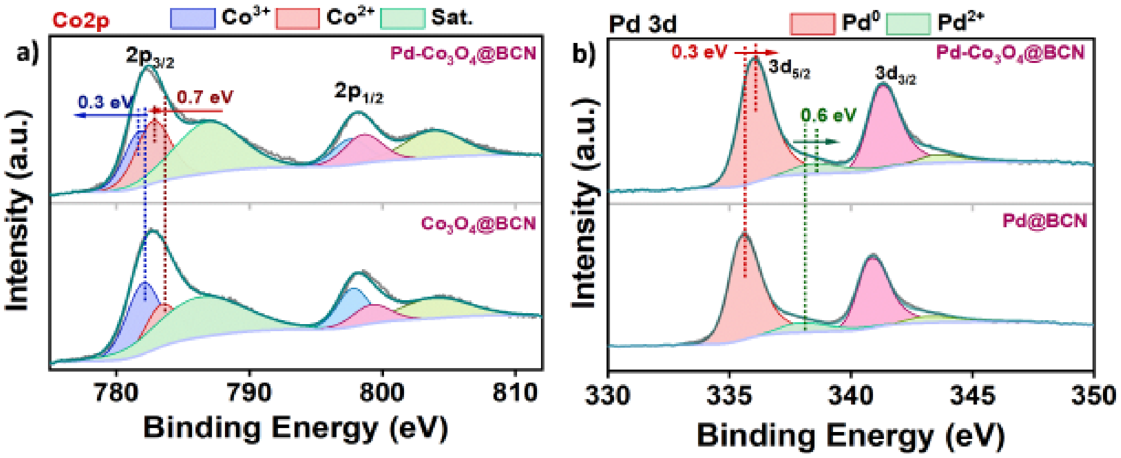

Figure 7. High-resolution XPS spectra of Co 2p for a) Pd-Co_3O_4@BCN and Co_3O_4@BCN compared. High-resolution XPS spectra of Pd 3d for a) Pd-Co_3O_4@BCN and Pd@BCN compared.

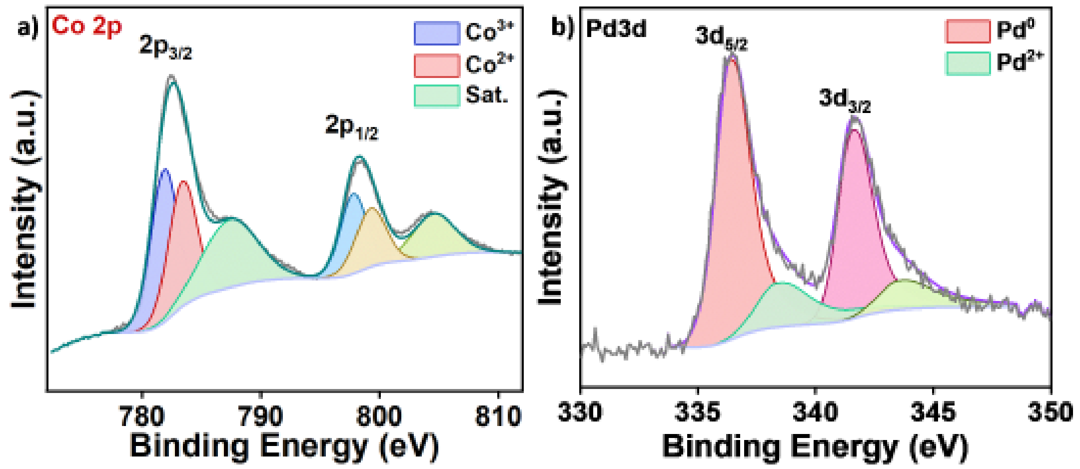

Figure 8. High-resolution XPS spectra of a) Co 2p and b) Pd 3d of Pd-Co_3O_4.

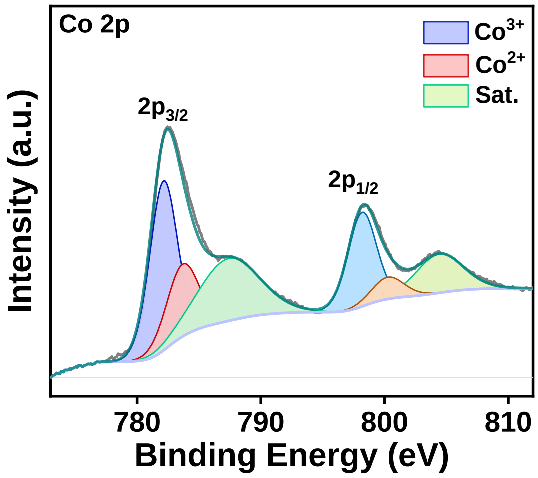

Figure 9. High-resolution XPS spectra of a) Co 2p for Co_3O_4 electrocatalyst.

Co 2p	**$Co^{3+}(2p_{3/2})$**	**$Co^{2+}(2p_{3/2})$**	**Sat.**
Co_3O_4	782.26	783.96	787.66
Co_3O_4@BCN	782.16	783.66	786.76
Pd-Co_3O_4	782	783.4	787.7
Pd-Co_3O_4@BCN	781.84	782.94	787.14

Table 2. Comparison of binding energy values of Co 2p for Pd-Co_3O_4, Co_3O_4@BCN, and Pd-Co_3O_4@BCN from high-resolution XPS spectra.

Pd 3d	**$Pd^0(3d_{5/2})$**	**$Pd^{2+}(3d_{5/2})$**

Pd-Co_3O_4	336.4	338.6
Pd@BCN	335.7	338.3
Pd-Co_3O_4@BCN	336	338.6

Table 3. Comparison of binding energy values of Pd 3d for Pd-Co_3O_4, Pd@BCN, and Pd-Co_3O_4@BCN from high-resolution XPS spectra.

In summarizing the charge transfer from XPS analysis, BCN exhibits charge transfer to both Pd and Co_3O_4, and Pd shows charge transfer to Co_3O_4, as simplified in **Figure 10**.

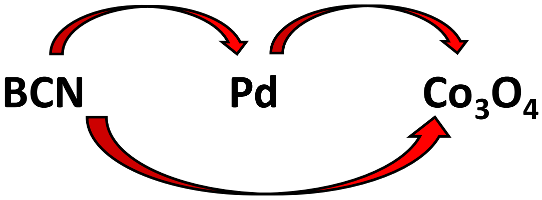

Figure 10. Schematic illustrating the direction of charge transfer in Pd-Co_3O_4@BCN based on shifts in binding energy values from XPS spectra.

To delve deeper into the heteroatom interaction in Pd-Co_3O_4@BCN with Pd/Co_3O_4, core level spectra of C1s, B1s, O1s, and N1s were examined (**Figures 11 and 12**). The high-resolution N1s spectra show a decrease in pyridinic-N+B-N peak content from 76% in BCN to 57% in Pd-Co_3O_4@BCN upon the introduction of Pd/Co_3O_4, indicating interaction between pyridinic-N+B-N and Pd/Co_3O_4.[20] The atomic and weight percentages of each element are tabulated in **Tables 4 and 5** for BCN and Pd-Co_3O_4@BCN.

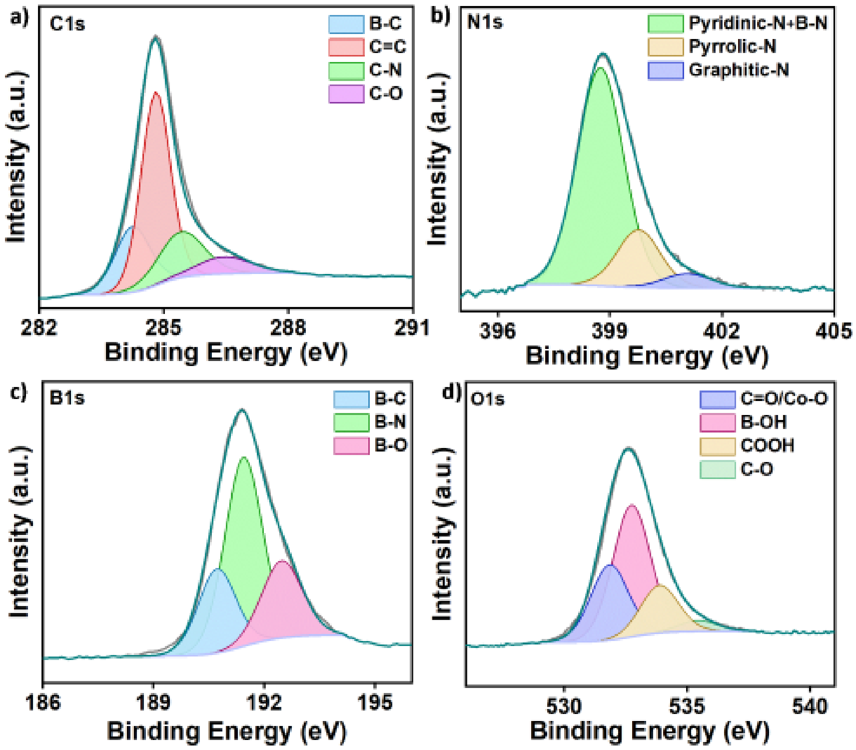

Figure 11. High-resolution XPS spectra of elements a) C 1s, b) N 1s, c) B 1s, and O 1s for BCN.

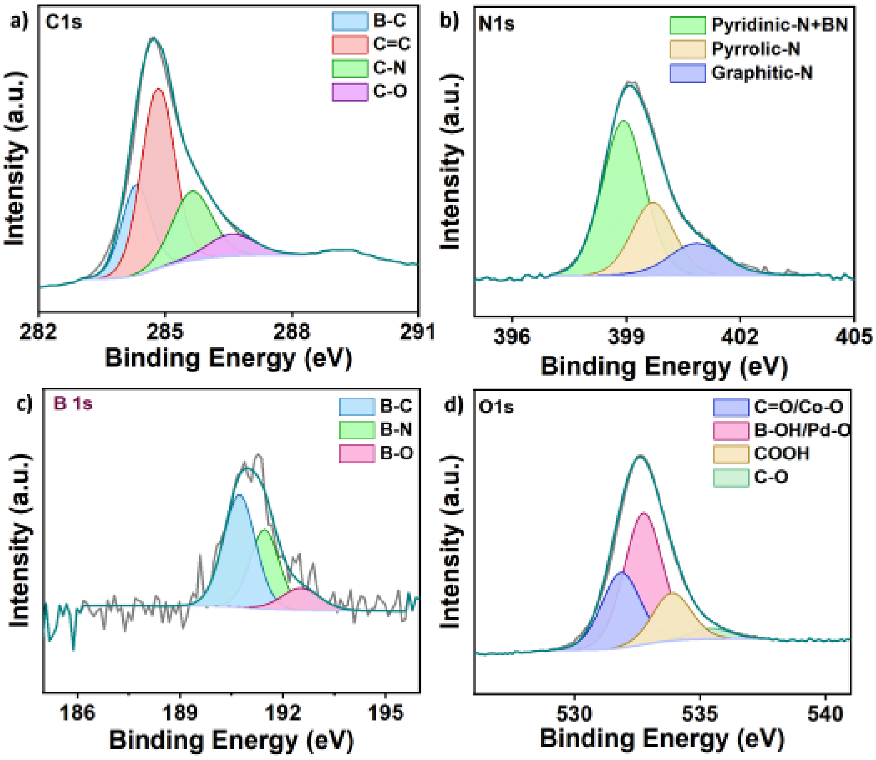

Figure 12. High-resolution spectra of elements a) C 1s, b) N 1s, c) B 1s, and d) O 1s for Pd-Co_3O_4@BCN.

BCN	Atomic%	Weight%
Boron	12.25	10.88
Nitrogen	10.46	12.03
carbon	74.59	73.59
oxygen	2.7	3.55

Table 4. Relative atomic and weight percentage in BCN.

Pd-Co_3O_4@BCN	Atomic%	Weight%
Boron	12.48	9.2
Nitrogen	6.74	6.44
carbon	57.1	46.76
oxygen	19.8	21.6
Co	3.73	15
Pd	0.14	1

Table 5. Relative atomic and weight percentage in Pd-Co_3O_4@BCN.

To corroborate the charge transfer process identified in the XPS analysis, X-ray Absorption Near Edge Structure (XANES) examinations were performed, as illustrated in **Figure 13**. The energy value of Co foil (K-edge) is 7709 eV, and Pd foil (K-edge) is 24350 eV. All the cobalt-based electrocatalysts show a higher oxidation state/ positive shift compared to Co metal foil, with Co_3O_4@BCN having the highest positive shift. Additionally, In the case of Pd K-edge spectra,[35] BCN-based samples show a lower oxidation state/ negative shift, indicating charge transfer from BCN to Pd/ Co_3O_4. The observed shift in the pre-edge region in XANES analysis aligns with the trends noted in the XPS results, further confirming the charge transfer from BCN to both Pd and Co_3O_4, as well as from Pd to Co_3O_4.

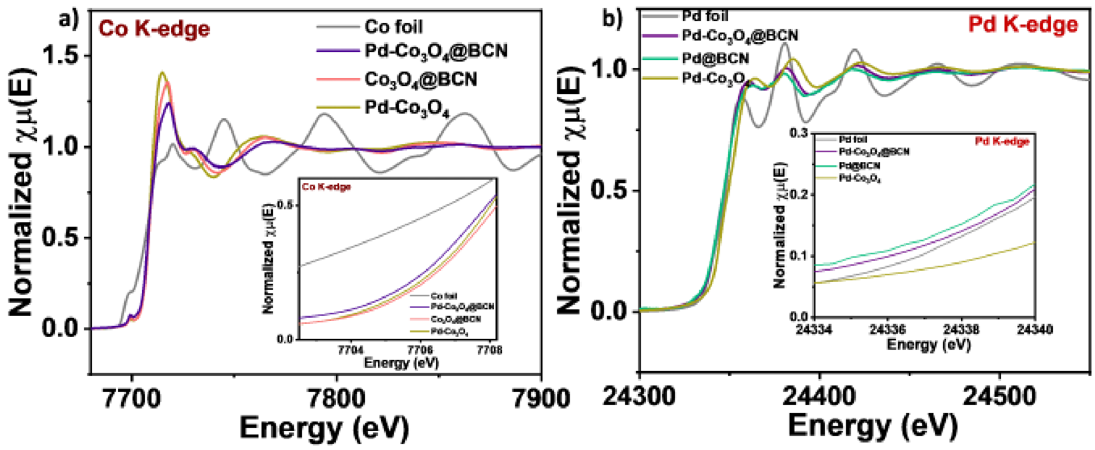

Figure 13. a) Comparison of normalized XANES spectra of Co-K edge of Pd-Co_3O_4@BCN, Co_3O_4@BCN, Pd-Co_3O_4 with Co foil. b) Comparison of normalized XANES spectra of Pd-K edge of Pd-Co_3O_4@BCN, Pd@BCN, Pd-Co_3O_4 with Pd foil.

To analyze the elemental distribution in the Pd-Co_3O_4@BCN composite, elemental mapping (EDS) was employed, as shown in **Figure 14.** This uniformity is crucial as it indicates a homogenous integration of Co_3O_4 and Pd nanoparticles within the BCN matrix, which is essential for ensuring consistent catalytic activity and stability.

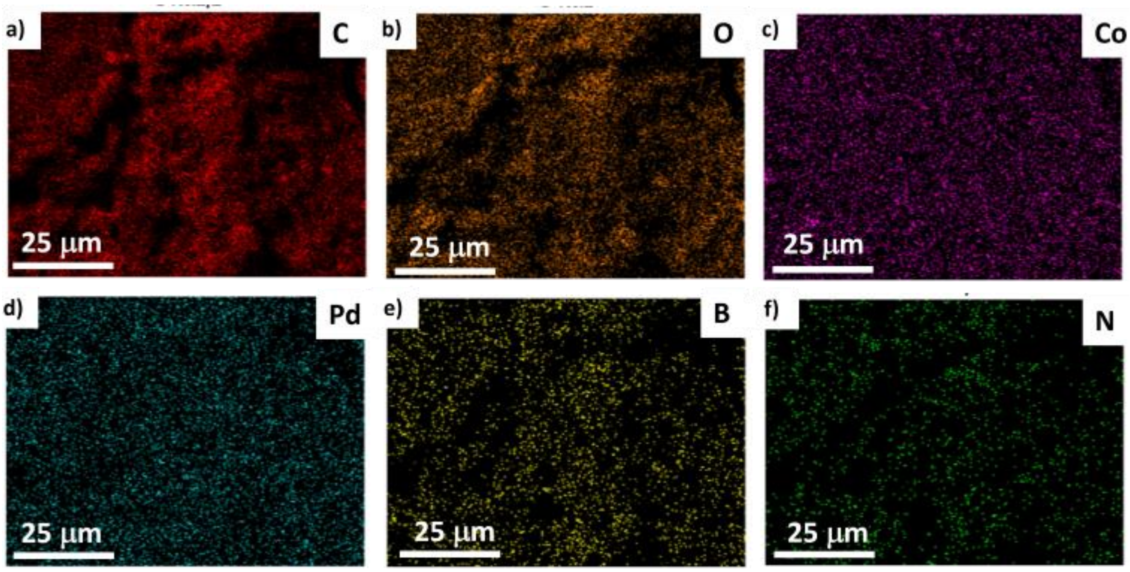

Figure 14. Elemental mapping images of Pd-Co_3O_4@BCN.

The bright field transmission electron microscopy (TEM) image (**Figure 15a**) and the high-angle annular dark-field scanning transmission electron microscopy (HAADF-STEM) image (**Figure 15b**), along with the accompanying elemental mapping (**Figures**

15c-g), reveal a uniform dispersion of both Pd nanoparticles(of size 2-3 nm), and Co_3O_4 folded nanosheets across the BCN nanosheets (spherical form like Vulcan carbon).

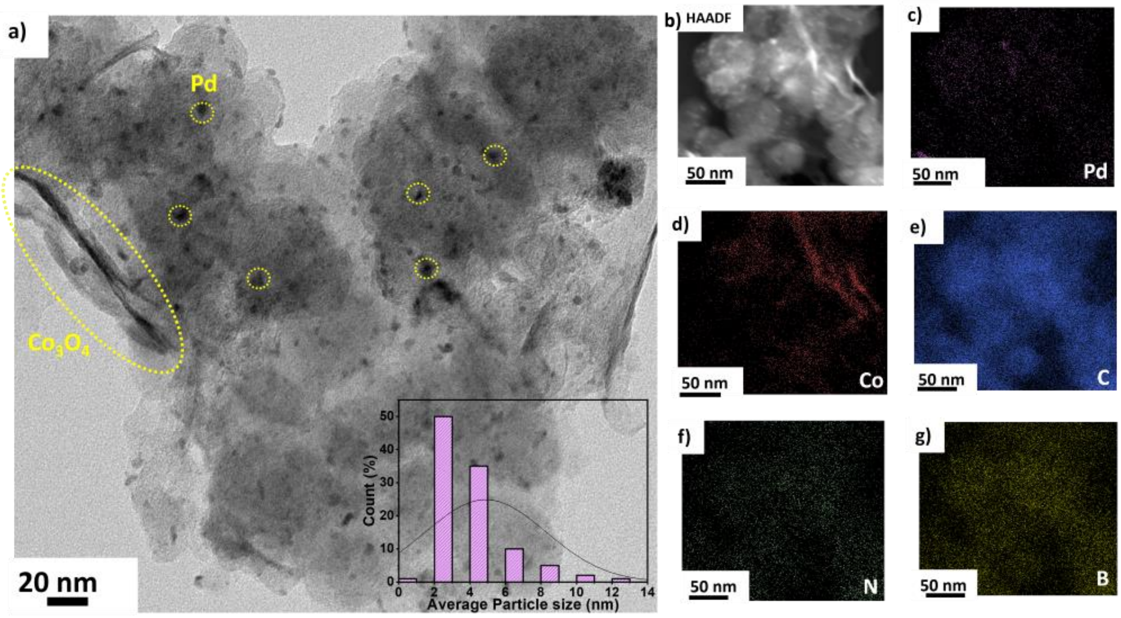

Figure 15. a) Bright-field TEM image of Pd-Co_3O_4@BCN with inset histogram of Pd nanoparticle size on BCN matrix. b) HAADF-STEM mapping image and c-g) elemental mapping of Pd, Co, C, N, and B elements for Pd-Co_3O_4@BCN.

Conversely, for Pd-Co_3O_4, the simultaneous reduction of Pd and Co_3O_4 results in a non-uniform distribution of larger Pd nanoparticles, ranging from 10-50 nm, aggregated on Co_3O_4 nanosheets (**Figure 16 and 17a**). BCN, on the other hand, helps stabilize 2- to 3-nm Pd nanoparticles as well as Co_3O_4 nanosheets on its surface (**Figure 17a** and **Figure 18b).**

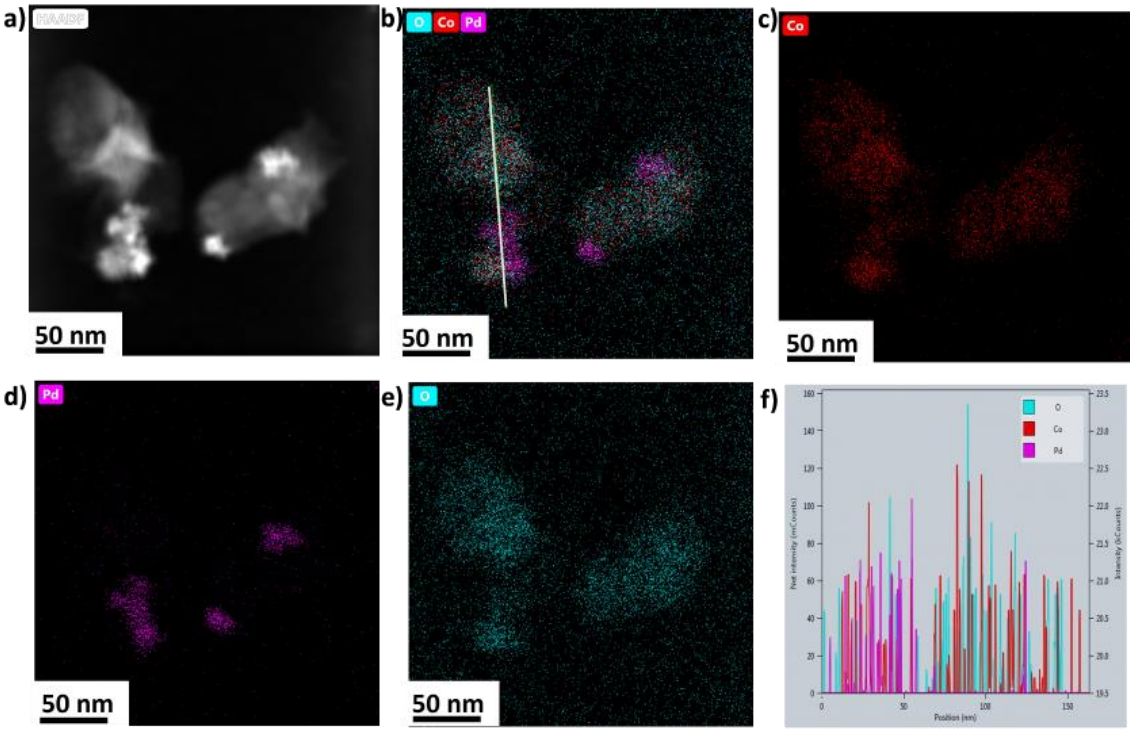

Figure 16. a) HAADF-STEM image and elemental mapping of elements b) overlapped, c) Co, d) Pd, e) O and line scan spectra for control sample Pd-Co_3O_4.

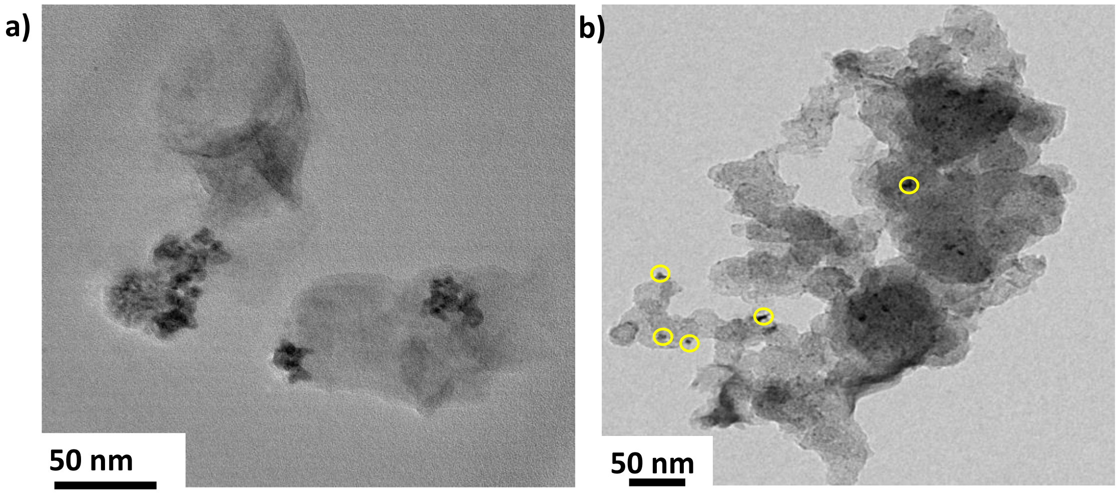

Figure 17. Bright field TEM images of a) Pd-Co_3O_4 and b) Pd@BCN.

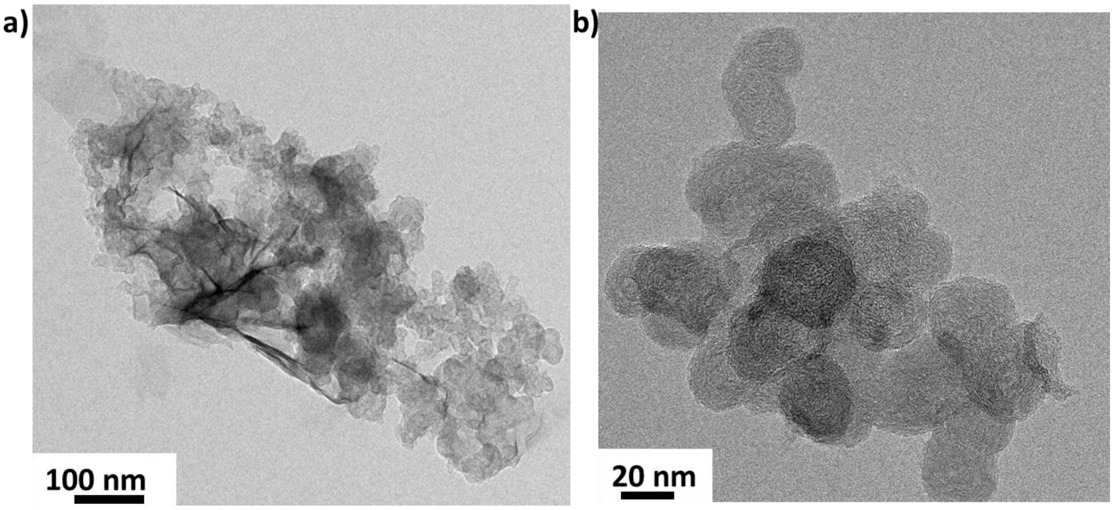

Figure 18. Bright-field TEM images of a) Co_3O_4@BCN and b) BCN.

a. Electrochemical studies for oxygen reduction reaction:

The promising attributes of Pd-Co_3O_4@BCN as a catalyst were further explored in an electrochemical setting, particularly for the oxygen reduction reaction (ORR) in an oxygen-saturated 0.1M KOH electrolyte. Key evaluation parameters for the catalyst included onset potential (E_{onset}), half-wave potential ($E_{1/2}$) as determined by linear sweep voltammograms, mass activity, Tafel slope, electrochemically active surface area (ECSA), and assessments from stability tests.

For the experimental setup, a rotating disk electrode (RDE) was coated with 14 µg cm^{-2} of the Pd-Co_3O_4@BCN catalyst. The RDE polarization curves (**Figure 19**) revealed that Pd-Co3O4@BCN exhibited the most positive onset overpotential at 1.056 V, surpassing the state-of-the-art Pt(20wt%)/C catalyst at 0.996 V. Notably, Pd-Co_3O_4@BCN achieved a higher half-wave potential ($E_{1/2}$ = 0.87 V vs. RHE) compared to Pd@BCN, Co_3O_4@BCN, BCN, and even Pt/C ($E_{1/2}$ = 0.85 V). In fact, the limiting current density for Pd-Co_3O_4@BCN exhibits a higher value than Pt/C and all the control catalysts, as shown in **Table 6**. It is to be noted that BCN, as such, shows better activity than Vulcan carbon in terms of half-wave potential and limiting current density, clearly indicating the role of boron and nitrogen (**Figure 20**).

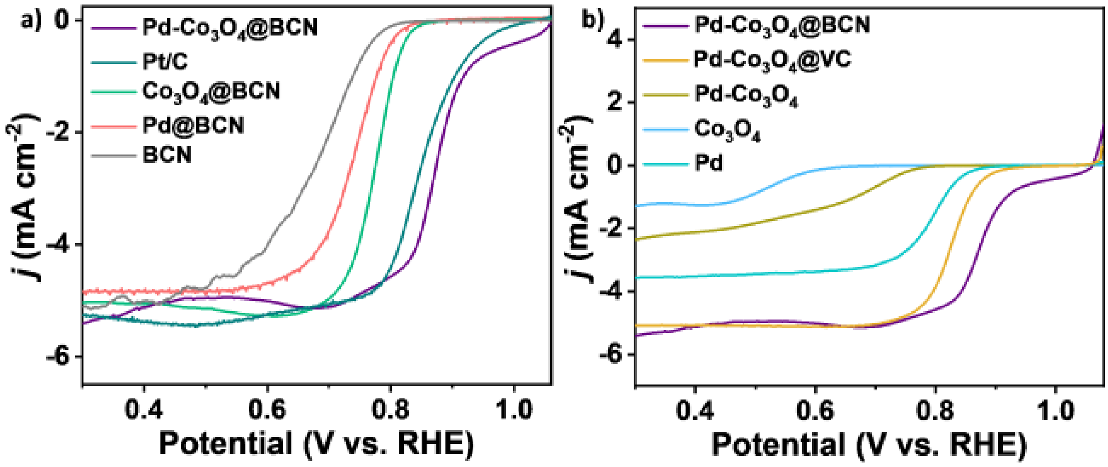

Figure 19. Comparison of linear sweep voltammograms of a) Pd-Co_3O_4@BCN, Pt/C, Co_3O_4@BCN, Pd@BCN, and BCN at a scan rate of 5 mV s^{-1} for oxygen reduction reaction. Comparison of linear sweep voltammograms of b) Pd-Co_3O_4@BCN, Pd-Co_3O_4@VC, Pd-Co_3O_4, Co_3O_4, and Pd.

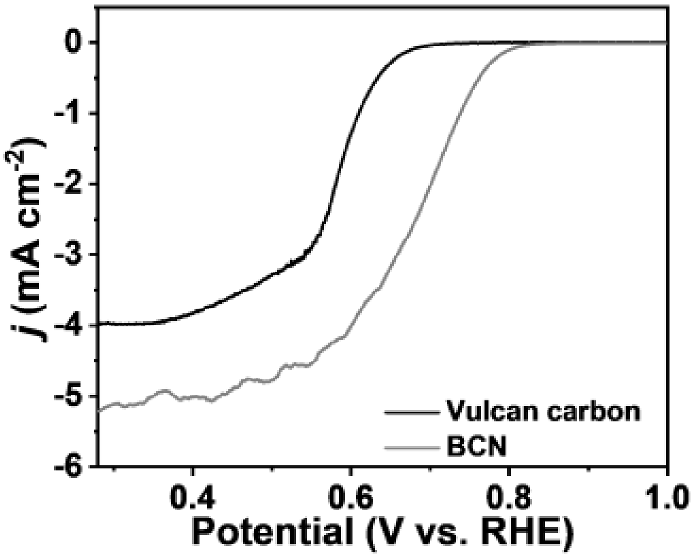

Figure 20. Linear sweep voltammograms of Vulcan carbon and BCN were compared at a scan rate of 5 mV s^{-1}.

Catalysts	Half-wave potential ($E_{1/2}$, V vs. RHE)	Limiting current density (mA cm^{-2})
Pd-Co_3O_4@BCN	0.87	-5.4
Pt/C	0.85	-5.2
Co_3O_4@BCN	0.78	-5.0
Pd@BCN	0.74	-4.8
BCN	0.68	-5.2
Pd-Co_3O_4	0.65	-2.3
Pd-Co_3O_4@VC	0.82	-5.8
Co_3O_4	0.53	-1.3
Pd	0.79	-3.5
VC	0.58	-3.9

Table 6. Table of comparison of half-wave potential and limiting current density for all catalysts Pd-Co_3O_4@BCN, Pt/C, Co_3O_4@BCN, Pd@BCN, BCN, Pd-Co_3O_4, Pd-Co_3O_4@VC, Co_3O_4, Pd and VC seen from linear sweep voltammograms.

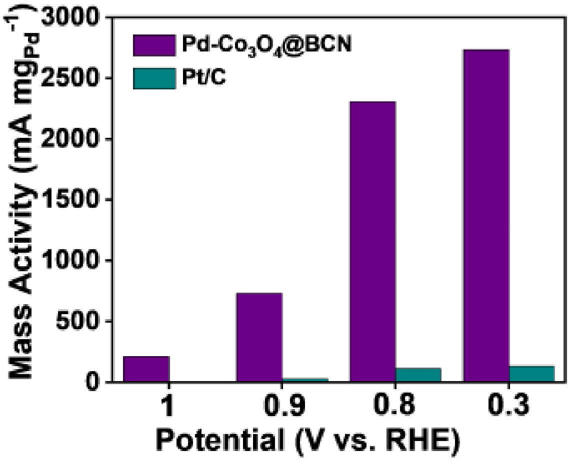

Figure 21. Mass activity compared for Pd-Co_3O_4@BCN and Pt/C.

The mass activity, as shown in the histogram (**Figure 21**), indicated that Pd-Co_3O_4@BCN (731 A g^{-1}) was 27 times more active than Pt/C (27 A g^{-1}) at 0.9V. This superior performance is attributed to the uniform distribution and low loading of Pd (1 wt%) and Co_3O_4 on defect-rich BCN. We have further assessed the double-layer capacitance (C_{dl}), which is proportional to electrochemically active surface area. The C_{dl} of Pd-Co_3O_4@BCN (2.84 mF cm^{-2}) is higher than Pt/C (0.972 mF cm-2) (**Figure 22**), which is calculated from **equation 2**. This suggests that Pd-Co_3O_4@BCN shows a greater number of electrochemical surface areas for ORR.

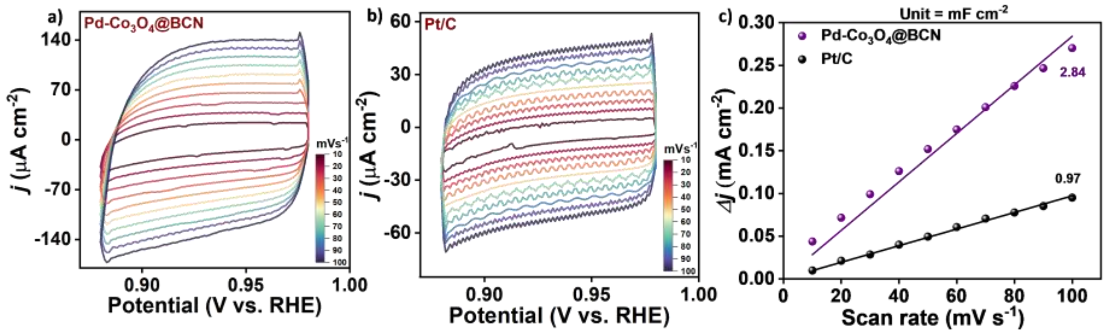

Figure 22. Cyclic voltammograms of a) Pd-Co_3O_4@BCN and b) Pt/C at different scan rates from 10-100 mV s^{-1}. c) Comparison of the electrochemically active surface area of Pd-Co_3O_4@BCN and Pt/C.

Additionally, Pd-Co_3O_4@BCN (107 mV dec^{-1}) displayed similar Tafel slopes to Pt/C (100 mV dec^{-1}), indicating enhanced ORR kinetics (**Figure 23**).

The Koutecky-Levich (K-L) equation (**equation 1**) used to determine the number of electron transfers (n) [36] shows a value close to 4 for the Pd-Co_3O_4@BCN indicative of efficient ORR kinetics, as opposed to Co_3O_4@BCN, where number of electrons transfers equal to 3 (**Figure 24 and 25**). This indicates a preference for OH* (4-e$^-$ process) adsorbates over OOH* (2-e$^-$ process) in Pd-Co_3O_4@BCN compared to Co_3O_4@BCN.

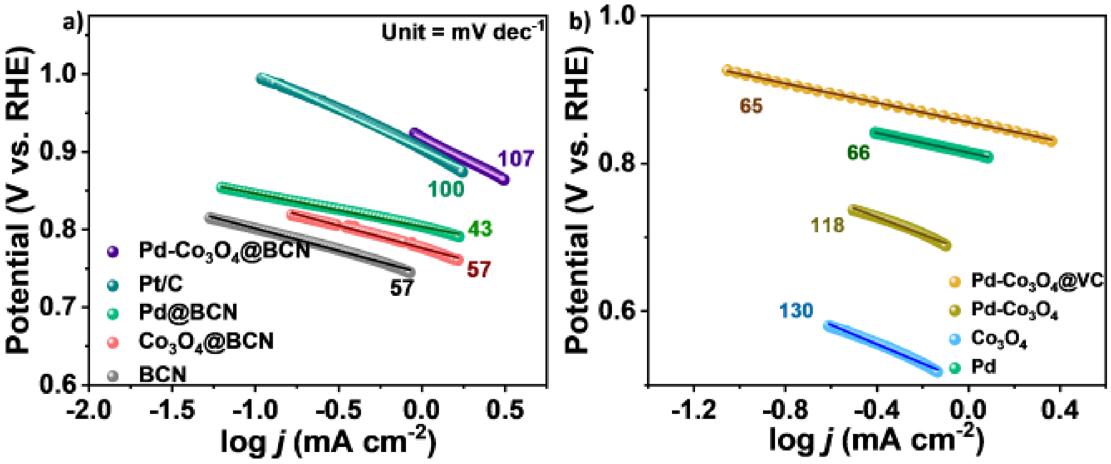

Figure 23. Tafel plots of a) Pd-Co_3O_4@BCN, Pt/C, Pd@BCN, Co_3O_4@BCN and BCN. Comparison of tafel plots for control samples b) Pd-Co_3O_4@VC, Pd-Co_3O_4, Co_3O_4 and Pd.

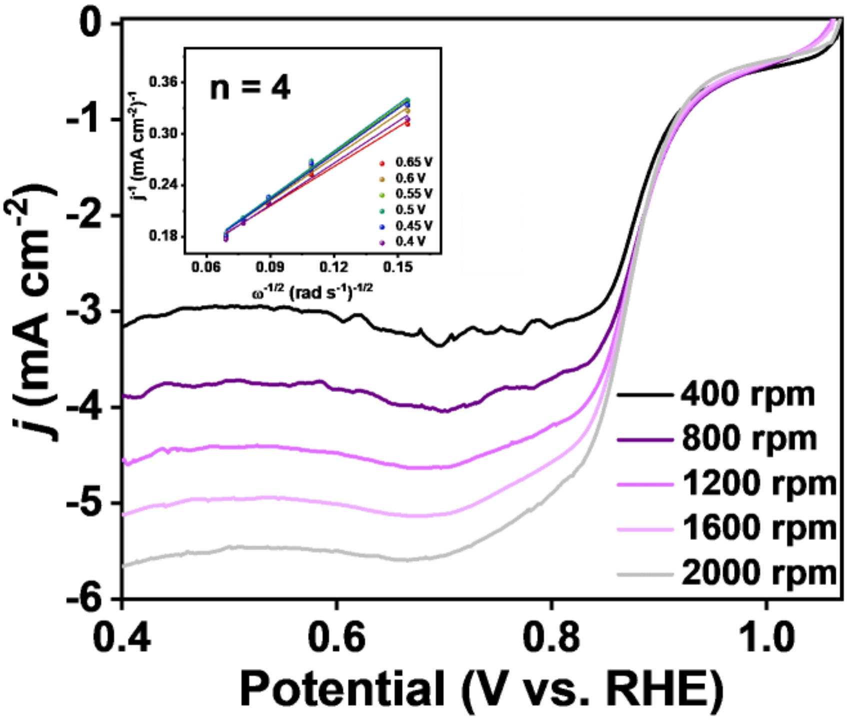

Figure 24. LSV curves of Pd-Co_3O_4@BCN at different rotation rates and KL-plot at different potentials (inset).

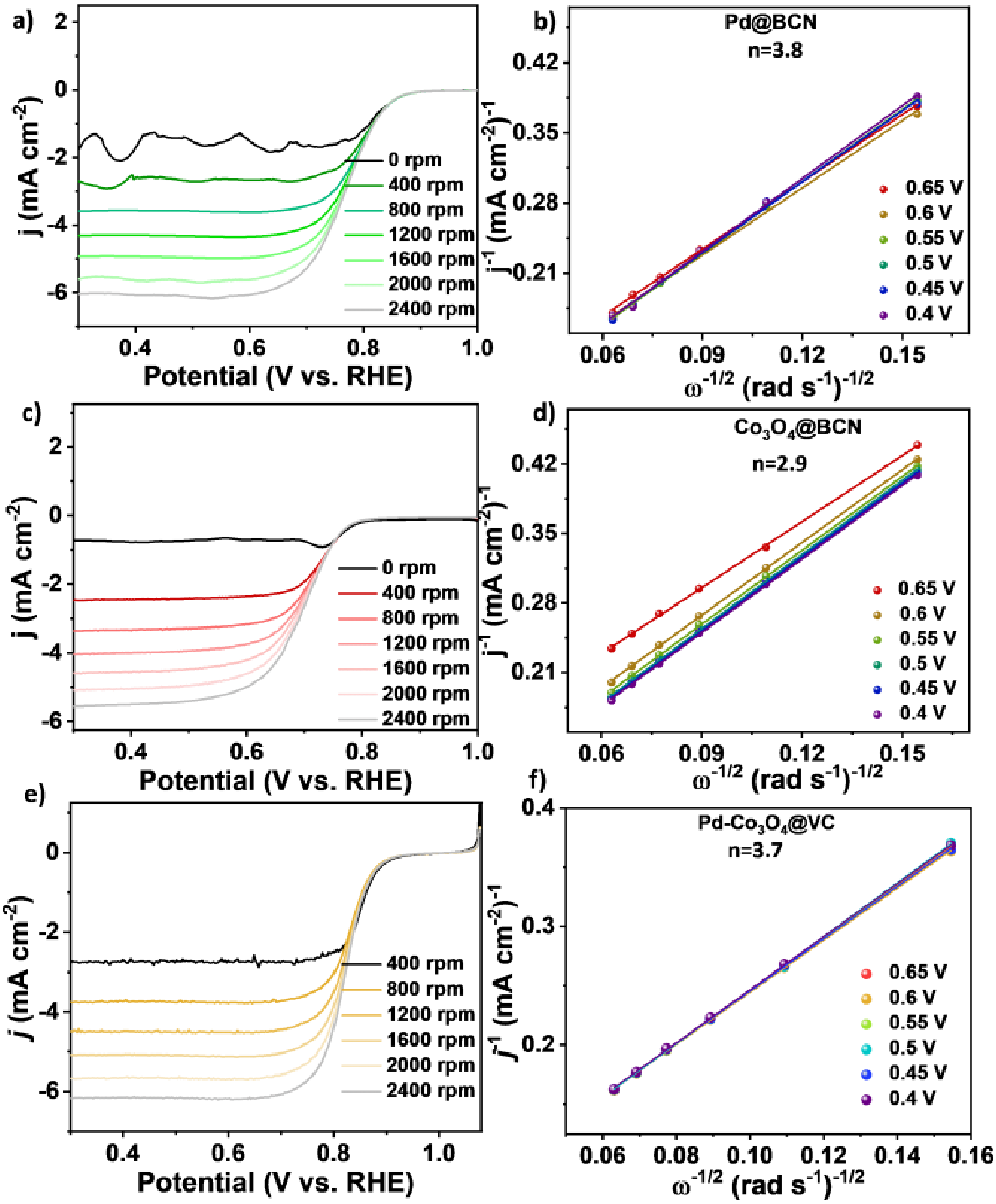

Figure 25. LSV curves at different rotation rates for a) Pd@BCN, c) Co_3O_4@BCN, and e) Pd-Co_3O_4@VC. KL-plot at different potentials for b) Pd@BCN, d) Co_3O_4@BCN, and f) Pd-Co_3O_4@VC.

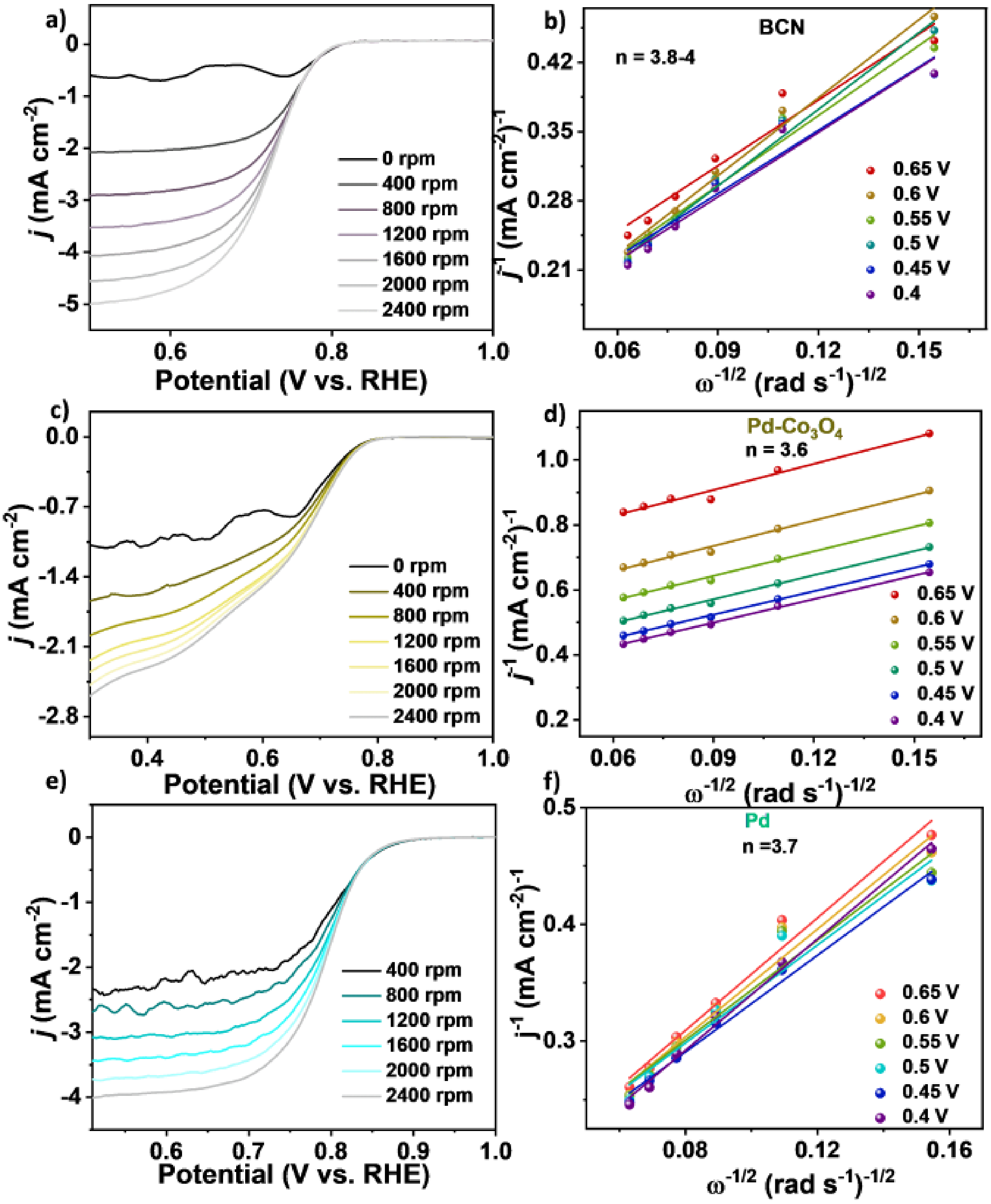

Figure 26. LSV curves at different rotation rates for a) BCN, c) Pd-Co_3O_4, and e) Pd. KL-plot at different potentials for b) BCN, d) Pd-Co_3O_4, and f) Pd.

Finally, the stability of the electrocatalyst was evaluated through an accelerated durability test (ADT) in a potential range of 0.6 to 1 V vs. RHE at 100 mV s^{-1}. The Pd-Co_3O_4@BCN catalyst demonstrated remarkable stability over 15,000 cycles with a negligible change in $E_{1/2}$ (**Figure 27**), underscoring its potential as a durable and efficient catalyst for ORR applications.

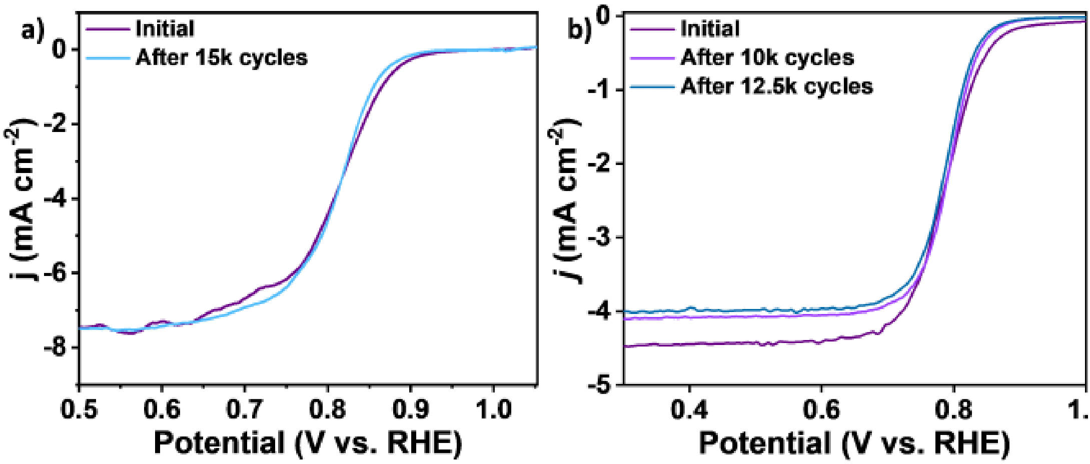

Figure 27. Linear sweep voltammograms were compared initially and after accelerated durability test a) after 15,000 cycles on carbon paper and b) after 10,000 and 12,500 cycles on glassy carbon electrode for Pd-Co_3O_4@BCN.

b. Electrochemical studies for oxygen evolution reaction:

Pd-Co_3O_4@BCN was evaluated for its potential in bifunctional catalysis, specifically for the oxygen evolution reaction (OER). Key catalyst evaluation parameters included overpotentials at different current densities (η_{10}, η_{100}, η_{1000}), specific activity, mass activity, and stability, determined using linear sweep voltammograms (LSVs). These studies were performed on carbon paper electrodes with a catalyst loading of 200 µg cm^{-2} in 1M KOH. Additionally, Tafel slopes were calculated from LSVs conducted on glassy carbon electrodes (GCE) with a catalyst loading of 14 µg cm^{-2}.

In terms of performance, Pd-Co_3O_4@BCN demonstrated the lowest overpotential ($E_{j=10}/\eta_{10}$ = 220 mV) for OER, significantly outperforming the state-of-the-art catalyst RuO_2 (η_{10} = 330 mV), as well as Co_3O_4@BCN (η_{10} = 340 mV), Pd@BCN (η_{10} = 420 mV), and BCN (η_{10} = 420 mV) at a current density of 10 mA cm^{-2} (**Figure 28**) (**Table 7**).

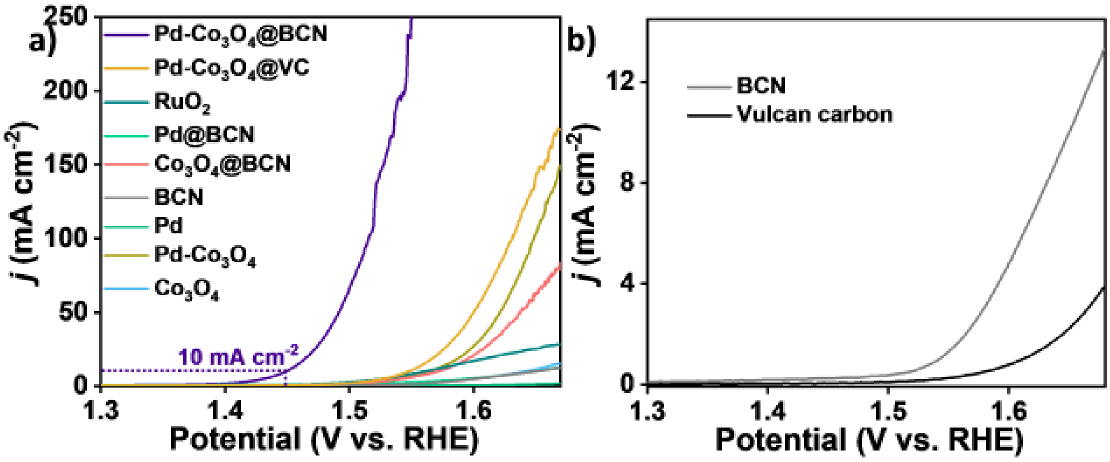

Figure 28. Comparison of LSV curves of all catalysts a) Pd-Co_3O_4@BCN, Pd-Co_3O_4@VC, RuO_2, Pd@BCN, Co_3O_4@BCN, BCN, Pd, Co_3O_4, Pd-Co_3O_4 and b) BCN and Vulcan carbon for oxygen evolution reaction at 5 mV s^{-1}.

Catalysts	Overpotential $E_{j=10}/\eta_{10}$ (mV)
Pd-Co_3O_4@BCN	220
RuO_2	330
Co_3O_4@BCN	340
Pd@BCN	420
BCN	420
Pd-Co_3O_4	330
Pd-Co_3O_4@VC	310
Co_3O_4	410

Table 7. potential values at 10 mA cm^{-2} compared for all catalysts i.e., Pd-Co_3O_4@BCN, Pd-Co_3O_4@VC, RuO_2, Pd@BCN, Co_3O_4@BCN, BCN, Pd, Co_3O_4, Pd-Co_3O_4, BCN and vulcan carbon on glassy carbon electrode.

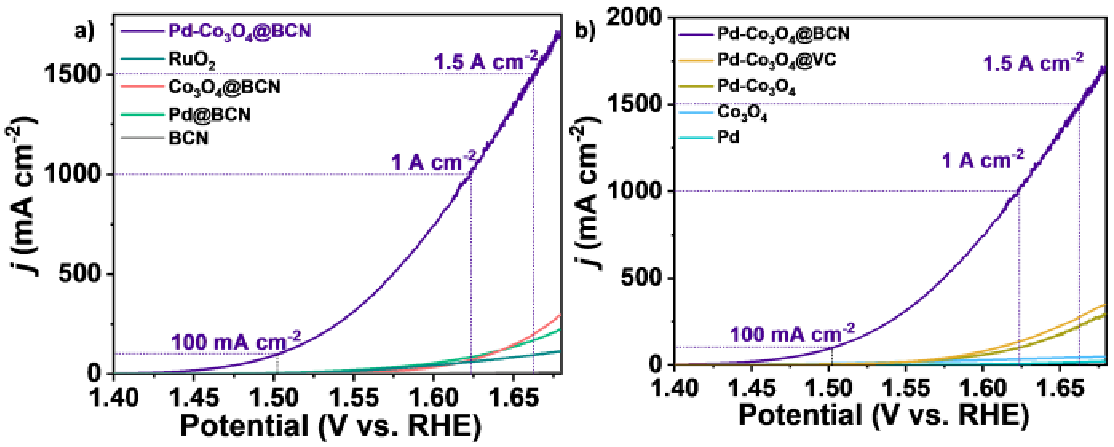

Figure 29. Comparison of LSV curves of all catalysts a) Pd-Co_3O_4@BCN, RuO_2, Pd@BCN, Co_3O_4@BCN, and BCN. LSV curves of b) Pd-Co_3O_4@VC, Pd, Co_3O_4, Pd-Co_3O_4, and Vulcan carbon on carbon paper.

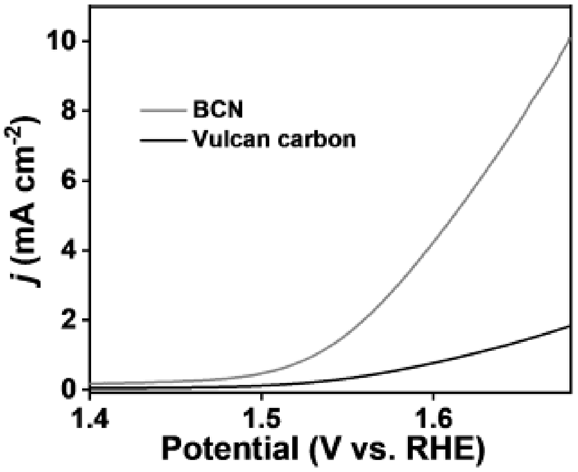

Figure 30. LSV curves of BCN and Vulcan carbon on carbon paper.

Notably, specific activity in Pd-Co_3O_4@BCN (18.6 mA cm^{-2}) was 31 times higher than RuO_2 (0.632 mA cm^{-2}) at 220 mV (**Figure 31**). Additionally, Pd-Co_3O_4@BCN (1681 mA cm^{-2}) exhibited specific activities that were 15 times higher than RuO_2 (112 mA cm^{-2}) at 448 mV. The enhanced activity for OER is attributed to the Co_3O_4/Pd interaction, which improves the adsorption of oxygenated intermediates. Furthermore, the mass activity of Pd-Co_3O_4@BCN (217 A g^{-1}_{Pd}) far exceeded that of RuO_2 (0.104 A g^{-1}_{RuO2}) at 448 mV.

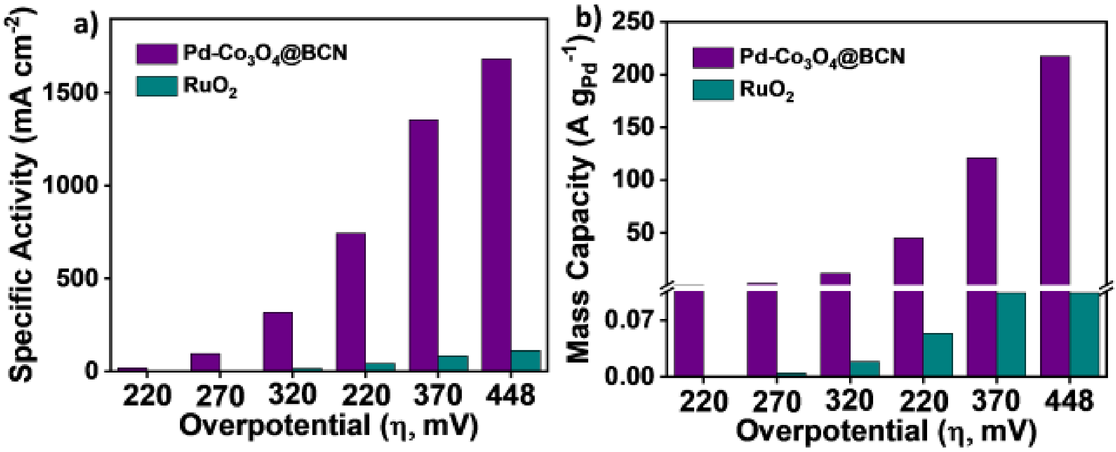

Figure 31. Comparison of a) areal/ specific activity and b) mass activity (normalized by noble metal loading) for Pd-Co_3O_4@BCN and RuO_2.

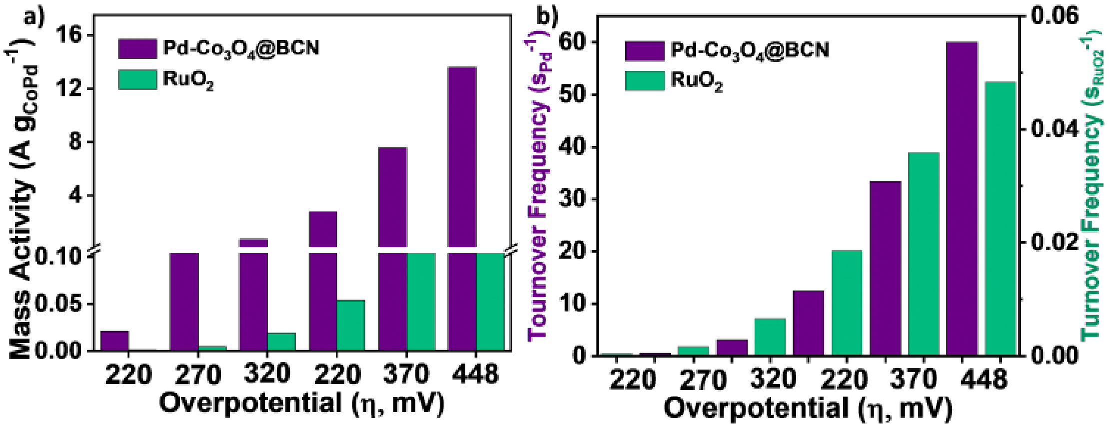

Figure 32. Comparison of a) mass activity (normalized by Pd-Co_3O_4 loading) and b) turnover frequency (normalized by noble metal) for Pd-Co_3O_4@BCN and RuO_2.

The turnover frequency (TOF) value obtained for O_2 production over Pd-Co_3O_4@BCN (60 s^{-1}) was 1250 times higher than the value obtained over RuO_2 (0.048 s^{-1}) at 448 mV (**Figure 32**).

Cyclic voltammetry at different scan rates from 10- 100 mV s^{-1} was carried out for all electrocatalysts to calculate the double-layer capacitance (C_{dl}), as shown in **Figures 33-35**. The high OER activity of Pd-Co_3O_4@BCN is linked to its higher C_{dl} (71 mF cm^{-2}) compared to RuO_2 (1.9 mF cm^{-2}) (**Figures 36**). The Tafel slope value for both Pd-Co_3O_4@BCN and RuO_2 is 60 mV dec^{-1} (**Figure 37**).

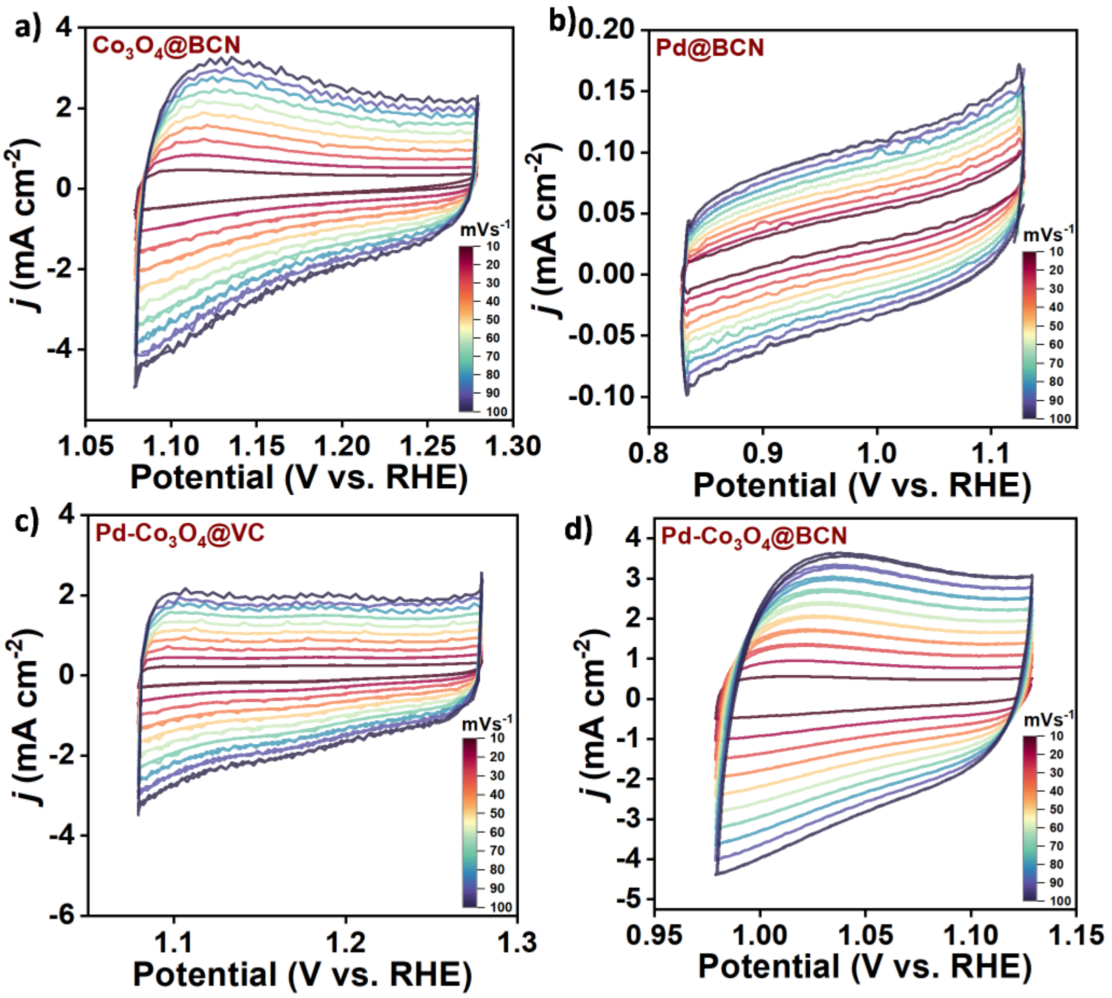

Figure 33. Cyclic voltammograms of a) Co_3O_4@BCN, b) Pd@BCN, c) Pd-Co_3O_4@VC, and d) Pd-Co_3O_4@BCN at different scan rates from 10-100 mV s^{-1}.

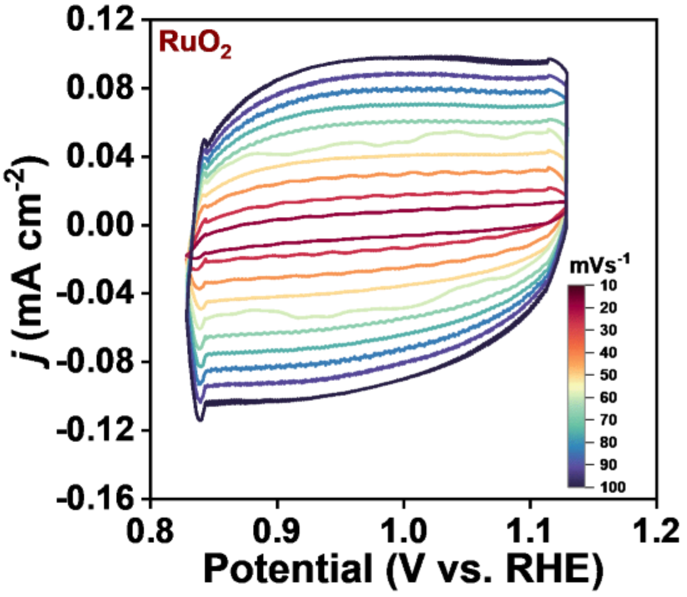

Figure 34. Cyclic voltammograms of RuO_2 at different scan rates from 10-100 mV s^{-1}.

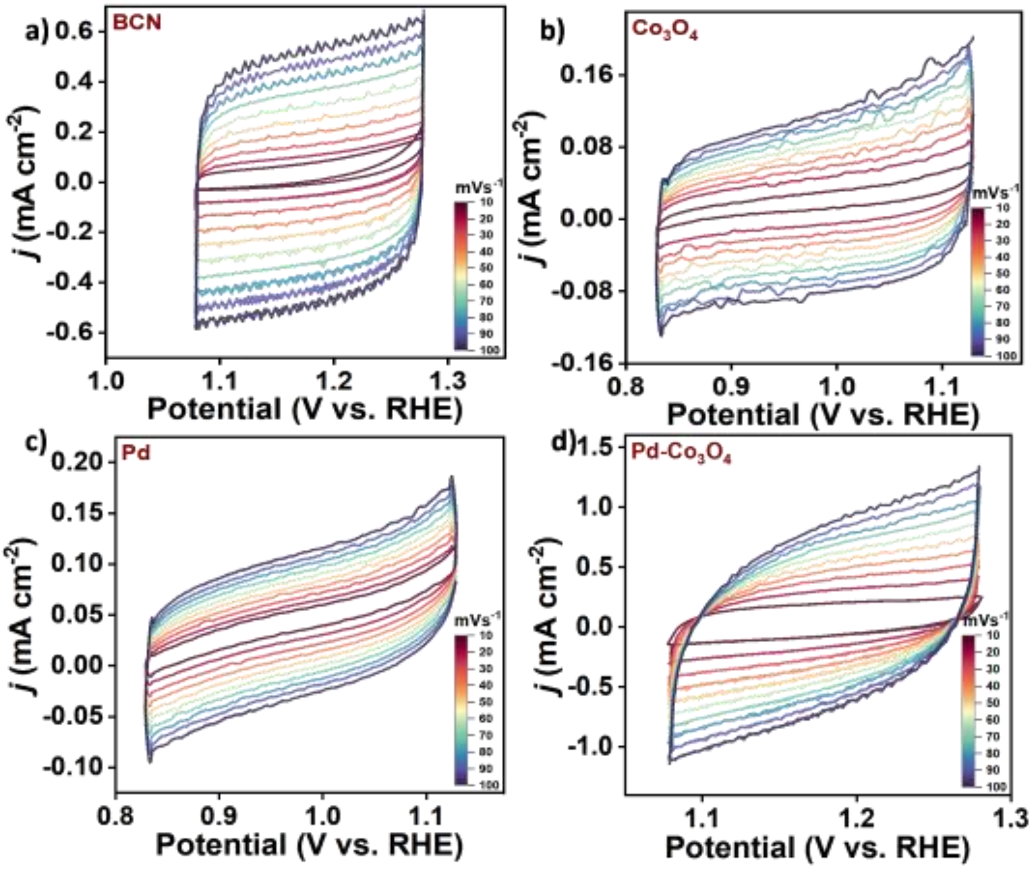

Figure 35. Cyclic voltammograms of a) BCN, b) Co_3O_4, c) Pd, and d) Pd-Co_3O_4 at different scan rates from 10-100 mV s^{-1}.

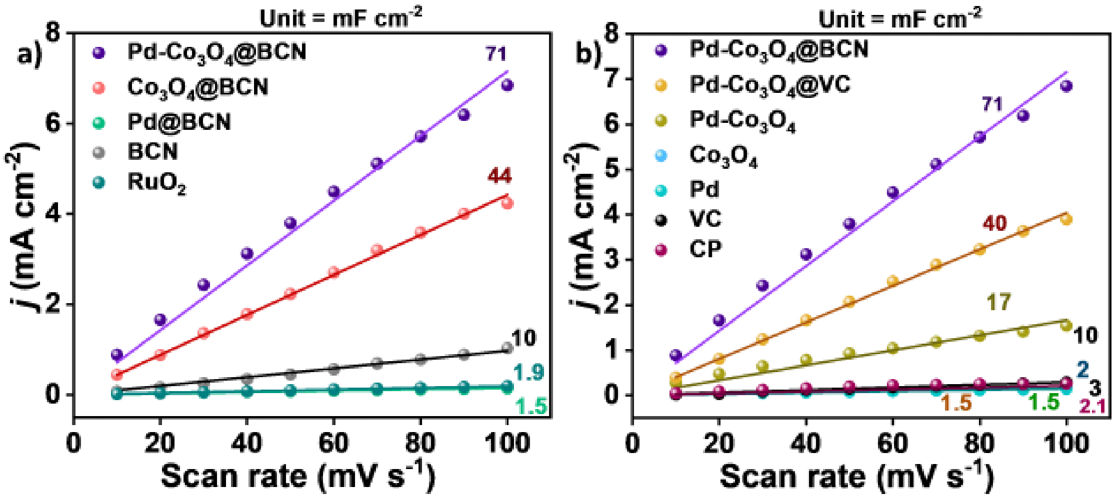

Figure 36. Comparison of C_{dl} values compared for a) and b) all electrocatalysts and blank carbon paper.

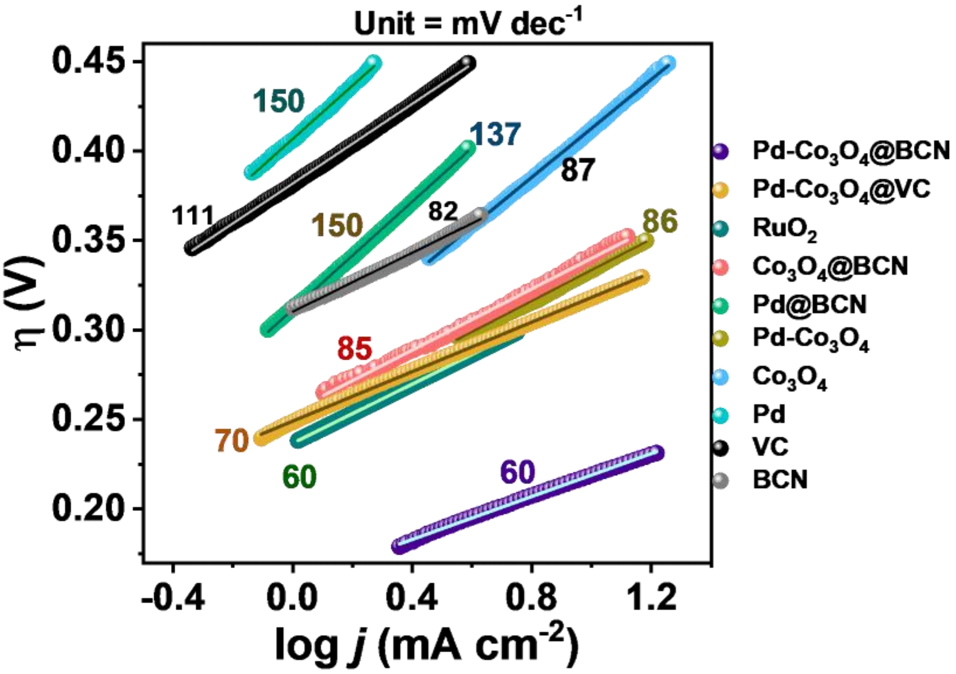

Figure 37. Tafel slopes compared for all electrocatalysts on carbon paper.

The durability test of Pd-Co_3O_4@BCN for OER was evaluated by chronoamperometry (CA) (**Figure 38**), which shows that Pd-Co_3O_4@BCN can sustain a high current density of 20 mA cm^{-2} for an impressive duration of 270 h without significant changes, owing to the intimate interaction of Pd-Co_3O_4 with BCN.

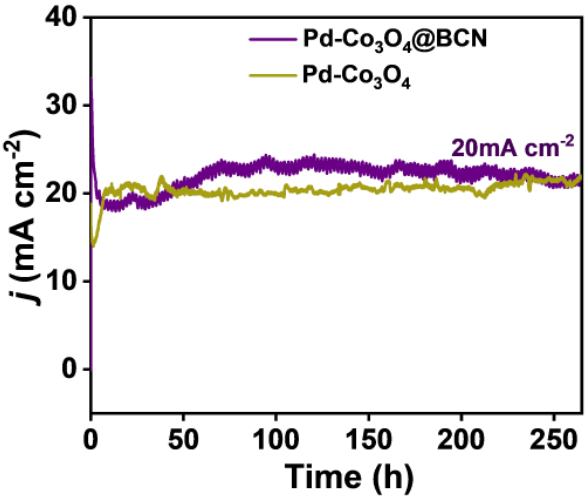

Figure 38. Long-duration oxygen evolution reaction with Pd-Co_3O_4@BCN at 20 mA cm^{-2} for 270 h.

c. Ex-situ microscopic analysis for spent Pd-Co_3O_4@BCN catalyst (OER @ 270 h)

Post-reaction characterizations of the spent catalyst (Pd-Co_3O_4@BCN after 270 h) were conducted to assess any structural or chemical changes. Field-emission scanning electron microscopy (FESEM) images and elemental mapping confirmed the uniform distribution of Pd, Co_3O_4, and BCN on the carbon paper electrode (**Figures 38 and 39a**). Energy-dispersive X-ray analysis (EDAX) showed negligible changes in the weight percentages of Pd (1.5 wt%) and Co (14 wt%) on BCN.

Additionally, transmission electron microscopy (TEM) images (**Figure 39b**) confirmed that no agglomeration of Pd nanoparticles occurred, maintaining the size range of 2-3 nm. This comprehensive analysis underscores the exceptional bifunctional catalytic potential of Pd-Co_3O_4@BCN for both ORR and OER.

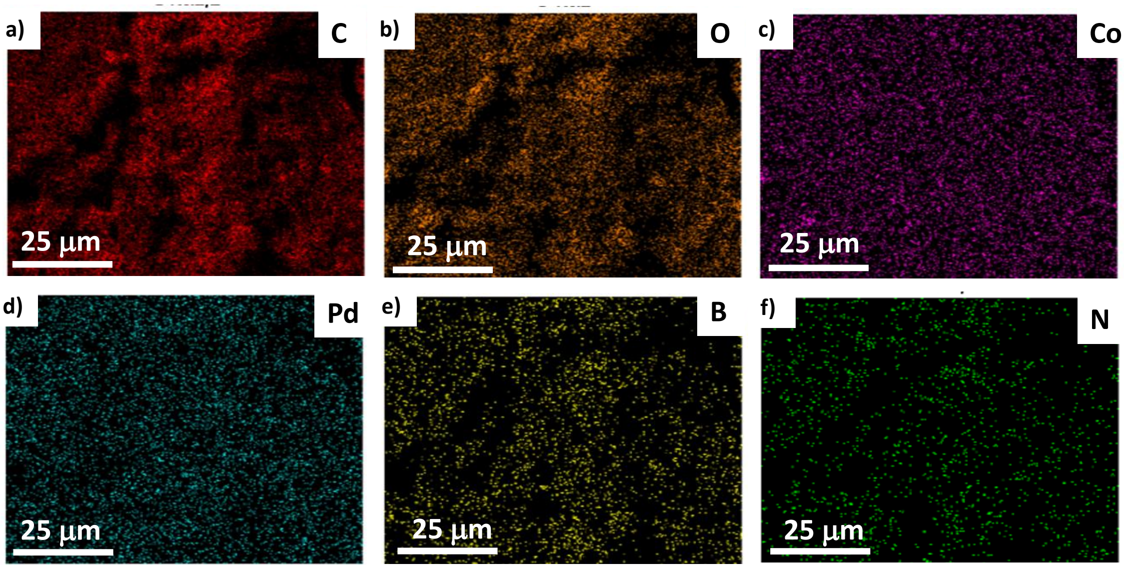

Figure 38. Post-reaction elemental mapping of a) C, b) O, c) Co, d) Pd, e) B, and f) N for Pd-Co_3O_4@BCN after OER.

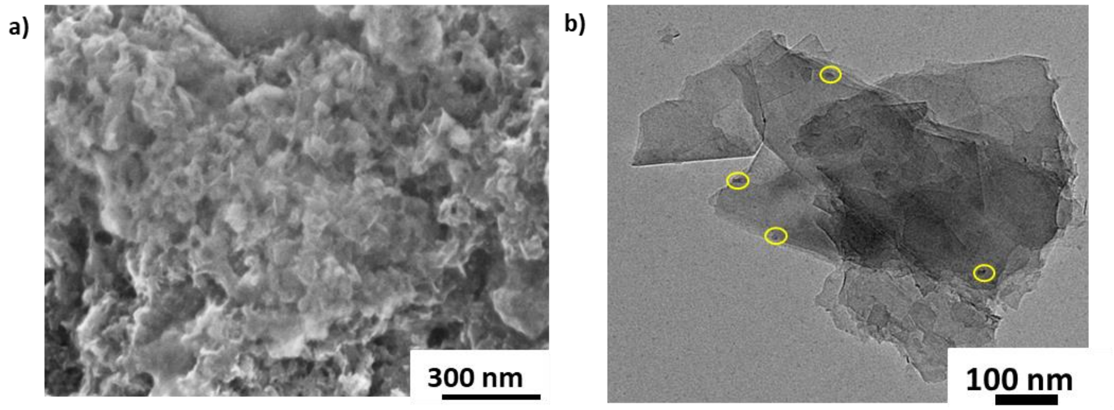

Figure 39. a) FESEM image and b) bright-field TEM image of Pd-Co_3O_4@BCN after 270 h of chronoamperometry for oxygen evolution reaction at 20 mA cm^{-2}.

d. Ex-situ XPS for spent Pd-Co_3O_4@BCN catalyst (OER @ 270 h)

To elucidate the active species present in the Pd-Co_3O_4@BCN surface during the oxygen evolution reaction (OER), we conducted a comprehensive ex-situ X-ray photoelectron spectroscopy (XPS) analysis both before and after 270 hours of OER cycle. The high-resolution XPS spectra of Co 2p, as depicted in **Figure 40a**, reveal a notable increase in the relative intensity of Co^{3+} in the spent BCN-Pd-Co_3O_4 catalyst post-OER.

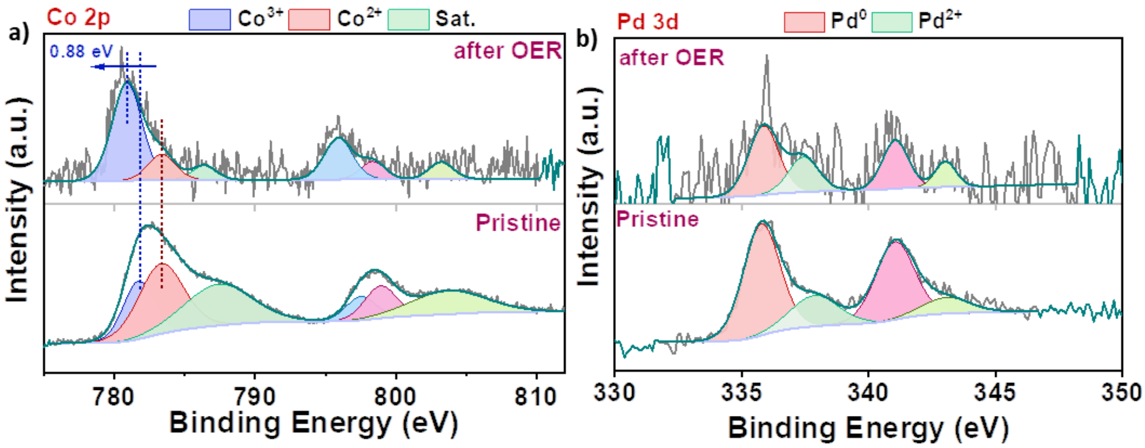

Figure 40. Comparison of high-resolution XPS spectra of a) Co 2p and b) Pd 3d for pristine and Pd-Co_3O_4@BCN (after 270 h OER) on carbon paper.

Furthermore, an increase in the Pd^{2+}/Pd^0 ratio was observed in the spent catalyst, as shown in **Figure 40b**. This change suggests surface oxidation of palladium following prolonged exposure to OER conditions. These insights from the ex-situ XPS analysis provide valuable information about the change in the chemical state of metal ions, thus offering a deeper understanding of the catalyst's behavior and stability during extensive OER operation.

BCN-associated C 1s spectra show peaks for C-F due to the Nafion binder used for Pd-Co_3O_4@BCN adherence on carbon paper, as shown in **Figure 41a**. **Figure 41b** presents N 1s spectra, demonstrating the stability of different nitrogen species before and after OER. Conversely, **Figure 41c** reveals the elimination of B-O species following OER, as evidenced by its absence compared to the pristine peak.

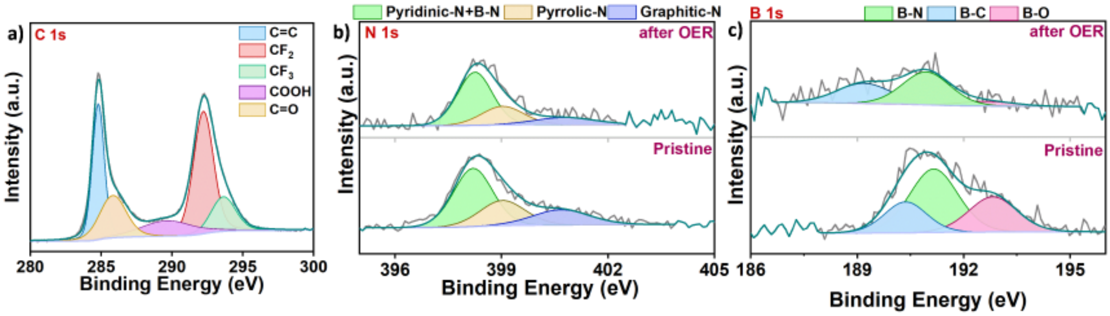

Figure 41. High-resolution spectra of a) C 1s element for Pd-Co_3O_4@BCN (270 h OER) on carbon paper. Comparison of XPS Spectra for (b) N 1s and (c) B 1s elements in Pd-Co_3O_4@BCN, both Pristine and After 270 h of OER.

The formation of intermediates in Pd-Co_3O_4@BCN during oxygen reduction reaction was robed using in-situ Fourier transformed infrared (FT-IR) spectroscopy. On the other hand, the oxygen evolution reaction was monitored using operando Raman spectroscopy as well as ex-situ X-ray photoelectron spectroscopy (XPS) analysis for OER.

e. In-situ Fourier Transformed Infrared Spectroscopy for ORR

The in-situ FT-IR spectroscopy was utilized to study the reaction kinetics of Pd-Co_3O_4@BCN in ORR. Pd-Co_3O_4@BCN showcased a selective four-electron process leading to OH- formation, as previously indicated in the KL-Plot (**Figure 23**). The mechanism hinges on the interaction between O_2 and the active catalyst, emphasizing

O=O stretching to favor OH* over OOH* intermediates. As evidenced in **Figure 42**, the concentration of oxygen adsorption and stretching at 1350 cm^{-1} increases with the potential and reaches saturation at the limiting current density. An O^{2-} intermediate observed at 1050 cm^{-1} was identified as a key determinant in the ORR process.[37–39]

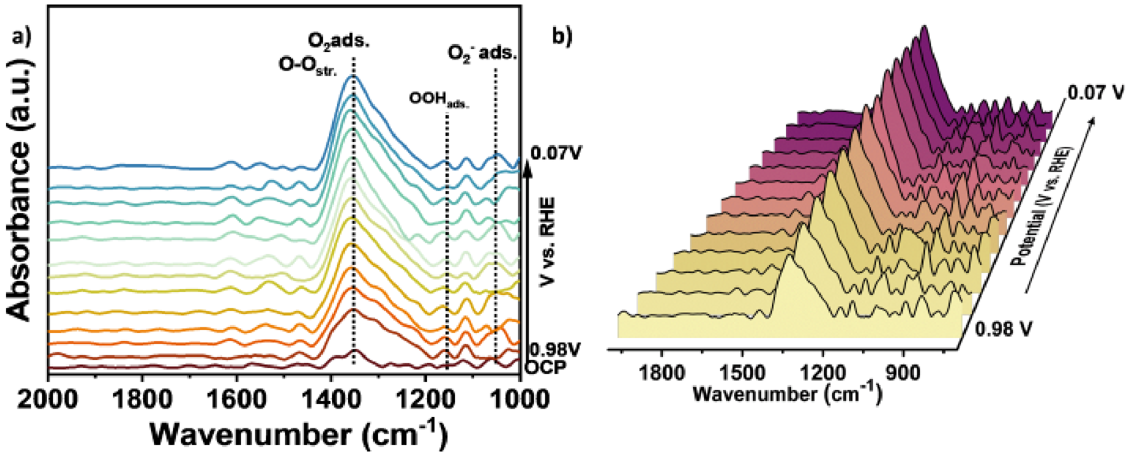

Figure 42. In situ FT-IR spectra for Pd-Co_3O_4@BCN at 0.98 V to 0.07 V vs. RHE in 0.1 M KOH a) with intermediates and b) showing increasing oxygen adsorption with potential.

f. Operando Raman Spectroscopy for OER

The operando Raman spectroscopy focused on the OER process, as shown in **Figure 43**. Pd-Co_3O_4 was primarily used to understand the structural evolution of Co_3O_4 and Pd due to their weak Raman signatures in Pd-Co_3O_4@BCN.[40–42] At open circuit potential (OCP), weak signals at 484 cm^{-1} and 682 cm^{-1} were noted, corresponding to the E_g and A_{1g} vibrational modes of Co_3O_4 in Pd-Co_3O_4. Additionally, Raman signatures associated with second-order scatterings for Pd-O were observed at 726 cm^{-1} and 795 cm^{-1}.

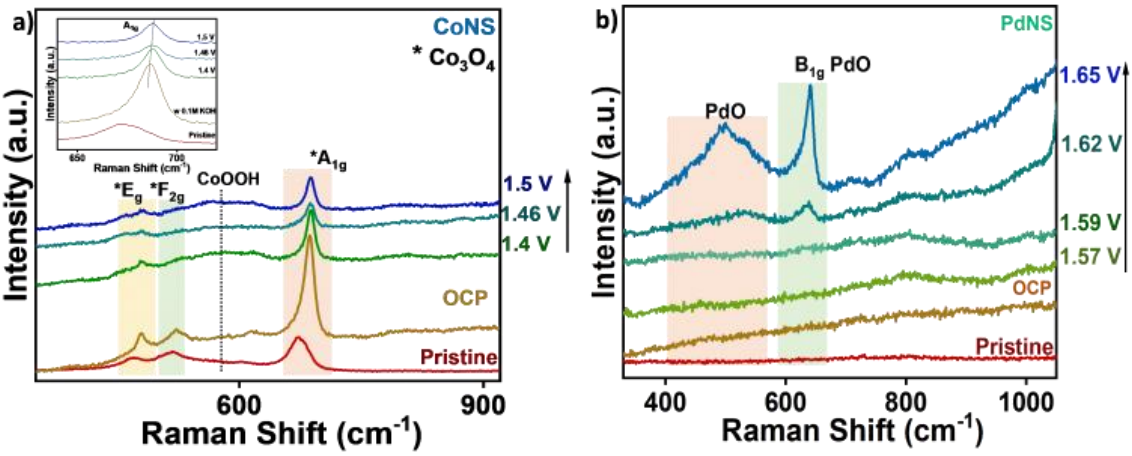

Figure 43. In situ Raman measurement of a) Co_3O_4 (inset: A_{1g} mode) and b) Pd evolution with potential.

Upon applying an oxidative potential, two new peaks emerged at 553 cm^{-1} (broad) and 1050 cm^{-1}, indicating the formation of amorphous cobalt oxyhydroxide (CoOOH) and cobalt superoxide intermediates, respectively, with the disappearance of E_g and A_{1g} modes of Co_3O_4. The intensity of these newly formed species increased with the rise in applied potential, suggesting their active role in OER. Similarly, for Pd-O, the B_{1g} phonon mode and new second-order scattering emerged at 641 cm^{-1} and 504 cm^{-1}, respectively. An increase in intensity for the B_{1g} mode and second-order scatterings of PdO with increasing oxidative potential also indicated their participation in OER.

In summary, the synergistic effects of Co (in the form of CoOOH and cobalt superoxide) and Pd (Pd-O) species are instrumental in enhancing the OER activity of the Pd-Co_3O_4@BCN catalyst, as shown in **Figure 44.**

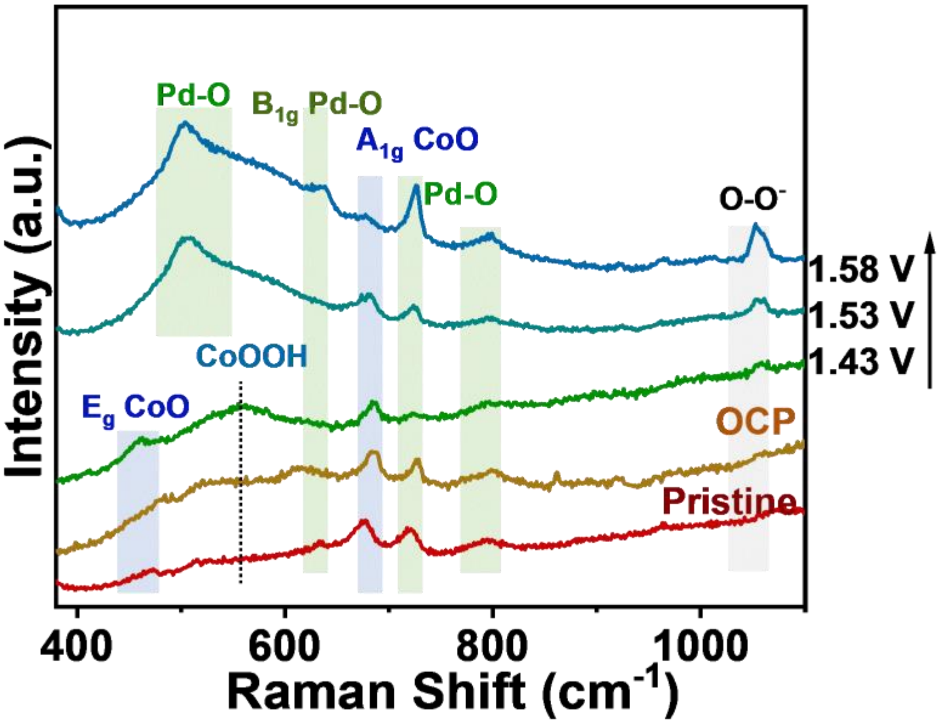

Figure 44. In situ Raman measurement of Pd-Co_3O_4@BCN evolution with potential.

This finding is in alignment with the ex-situ XPS of Pd-Co_3O_4@BCN of structural changes in cobalt oxide (**Figure 40a**), confirming the transformation of Co^{2+} to a higher oxidation state, indicative of CoOOH formation during the OER process.

The superior performance of Pd-Co_3O_4@BCN as a bifunctional catalyst is highlighted by its low voltage gap (0.58V), achieved with minimal loading of noble metal (Pd: 2 μg cm^{-2}), as compared to other recent studies in the literature (**Figure 45**). The voltage gap between the Oxygen Evolution Reaction (OER) and Oxygen Reduction Reaction (ORR) was determined using the formula

$E_{j=10} - E_{1/2}$

where $E_{j=10}$ is potential at current density 10 mA cm^{-2} (OER), and $E_{1/2}$ is half-wave potential (ORR). This low voltage gap positions the Pd-Co_3O_4@BCN catalyst as an ideal candidate for air-cathode material in rechargeable zinc-air batteries (ZABs).

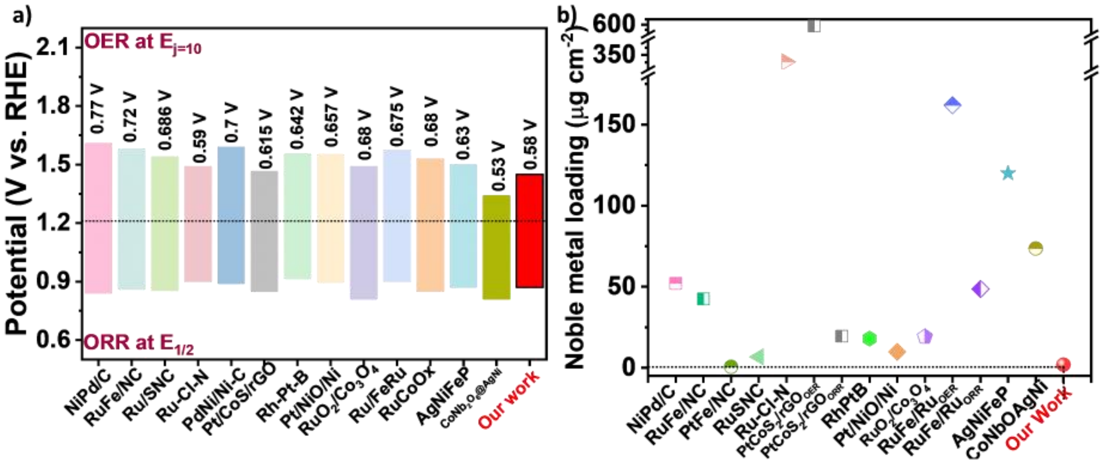

Figure 46. Comparison graph of Pd-Co_3O_4@BCN in terms of a) voltage gap and b) noble metal loading with other recent reports.[43–56]

g. Zinc-air battery

To demonstrate this application, a rechargeable ZAB was assembled using Pd-Co_3O_4@BCN coated on a gas diffusion electrode (GDE) as the cathode, a 2 mm zinc plate as the anode, and a mixed solution of 6M KOH + 0.2M $Zn(ac)_2$ as the electrolyte.[57] The Pd-Co_3O_4@BCN-based ZAB successfully powered an LED bulb, maintaining an open circuit voltage of 2.8 V for up to 1 h, as shown in **Figure 47a**. The galvanostatic discharge curves at current densities of 10 mA cm^{-2} and 50 mA cm^{-2} are displayed in **Figure 47b**. The specific capacity of Pd-Co_3O_4@BCN (normalized by the change in Zn weight) was 905 mA h g_{Zn}^{-1} at both 10 mA cm^{-2} and 50 mA cm^{-2}. Correspondingly, the calculated energy densities are 978 Wh kg_{Zn}^{-1} (at 10 mA cm^{-2}) and 733 Wh kg_{Zn}^{-1} (at 50 mA cm^{-2}).

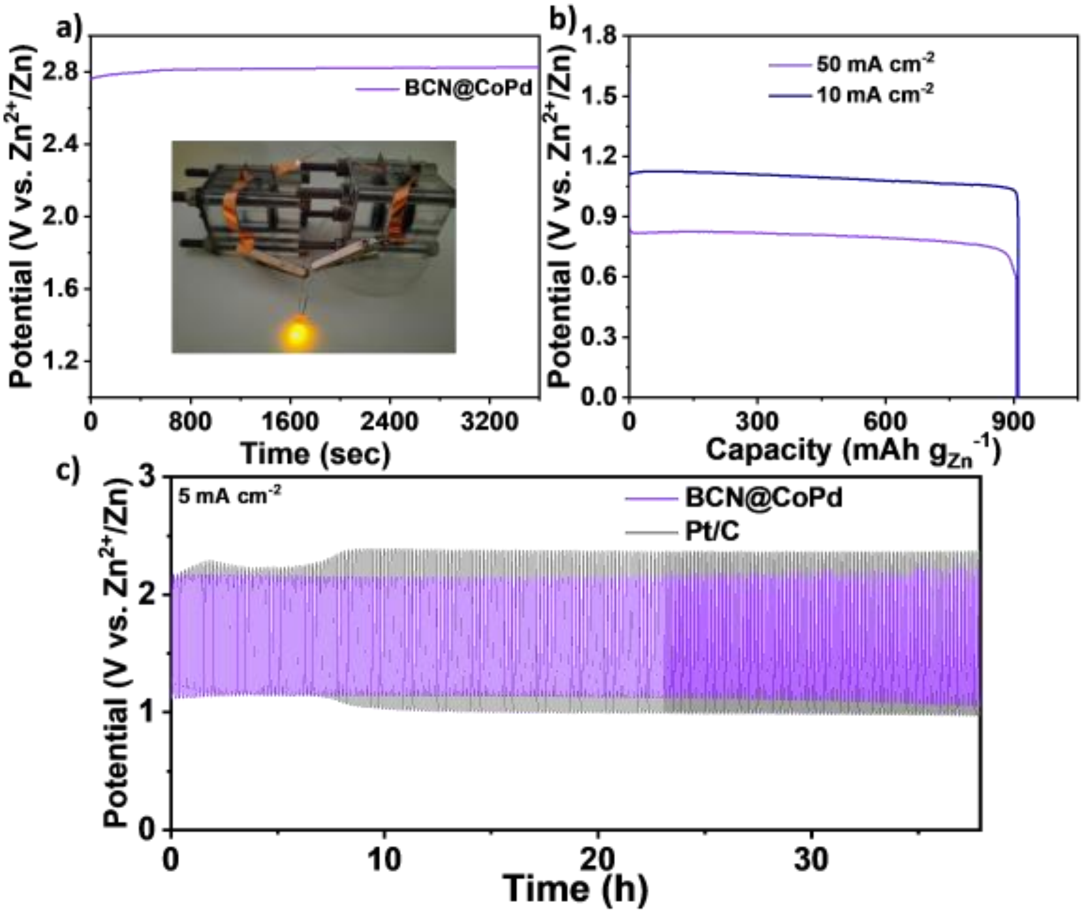

Figure 47. Zinc-air battery with a) Pd-Co_3O_4@BCN at open circuit potential and inset Zn-air battery homemade setup powering an LED. b) Galvanostatic charge-discharge at 10 mA cm^{-2} and 50 mA cm^{-2} with Pd-Co_3O_4@BCN. c) Comparison of rechargeable battery with Pd-Co_3O_4@BCN and Pt/C at 5 mA cm^{-2}.

The cycling stability of Pd-Co_3O_4@BCN was further evaluated through galvanostatic charge-discharge curves at 5 mA cm^{-2} and 2 mA cm^{-2} (**Figure 47c** and **Figure 48**). The catalyst maintained high stability for up to 330 cycles at 2 mA cm^{-2}. These results indicate the importance of Pd-Co_3O_4@BCN for practical applications in energy storage devices like zinc-air batteries, reaffirming its effectiveness as a bifunctional catalyst.

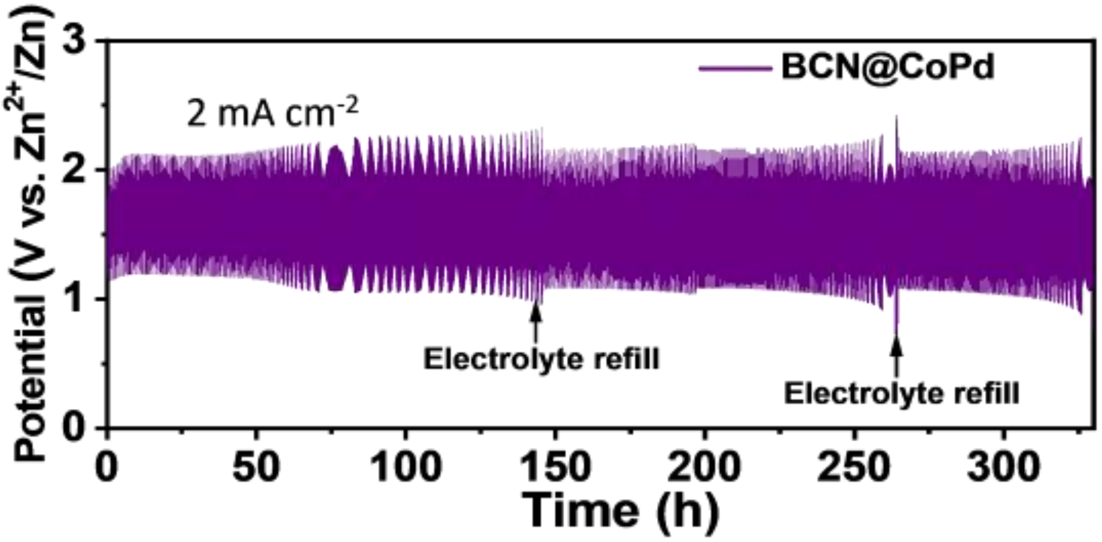

Figure 48. Long-term cycling in rechargeable Zn-air battery with Pd-Co_3O_4@BCN at 2 mA cm^{-2}.

2.2.5 Conclusion:

In summary, the Pd-Co_3O_4@BCN catalyst, synthesized via a simple wet chemical process, shows very good activity and stability for both OER and ORR. This is attributed to the ultra-low Pd loading (1 wt%) and its synergistic interaction with Co_3O_4 and BCN, resulting in a low voltage gap of 0.58 V. Pd-Co_3O_4@BCN outperforms Pt (20 wt%)/C in ORR and RuO_2 in OER by significant margins, demonstrating high mass activity and long-term stability. Operando spectroscopy reveals key insights into the reaction mechanisms. The catalyst has a high capacity, i.e., 905 mAh g^{-1}_{Zn} at 50 mA cm^{-2}, and stability for 330 hours, attaining high rechargeability for zinc-air batteries.

2.2.6 References:

1. Zhou, G., Liu, G., Liu, X., Yu, Q., Mao, H., Xiao, Z., Wang, L., Zhou, G., Liu, G., Liu, X., Yu, Q., Mao, H., Xiao, Z., and Wang, L. (2022) 1D/3D Heterogeneous Assembling Body as Trifunctional Electrocatalysts Enabling Zinc–Air Battery and Self-Powered Overall Water Splitting. *Adv Funct Mater*, **32** (4), 2107608.

2. Gao, Y., Zheng, D., Li, Q., Xiao, W., Ma, T., Fu, Y., Wu, Z., and Wang, L. (2022) 3D Co3O4-RuO2 Hollow Spheres with Abundant Interfaces as Advanced Trifunctional Electrocatalyst for Water-Splitting and Flexible Zn–Air Battery. *Adv Funct Mater*, **32** (38), 2203206.

3. Shan, J., Guo, C., Zhu, Y., Chen, S., Song, L., Jaroniec, M., Zheng, Y., and Qiao, S.Z. (2019) Charge-Redistribution-Enhanced Nanocrystalline Ru@IrOx Electrocatalysts for Oxygen Evolution in Acidic Media. *Chem*, **5** (2), 445–459.

4. Zhao, C.X., Liu, J.N., Wang, J., Ren, D., Li, B.Q., and Zhang, Q. (2021) Recent advances of noble-metal-free bifunctional oxygen reduction and evolution electrocatalysts. *Chem Soc Rev*, **50** (13), 7745–7778.

5. Wu, Z.-P., Lu, F., Zang, S.-Q., Wen, X., Lou, D., Wu, Z.-P., Lu, X.F., Lou, X.W., and Zang, S.-Q. (2020) Non-Noble-Metal-Based Electrocatalysts toward the Oxygen Evolution Reaction. *Adv Funct Mater*, **30** (15), 1910274.

6. Wang, T., Chutia, A., Brett, D.J.L., Shearing, P.R., He, G., Chai, G., and Parkin, I.P. (2021) Palladium alloys used as electrocatalysts for the oxygen reduction reaction. *Energy Environ Sci*, **14** (5), 2639–2669.

7. Gunji, T., Noh, S.H., Ando, F., Tanabe, T., Han, B., Ohsaka, T., and Matsumoto, F. (2018) Electrocatalytic activity of electrochemically dealloyed PdCu3 intermetallic compound towards oxygen reduction reaction in acidic media. *J Mater Chem A Mater*, **6** (30), 14828–14837.

8. Xu, Y., Zhang, F., Sheng, T., Ye, T., Yi, D., Yang, Y., Liu, S., Wang, X., and Yao, J. (2019) Clarifying the controversial catalytic active sites of Co3O4 for the oxygen evolution reaction. *J Mater Chem A Mater*, **7** (40), 23191–23198.

9. Hyun, S., Saejio, A., and Shanmugam, S. (2020) Pd nanoparticles deposited on Co(OH)2 nanoplatelets as a bifunctional electrocatalyst and their application in Zn–air and Li–O2 batteries. *Nanoscale*, **12** (34), 17858–17869.

10. Man, I.C., Su, H.Y., Calle-Vallejo, F., Hansen, H.A., Martínez, J.I., Inoglu, N.G., Kitchin, J., Jaramillo, T.F., Nørskov, J.K., and Rossmeisl, J. (2011) Universality in Oxygen Evolution Electrocatalysis on Oxide Surfaces. *ChemCatChem*, **3** (7), 1159–1165.

11. Nørskov, J.K., Rossmeisl, J., Logadottir, A., Lindqvist, L., Kitchin, J.R., Bligaard, T., and Jónsson, H. (2004) Origin of the Overpotential for Oxygen Reduction at a Fuel-Cell Cathode. *Journal of Physical Chemistry B*, **108** (46), 17886–17892.

12. Du, C., Gao, Y., Wang, J., and Chen, W. (2020) A new strategy for engineering a hierarchical porous carbon-anchored Fe single-atom electrocatalyst and the insights into its bifunctional catalysis for flexible rechargeable Zn–air batteries. *J Mater Chem A Mater*, **8** (19), 9981–9990.

13. Zhong, X., Yi, W., Qu, Y., Zhang, L., Bai, H., Zhu, Y., Wan, J., Chen, S., Yang, M., Huang, L., Gu, M., Pan, H., and Xu, B. (2020) Co single-atom anchored on Co3O4 and nitrogen-doped active carbon toward bifunctional catalyst for zinc-air batteries. *Appl Catal B*, **260**, 118188.

14. Chakraborty, S., Servottam, S., Samal, K., Kalita, D., Rao, A., Bagchi, D., Peter, S.C., Eswaramoorthy, M., Chakraborty, S., Servottam, S., Samal, P.K., Kalita, D., Eswaramoorthy, M., Rao, A., Bagchi, D., and Peter, S.C. (2023) Highly Efficient Electrochemical Hydrogen Evolution with Ultra-Low Loading of Strongly Adhered Pt Nanoparticles on Carbon. *Small*, **19** (45), 2303495.

15. Ma, R., Lin, G., Zhou, Y., Liu, Q., Zhang, T., Shan, G., Yang, M., and Wang, J. (2019) A review of oxygen reduction mechanisms for metal-free carbon-based electrocatalysts. *npj Computational Materials 2019 5:1*, **5** (1), 1–15.

16. Jiang, H., Gu, J., Zheng, X., Liu, M., Qiu, X., Wang, L., Li, W., Chen, Z., Ji, X., and Li, J. (2019) Defect-rich and ultrathin N doped carbon nanosheets as advanced trifunctional metal-free electrocatalysts for the ORR, OER and HER. *Energy Environ Sci*, **12** (1), 322–333.

17. Zhang, J., Xia, Z., and Dai, L. (2015) Carbon-based electrocatalysts for advanced energy conversion and storage. *Sci Adv*, **1** (7).

18. Wang, S., Iyyamperumal, E., Roy, A., Xue, Y., Yu, D., and Dai, L. (2011) Vertically Aligned BCN Nanotubes as Efficient Metal-Free Electrocatalysts for the Oxygen Reduction Reaction: A Synergetic Effect by Co-Doping with Boron and Nitrogen. *Angewandte Chemie International Edition*, **50** (49), 11756–11760.

19. Wang, S., Zhang, L., Xia, Z., Roy, A., Wook Chang, D., Baek, J.-B., Dai, L., Wang, S., Dai, L., Zhang, L., Xia, Z., Roy, A., Chang, D.W., and Baek, J. (2012) BCN Graphene as Efficient Metal-Free Electrocatalyst for the Oxygen Reduction Reaction. *Angewandte Chemie International Edition*, **51** (17), 4209–4212.

20. Bai, X., Zhang, X., Sun, Y., Huang, M., Fan, J., Xu, S., and Li, H. (2023) Low Ruthenium Content Confined on Boron Carbon Nitride as an Efficient and Stable Electrocatalyst for Acidic Oxygen Evolution Reaction. *Angewandte Chemie International Edition*, **62** (38), e202308704.

21. Fan, M., Yuan, Q., Zhao, Y., Wang, Z., Wang, A., Liu, Y., Sun, K., Wu, J., Wang, L., and Jiang, J. (2022) A Facile “Double-Catalysts” Approach to Directionally Fabricate Pyridinic N?B-Pair-Doped Crystal Graphene Nanoribbons/Amorphous Carbon Hybrid Electrocatalysts for Efficient Oxygen Reduction Reaction. *Advanced Materials*, **34** (13), 2107040.

22. Shinde, S.S., Wagh, N.K., Lee, C.H., Kim, D.H., Kim, S.H., Um, H.D., Lee, S.U., and Lee, J.H. (2023) Scaling-Up Insights for Zinc–Air Battery Technologies Realizing Reversible Zinc Anodes. *Advanced Materials*, **35** (48), 2303509.

23. Pei, Y., Wu, W.Y., Wilkinson, D.P., and Gyenge, E.L. (2024) High-Performance Reversible Oxygen Reduction/Evolution Gas Diffusion Electrodes with Multivalent Cation Doped Core-Shell Mn/Mn3O4 Catalysts. *ChemElectroChem*, e202300558.

24. Kwon, O., Hwang, H.J., Ji, Y., Jeon, O.S., Kim, J.P., Lee, C., and Shul, Y.G. (2019) Transparent Bendable Secondary Zinc-Air Batteries by Controlled Void Ionic Separators. *Scientific Reports 2019 9:1*, **9** (1), 1–9.

25. Kim, J., and Bard, A.J. Application of Koutecký-Levich Method to the Analysis of Steady State Voltammograms with Ultramicroelectrodes Supporting information.

26. Chen, W., Xiang, Q., Peng, T., Song, C., Shang, W., Deng, T., and Wu, J. (2020) Reconsidering the Benchmarking Evaluation of Catalytic Activity in Oxygen Reduction Reaction. *iScience*, **23** (10), 101532.

27. Balamurugan, C., Lee, C., Cho, K., Kim, J., Park, B., Kim, W., Lim, N., Kim, H., Pak, Y., Chae, K.H., Shim, J.H., and Kwon, S. (2023) High-performance rechargeable metal–air batteries enabled by efficient charge transport in multielement random alloy electrocatalyst. *Appl Catal B*, **330**, 122631.

28. Janssen, A., Pawlik, V., Von Rueden, A.D., Xu, L., Wang, C., Mavrikakis, M., Xia, Y., Janssen, A., Pawlik, V., Wang, C., Xia, Y., Von Rueden, A.D., Xu, L., and Mavrikakis, M. (2021) Facile Synthesis of Palladium-Based Nanocrystals with Different Crystal Phases and a Comparison of Their Catalytic Properties. *Advanced Materials*, **33** (49), 2103801.

29. Rivas-Murias, B., and Salgueiriño, V. (2017) Thermodynamic CoO–Co3O4 crossover using Raman spectroscopy in magnetic octahedron-shaped nanocrystals. *Journal of Raman Spectroscopy*, **48** (6), 837–841.

30. Baylet, A., Marécot, P., Duprez, D., Castellazzi, P., Groppi, G., and Forzatti, P. (2011) In situ Raman and in situXRD analysis of PdO reduction and Pd° oxidation supported on γ-Al2O3 catalyst under different atmospheres. *Physical Chemistry Chemical Physics*, **13** (10), 4607–4613.

31. Zhang, X., Yan, P., Xu, J., Li, F., Herold, F., Etzold, B.J.M., Wang, P., Su, D.S., Lin, S., Qi, W., and Xie, Z. (2020) Methanol conversion on borocarbonitride catalysts: Identification and quantification of active sites. *Sci Adv*, **6** (26).

32. Li, Y., Qiu, W., Qin, F., Fang, H., Hadjiev, V.G., Litvinov, D., and Bao, J. (2016) Identification of Cobalt Oxides with Raman Scattering and Fourier Transform Infrared Spectroscopy. *Journal of Physical Chemistry C*, **120** (8), 4511–4516.

33. Jose, J., Jose, S.P., Prasankumar, T., Shaji, S., Pillai, S., and B, S.P. (2021) Emerging ternary nanocomposite of rGO draped palladium oxide/polypyrrole for high performance supercapacitors. *J Alloys Compd*, **855**, 157481.

34. Do, V.H., Prabhu, P., Jose, V., Yoshida, T., Zhou, Y., Miwa, H., Kaneko, T., Uruga, T., Iwasawa, Y., and Lee, J.M. (2023) Pd–PdO Nanodomains on Amorphous Ru Metallene Oxide for High-Performance Multifunctional Electrocatalysis. *Advanced Materials*, **35** (12), 2208860.

35. Li, X., Shen, P., Luo, Y., Li, Y., Guo, Y., Zhang, H., and Chu, K. (2022) PdFe Single-Atom Alloy Metallene for N2 Electroreduction. *Angewandte Chemie*, **134** (28), e202205923.

36. Bouleau, L., Pérez-Rodríguez, S., Quílez-Bermejo, J., Izquierdo, M.T., Xu, F., Fierro, V., and Celzard, A. (2022) Best practices for ORR performance evaluation of metal-free porous carbon electrocatalysts. *Carbon N Y*, **189**, 349–361.

37. Briega-Martos, V., Cheuquepán, W., and Feliu, J.M. (2021) Detection of Superoxide Anion Oxygen Reduction Reaction Intermediate on Pt(111) by Infrared Reflection Absorption Spectroscopy in Neutral pH Conditions. *Journal of Physical Chemistry Letters*, **12** (6), 1588–1592.

38. Kunimatsu, K., Yoda, T., Tryk, D.A., Uchida, H., and Watanabe, M. (2009) In situ ATR-FTIR study of oxygen reduction at the Pt/Nafion interface. *Physical Chemistry Chemical Physics*, **12** (3), 621–629.

39. Mondal, S., Bagchi, D., Riyaz, M., Sarkar, S., Singh, A.K., Vinod, C.P., and Peter, S.C. (2022) In Situ Mechanistic Insights for the Oxygen Reduction Reaction in Chemically Modulated Ordered Intermetallic Catalyst Promoting Complete Electron Transfer. *J Am Chem Soc*, **144** (26), 11859–11869.

40. Yeo, B.S., and Bell, A.T. (2011) Enhanced activity of gold-supported cobalt oxide for the electrochemical evolution of oxygen. *J Am Chem Soc*, **133** (14), 5587–5593.

41. Moysiadou, A., Lee, S., Hsu, C.S., Chen, H.M., and Hu, X. (2020) Mechanism of Oxygen Evolution Catalyzed by Cobalt Oxyhydroxide: Cobalt Superoxide

Species as a Key Intermediate and Dioxygen Release as a Rate-Determining Step. *J Am Chem Soc*, **142** (27), 11901–11914.

42. Lin, Y., Yu, L., Tang, L., Song, F., Schlögl, R., and Heumann, S. (2022) In Situ Identification and Time-Resolved Observation of the Interfacial State and Reactive Intermediates on a Cobalt Oxide Nanocatalyst for the Oxygen Evolution Reaction. *ACS Catal*, **12** (9), 5345–5355.

43. Wang, S., Lin, Z., Li, M., Yu, Z., Zhang, M., Gong, M., Tang, Y., and Qiu, X. (2022) Coupling isolated Ni single atoms with sub-10 nm Pd nanocrystals embedded in porous carbon frameworks to boost oxygen electrocatalysis for Zn–air batteries. *J Mater Chem A Mater*, **10** (11), 6086–6095.

44. Hong, J., Hyun, S., Tsipoaka, M., Samdani, J.S., and Shanmugam, S. (2022) RuFe Alloy Nanoparticle-Supported Mesoporous Carbon: Efficient Bifunctional Catalyst for Li-O2and Zn-Air Batteries. *ACS Catal*, **12** (3), 1718–1731.

45. Zhong, X., Ye, S., Tang, J., Zhu, Y., Wu, D., Gu, M., Pan, H., and Xu, B. (2021) Engineering Pt and Fe dual-metal single atoms anchored on nitrogen-doped carbon with high activity and durability towards oxygen reduction reaction for zinc-air battery. *Appl Catal B*, **286**, 119891.

46. Guo, Y., Wu, D., Li, M., Wang, K., Zhang, S., He, G., Yin, H., Huang, C., Yang, B., and Zhang, J. (2022) Coordination Engineering of Ultra-Uniform Ruthenium Nanoclusters as Efficient Multifunctional Catalysts for Zinc–Air Batteries. *Small Science*, **2** (10), 2200035.

47. Chen, J., Huang, J., Wang, R., Feng, W., Wang, H., Luo, T., Hu, Y., Yuan, C., Feng, L., Cao, L., Kajiyoshi, K., He, C., Liu, Y., Li, Z., and Feng, Y. (2022) Atomic ruthenium coordinated with chlorine and nitrogen as efficient and multifunctional electrocatalyst for overall water splitting and rechargeable zinc-air battery. *Chemical Engineering Journal*, **441**, 136078.

48. Li, Z., Li, H., Li, M., Hu, J., Liu, Y., Sun, D., Fu, G., and Tang, Y. (2021) Iminodiacetonitrile induce-synthesis of two-dimensional PdNi/Ni@carbon nanosheets with uniform dispersion and strong interface bonding as an effective bifunctional eletrocatalyst in air-cathode. *Energy Storage Mater*, **42**, 118–128.

49. Logeshwaran, N., Ramakrishnan, S., Chandrasekaran, S.S., Vinothkannan, M., Kim, A.R., Sengodan, S., Velusamy, D.B., Varadhan, P., He, J.H., and Yoo, D.J. (2021) An efficient and durable trifunctional electrocatalyst for zinc–air batteries driven overall water splitting. *Appl Catal B*, **297**, 120405.

50. Wang, Y., Guo, W., Zhu, Z., Xu, K., Zhang, H., Wei, W., Xiao, X., Liang, W., He, M., Yu, T., Zhang, D., Zhao, H., Xu, X., and Yang, T. (2022) Interfacial boron modification on mesoporous octahedral rhodium shell and its enhanced electrocatalysis for water splitting and oxygen reduction. *Chemical Engineering Journal*, **435**, 134982.

51. Zhuang, X., Zhou, Y., Jiang, Z., Yao, X., and Yu, X.Y. (2021) Synergetic electronic modulation and nanostructure engineering of heterostructured RuO 2 /Co 3 O 4 as advanced bifunctional electrocatalyst for zinc–air batteries. *J Mater Chem A Mater*, **9** (47), 26669–26675.

52. Zhang, F., Ji, R., Zhu, X., Li, H., Wang, Y., Wang, J., Wang, F., and Lan, H. (2023) Strain-Regulated Pt–NiO@Ni Sub-Micron Particles Achieving Bifunctional Electrocatalysis for Zinc–Air Battery. *Small*, **19** (34), 2301640.

53. Feng, W., Feng, Y., Chen, J., Wang, H., Hu, Y., Luo, T., Yuan, C., Cao, L., Feng, L., and Huang, J. (2022) Interfacial electronic engineering of Ru/FeRu nanoparticles as efficient trifunctional electrocatalyst for overall water splitting and Zn-air battery. *Chemical Engineering Journal*, **437**, 135456.

54. Zhou, C., Zhao, S., Meng, H., Han, Y., Jiang, Q., Wang, B., Shi, X., Zhang, W., Zhang, L., and Zhang, R. (2021) RuCoOxNanofoam as a High-Performance Trifunctional Electrocatalyst for Rechargeable Zinc-Air Batteries and Water Splitting. *Nano Lett*, **21** (22), 9633–9641.

55. Xu, Z., Zhang, X., Wang, X., Fang, J., Zhang, Y., Liu, X., Zhu, W., Yan, Y., and Zhuang, Z. (2021) Synthesis of Ag-Ni-Fe-P Multielemental Nanoparticles as Bifunctional Oxygen Reduction/Evolution Reaction Electrocatalysts. *ACS Nano*, **15** (4), 7131–7138.

56. Balamurugan, C., Lee, C., Cho, K., Kim, J., Park, B., Kim, W., Lim, N., Kim, H., Pak, Y., Chae, K.H., Shim, J.H., and Kwon, S. (2023) High-performance

rechargeable metal–air batteries enabled by efficient charge transport in multielement random alloy electrocatalyst. *Appl Catal B*, **330**, 122631.

57. Li, Y., Gong, M., Liang, Y., Feng, J., Kim, J.E., Wang, H., Hong, G., Zhang, B., and Dai, H. (2013) Advanced zinc-air batteries based on high-performance hybrid electrocatalysts. *Nature Communications 2013 4:1*, **4** (1), 1–7.

Chapter 2.3

NiPd as an efficient electrocatalyst for Zinc-CO_2 batteries

Summary

This chapter investigates the performance of NiPd and Pd catalysts towards zinc-CO_2 *batteries. The zinc-*CO_2 *batteries are increasingly recognized for their role in mitigating climate change impacts through the electrochemical sequestration of* CO_2*. These batteries not only contribute to energy conversion but are also pivotal in producing valuable carbonaceous fuels. The use of formate as a liquid byproduct is especially advantageous due to its ease of handling and storage and its non-accumulative nature on the cathode's active surface, as opposed to solid or gaseous byproducts. This chapter discusses the use of bifunctional palladium (Pd) cathode in Zn-*CO_2 *batteries, which significantly enhances the conversion of* CO_2 *to formate, thus optimizing the battery's efficiency and rechargeability. Our detailed analysis focuses on the performance enhancements observed when nickel is incorporated into palladium nanostructures (NiPd), forming an effective catalyst in zinc-*CO_2 *batteries. The addition of nickel to Pd not only increased the Faradaic efficiency for formate production but also maintained stability even at higher current densities.*

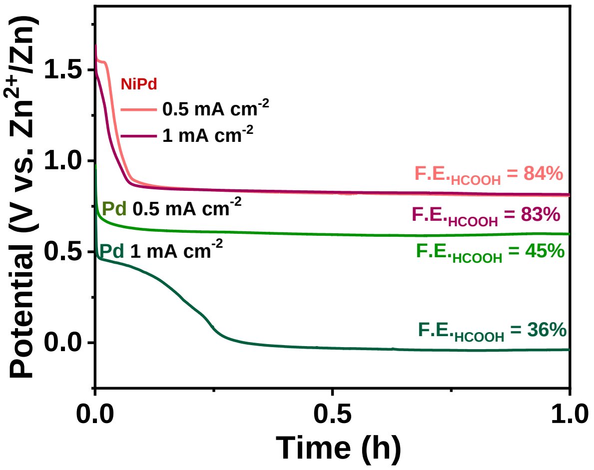

2.3.1 Introduction

Zinc-CO_2 batteries emerge as a noteworthy solution in mitigating climate change impacts by facilitating the electrochemical sequestration of carbon dioxide (CO_2).[1] Besides energy conversion, these batteries are instrumental in producing valuable carbonaceous fuels. A distinctive feature of specific zinc-CO_2 batteries is a reversible reaction wherein zinc, CO_2, water, and hydroxide ions interchangeably react to yield zinc oxide, formate, and water[2], as depicted in **Figure 1**:

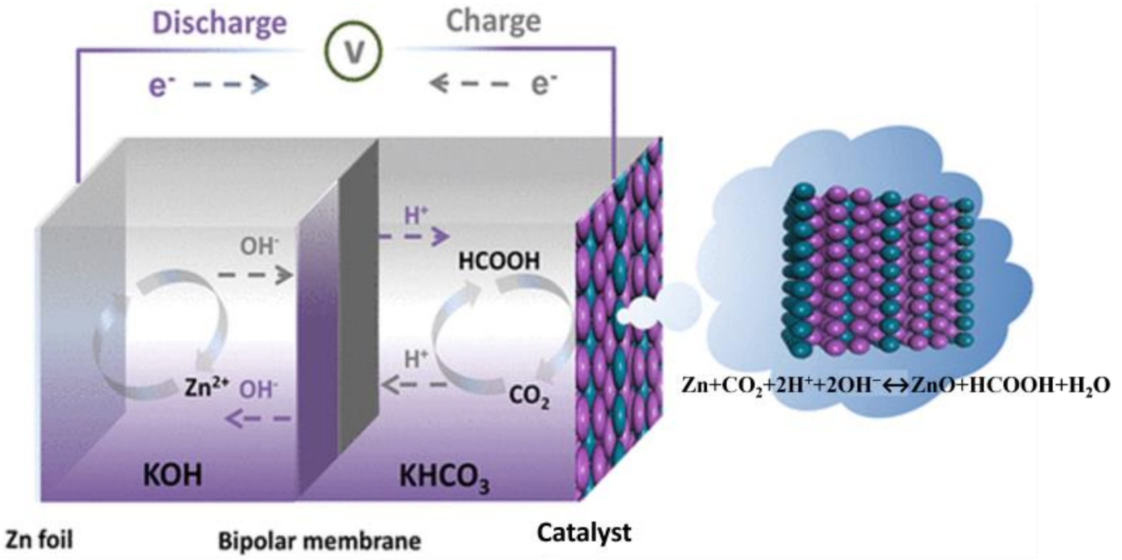

Figure 1. Schematic illustration of Pd-based cathode for Zn-CO_2 battery. *Reproduced with permission from reference* [3]

Liquid byproducts, such as formate, are preferred over gaseous or solid products in zinc-CO_2 batteries for a few key reasons.[4][5] Firstly, they offer easier handling and storage compared to gases. Secondly, unlike solid byproducts, they do not accumulate on the active surface of the cathode. Formic acid (HCOOH), earmarked as a prime example here, is of notable importance given its broad-based applications in the agricultural and industrial sectors. Therefore, formate is one of the three identified discharge products in advanced Zinc-CO_2 batteries, distinguished from other tested byproducts like carbon monoxide (CO)[6][7,8], methanol[9], and methane (CH_4)[10]. In Zinc-CO_2 batteries, the conversion of CO_2 to formate is accelerated by a bifunctional palladium (Pd) cathode, which facilitates the reversible interchange between these two chemical species. [3,5] Our initial investigations with palladium (Pd), known for its strong CO binding capabilities, predominantly produced CO and H_2.[11–13] Snyder's group demonstrated that nanoporous Pd–X alloys(where X represents Ni, Co, Ag, or Cu) improve resistance to

CO poisoning during prolonged CO_2 reduction reactions (CO_2RR).[14] Employing palladium (Pd) with various elements as a catalyst can augment the battery's performance by facilitating streamlined electrochemical reactions at reduced overpotentials and rechargeability.[15] These features culminate in cycling robustness and facilitate both reduction and oxidation reactions, which are pivotal attributes for the pragmatic deployment of Zinc-CO_2 batteries.

2.3.2 Scope of Investigation

In this chapter, we have analyzed the performance of Zinc-CO_2 batteries for a Pd-based catalyst, which shows enhanced Faradaic efficiency and stability upon incorporating nickel into palladium nanostructures (NiPd). The developed NiPd catalyst demonstrated an impressive Faradaic efficiency of 83% for formate production after 1.5 hours of discharge. This performance is notably superior to pure Pd, which showed a 45% efficiency after 1 hour at a current density of 0.5 mA cm^{-2}. It is significant to note that as the current density increased, the Faradaic efficiency of the NiPd catalyst remained relatively stable, demonstrating robust performance. Additionally, the NiPd catalyst displayed a superior peak power density, reaching 5 mW cm^{-2}, distinctly surpassing Pd, which only achieved a peak power density of 0.7 mW cm^{-2}.

2.3.3 Experimental Procedure:

i. Materials and characterization techniques:

$NiCl_2.6H_2O$ was procured from Loba chemicals, while $PdCl_2$ and $NaBH_4$ were procured from Sigma Aldrich. Milli-Q water was used for all experiments.

The synthesized materials were characterized through various techniques such as XRD, TEM, FESEM, and XPS. Powder X-ray diffraction (PXRD) patterns were acquired using a Rigaku diffractometer, which employs a copper anode generating X-rays at a wavelength of 1.54 Å, under 30 mA and 40 kV. Transmission electron microscopy (TEM) images were captured using a JEOL JEM 2100 Plus for the microscopic analysis. The Thermofisher (FEI) Apreo 2S obtained Field emission scanning electron microscopy (FESEM) images. X-ray photoelectron spectroscopy (XPS) data were collected using a Thermo K-alpha+ spectrometer, which utilized micro-focused and monochromated Al Kα radiation of 146.6 eV energy, and the pass energy for recording core-level spectra was maintained at 50 eV. The composition of the elements within the samples was ascertained using inductively coupled plasma optical emission spectroscopy (ICP-OES) through a PerkinElmer Optima 700DV.

ii. Protocol for Zn-CO$_2$ Battery studies:

A two-electrode configuration was employed for Zn-CO$_2$ battery studies within a semi-batch arrangement, segregated by a membrane, as delineated in **Figure 2**. The selected working electrode, the cathode, was a gas diffusion electrode (GDE) comprising both micro- and macroporous carbon layers. This configuration allowed for the deposition of the catalyst ink onto the microstructured carbon layer. A stainless steel mesh was incorporated as the current collector. A zinc foil was utilized as an anode for the counter and reference electrode. The electrodes were calibrated to an effective surface area of 1 cm^2.

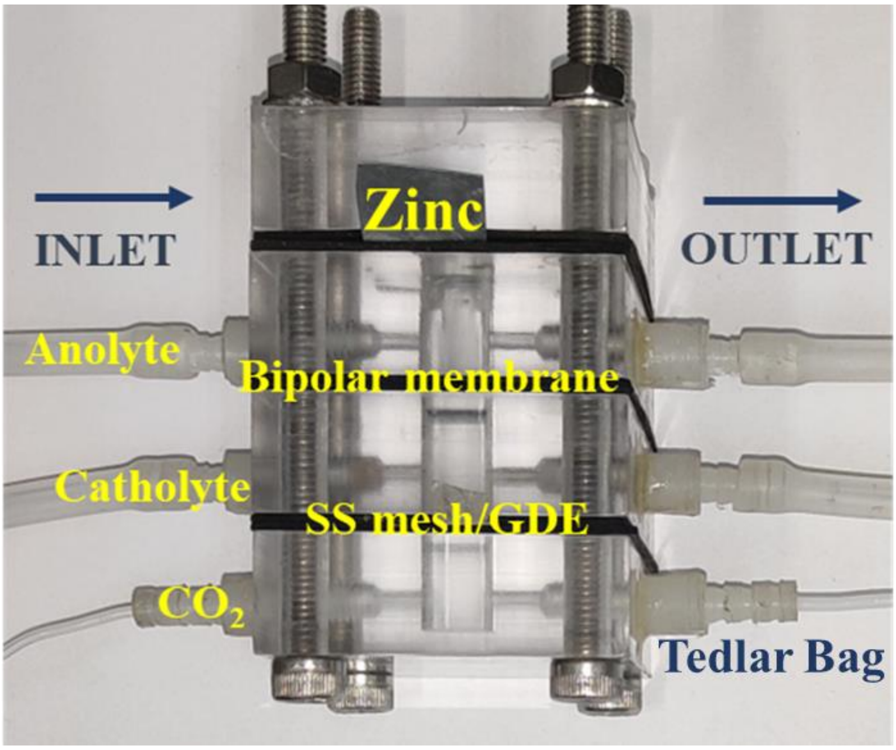

Figure 2. Setup for Zn-CO$_2$ battery with anode, cathode, and electrolyte in flow condition. The gas purged into the system is collected in the gas bag.

Regarding the electrolytic medium, the catholyte (on the cathode side) was composed of 0.1M potassium bicarbonate ($KHCO_3$). The anolyte (on the anode side) was formulated from a mixture of 6M potassium hydroxide (KOH) and 0.2M zinc acetate.[16] The flow rate of the electrolyte was meticulously controlled at 30 mL/min using a peristaltic pump. Concurrently, carbon dioxide was continuously purged at an equivalent flow rate using a mass flow controller directed toward the macroporous side of the GDE. A bipolar membrane was deployed to effectuate the separation of the electrolytes, which exhibited distinct pH values. This membrane was routinely conditioned and preserved in milli-Q water.

The galvanostatic studies were carried out for product quantification, i.e., formate or hydrogen.

iii. Synthesis of Pd nanosponges:

In the synthesis of Pd nanosponges, a methodical approach was adopted. The initial step involved the preparation of 50 mL of a 0.1M H_2PdCl_4 solution. This solution was prepared by dispersing 0.88 g of $PdCl_2$ in 50 mL of distilled water (H_2O), to which 0.2M HCl was subsequently added. This mixture underwent continuous stirring for 24 hours, ensuring a complete dissolution of the salt.[17]

Following this dissolution, a 5 mL aliquot of the H_2PdCl_4 solution (at 0.1 M concentration) was measured out. To this, 25 mL of a 0.1M $NaBH_4$ solution was rapidly introduced while maintaining vigorous stirring. The stirring was sustained for an additional 10 minutes post-addition. This reaction resulted in the precipitation of a black residue, which was subsequently collected. Purification procedures included washing the precipitate with milli-Q water to remove unreacted species or side products. Following this, the precipitate was dried at a temperature of 40°C, extending over an overnight period.

The final product, designated as Pd, was thoroughly characterized to ascertain its properties and confirm its structure. After this characterization, the synthesized Pd was employed as an electrocatalyst in battery experimentation.

iv. Synthesis of NiPd nanosponges:

Nickel was introduced into Pd nanosponges by mixing 3.76 mL of 0.1M H_2PdCl_4 with 24 mL of 0.1M $NiCl_2$ solution under vigorous stirring. 150 mL of 0.1M $NaBH_4$ solution was added under vigorous stirring conditions of metal salt solutions. The black residue was collected and dried at 40^oC overnight. The obtained product, i.e., approximately 200 mg, was added to 120 mL of 0.1M HCl, followed by 2 mL of H_2O_2 (30 wt%), and stirred for 2 minutes. The residue is washed with milli-Q H_2O and dried at 40^oC overnight. The obtained product, i.e., $Ni_{0.07}Pd$, was characterized and used as an electrocatalyst for battery studies.

v. Working electrode preparation:

The preparation of the working electrode was meticulously conducted as follows: 1 mg of each of the electrocatalysts, specifically NiPd and Pd, was independently dispersed in solvents where NiPd was mixed in 1 mL of isopropyl alcohol and Pd in 1 mL of H_2O. Each dispersion was then subjected to ultrasonic treatment for one hour to ensure uniform particle distribution. After the sonication process, 30 µl of Nafion solution (5 wt%) was added to each dispersion. The mixtures containing Nafion were then further sonicated for an additional hour to foster homogeneity and stabilize the dispersion. For the coating of these catalysts onto the electrodes, 600 µl of each sonicated dispersion (NiPd and Pd) was carefully drop-casted onto the gas diffusion electrode (GDE). The coating aimed to uniformly cover an area of 1 cm^2, achieving a catalyst loading density of 0.5 mg cm^{-2} on the electrode. After the drop-casting process, the electrodes were left out to dry. This drying phase was extended over two days under normal atmospheric conditions, ensuring the solvents' gradual and steady evaporation and forming a consistent catalyst layer on the GDE.

vi. Protocol for product estimation

a. **Gaseous product**: Gaseous products were detected and quantified by gas chromatography (GC) from Agilent 7890B.

b. **Liquid product**: The catholyte was collected immediately after the reaction, filtered with 0.2-micron filters, and then analyzed in HPLC with RID (Refractive index detector). It was calibrated with known concentrations of potassium formate in milli-Q water, as shown in **Figure 3**.

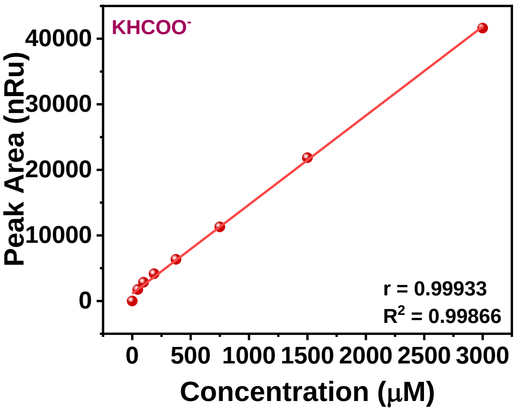

Figure 3. Calibration plot for formate analyzed from HPLC.

A calibration plot was prepared from H2 calibration gas of concentrations 20 ppm, 100 ppm, 500 ppm, 1000 ppm, and 3000 ppm, as shown in **Figure 4**.

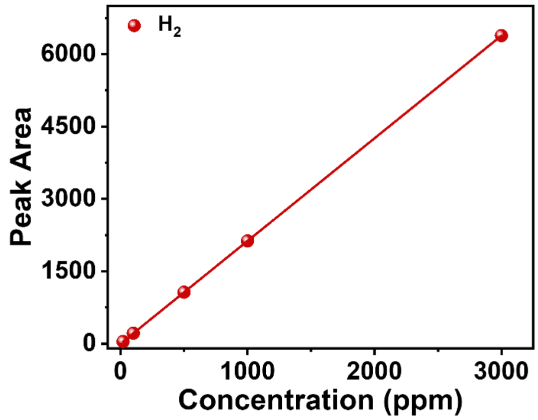

Figure 4. A calibration plot for H_2 was detected from a gas chromatography instrument.

vii. Catalyst Evaluation parameters:

Faradaic efficiency can be calculated as follows[18]:

$$\text{Faradaic efficiency (\%)} = (Q_{experimental}/\ Q_{theoretical}) \times 100$$

$$= (z \times n \times F) \times 100$$

z = no. of electrons transferred, n = number of moles of product, and F is the Faraday constant.

viii. Protocol for Post reaction characterizations:

After the reaction, NiPd and Pd electrodes (coated on GDL) were washed with milli-Q water, followed by ethanol, and dried under ambient conditions. The electrodes were analyzed using XRD, FESEM, Raman, and XPS to understand the change in the structure after the electrochemical reaction.

2.3.4 Results and Discussion:

PXRD (powder X-ray diffraction) studies were conducted to examine the crystal facets of synthesized NiPd and Pd. The PXRD patterns for both NiPd and Pd displayed similarities, revealing facets characteristic of the face-centered cubic (fcc) crystal structure inherent to Pd.[19] These findings are detailed in **Figure 5**. Additionally, ICP-OES (inductively coupled plasma optical emission spectroscopy) investigations determined the weight percentage of Ni in the NiPd sample to be approximately 7 wt%.

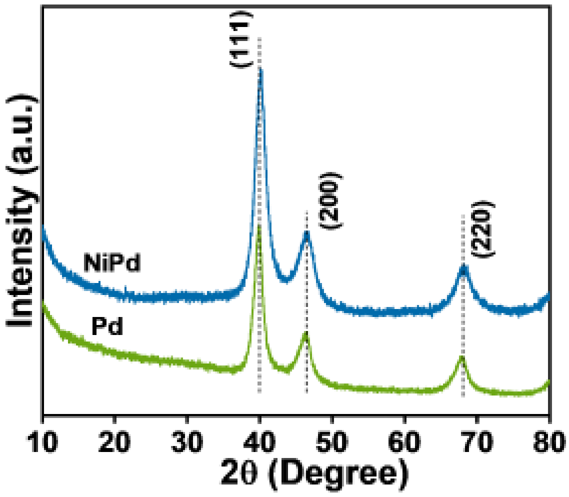

Figure 5. PXRD pattern for Pd and NiPd catalyst.

XPS (X-ray photoelectron spectroscopy) studies were conducted to examine the surface chemical composition and the oxidation states of Pd and NiPd. In **Figure 6a**, a survey scan of the synthesized Pd reveals the presence of Pd and O species. For accurate binding energy evaluation, carbon was used as a reference for calibration corrections. The high-resolution Pd 3d core-level spectra depicted in **Figure 6b** indicate the presence of metallic Pd^0 at a binding energy of 335.4 eV and Pd^{2+} species, representing surface oxides at 336.5 eV for the $3d_{5/2}$ orbital.[20,21] The presence of Pd-O species was further corroborated by the O 1s spectra, as illustrated in **Figure 6c**.

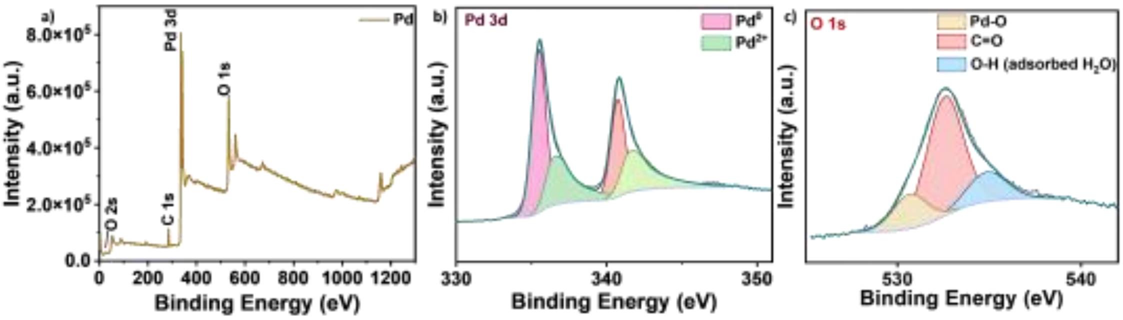

Figure 6. XPS spectra for Pd show a) survey scan, b) Pd 3d, and c) O 1s spectra.

In the case of NiPd, the survey scan showed an additional peak of Ni, as shown in **Figure 7a**. Additionally, due to Ni's introduction, the Pd^0 (335.6 eV) and Pd^{2+} (336.7 eV) peak positions are positively shifted by 0.2 eV, as shown in **Figure 7b**. **Figure 7c** shows Ni 2p spectra comprising mixed oxidation state, i.e., Ni metallic form and Ni^{2+} oxidation state.[22] For NiPd, the O 1s spectra showed similar Pd-O linkages to that of Pd, as shown in **Figure 7d**.

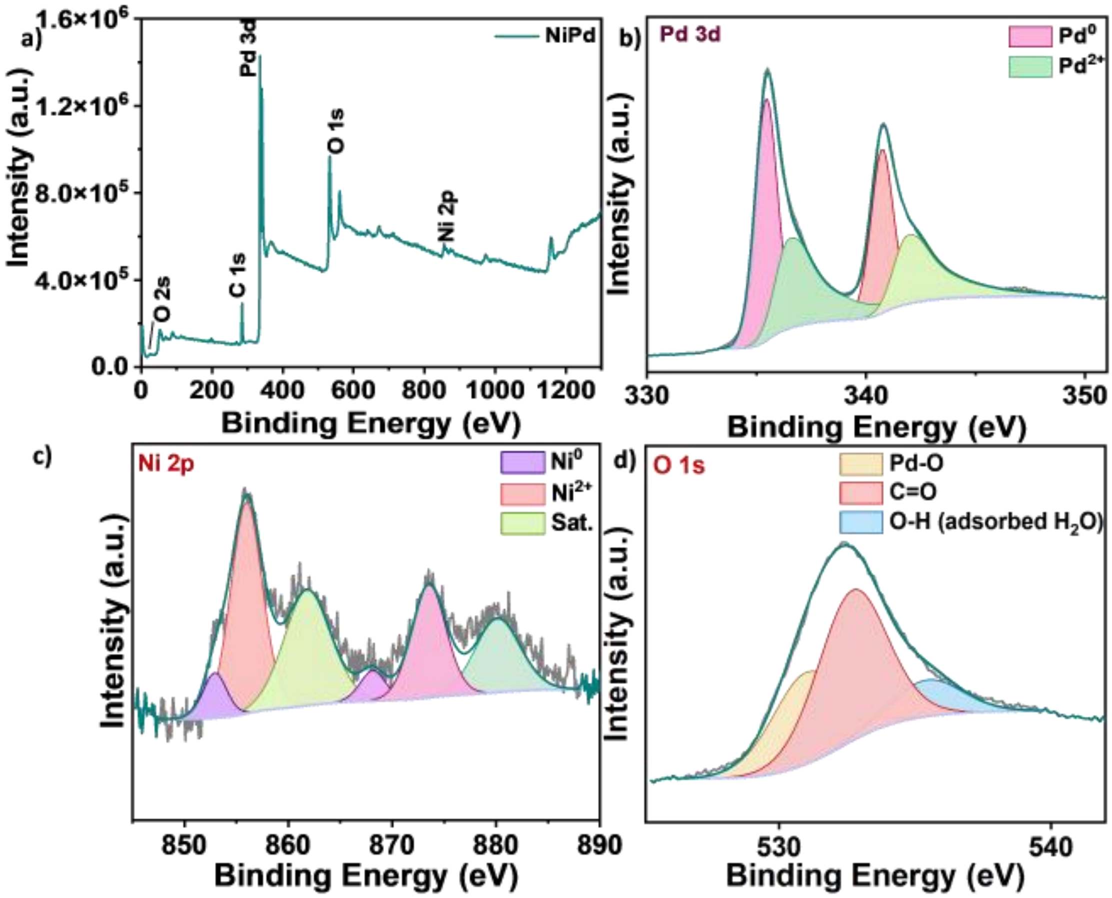

Figure 7. The XPS pattern of NiPd shows a) survey scan, b) Pd 3d, c) Ni 2p, and d) O 1s spectra.

Field emission scanning electron microscopy (FESEM) image exhibits fused metal particles with interdigitated morphology (**Figure 8a**). TEM (transmission electron microscopy) and HRTEM (high-resolution transmission electron microscopy) imaging techniques were utilized to characterize the primary sample. Figures **8b** and **9a** depict the NiPd electrocatalyst, presenting an interconnected nanosponge-like morphology, thus illuminating its nanostructural attributes.[17] The HRTEM image of NiPd illustrates nanoscale crystallites, with the (111) plane of Pd identified by the lattice spacing of 0.23 nm.

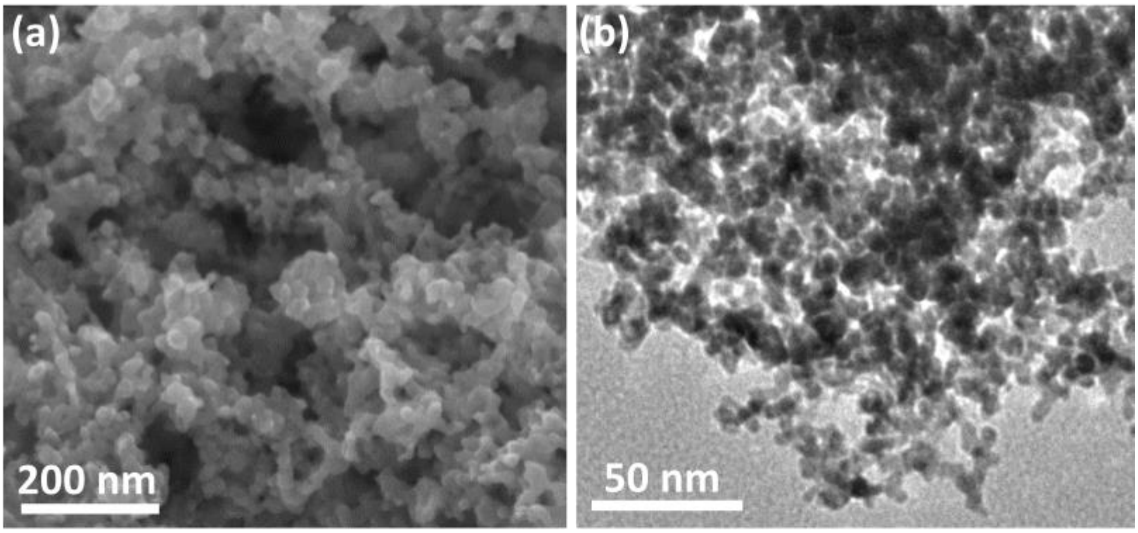

Figure 8. a) FESEM and b) TEM image of Pd catalyst.

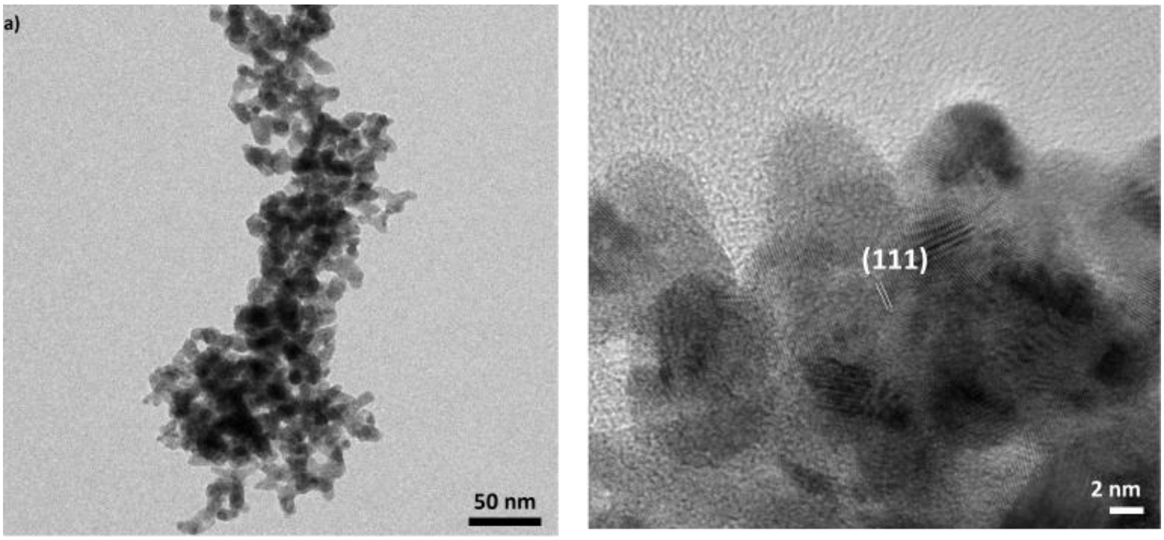

Figure 9. a) TEM and b) HRTEM image of NiPd catalyst.

For electrochemical investigations in a zinc-CO_2 battery setup, NiPd and Pd catalysts were employed. These catalysts were opposite to a Zn foil, separated by a bipolar membrane. The primary function of this bipolar membrane is to regulate the pH values, a crucial aspect considering that both charging and discharging processes occur within the same configuration.[23]

A detailed examination was carried out on the discharge polarization curves of NiPd and Pd in both argon (serving as a control) and CO_2 atmospheres, as presented in **Figure 8**. Notable differences in performance were observed for NiPd and Pd samples under different atmospheric conditions, thereby demonstrating their ability for CO_2 conversion. The generation of current density in the argon atmosphere is attributed to the hydrogen evolution reaction (HER).[24] In contrast, in CO_2 conditions, the current could arise from a combination of CO_2 reduction products and HER.

When Ni is incorporated into Pd (resulting in NiPd) and exposed to a CO_2 atmosphere, there is a remarkable increase in current density, achieving levels up to 10 mA cm^{-2}, in stark contrast to Pd alone, which attains only about 3 mA cm^{-2}. This substantial enhancement in current density with NiPd under CO_2 conditions underscores the pivotal role of Ni in the NiPd catalyst for effective CO_2 conversion. The reason behind lower current density in the case of Pd can be CO poisoning of Pd's active sites. The peak power density calculated from discharge polarization curves for Pd and NiPd are shown in **Figures 10a and 10b**. NiPd shows a higher peak power density value of 5 mW cm^{-2} compared to 0.7 mW cm^{-2} for Pd in the CO_2 atmosphere.

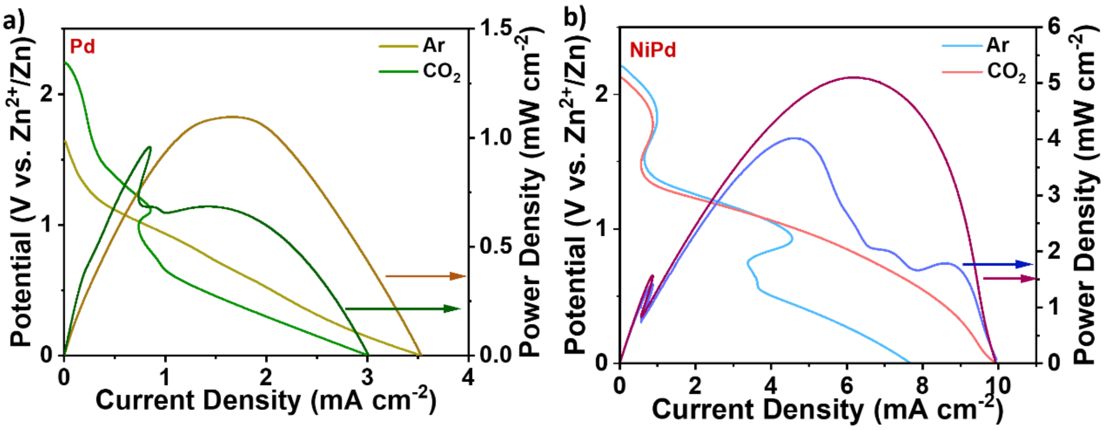

Figure 10. Discharge polarization curves and power density plot for a) Pd and b) NiPd in Ar and CO_2 atmosphere.

In a CO_2 atmosphere, product analysis for both Pd and NiPd was conducted under galvanostatic discharge conditions. The primary products identified for these catalysts, as determined by gas chromatography (GC) and high-performance liquid chromatography (HPLC) analyses, were hydrogen gas (H_2) and formate (a liquid product). For Pd, at a current density of 0.5 mA cm^{-2}, the Faradaic efficiency (FE) for formate formation was 45%. However, when the current density was increased to 1 mA cm^{-2}, the FE declined to 36% after an hour of discharge, as illustrated in **Figure 11a**.

In contrast, the NiPd catalyst exhibited a notably higher FE for formate production. At a current density of 0.5 mA cm^{-2}, the FE was recorded at 83%, with only a slight decrease to 79% even when the current density was raised to 1 mA cm^{-2} after 1.5 hours, as shown in **Figure 11b**. It was also observed that to maintain a current density of 1 mA cm^{-2}, Pd experienced an increase in overpotential, ultimately falling below 0 V. In stark contrast, NiPd maintained a stable performance under these conditions. This distinction underscores the enhanced efficiency and stability of NiPd compared to Pd in the context of CO$_2$ reduction. It is noteworthy that NiPd provided a high F.E. (83%) with a low overpotential of 0.82 V.

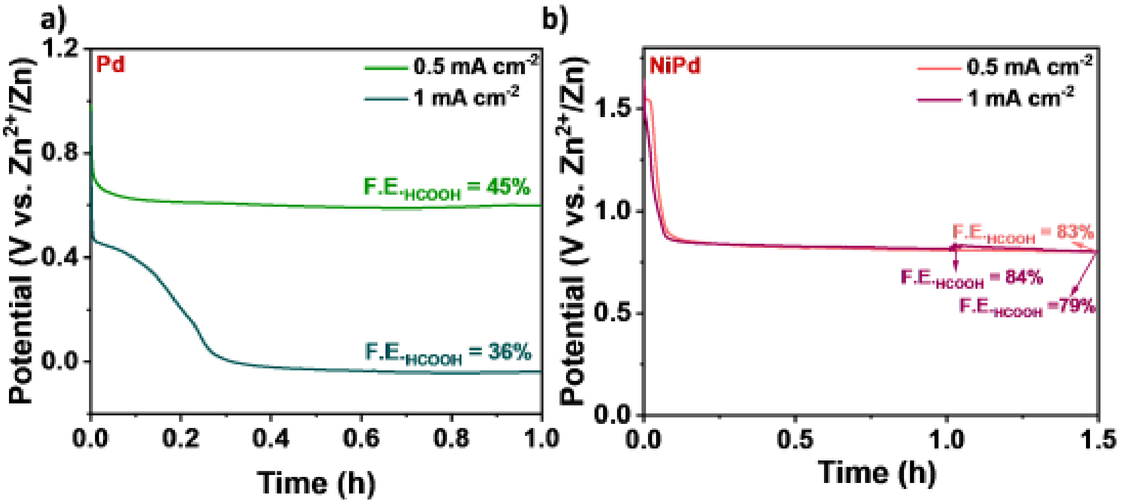

Figure 11. Galvanostatic discharge curves show Faradaic efficiency for formate formation in a) Pd and b) NiPd in a CO$_2$ atmosphere.

Figure 12 highlights the substantial stability and endurance of the NiPd catalyst under extended galvanostatic discharge conditions. This endurance is quantified by maintaining a high FE of 73% at a current density of 0.5 mA cm^{-2} over 7 hours. At an increased current density of 1 mA cm^{-2}, the NiPd catalyst exhibits robust performance, maintaining an FE of 65% for 6.5 hours. These results underscore the NiPd catalyst's capacity for reliable, long-term functionality across various current densities. As the current density was escalated from 1 mA cm^{-2} to 1.5 mA cm^{-2}, 2 mA cm^{-2}, and finally 3 mA cm^{-2}, there was a notable decrease in the potential, which dropped from 0.73 V to 0.5 V, then further to 0.37 V, and ultimately reached 0.2 V (**Figure 13**).

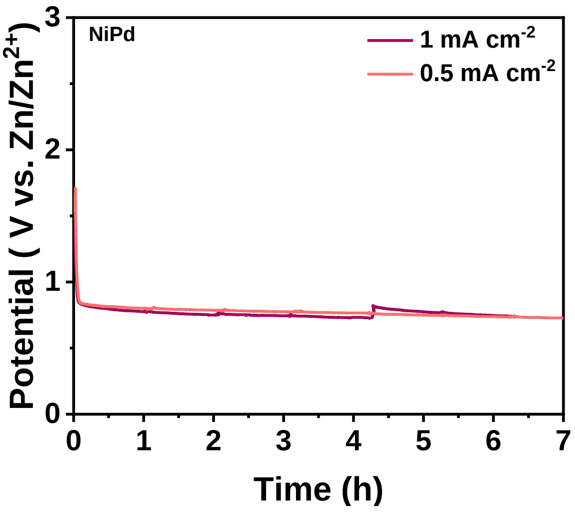

Figure 12. Long-term stability under discharge conditions for NiPd in CO_2 atmosphere.

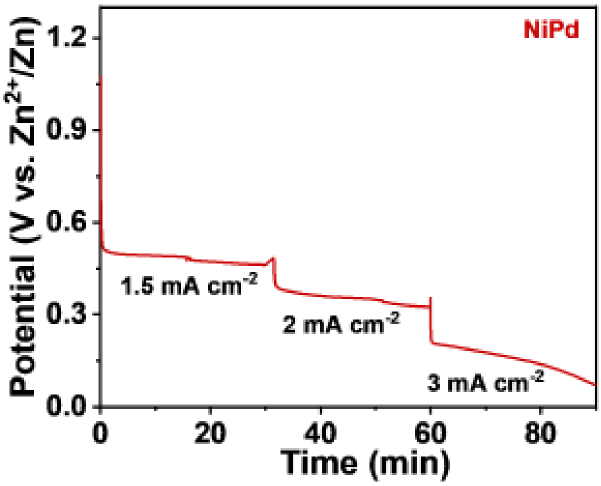

Figure 13. Galvanostatic discharge at different potentials for NiPd catalyst.

The galvanostatic charge-discharge profiles of Pd and NiPd were analyzed within a Zn-CO2 battery framework to evaluate the catalysts' reversibility. Due to observed degradation at 1 mA cm^{-2}, Pd was tested at a reduced current density of 0.5 mA cm^{-2}, with 5 minutes of charging and 5 minutes of discharging cycles, as depicted in **Figure 14a**. Pd maintained a discharge potential of 0.69 V and a charge potential of 2.88 V, giving a voltage gap of 2.19 V for up to 20 hours at this lower current density. In contrast, NiPd, presented in **Figures 14b and 14c**, exhibited superior performance by maintaining a discharge potential of 0.72 V and a charge potential of 2.69 V and exhibiting a lower voltage gap of 1.97 V at 0.5 mA cm^{-2}. After 35 hours of charge-discharge cycling, NiPd showed a highly reversible behavior in the battery, confirming the catalyst's exceptional robustness and efficiency.

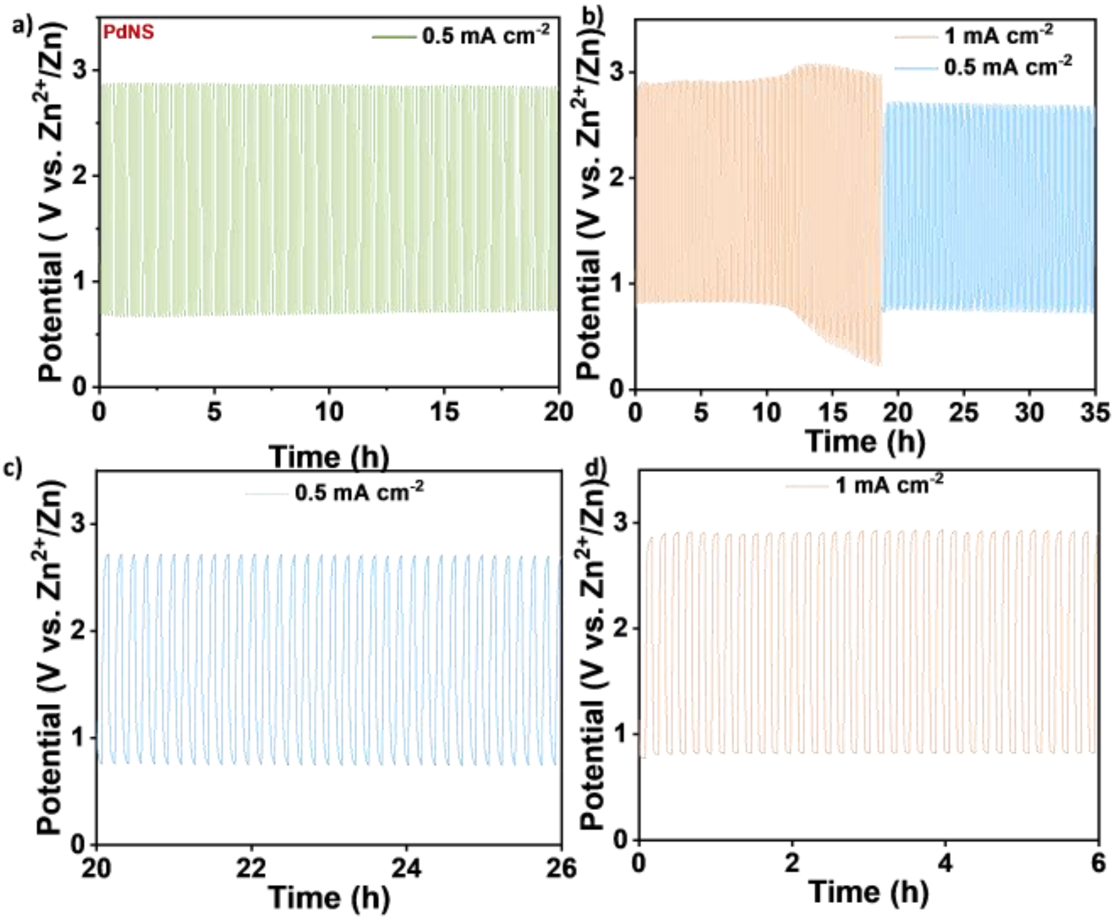

Figure 14. Galvanostatic charge-discharge profile of catalyst a) Pd and b) NiPd. C) and d) show close profiles of NiPd at 1 mA cm^{-2} and 0.5 mA cm$^{-2,}$ respectively.

At a higher current density of 1 mA cm^{-2}, NiPd exhibited a 2.06 V voltage gap, which increased to 2.76 V after 18.6 hours. Remarkably, when NiPd's charge-discharge cycle was tested at 0.5 mA cm^{-2}, it displayed no significant change in 25 hours. The charge storage capabilities of NiPd at both 1 mA cm^{-2} are illustrated in **Figures 14b and 14d**.

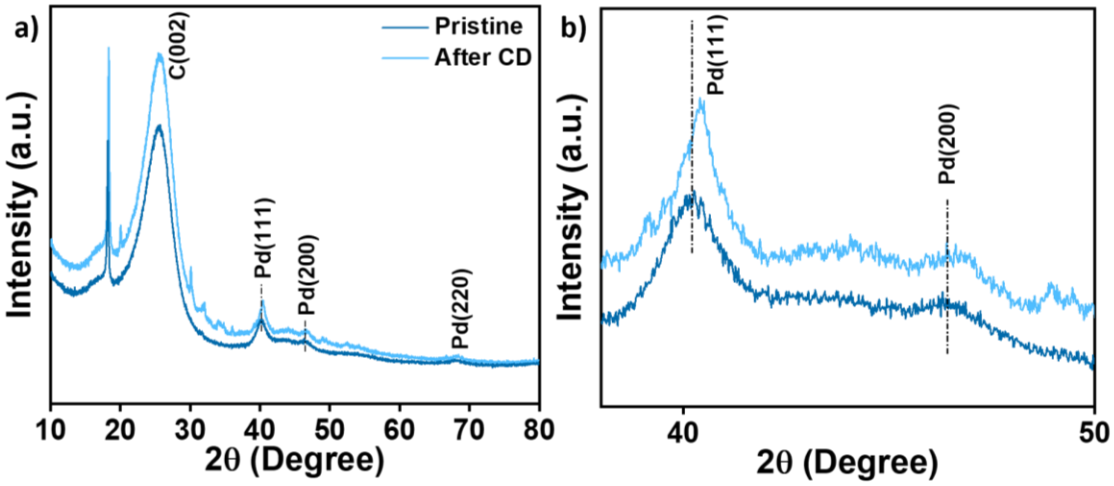

Figure 15. a) PXRD pattern of NiPd comparing pristine and after charge-discharge (CD) for NiPd catalyst on GDL and b) its closeup for peaks of interest.

After the charge-discharge (CD) cycling, which entailed 35 hours of reaction, X-ray diffraction (XRD) analysis was conducted for the NiPd catalyst-supported GDL (**Figure 14**), the results revealed a minor shift at 40° of (111) plane towards a higher 2θ value for Pd in the NiPd composite, as delineated in **Figures 15a and 15b**, when compared to its pristine state.

X-ray photoelectron spectroscopy (XPS) analysis was performed to shed light on the changes in oxidation states of NiPd after charge-discharge cycling. The results of this analysis, crucial for understanding the chemical and electronic shifts within the catalyst, are illustrated in **Figure 16**. This figure visually conveys how the electrochemical cycling influences the oxidation states within the NiPd catalyst, offering critical insights into its chemical dynamics during operation. The high-resolution C 1s scan illustrated in **Figure 16a** reveals the emergence of additional C-F-based linkages associated with Nafion, namely CF_3, CF_2, and CF.[25,26] **Figure 16b** delineates a positive Pd 3d core-level spectra shift relative to the pristine state. Notably, a shift of 0.4 eV in the Pd^0 peak and 0.5 eV in the Pd^{2+} peak were observed, with their respective binding energies enumerated in **Table 1**. Furthermore, **Table 2** presents a surge in the content of oxidized Pd, indicating an increase in Pd^{2+} content following the charge-discharge cycling relative to Pd^0.

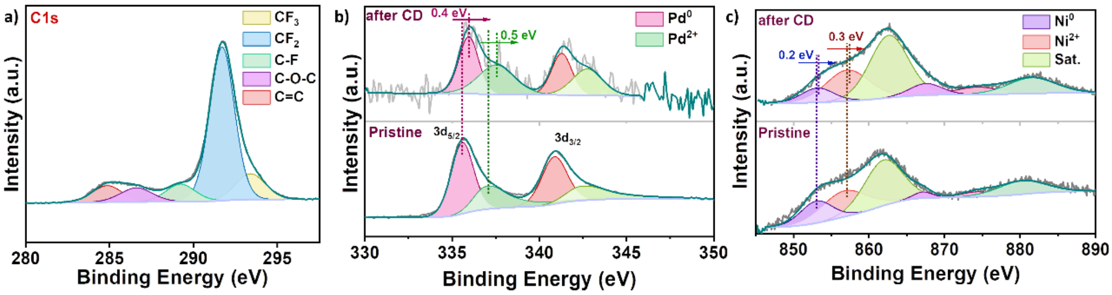

Figure 16. The XPS spectra showcasing a) C 1s, b) Pd 3d, and c) Ni 2p elements are juxtaposed for the NiPd catalyst in its pristine state and post-charge-discharge (CD) cycling.

Pd 3d	**Pd$^0_{5/2}$**	**Pd$^0_{3/2}$**	**Pd$^{2+}_{5/2}$**	**Pd$^{2+}_{3/2}$**
Pristine	335.6	340.9	337.1	342.5
After CD	336	341.3	337.6	342.9

Table 1. Binding energy values from Pd 3d spectra compared for pristine and after CD analysis.

Pd wt%	**Pd^0**	**Pd^{2+}**
Pristine	72.1	27.9
After CD	60.3	39.6

Table 2. Comparison of the relative percentage change in Pd and Pd^{2+} species before and after cycling.

In **Figure 16c**, the Ni 2p spectra of NiPd reveal a notable positive shift following charge-discharge (CD) cycling compared to its initial state. Specifically, the Ni metallic peak experiences a shift upwards by 0.2 eV, while the Ni^{2+} peak shifts by an increased magnitude of 0.3 eV relative to the pristine sample. Detailed values of the binding energies for Ni^0, Ni^{2+}, and the associated satellite peaks in the Ni 2p spectra, both in the original (pristine) state and after the CD cycling, are comprehensively cataloged in **Table 3**.

Ni 2p	**Ni$^0_{3/2}$**	**Ni$^0_{1/2}$**	**Ni$^{2+}_{3/2}$**	**Ni$^{2+}_{1/2}$**	**Sat.$_{3/2}$**	**Sat.$_{1/2}$**
Pristine	853.2	867.2	857.6	874.3	862.1	880.8
After CD	853.5	867.7	857.4	874.5	862.7	881.5

Table 3. Binding energy values from Ni 2p spectra compared for pristine and after CD analysis.

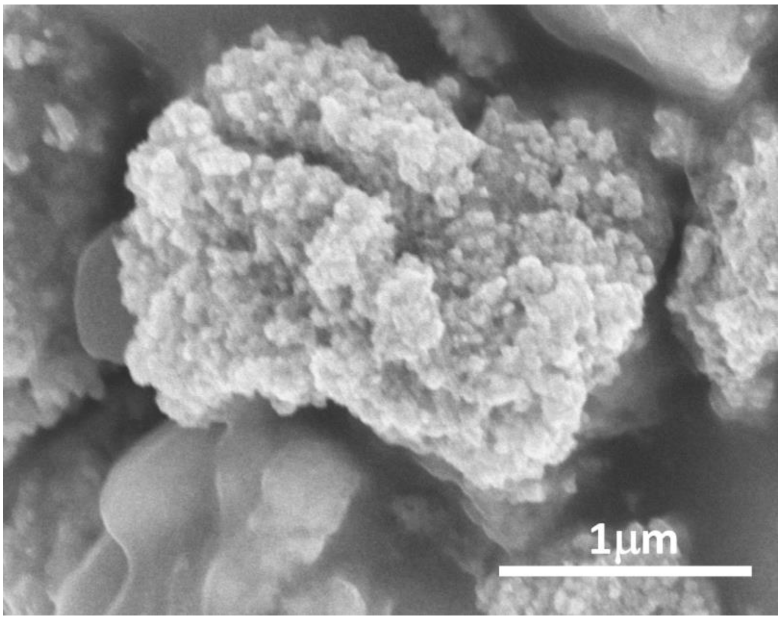

Figure 17. Post-reaction SEM analysis of NiPd on GDL after CD.

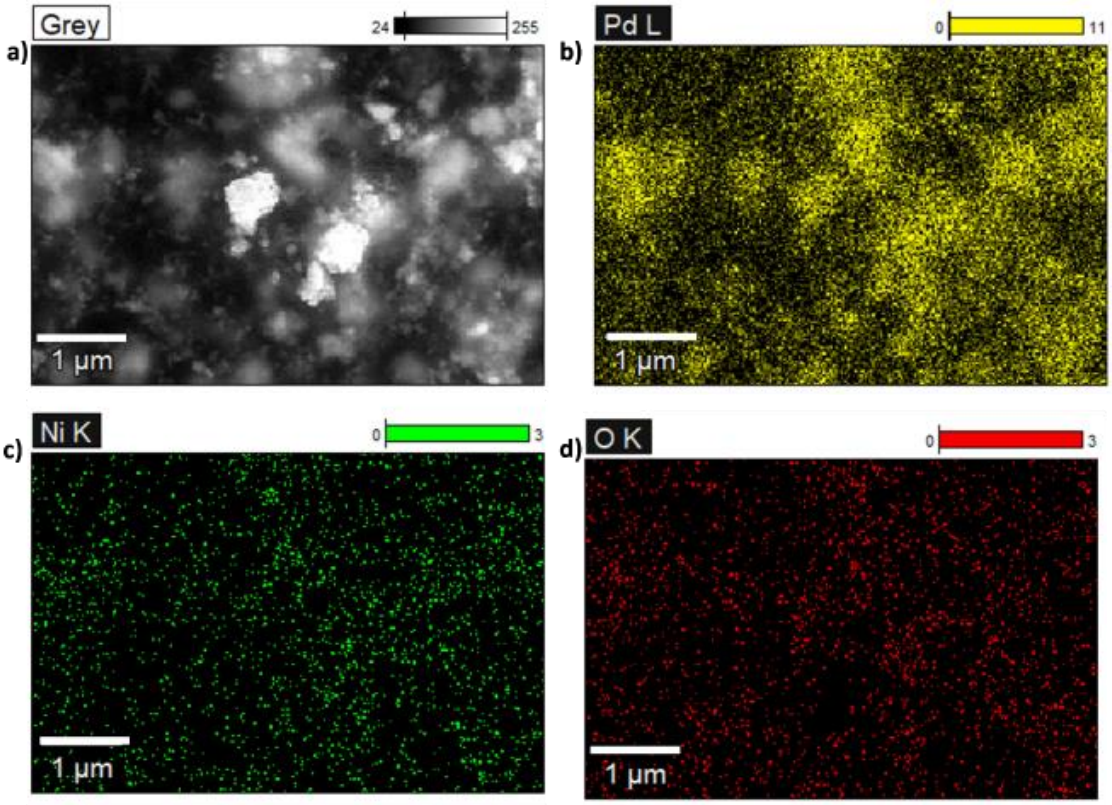

Figure 18. Post-reaction elemental mapping of NiPd with a) image and elements, b) Pd, c) Ni, and d) O.

The FESEM image depicted in **Figure 17** demonstrates that the nanosponge-like morphology of the sample is maintained even after the CD process. Elemental mapping analysis of NiPd following CD, as shown in **Figure 18**, reveals a uniform distribution of Ni alongside Pd. Additionally, a modest presence of surface oxygen was observed on both Ni and Pd elements.

Electrocatalyst	**Peak power Density**	**References**
NiPd	5mW/cm^2	**Our Work**
BiPd	0.42mW/cm^2	[3]
Bi nanoparticles on carbon	1.4mW/cm^2	[27]
Coralloid Au	0.7mW/cm^2	[28]
$La_2Cu_{1-x}Pd_xO_4$ (x = 0.05)	0.75mW/cm^2	[15]
$Pd_1O_3C_1$	1.72mW/cm^2	[29]

Table 4. Table of comparison for powder density of noble metal-based electrocatalysts compared with our work, i.e., NiPd for Zn-CO_2 battery.

2.3.5 Conclusion:

This chapter examines the enhanced performance of nickel-palladium (NiPd) and palladium (Pd) catalysts in zinc-CO_2 batteries, which are vital for CO_2 reduction and producing valuable fuels like formate. Incorporating nickel into palladium significantly boosts the Faradaic efficiency for formate production in NiPd to 83%, compared to 45% for Pd, and shows remarkable stability even at higher current densities. NiPd outperforms Pd in peak power density (5 mW cm^{-2} for NiPd vs. 0.7 mW cm^{-2} for Pd) and maintains structural and functional integrity post-charge-discharge cycling. These advancements highlight NiPd's potential in elevating Zn-CO_2 battery technology, which is vital for sustainable energy conversion and climate change mitigation.

2.3.6 References:

1. Xie, J., and Wang, Y. (2019) Recent Development of CO_2 Electrochemistry from Li-CO_2 Batteries to Zn-CO_2 Batteries. *Acc Chem Res*, **52** (6), 1721–1729.

2. Gao, S., Wei, T., Sun, J., Liu, Q., Ma, D., Liu, W., Zhang, S., Luo, J., and Liu, X. (2022) Atomically Dispersed Metal-Based Catalysts for Zn–CO_2 Batteries. *Small Struct*, **3** (12), 2200086.

3. Gao, S., Chen, S., Liu, Q., Zhang, S., Qi, G., Luo, J., and Liu, X. (2022) Bifunctional BiPd Alloy Particles Anchored on Carbon Matrix for Reversible Zn-CO_2 Battery. *ACS Appl Nano Mater*, **5** (9), 12387–12394.

4. Wang, Y., Huang, Z., Lei, Y., Wu, J., Bai, Y., Zhao, X., Liu, M., Zhan, L., Tang, S., Zhang, X., Luo, F., and Xiong, X. (2022) Bismuth with abundant defects for electrocatalytic CO_2 reduction and Zn–CO_2 batteries. *Chemical Communications*, **58** (22), 3621–3624.

5. Xie, J., Wang, X., Lv, J., Huang, Y., Wu, M., Wang, Y., and Yao, J. (2018) Reversible Aqueous Zinc–CO_2 Batteries Based on CO_2–HCOOH Interconversion. *Angewandte Chemie International Edition*, **57** (52), 16996–17001.

6. Hao, X., An, X., Patil, A.M., Wang, P., Ma, X., Du, X., Hao, X., Abudula, A., and Guan, G. (2021) Biomass-Derived N-Doped Carbon for Efficient Electrocatalytic CO_2 Reduction to CO and Zn-CO_2 Batteries. *ACS Appl Mater Interfaces*, **13** (3), 3738–3747.

7. Gao, S., Liu, Y., Xie, Z., Qiu, Y., Zhuo, L., Qin, Y., Ren, J., Zhang, S., Hu, G., Luo, J., and Liu, X. (2021) Metal-Free Bifunctional Ordered Mesoporous Carbon for Reversible Zn-CO_2 Batteries. *Small Methods*, **5** (4), 2001039.

8. Wang, T., Sang, X., Zheng, W., Yang, B., Yao, S., Lei, C., Li, Z., He, Q., Lu, J., Lei, L., Dai, L., Hou, Y., Wang, T., Zheng, W., Yang, B., Yao, S., Lei, C., Li, Z., He, Q., Lei, L., Hou, Y., Sang, X., Lu, J., and Dai, L. (2020) Gas Diffusion Strategy for Inserting Atomic Iron Sites into Graphitized Carbon Supports for Unusually High-Efficient CO_2 Electroreduction and High-Performance Zn–CO_2 Batteries. *Advanced Materials*, **32** (29), 2002430.

9. Kaur, S., Kumar, M., Gupta, D., Mohanty, P.P., Das, T., Chakraborty, S., Ahuja, R., and Nagaiah, T.C. (2023) Efficient CO_2 utilization and sustainable energy conversion via aqueous Zn-CO_2 batteries. *Nano Energy*, **109**, 108242.

10. Wang, K., Wu, Y., Cao, X., Gu, L., Hu, J., Wang, K., Cao, X., Gu, L., Hu, J., and Wu, Y. (2020) A Zn–CO_2 Flow Battery Generating Electricity and Methane. *Adv Funct Mater*, **30** (9), 1908965.

11. Chatterjee, S., Griego, C., Hart, J.L., Li, Y., Taheri, M.L., Keith, J., and Snyder, J.D. (2019) Free Standing Nanoporous Palladium Alloys as CO Poisoning Tolerant Electrocatalysts for the Electrochemical Reduction of CO_2 to Formate. *ACS Catal*, **9** (6), 5290–5301.

12. Yin, Z., Gao, D., Yao, S., Zhao, B., Cai, F., Lin, L., Tang, P., Zhai, P., Wang, G., Ma, D., and Bao, X. (2016) Highly selective palladium-copper bimetallic electrocatalysts for the electrochemical reduction of CO_2 to CO.

13. Torralba, E., Blanchard, N., Cachet-Vivier, C., Muller-Bouvet, D., González, J., and Bastide, S. (2020) Electrochemical study of carbon dioxide reduction at copper–palladium nanoparticles: Influence of the bimetallic composition in the CO poisoning tolerance. *Electrochim Acta*, **354**, 136739.

14. Chatterjee, S., Griego, C., Hart, J.L., Li, Y., Taheri, M.L., Keith, J., and Snyder, J.D. (2019) Free Standing Nanoporous Palladium Alloys as CO Poisoning Tolerant Electrocatalysts for the Electrochemical Reduction of CO_2 to Formate. *ACS Catal*, **9** (6), 5290–5301.

15. Xie, H., Liao, H., Zhai, S., Liu, T., Wu, Y., Wang, F., Li, J., Zhang, Y., and Chen, B. (2023) Enhancing Zn–CO_2 battery with a facile Pd doped perovskite cathode for efficient CO_2 to CO conversion. *Energy*, **263**, 125688.

16. Yang, M., Liu, S., Sun, J., Jin, M., Fu, R., Zhang, S., Li, H., Sun, Z., Luo, J., and Liu, X. (2022) Highly dispersed Bi clusters for efficient rechargeable Zn−CO_2 batteries. *Appl Catal B*, **307**, 121145.

17. Krishna, K.S., Sandeep, C.S.S., Philip, R., and Eswaramoorthy, M. (2010) Mixing does the magic: A rapid synthesis of high surface area noble metal nanosponges showing broadband nonlinear optical response. *ACS Nano*, **4** (5), 2681–2688.

18. Marcandalli, G., Goyal, A., and Koper, M.T.M. (2021) Electrolyte Effects on the Faradaic Efficiency of CO_2 Reduction to CO on a Gold Electrode. *ACS Catal*, **11** (9), 4936–4945.

19. Ge, Y., Wang, X., Chen, B., Huang, Z., Shi, Z., Huang, B., Liu, J., Wang, G., Chen, Y., Li, L., Lu, S., Luo, Q., Yun, Q., Zhang, H., Ge, Y., Wang, X., Chen, B., Huang, Z., Shi, Z., Huang, B., Li, L., Lu, S., Luo, Q., Yun, Q., Zhang, H., Kong Branch, H., Liu, J., Wang, G., and Chen, Y. (2022) Preparation of fcc-2H-fcc Heterophase Pd@Ir Nanostructures for High-Performance Electrochemical Hydrogen Evolution. *Advanced Materials*, **34** (4), 2107399.

20. Do, V.H., Prabhu, P., Jose, V., Yoshida, T., Zhou, Y., Miwa, H., Kaneko, T., Uruga, T., Iwasawa, Y., and Lee, J.M. (2023) Pd–PdO Nanodomains on Amorphous Ru Metallene Oxide for High-Performance Multifunctional Electrocatalysis. *Advanced Materials*, **35** (12), 2208860.

21. Kibis, L.S., Simanenko, A.A., Stadnichenko, A.I., Zaikovskii, V.I., and Boronin, A.I. (2021) Probing of Pd4+Species in a PdOx-CeO_2System by X-Ray Photoelectron Spectroscopy. *Journal of Physical Chemistry C*, **125** (38), 20845–20854.

22. Chen, H., Wu, X., Liu, D., Ye, C., Huang, L., Long, X., Wang, L., Zhang, J., Luo, J.L., and Fu, X.Z. (2023) Highly efficient C@Ni-Pd bifunctional electrocatalyst for energy-saving hydrogen evolution and value-added chemicals co-production from ethanol aqueous solution. *Chemical Engineering Journal*, **474**, 145639.

23. Blommaert, M.A., Aili, D., Tufa, R.A., Li, Q., Smith, W.A., and Vermaas, D.A. (2021) Insights and Challenges for Applying Bipolar Membranes in Advanced Electrochemical Energy Systems. *ACS Energy Lett*, **6**, 2539–2548.

24. Goyal, A., Marcandalli, G., Mints, V.A., and Koper, M.T.M. (2020) Competition between CO_2 Reduction and Hydrogen Evolution on a Gold Electrode under Well-Defined Mass Transport Conditions. *J Am Chem Soc*, **142** (9), 4154–4161.

25. Shutthanandan, V., Nandasiri, M., Zheng, J., Engelhard, M.H., Xu, W., Thevuthasan, S., and Murugesan, V. (2019) Applications of XPS in the characterization of Battery materials. *J Electron Spectros Relat Phenomena*, **231**, 2–10.

26. Friedman, A.K., Shi, W., Losovyj, Y., Siedle, A.R., and Baker, L.A. (2018) Mapping Microscale Chemical Heterogeneity in Nafion Membranes with X-ray Photoelectron Spectroscopy. *J Electrochem Soc*, **165** (11), H733–H741.

27. Wang, Y., Xu, L., Zhan, L., Yang, P., Tang, S., Liu, M., Zhao, X., Xiong, Y., Chen, Z., and Lei, Y. (2022) Electron accumulation enables Bi efficient CO_2 reduction for formate production to boost clean Zn-CO_2 batteries. *Nano Energy*, **92**, 106780.

28. Gao, S., Jin, M., Sun, J., Liu, X., Zhang, S., Li, H., Luo, J., and Sun, X. (2021) Coralloid Au enables high-performance Zn–CO_2 battery and self-driven CO production. *J Mater Chem A Mater*, **9** (37), 21024–21031.

29. Li, J., Chen, L.W., Hao, Y.C., Yuan, M., Lv, J., Dong, A., Li, S., Gu, H., Yin, A.X., Chen, W., Li, P., and Wang, B. (2023) Asymmetric coordinated single-atom Pd sites for high performance CO_2 electroreduction and Zn–CO_2 battery. *Chemical Engineering Journal*, **461**, 141865.

Chapter 3

Conclusion

The thesis is on different type of battery systems and is divided into two parts. The first introduction chapter discusses the evolution of energy storage, featuring li-ion batteries'(LIB) success and the rising interest in Na-ion (SIBs) and K-ion batteries (PIBs). It offers a thorough review of anode materials in alkali-ion batteries, emphasizing design for optimal capacity and addresses anode limitations like volume expansion, while also exploring electrolyte-SEI dynamics, essential techniques, and measurements guiding future battery advancements. From this understanding, the first working chapter revolves around superior performance of BTEG carbon as an anode material across alkali-ion batteries. BTEG exhibits impressive reversible capacities for LIBs (1014 mAh g^{-1}), SIBs (295 mAh g^{-1}), and PIBs (369 mAh g^{-1}), measured at a current density of 25 mA g^{-1}. Moreover, at a higher current density of 1 A g^{-1}, BTEG maintains remarkable capacity retentions over 1000 cycles for LIBs (75%), SIBs (100%), and PIBs (87%). Electrokinetic and in-situ analyses confirm BTEG carbon as a universally effective anode material for alkali-ion batteries, exhibiting diffusion-dominated processes for LIBs and capacitive-dominated processes for SIBs and PIBs. In the next part of this chapter, the emphasis is on the electrolyte optimization which has enabled to achieve high stability of BTEG with PIBs. Potassium-based electrolytes, particularly at higher concentrations like 5M KFSI, produce solid electrolyte interphase rich in inorganic components which enables BTEG to exhibit enhanced stability. The next chapter of this part involves the investigation of a tin-carbon composite anode material which exhibits high electrochemical stability and capacity retention, maintaining 94.6% over 700 cycles at 500 mA g^{-1}, respectively, in lithium-ion batteries. This exceptional performance is credited to the effective encapsulation of tin nanoparticles within a conductive graphitic matrix, alleviating typical volume expansion concerns. These results indicate promising potential for the Sn@C composite to bolster the durability and capacity of LIB anodes.

The next part of thesis explores zinc-air and zinc-CO_2 batteries as promising frontiers for advanced energy storage systems, balancing energy density, safety, and economic considerations. Innovations in cathode materials and catalyst design are highlighted as crucial for enhancing their efficiency and lifecycle, with the added benefit of contributing to carbon capture and conversion, thereby fostering environmental sustainability and technological advancement. In the first working chapter, the Pd-Co_3O_4@BCN catalyst exhibits high activity and stability for both oxygen evolution reaction (OER) and oxygen reduction reaction (ORR), outperforming conventional catalysts like Pt/C and RuO_2. Operando spectroscopy provides key insights into reaction mechanisms, further enhancing our understanding of catalyst performance. Moreover, NiPd catalysts show enhanced Faradaic efficiency (83%) for CO_2 reduction and offers promising prospects for elevating Zn-CO_2 battery technology. The high-power density (5 mW cm^{-2}) on Ni incorporation in Pd (0.7 mW cm^{-2}) helps to understand the importance of catalyst designing in advancing sustainable energy conversion and climate change mitigation efforts.

Chapter 4

Perspective

Summary:

In this chapter, we systematically amalgamate the insights gleaned from literature reviews and experiments to comprehensively encapsulate the current perspective on the domain of battery technology.

4.1 Introduction

Batteries have been clearly recognized as integral to addressing global environmental concerns and reducing reliance on non-renewable energy sources. Batteries have evolved significantly, from the invention of Baghdad battery in 200 BC, to the contemporary commercialization of lithium-ion batteries (LIB).

Central to battery functionality are the basic components of anode, cathode, and electrolyte. Strategic optimizations of the battery components can lead to the development of more efficient batteries suitable for applications ranging from electric vehicles to grid-scale storage solutions. Spanning from small-scale to larger-scale applications and the overarching objective of achieving high energy densities and prolonged battery life. This thesis work highlights the importance of structural designing and mechanistic understanding to achieve high battery performance.

4.2 Material Design Strategies

In the first part of this study, we explore the tunability of different anode materials alongside a subsection focusing on electrolyte comprehension related to ion batteries. We have investigated alkali ion batteries. This is due to limited elemental abundance of Li, which has been addressed by favourable cost-effective alternatives such as Na and K ion batteries.

Various anode materials are investigated to achieve high capacity and fast charging capabilities. We have developed materials to investigate various chemistries, including intercalation, alloying, and conversion processes. Chapter 1.2a discusses about carbon-based materials following intercalation-based chemistry. The most common example is graphite, which exhibits minimal volume expansion compared to other materials. However, it faces a limitation of poor theoretical capacity of 372 mAh g^{-1} for LIB. This can be solved by introducing surface defects, heteroatom dopants, increasing interlayer spacing, etc. thus increasing charge storage sites for Li/Na /K-ion batteries (LIB/SIB/PIB). In this chapter, a boron-doped thermally exfoliated graphene (BTEG) is prepared which serves as a universal anode for alkali-ion batteries in terms of high capacity as well as stability. Nevertheless, as the size of alkali ions increases, volume expansion becomes a challenge with BTEG, particularly with insertion of bulkier sized K^+. This issue has been overcome by electrolyte modulation, with the use of highly concentrated electrolytes, such as 5M KFSI (chapter 1.2b). It shows significant improvement in cyclability.

The other class of anode materials includes alloying/conversion-based materials which is discussed in chapter 1.3. This class of materials exhibit high theoretical capacity but since it faces volume expansion, therefore, it is only tested for LIBs. Sn/SnO_2 anodes with core-shell morphology, nanosizing, and carbon introduction has proven to be effective in attaining high capacity along with enhanced stability.

Organic electrolytes, due to their flammability, pose handling challenges, prompting a shift towards aqueous electrolyte-based batteries, which is discussed in part two of the thesis. In this part batteries with theoretical energy density higher than alkali-ion batteries is utilized. Such batteries utilize gases from the ambient atmosphere as active materials, thereby, yielding higher energy density values. Chapter 2.2 explores the intricacies of material design for cathodes in Zn-air batteries. The cathode side interfaces constitute of air and requires electrocatalysts to facilitate electrochemical reactions, i.e., oxygen evolution (OER) and reduction (ORR). Noble metals have traditionally been preferred for OER/ORR, but due to cost constraints, electrocatalysts have been designed with minimal use of Pd (ORR active). Bifunctionality can be achieved with Co_3O_4 which is OER active, while electronic conductivity is facilitated by a Borocarbonitride-based matrix. The morphological tuning of Pd to 2-3 nm nanoparticles and folded Co_3O_4 nanosheets on BCN matrix serves as a bifunctional electrocatalyst. Pd-Co_3O_4@BCN exhibits low overpotentials and high stability, making it suitable for Zinc-air batteries. Chapter 2.3 discusses the idea of reducing CO2 present in the air and utilizing it to form value-added products, such as formate, as demonstrated. Pd-based catalysts play a crucial role in reducing CO_2 and Ni incorporation helps in achieving efficient battery operation.

4.3 Advancement in Battery Technology

The primary objective of this thesis is to develop batteries with a structural design utilizing appropriate materials to achieve high capacity and structural stability. Boron-doped thermally exfoliated graphene (BTEG) represents a novel approach that has not yet been extensively tested across all three battery types. Research on BTEG has significantly contributed to capacity enhancement, stability improvement, and the elucidation of kinetic mechanisms, thereby provides insights into the necessary chemistry required for an anode to be universal (LIB/SIB/PIB). Through various techniques, the investigation of electrolytes in conjunction with BTEG has elucidated the types of electrolytes advantageous for long-term stability in potassium-ion batteries. The preparation of industrially relevant Sn@C highlights the importance of structural design in stabilizing alloy-based materials as well. Pd-Co_3O_4@BCN exemplifies how the nanosizing of Pd nanoparticles and Co_3O_4 nanosheets can increase atomic utilization of noble metals which can effectively enhance performance in oxygen evolution reaction (OER) and oxygen reduction reaction (ORR). In-situ studies have elucidated the intermediates and understanding of structural evolution has been observed to be essential for understanding the reason of such low overpotential and high stability. The real-world application of Zn-air batteries demonstrates the synthesized materials potential for everyday use. Additionally, the exploration of Zn-CO_2 batteries, albeit limited, introduces a promising candidate, NiPd, which exhibits favourable performance. This material could pave the way for further research into materials capable of meeting energy density metrics essential for pushing Zn-CO_2 to commercialization.

4.4 Future Perspectives

The potential of BTEG can be fully realized by testing it in full cell configurations with cathode materials such as $LiNiCoMnO_2$ (NCM) (LIB), $Na_3V_2(PO_4)_3$ (SIB), and Prussian blue or its analogue (PIB), thereby transitioning from laboratory-scale investigations to real-world applications. This approach aims to validate the commercial viability of BTEG in diverse battery systems.

Sn@C, with its industrially feasible synthesis, can be integrated into full cells with compatible cathode material like NCM, paving the way for scalable battery production. Additionally, these anode materials from part 1, hold promise for application as anodeless for solid-state batteries.

In the realm of Zn-air batteries, efforts should also focus on enhancing the longevity of zinc anodes to enable prolonged rechargeability. This can be achieved through structural design considerations aimed at mitigating side reactions that lead to zinc consumption and compromise cyclability.

For Zn-CO_2 batteries, a deeper understanding of formate oxidation chemistry is crucial, particularly for materials like NiPd, to optimize battery rechargeability and ensure sustained performance over multiple charge-discharge cycles.

List of Publications:

1. Surishi Vashishth, Dheeraj Kumar Singh, Vinod Chathakudath Prabhakaran, Muthusamy Eswaramoorthy, (**Published**) Single step strategy for crafting tin/carbon soot composite as highly stable Li-ion battery anode, *Electrochemical Science Advances,*
   Volume2, Issue4, August 2022, e2100019
2. Probing akali-ion storage mechanism and electrolyte engineering for high performance Boron doped graphene (**Manuscript under preparation**), Surishi Vashishth, Abhishek Garg, Swaraj Servottam, Ujjwal Vidyarthi, Muthusamy Eswaramoorthy.
3. Efficient ORR/OER Electrocatalysis through Synergistic Interaction of Pd and Co_3O_4 on Borocarbonitride with Minimized Voltage Gap (**Manuscript under preparation**), Surishi Vashishth, Swaraj Servottam, Abhishek Kumar, Ujjwal Vidhyarthi, Mutthusamy Eswaramoorthy
4. NiPd as an efficient electrocatalyst for Zn-CO_2 batteries (**Manuscript under preparation**) Soumita Chakraborty, Daizy Kalita, Surishi Vashishth, Nijita Mathew, Muthusamy Eswaramoorthy.